Grid-forming control strategies of power electronic converters in transmission grids : application to HVDC link

Ebrahim Rokrok

Centrale Lille

THESE

présentée en vue
d'obtenir le grade de

DOCTEUR

en

Spécialité: Génie Électrique

par

Ebrahim Rokrok

DOCTORAT DELIVRE PAR CENTRALE LILLE

Titre de la thèse:

Grid-forming control strategies of power electronic converters in transmission grids: application to HVDC link

Contrôle en grid-forming pour convertisseurs d'électronique de puissance: application aux liaisons à courant continu de Haute Tension (HVDC)

Soutenue le 04 Juillet 2022 devant le jury d'examen:

Président	Mohamed Machmoum, Professor, Nantes University
Rapporteur	Reza Iravani, Professor, University of Toronto
Rapporteur	Lie Xu, Professor, University of Strathclyde
Examinateur	Sahar Pirouz Azad, Assistant Professor, University of Waterloo
Examinateur	Jon Are Suul, Associate Professor, Norwegian University of Science and Technology
Invité	Thibault Prevost, Engineer, RTE
Invité	Rodrigo Teixeira Pinto, Engineer, Siemens Energy
Co-directeur	Xavier Guillaud, Professor, Centrale Lille Institut
Co-directeur	Bruno Francois, Professor, Centrale Lille Institut
Encadrant	Antoine Bruyère, Associate professor, Centrale Lille Institut

Thèse préparée dans le Laboratoire L2EP
ED 632 ENGSYS

This PhD is supported by the project “HVDC Inertia Provision” (HVDC Pro), financed by the ENERGIX program of the Research Council of Norway (RCN) with project number 268053/E2, and the industry partners; Statnett, Statoil, RTE and ELIA.

Acknowledgements

I would like to thank my esteemed supervisors – Prof. Xavier Guillaud, Prof. Bruno Francois and Dr. Antoine Bruyere for their valuable supervision, support, and tutelage during my PhD program. My gratitude extends to the Research Council of Norway for the funding opportunity within "HVDC inertia provision project" (coordinated by SINTEF research institute) to undertake my studies at Ecole Centrale de Lille, Laboratory of Electrical Engineering and Power Electronics of Lille (L2EP).

Special thanks go to Prof. Reza Iravani and Prof. Lie Xu for being the reviewers of this thesis. I appreciate the time they spent on reading my thesis and providing valuable comments that helped me to improve the quality of the final manuscript.

Other special thanks go to Prof. Mohamed Machmoum, Dr. Sahar Pirouz Azad, Dr. Jon Are Suul, Dr. Thibault Prevost, and Dr. Rodrigo Teixeira Pinto for accepting to be in the thesis evaluation committee. I really appreciated the rich scientific exchange with them during the defense session.

A special note of thanks to Dr. Taoufik Qoria for valuable and timely feedback at key stages in the research process. The meetings and conversations with him were vital in inspiring me to think outside the box, from multiple perspectives to form a comprehensive and objective study. I also would like to thank my lab mates, colleagues, and research team – Frederic, Moez, Artur, Haibo, Hicham, Riad, Hedi, Martin and Pierre for a cherished time spent together in the lab, and in social settings. My appreciation also goes out to my family and friends for their encouragement and support all through my studies.

Outline

List of Figures

List of Tables

Résumé étendu

Les paradigmes énergétiques ont connu une transition significative des énergies fossiles vers des énergies renouvelables propres au cours des dernières décennies. Le bénéfice le plus crucial de cette transition énergétique est la réduction des émissions de gaz à effet de serre (GES). Des pays comme le Danemark, l'Irlande et l'Allemagne ont massivement installé des énergies renouvelables intermittentes systèmes énergétiques et ils fonctionnent avec des pénétrations annuelles de plus de 20% au niveau national. Certains scénarios de l'association européenne de l'énergie éolienne (EWEA) montrent qu'au cours des dix prochaines années, l'énergie éolienne pourrait satisfaire un cinquième de la demande d'électricité en Europe d'ici 2020, un tiers d'ici 2030 et la moitié d'ici 2050. Les sources d'énergie renouvelables (SER) sont interfacées avec des convertisseurs électroniques de puissance pour être connectées aux réseaux électriques alternatifs. Par conséquent, un nombre croissant de convertisseurs électroniques de puissance sont installés dans les systèmes électriques.

Dans les systèmes électriques classiques dominés par les générateurs synchrones (SG), l'amplitude de la tension et la fréquence du système AC au point de connexion des convertisseurs de puissance sont bien maintenues. Cela permet aux convertisseurs de puissance d'être synchronisés avec le système AC via une boucle à verrouillage de phase (PLL) et de suivre pour injecter une quantité de puissance (active et réactive) donnée. Une telle stratégie de commande de convertisseur est connue sous le nom de « grid-following ». L’ intégration de ce type de convertisseurs grid-following dans les systèmes électriques pose des défis pour ces systèmes. Par exemple, si une partie d'un système électrique qui est dominée par des SER avec des convertisseurs interfacés suivant le réseau est isolée du réseau AC principal en raison d'un défaut ou d'un déclenchement de ligne, cela entraînera une perte de synchronisme du fait de l'absence d'une tension alternative sur laquelle se synchroniser. Une autre conséquence est la diminution de l'inertie totale du réseau, ce qui induit une réponse dynamique plus rapide de la fréquence. Le phénomène de faible inertie a déjà été remarqué dans plusieurs régions, comme l'Irlande et le Royaume-Uni. Plus de détails sur ces données sont publiés par l'ENTSO-E.

Pour pallier cet inconvénient, un concept « d'inertie synthétique » a été proposé pour les convertisseurs grid-following. Cependant, en raison d'un retard dans l'estimation de fréquence nécessaire dans cette méthode, la solution d'inertie synthétique n'est pas aussi efficace qu'une inertie réelle pour limiter la dérivée de fréquence. De plus, puisque le contrôle d'inertie synthétique utilise la dérivée de fréquence pour émuler l'effet d'inertie, il induit plus de bruit qui peut perturber le fonctionnement du système et mettre en danger la stabilité de celui-ci. Une autre limitation des convertisseurs grid-following est leur incapacité à fonctionner correctement dans des conditions de réseau faible. En fait, les grands parcs éoliens sont généralement situés dans des zones éloignées et offshore. Les systèmes de transmission à haute tension qui ont de longues distances de transmission sont utilisés pour fournir de l'énergie éolienne aux réseaux principaux. Ceci entraîne une impédance de réseau élevée et, par conséquent, un réseau AC plus faible. De nombreuses études montrent que le fonctionnement des grid-following est limité et très sensible dans des conditions de réseau faible. Par conséquent, un fonctionnement

acceptable avec les performances souhaitées ne peut être garanti. Pour toutes ces raisons et pour éviter plusieurs limitations du contrôle de suivi de réseau, certains pays comme l'Irlande ont fait le choix de limiter l'intégration des convertisseurs de suivi de réseau dans leur réseau à 60 %.

Pour relever ces défis, la manière de contrôler les convertisseurs de puissance pourrait être modifiée, passant du contrôle grid-following à une stratégie différente, qui peut ramener les caractéristiques bénéfiques des SG au système. À cette fin, le nouveau concept de commande grid-forming a été développé. Fondamentalement, un convertisseur grid-forming est un convertisseur qui permet de contrôler directement la tension à ses bornes indépendamment de la tension du réseau. D'un point de vue conceptuel, un convertisseur grid-forming peut être représenté, dans sa forme la plus simple, comme une source de tension à faible impédance série, tandis qu'un convertisseur grid-following est représenté, comme source de courant à haute impédance parallèle.

Les principales questions de recherche de cette thèse sont:

1- Comment expliquer l'origine de la commande grid-forming de manière à déterminer différents types de contrôle et en donner une définition commune? Quelles sont les différentes tâches du contrôle ainsi que les services que les différents types de contrôles grid-forming peuvent fournir ?

2- Quelles sont les différentes stratégies de limitation de courant qui pourraient être utilisées pour les convertisseurs grid-forming en cas de défauts sur le réseau AC? Quel sera l'impact de l'utilisation d'une stratégie de limitation de courant spécifique sur la stabilité transitoire et la synchronisation post-défaut des convertisseurs grid-forming, et comment améliorer la stabilité transitoire ?

3- Est-il possible d'obtenir les mêmes performances pour des convertisseurs grid-forming avec des topologies différentes (c'est-à-dire des convertisseurs de source de tension à 2 niveaux (VSC) et des convertisseurs multiniveaux modulaires (MMC)) dans des conditions normales et défectueuses?

4- Quels sont les défis potentiels pour intégrer le contrôle grid-forming réseau aux interconnexions HVDC?

Les solutions proposées pour répondre aux questions précitées sont adaptées aux réseaux de très haute tension. Cette thèse fait partie du lot 2 du projet de HVDC pro piloté par SINTEF-Trondheim. Dans ce qui suit, les principales conclusions du chapitre sont résumées :

1- Le chapitre 2 présente les fondamentaux du contrôle de puissance active dans un convertisseur électronique de puissance à comportement source de tension. À partir de là, deux solutions différentes, à savoir basées sur PLL et IP-control, sont proposées et les modèles quasi-statiques correspondants sont développés afin d'expliquer leur dynamique dominante. Il est démontré que plusieurs autres variantes de commande grid-

forming pourraient être déduites de l’approche proposée et ils peuvent être classés en quatre groupes fondamentalement différents. Du point de vue de la stabilité et de la robustesse des petits signaux, les commandes grid-forming étudiées dans ce chapitre montrent leur capacité à fonctionner dans des conditions de réseau très faibles. De plus, les services auxiliaires tels que la réponse inertielle et le support de fréquence peuvent être fournis de manière appropriée au réseau AC.

2- Le chapitre 3 traite de la limitation en courant et de la stabilité transitoire des convertisseurs grid-forming. Deux approches générales pour la limitation de courant qui sont l'impédance virtuelle et la saturation du courant de référence sont abordées. Il est mis en évidence que le choix de la stratégie de limitation de courant influence les performances du convertisseur grid-forming en termes de resynchronisation au réseau AC après une perturbation importante. Une analyse approfondie de la resynchronisation post-défaut d’un convertisseur grid-forming utilisant une stratégie de saturation de référence en courant est alors fournie. L'impact de l'angle de référence sur la stabilité transitoire est étudié. Dans le cas d'un creux de tension équilibré, des formules analytiques pour estimer le temps critique d’élimination de défaut est proposé. Il est démontré que le choix de cet angle de référence a une grande influence sur la stabilité transitoire et une valeur sa valeur optimale qui améliore cette stabilité transitoire et permet est calculé. Ensuite, l'efficacité de ce choix optimal pour garantir la stabilité en cas de déphasage provoqué par un événement de refermeture de ligne est vérifiée.

3- Le chapitre 4 couvre principalement l'extension des études dynamiques, qui sont menées sur une topologie VSC à 2 niveaux dans le chapitre précédent, à une topologie MMC. Il est démontré que le comportement dynamique d'un MMC avec contrôle d'énergie interne est similaire à un VSC équivalent à 2 niveaux, non seulement en mode de fonctionnement de contrôle de tension normal, mais également lorsque le MMC passe en mode de contrôle de courant en réponse aux défauts du réseau. Ceci est utile pour simplifier l'analyse en évitant plusieurs dynamiques MMC qui ne sont pas dominantes. Selon cette conclusion, en considérant un VSC équivalent simplifié à 2 niveaux, une liaison HVDC interconnectant deux zones AC est modélisée afin d'évaluer la fourniture d'inertie en contrôlant les convertisseurs HVDC avec la stratégie de formation de grille. Il est montré que le convertisseur grid-forming peut fournir l'inertie s'il n'est pas responsable du contrôle de la tension du bus DC. Cela est dû à un conflit fondamental entre les deux tâches de contrôle. Si l'objectif est d'avoir un support inertiel identique aux deux sous-stations, il est proposé d'intégrer un élément de stockage à la liaison HVDC pour contrôler la tension du bus continu afin que les deux sous-stations puissent assurer directement le support inertiel.

Chapter I: Introduction

I.1 Background

The energy paradigms have been experiencing a significant transition from fossil-based to clean renewables in the past few decades. The most crucial benefit of this energy transitioning is the reduction of greenhouse gas (GHG) emissions. Countries such as Denmark, Ireland, and Germany have massively installed intermittent renewable energy systems and they are operating with annual penetrations of more than 20% at the national level [1]. Some scenarios from the European wind energy association (EWEA) show that over the next ten years, wind energy could meet one-fifth of the electricity demand in Europe by 2020, one-third by 2030, and half by 2050 [2], [3]. Renewable energy sources (RESs) are interfaced with power electronic converters to be connected the AC power grids. Hence, a growing number of power electronic converters are being installed in power systems [4].

In classical power systems dominated by the synchronous generators (SGs), the voltage magnitude and frequency of the AC system at the connection point of the power converters are well maintained. This enables the power converters to be synchronized with the AC system through a phase-locked loop (PLL) and follow to inject a controlled amount of power (active and reactive). Such converter control strategy is known as "grid-following control". Over-integration of grid-following converters in power systems poses challenges for these systems. For example, if a part of a power system that is dominated by RESs with grid-following interfaced converters is isolated from the main AC grid due to a fault or line tripping, it will lead to a loss of synchronism because of the absence of an AC voltage to follow. Another consequence is the decrease of the total grid inertia, which induces a faster dynamic response of the frequency [5]. The low-inertia phenomenon has been already noticed in several areas, such as Ireland and UK. More details about those data are published by ENTSO-E [6]. To overcome this drawback, a "synthetic inertia" concept has been proposed for grid-following converters. However, due to a delay in frequency estimation required in this method, synthetic inertia solution is not as efficient as a real inertia to limit the frequency derivative. Moreover, since the synthetic inertia control uses the frequency derivative to emulate the inertial effect, it induces more noise that may disturb the system operation and endanger the system stability [7]. Another limitation of grid-following converters is their inability to operate correctly under weak grid conditions. In fact, large wind farms are usually located in remote and offshore areas. High voltage transmission systems that have long transmission distances are used to deliver wind power to main grids. Long transmission lines or cables result in a high grid impedance, and thereby, a weaker AC grid. Many studies show that the operation of grid-following converters is limited and highly sensitive under weak grid conditions. Hence, an acceptable operation with desired performances cannot be guaranteed [8]. Because of all these reasons and to avoid several limitations of the grid-following control, some countries such as Ireland made a choice to limit the integration of grid-following converters in their grid to 60 percent [9], [10].

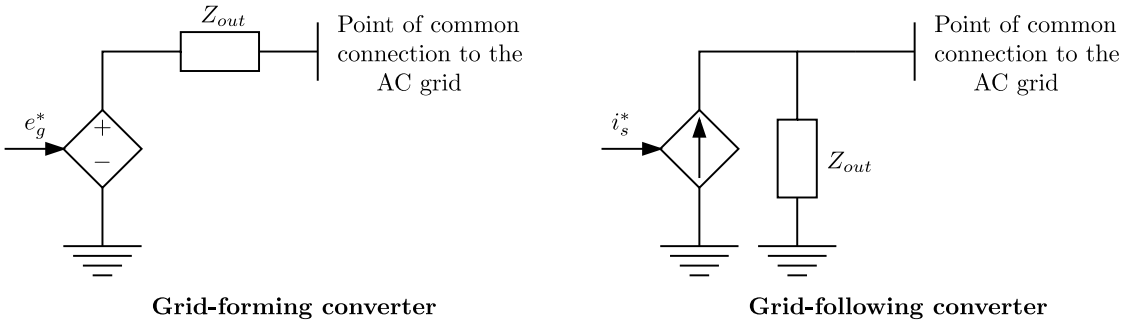

Figure I-1: Basic representation of the grid-forming and grid-following converters.

To tackle these challenges, the way to control power converters could be changed from grid-following control to a different strategy, which can bring back the beneficial characteristics of SGs to the system. To this end, the new concept of grid-forming control has been developed. The first publication that proposed the use of power converters to support the grid during power imbalances and frequency deviations is back to 2008 by introducing the virtual synchronous generator (VSG) concept [11]. At that time, there was no exact talk on the grid-forming concept. The interest in this type of control has grown significantly in recent years, both in terms of academic research and development of industrial projects. However, no common definition of grid-forming control is admitted by the scientific community yet. Neither IEEE standards nor international electro-technical vocabulary (IEV) comprise any definition of the term "grid-forming".

Basically, a grid forming converter is a converter that allows to directly control the voltage at its terminals independently to the grid voltage. From a conceptual point of view, a grid-forming converter can be represented, in its simplest form, as a voltage source with a low series impedance, while a grid-following converter is represented, in a dual way, as a current source with a high parallel impedance (see Figure I-1) [12].

According to the national renewable energy laboratory (NREL) defines grid-forming control as any converter control that regulates an instantaneous terminal voltages without any PLL [13]. As said by the European network of transmission system operators for electricity (ENTSO-E), the grid-forming capabilities need to be defined in the grid codes to enable harmonized solutions [14]. More specifically, the grid-forming capabilities are defined as follow [14]:

• Creating (forming) system voltage
• Contribution to fault level (short circuit power)
• Preventing adverse control interactions
• Contribution to inertia provision
• Sink for unbalance
• Sink for harmonics
• Supporting system survival to enable the effective operation of low frequency demand disconnection for rare system splits

Over the past years, various grid-forming control strategies have been proposed and analyzed [15], [16]. They include: droop methods [12], [17], power synchronization control [18], [19], Synchronverter [20], virtual synchronous machine (VSM) [21], [22], direct power control [23], matching control [24], etc. The studied grid-forming controls

in the literature are based on different implementations and realizations of specific functionalities, however they all share the common principle of forming the output voltage by controlling its magnitude and angle.

Today, the research on grid-forming control is mainly oriented toward proposing new and more effective control schemes for different applications and evaluating their performances with simulation tools. For instance, in [25] the authors discuss the applicability of VSM-based grid-forming scheme to high-voltage direct-current (HVDC) converters, while in [26], an interesting study is performed on the frequency stability of the Irish grid when replacing all the SGs in the system by grid-forming converters. A similar analysis has been presented in [27] on the IEEE 39-bus test case. Grid-forming converters are not only applicable to the high voltage transmission system but also to the distribution system and low voltage microgrids. As an example, in [28], a bidirectional grid-forming converter with a fault-tolerant functionality is applied to an islanded AC microgrid using a centralized control architecture. Some experimental results are presented. These works represent only a very small part of the vast literature on this topic. In general, it can be said that most of the studies in the literature provide control methods for grid-forming converters and example of theoretical applications of those controls. There are also some grid-forming pilot projects and demonstrators developed worldwide with focus on the results of on-field experimentation.

I.2 Overview of the research and pilot projects on grid-forming control in Europe

I.2.1 SMA projects - St. Eustatius and Saba islands

As a leading global company in solar systems technology, SMA has demonstrates great interest in grid-forming converters for large-scale application carrying out various projects all over the world with different size and targets. SMA Sunbelt Energy GmbH planned and executed a solar and battery storage project on the Caribbean island of St. Eustatius [29]. The project was installed and commissioned in two phases, where the second phase (commissioned in November 2017) included large grid-forming converters with batteries. Figure I-2 illustrates the schematics setup of the solar and battery storage system when it was completed by phase 2.

The setup consists of 5.2 MVA of battery converter with grid-forming control, 5.77 MWh battery capacity, 3.85 MVA solar converters and a hybrid plant controller to supply the electrical grid with a peak demand of about 2 MW. The grid-forming converters by SMA use droop control for generating both frequency and voltage magnitude references. The implemented solution allows a 100 % solar power feeding for 10.5 hours per day in diesel-off mode without compromising the reliability of the system. In the first year, the total energy provided was around 6.49 GWh with a diesel saving of 1.7 million liters and 4600 tons of CO^2 reduction.

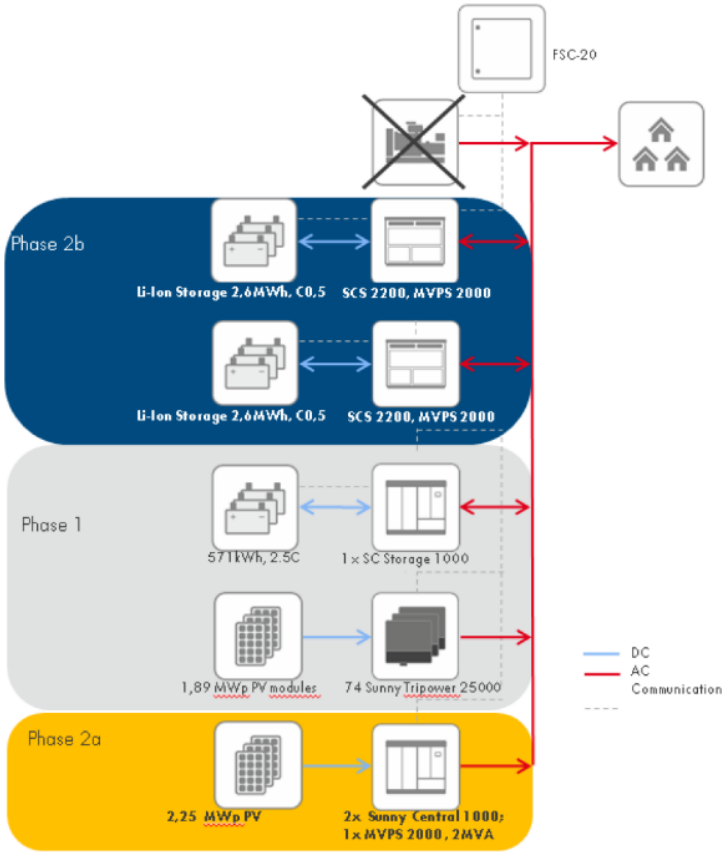

Figure I-2: Solar and storage system after Phase 2 in St. Eustatius island [29].

Another similar experience was done in February 2019 in the island of Saba, neighboring to the island of St. Eustatius. The storage integration in the generation system was conducted in two phases: in phase one, an 800 kW / 393 kWh storage system was designed and installed for the ramp rate control of a 1.142 MW PV plant. In phase two, both the storage capacity and the installed PV power were increased to 2.3 MWh and 2 MWp, respectively. Batteries were connected to the grid via a grid-forming converter of 2.2 MW while the PV plant was connected via 64 decentralized converters of 25 kW each. Even in this case, with a total load of about 1.2 MW in the island, the system could provide up to 10 hours/day of 100 % renewable supply in diesel-off mode operation, which resulted in the saving of around one million liters of diesel [29].

I.2.2 Dersalloch Wind Park

From May to June 2019, for approximately six weeks, a 69 MW wind park in Dersalloch, Scotland owned by Scottish Power Renewable (SPR) was operated in grid-forming mode with VSM control strategy. Each of the 23 wind turbine generators with 3 MW power rating were controlled for exploring inertia contributions of between H=0.2 s and H=8 s. Events applied in the test phase include phase step response, interconnection tripping, and frequency events. During all recorded events, the park responded immediately and autonomously with power responses appropriate to the type of adverse event and in the absence of over-currents, over-voltages, or detachments [30]. All this turned out to be true, however, in the presence of appropriate weather conditions, which means in the persistence of sufficient wind to guarantee the nominal power of the park. The trial continued the following year from August to October 2020 [31]. In this

case, the aim of the experimentation was to verify the islanded mode and black start capabilities of the park. Results confirmed that the park can operate in islanded mode with a minimum number of turbines in grid-forming mode and it is possible to perform a black start process from a certain number of turbines and energizing the transmission grid up to the 132 kV / 275 kV level.

I.2.3 La Plana Hybrid Pilot Plant

Siemens Gamesa owns a testing plant located in La Plana, near Zaragoza (Spain). A wind turbine generator (850kW), a solar PV plant (245 kW), 3 diesel gensets (3 x 222kW) and two different battery technologies (Li-Ion, 435kW / 145kWh and Redox-Flow 120kW, 400kWh) are combined with variable loads to emulate/test customer load data sets on an adequate scale in a real plant [32]. This hybrid system was commissioned in December 2015, and it is under testing since 2018. The system is shown in Figure I-3 [33].

By modifying the bi-directional converters for energy storage, the black start and grid forming capabilities are provided. This allows the hybrid system to enable the zero diesel operation (ZDO) mode, being able to both generate the electrical grid without the participation of the diesel gensets [32]. Apart from energy saving purposes, this type of projects is attracting attention for its economic prospects in providing different services. Thanks to the storage units, this solution can be used for energy shifting application; thanks to the GFM capabilities, the plant can be allocated in strategic electrical nodes and provide ancillary services, such as frequency support, peak shaving, synthetic inertia, and black start.

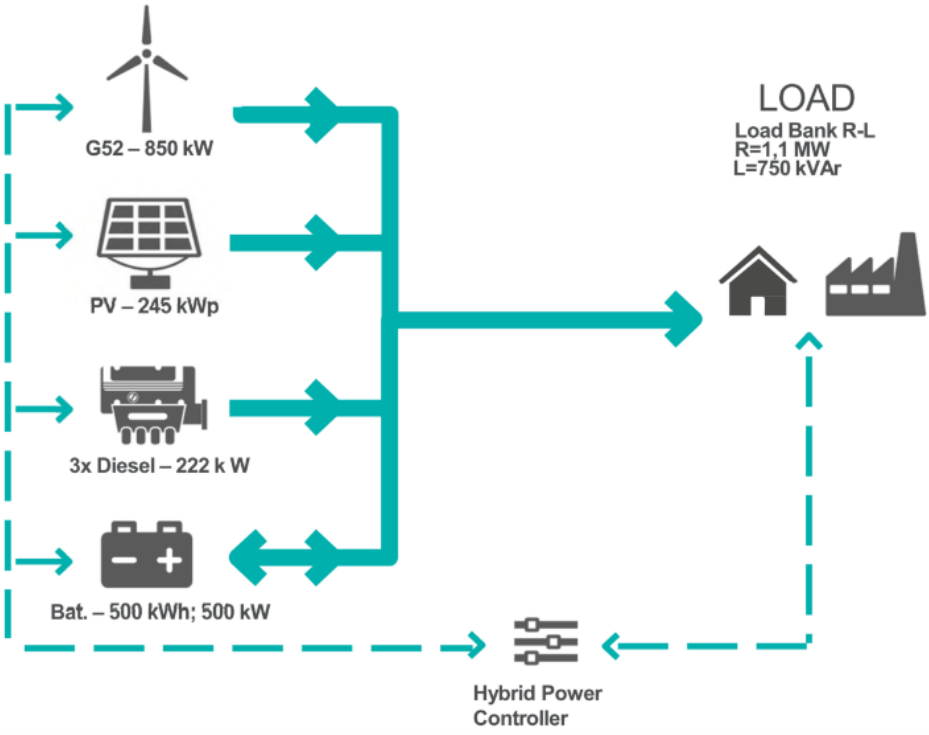

Figure I-3: Scheme of La Plana pilot plant [33].

Figure I-4: The two demonstrators deployed by the OSMOSE WP3 partners [36].

I.2.4 OSMOSE Project

The optimal system-mix of flexibility solutions for European electricity (OSMOSE) is a four-year project started in 2018 and funded under the H2020 research and innovation program. Four large-scale demonstrators led by Transmission System Operators (TSOs) explore the technical and economic feasibility of innovative flexibility services and providers, including: grid forming, multi-services by hybrid storage, near real-time cross border exchanges, and smart zonal energy management system [34]. The project includes 33 partners among research centers, industries, TSOs and market operators from nine European countries. The work package 3 (WP3) of the project is titled: Grid Forming for the synchronization of large power systems by multi-service hybrid storage [35]. The WP3 of the OSMOSE project gathered RTE (Reseau de Transport d'Electricite), EPFL (Ecole Polytechnique Federale de Lausanne) and Ingeteam R&D to demonstrate [36]:

•the technical feasibility to provide grid-forming capability of commercially available power-electronics interfaced energy storage systems (ESS).

• that this solution can be industrially deployed without converter oversizing, and

• that its contribution to power system stability can be quantified by means of external measurements without a detailed knowledge of specific low-level controls.

For these purposes, 2 demonstrators were deployed (see Figure I-4):

- On the left: Ingeteam implemented a grid-forming control on the power converter interfacing a hybrid energy storage system (HESS) to the grid. The 1 MVA fully containerized solution was specifically built for the OSMOSE project using off-the-shelf equipment and connected to a 20 kV feeder in a RTE substation. It included four lithium-ion battery racks (0.5 MVA 60 min) and six ultra-capacitor (UC) racks (for a total of 1MW-10s).
- On the right: the EPFL demonstrator quantified that the provision of synchronization services (inertial response) superposed to traditional ancillary services (e.g., voltage and frequency regulation) and dispatch tracking can effectively reduce local frequency variations. This was achieved with a pre-existing battery energy storage system (BESS) composed by a 720kVA/560kWh Lithium Titanate Oxide BESS, connected to a 20 kV feeder of the EPFL Campus.

After some modelling and simulation phases for control design and performance assessment purposes, the demonstrators entered the testing, installation and operational phases. RTE and Ingeteam performed factory acceptance tests (FAT) using a power

hardware in the loop (PHIL) platform available at Ingeteam power laboratory facilities. On EPFL side, the BESS demonstrator was successfully operated in both grids connected and GFM mode and was used to validate the multi-service provision originally scheduled to be carried out on the RTE-Ingeteam demonstrator. Finally, results were assessed through key performance indicators (KPI) and scaled-up using a real-time simulation benchmark released open source by EPFL and referring to a modified low-inertia IEEE 39-bus network [36].

I.2.5 Fluence, Siemens and Litgrid Project on Baltic's first storage as transmission pilot project

Lithuania has planned to pursue energy independence as it integrates synchronously to the continental European synchronous area in 2025 and to increase its use of RESs from 20 percent to 45 percent in 2030, rising to nearly 100 percent by 2050. However, high penetration of non-synchronous renewable generation is likely to create system stability challenges. Securing the stable operations of Lithuania's power system during this energy transition requires further innovation and development demonstration. Fluence, the leading global energy storage technology, software and services provider, Siemens AG and Litgrid, Lithuania's TSO, have announced the first pilot project in the Baltics (in April 2021) to use BESS in the transmission system. The 1 MW pilot near Vilnius will serve as a proof-of-concept for much larger planned projects in Lithuania. Increasing amounts of renewable energy require additional power flow capacity on key transmission lines at certain points of the grid. With "virtual transmission lines" (VTL), energy storage is placed along a transmission line and operated to inject or absorb active and reactive power, mimicking transmission line flows. Storage deployed this way can also provide numerous other critical network services, including grid-forming capabilities, virtual inertia for local grid stability, black start capability, power oscillation damping and voltage regulation service. These capabilities are an important step toward the next level of grid protection and resiliency, enabling the use of energy storage systems to mitigate different types of potential events affecting grid reliability and stability [37].

I.2.6 HVDC inertia provision project

ENTSO-E is planning the future grid with the Ten Years Network Development Plan, (TYNDP) , where many new HVDC links are mentioned as highlighted on the map in Figure I-5 [38]. This factor, in turn, results in a significant increase of power electronic converters in the transmission level. The project "HVDC inertia provision" [39], commissioned in 2017, aims to develop methods for assessing the value of and the requirements for inertia emulation from HVDC transmission schemes. Furthermore, control strategies suitable for inertia emulation by HVDC converter stations with

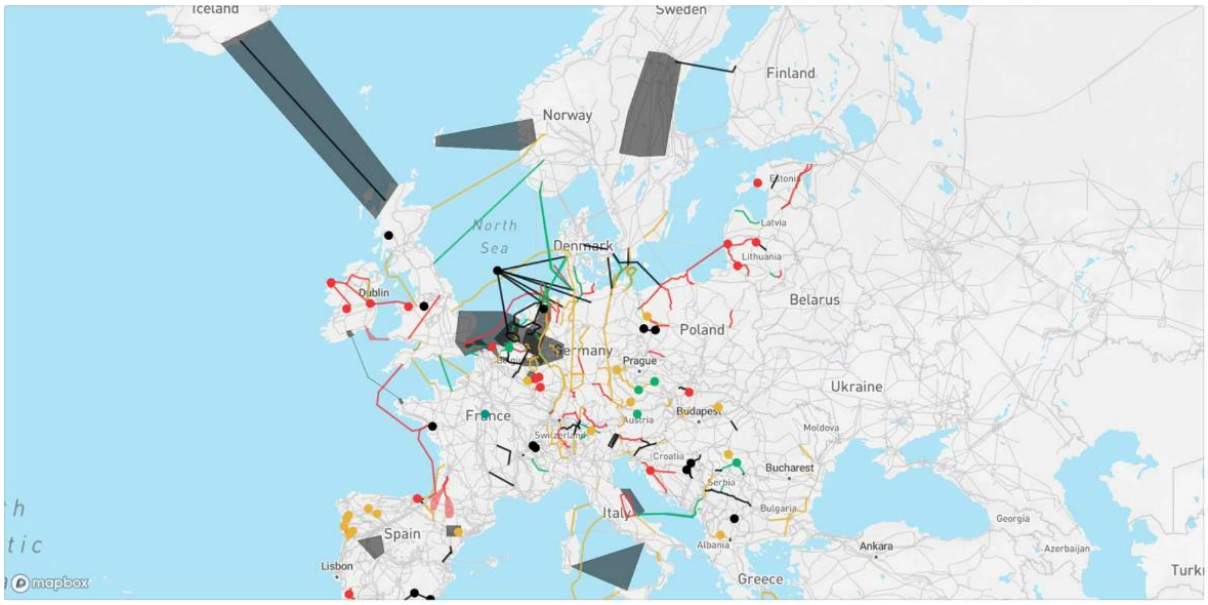

Figure I-5: HVDC links in Europe [38].

different power converter topologies are under investigation, and their performance and stability characteristics are being analyzed. Detailed models of HVDC transmission schemes with inertia emulation capability will also be developed for analyzing the influence on the stability of large-scale power systems. The project includes eight partners among universities, TSOs and energy companies from Norway, Belgium, and France. The methods and techniques resulting from the research activities within the project will support the development of "smarter transmission systems" in a future context with limited physical inertia from traditional generation plants.

I.3 Objectives of the thesis and main contributions

This PhD is a part of the work package 2 within the HVDC inertia provision project. The main research questions of this thesis are:

1- How the origin of the grid-forming control can be explained to help deriving various types of this control and giving a common definition of it? What are the different tasks of the control also the services that various types of the grid-forming controls can provide? Is there any coupling between the control tasks?

2- What are the different current limitation strategies that could be utilized for grid-forming converters in case of faults at the AC grid? What will be the impact of employing a specific current limitation strategy on the transient stability and post-fault synchronization of the grid-forming converters, and how to enhance the transient stability?

3- Is it possible to obtain the same performance for grid-forming converters with different topologies (i.e., 2-level voltage source converters (VSCs) and modular multi-level converters (MMCs)) under normal and faulty conditions?

4- What are the potential challenges for integrating grid-forming control to the HVDC interconnections?

The solutions proposed to answer the aforementioned questions are compatible with the highest voltage and highest power rating of existing power converters in transmission systems. It should be noted that the secondary and the tertiary control are not discussed in the thesis. Moreover, conducting studies on the harmonics, nonlinear loads and motor loads are out of the scope of this thesis. The main contributions of this work in each chapter are listed below:

1- A fundamental explanation of active power control with a voltage source behavior, which is considered as the principal of the grid-forming control definition is presented. Based on that, two grid-forming control with different capabilities and functionalities are then derived and along with other existing grid-forming variants in the literature, they are classified in four main types. The criteria for the classification consist in active power response under various grid strength, inertial effect provision, and coupling/decoupling of frequency support from the active power control (Chapter 2).
2- A novel current limitation strategy based on a current saturation algorithm (CSA) for grid-forming converters is proposed. The proposed CSA includes a new degree of freedom in the control that, by an optimal tuning, leads to an improvement in transient stability (Chapter 3).
3- The proposed solutions are implemented to an MMC-VSC topology, where the MMC internal energy control has been highlighted as a critical factor in achieving similar performance to a 2-level VSC both in normal and abnormal conditions (Chapter 4).
4- The challenges ahead of the HVDC interconnections with grid-forming control operation for virtual inertia emulation is addressed and a solution based on integrating a storage device to the DC link is proposed to stabilize the system (Chapter 4).

I.4 List of publications derived from this work

The publications resulting from this thesis are listed below:

- **Journal I**: "*Transient Stability Assessment and Enhancement of Grid-Forming Converters Embedding Current Reference Saturation as Current Limitation Strategy*", **E. Rokrok**, T. Qoria, A. Bruyere, B. Francois, X. Guillaud, IEEE Transactions on Power Systems, 2022.
- **Journal II**: "*Integration of a Storage Device to the DC Bus of a Grid-Forming Controlled HVDC Interconnection*", **E. Rokrok**, T. Qoria, A. Bruyere, B. Francois, X. Guillaud, Electric Power System Research, 2022.
- **Journal III**: "*Classification and Dynamic Assessment of Droop-Based Grid-Forming Control Schemes: Application in HVDC Systems*", **E. Rokrok**, T. Qoria, A. Bruyere, B. Francois, X. Guillaud, Electric Power System Research, 2020.
- **Journal IV**: "*A PLL-Free Grid-Forming Control with Decouple Functionalities for High-Power Transmission System Applications*", T. Qoria, **E.Rokrok**, A. Bruyere, B. Francois, X. Guillaud, IEEE Access, 2020.

- **Conference I**: "*Integration of a Storage Device to the DC Bus of a Grid-Forming Controlled HVDC Interconnection*", **E. Rokrok**, T. Qoria, A. Bruyere, B. Francois, X. Guillaud, Power System Computation Conference (PSCC2022), Porto, Portugal, 2022.
- **Conference II**: "*Classification and Dynamic Assessment of Droop-Based Grid-Forming Control Schemes: Application in HVDC Systems*", **E. Rokrok**, T. Qoria, A. Bruyere, B. Francois, X. Guillaud, Power System Computation Conference (PSCC2020), Virtual Conference, 2020.
- **Conference III**: "*Impact of Grid-Forming Control on the Internal Energy of a Modular-Multi-Level Converter*", **E. Rokrok**, T. Qoria, A. Bruyere, B. Francois, X. Guillaud, 22nd European Conference on Power Electronics and Applications (EPE'20 ECCE Europe), Virtual Conference, 2020.
- **Conference IV**: "*Effect of Using PLL-Based Grid-Forming Control on the Active Power Dynamics Under Various SCR*", **E. Rokrok**, T. Qoria, A. Bruyere, B. Francois, X. Guillaud, IECON 2019-45th Annual Conference of the IEEE Industrial Electronics Society, Lisbon, Portugal, 2019.

Chapter II: Fundamentals on synchronization, power control and service provision of a power electronic converter connected to an AC system

The fundamental aim of a voltage source converter connected to an AC grid is to convert the DC power into an active power on the AC grid and vice versa depending on the direction of the power flow. In order to achieve this goal, power converters may behave as current injectors (grid-following) or voltage sources (grid-forming). In both solutions, the question of the synchronization and the way to manage the active power exchange with the grid plays a crucial role. Until now, the grid-following concept has been used in most applications. However, using the power converters based on the grid-forming concept may come up to be an interesting solution in certain situations.

In this chapter, first a fundamental concept is proposed to explain two different ways of controlling the active power in section II-1. Then, some brief recalls about the grid-following control are given in section II-2. In section II.3, the operating principle of a converter based on “grid-forming control” is explained with some simplified quasi-static models and two different types of grid-forming structures are proposed. Section II.4 is devoted to dynamic assessment of the proposed grid-forming control schemes. Assuming that the power converter is connected to an infinite bus with constant frequency, the proposed control schemes, while considering their dynamic behavior, stability and robustness aspects are studied. Thereafter, the dynamic studies are expanded to ancillary service provision to an AC grid where the grid frequency is not constant anymore. Apart from the synchronization and constant power injection achieved by the developed control schemes, the ability of the proposed controls to contribute to the grid support i.e., inertia provision and frequency support is assessed. Section II.5 describes, in general, some other grid-forming control variants that are available in the literature and classifies them together with two proposed strategies into four fundamentally different groups according to their capabilities/functionalities. Finally, section II.6 concludes this chapter.

II.1 Two solutions for active power control with a simplified VSC

The main aim of a power electronic converter is to convert a DC power to AC power and vice-versa. In this section, the simplest topology to connect a DC grid to an AC grid at the point of common coupling (PCC) is considered as shown in Figure II-1. It consists of a voltage source converter (VSC) connected on one side to a DC voltage source u_{DC} and on the other side to an AC grid through an RL circuit (an ideal VSC). $v_{m_{abc}} = [v_{m_a} \quad v_{m_b} \quad v_{m_c}]^T$ is the modulated voltage obtained by the modulation of the DC bus voltage through the switching stage. In the following, the switching time (T_s) is supposed to be small enough to assimilate $v_{m_{abc}}$ to its average value. The low-level control is not taken into account in this chapter. It is assumed that the modulated voltage is directly driven by a set of three-phase reference signal $v^*_{m_{abc}}$ in the control (i.e., $< v_{m_{abc}} >_{T_s} = v^*_{m_{abc}}$). The power converter is assumed to be connected to the AC grid through a simple RL filter (R_c, L_c). The reactance usually represents the leakage reactance of the transformer. For this kind of application, the typical value of X_c in per-unit is around 0.15 [pu] [40]. The AC grid is assumed to be balanced. It is modeled by a Thevenin equivalent composed of a voltage source $v_{e_{abc}}$, an inductance L_g and a resistance R_g. For high voltage applications such as power transmission systems, the resistance of this connection filter is assumed much smaller than the reactance ($R_g \ll X_g = L_g\omega_g$). Although the model from of Figure II-1 is oversimplified, however, it is very useful for introducing the synchronization and the power exchange principle between power converters and AC grids.

In this thesis, modelling and control are done in per-unit system. The base quantities are defined in Table II-1 [40].

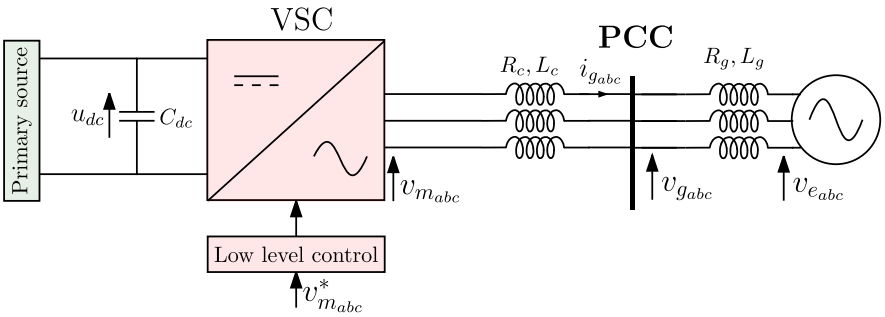

Figure II-1: Representation of a VSC connected to an AC system.

Table II-1: Base quantities in per-unit system [40].

Base quantity	Value	Base quantity	Value
Base power S_b	1 [GW]	Base current I_b	$\frac{S_b}{\sqrt{3}V_b}$ =1804.22 [A]
Base voltage V_b: nominal line-toline voltage	320 [kV]	Base impedance Z_b	$\frac{V_b^2}{S_b}$ =102.4 [Ω]
Base angular frequency ω_b	314.16 [rad/s]	Base inductance L_b	$\frac{Z_b}{\omega_b}$ =0.326 [H]
Base frequency f_b	$\frac{\omega_b}{2\pi}$ =50 [Hz]	Base capacitance C_b	$1/(\frac{Z_b}{\omega_b})$ =3.067 [F]

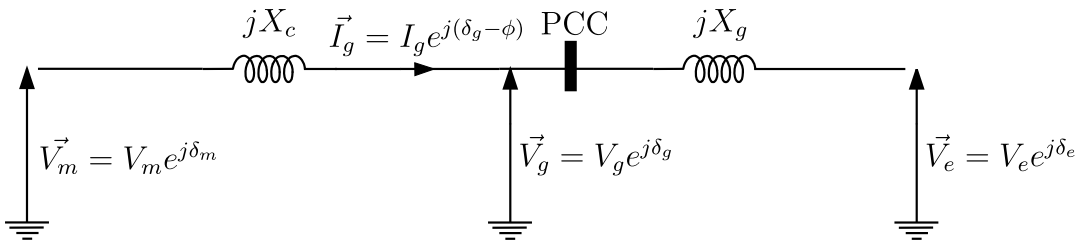

Figure II-2: Single-phase quasi-static model of the VSC connected to the grid.

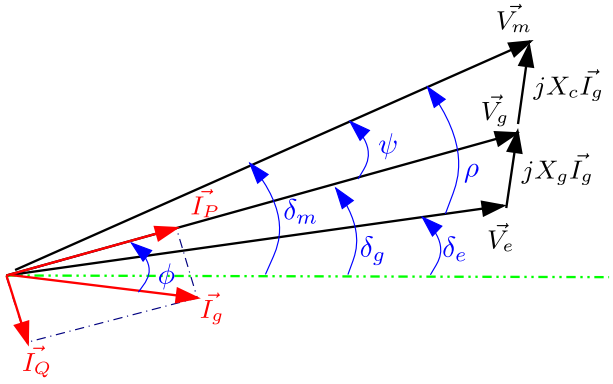

Figure II-3: Phasor representation of the studied system.

The single-line phasor model of the studied system of Figure II-1 that is illustrated in Figure II-2 can explain the basis of active power control in a power electronic converter. The phasor diagram of associated to this model is drawn in Figure II-3.
Let us define the notation that will be used in the sequel:

- Phasor angles: Ideal voltage source angle δ_e
  Grid voltage angle δ_g
  Estimated grid voltage angle $\tilde{\delta}_g$
  Modulated voltage angle δ_m
- Frequencies Ideal voltage source frequency ω_e
  Grid voltage frequency ω_g
  Estimated grid voltage frequency $\tilde{\omega}_g$
  Modulated voltage frequency ω_m
- Time domain angles: Ideal voltage source angle $\theta_e(t) = \omega_e\omega_b t + \delta_e$
  Grid voltage angle $\theta_g(t) = \omega_g\omega_b t + \delta_g$
  Estimated grid voltage angle $\tilde{\theta}_g(t) = \tilde{\omega}_g\omega_b t + \tilde{\delta}_g$
  Modulated voltage angle $\theta_m(t) = \omega_m\omega_b t + \delta_m$

According to the phasor diagram of Figure II-3, there are two different ways to control the active power of the converter:

1- Power control with the grid current:
The active power at the PCC can be expressed as:

$$P = \Re\left(\overrightarrow{V_g}\,\overrightarrow{\bar{I}_g}\right) = \overrightarrow{V_g}\,\overrightarrow{I_p} = V_g I_P = V_g I_g\, cos(\phi) \qquad \text{(II- 1)}$$

where $\overrightarrow{\overline{I_g}}$ is the complex conjugate of the grid current vector. As the voltage is assumed to be set by the electrical network, the power is controlled by varying the magnitude of the current vector, e.g. I_g. $\overrightarrow{I_P}$ is the control input vector of the power. The VSC operates as a controlled current source that can be managed by automatically adapting the power electronic converter output voltage $\overrightarrow{V_m}$.

In other word, the power control is linked to the current management. The reference for the active current I_P^* is obtained through a simple division of the power reference P^* by the RMS measurement of the PCC voltage as shown in Figure II-4. In steady-state $I_P^* = I_P$, thanks to a current control loop.

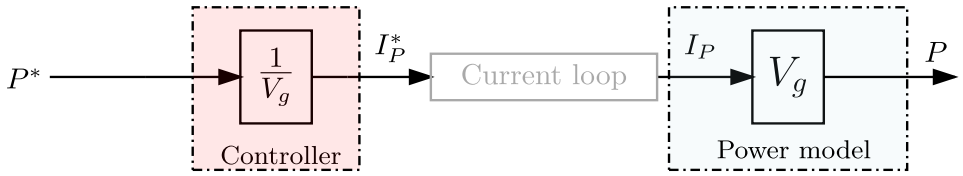

Figure II-4: Principle of the open loop power control with the current controlled mode.

A more robust control of the active power can be achieved based on the closed-loop control:

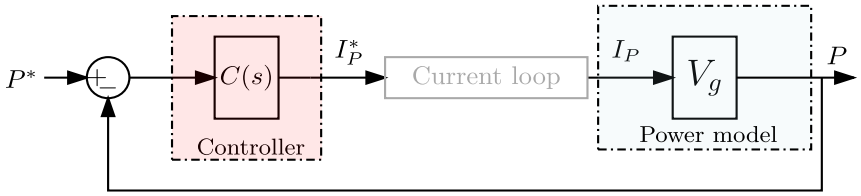

Figure II-5: Principle of the closed-loop power control with the current controlled mode.

2- Power control with the modulated voltage:

In steady state, another formulation based on the modulated voltage can be derived for the active power. Applying Kirchhoff's voltage law to the electrical circuit of Figure II-2 gives:

$$\overrightarrow{V_m} = j(X_c + X_g)\overrightarrow{I_g} + \overrightarrow{V_e} \qquad \text{(II- 2)}$$

$$\overrightarrow{V_m} = jX_c\overrightarrow{I_g} + \overrightarrow{V_g} \qquad \text{(II- 3)}$$

As no losses are considered ($R_c = R_g = 0$), the active power at the PCC is equal to the one at the VSC output: $P = \Re\left(\overrightarrow{V_g}\,\overrightarrow{\overline{I_g}}\right) = \Re\left(\overrightarrow{V_m}\,\overrightarrow{\overline{I_g}}\right)$.

By substituting $\overrightarrow{I_g}$ from (II-2) and (II-3) in the active power expression at the modulated voltage terminal ($P = \Re\left(\overrightarrow{\mathrm{V_m}}\,\overrightarrow{\overline{I_g}}\right)$) two following expressions for the active power are derived [41]:

$$P = \Re\left[\overrightarrow{V_m}\,\overline{\left(\frac{\overrightarrow{V_m} - \overrightarrow{V_e}}{j(X_c+X_g)}\right)}\right] = \frac{V_m V_e}{X_c+X_g} sin(\rho) \;\;,\;\; \rho = \delta_m - \delta_e \qquad \text{(II- 4)}$$

$$P = \Re\left[\overrightarrow{V_m}\overline{\left(\frac{\overrightarrow{V_m} - \overrightarrow{V_g}}{jX_c}\right)}\right] = \frac{V_m V_g}{X_c} sin(\psi) \;\;,\; \psi = \delta_m - \delta_g \qquad \text{(II- 5)}$$

In these cases, the control vector is the modulated voltage $\overrightarrow{V_m}$ and the current $\overrightarrow{I_g}$ is a consequence. The VSC operates as a controlled voltage source. Since it is not possible to accept a large variation on the magnitude of the VSC output voltage, instead the active power is controlled by varying its angle δ_m.

Either way, the active power control needs to generate a control reference (I_P^* or δ_m^*) in such a way that the active power tracks a given power reference P^* in steady-state. To this end, each of the presented solutions has specific requirements in order to be adapted to the converter control that will be elaborated in following sections.

II.2 Power control with a controlled current source (grid-following principle)

For a given power reference P^*, the active current I_P^* is deduced as shown in fig.4 or fig.5. In order to control the active current I_P, the grid voltage magnitude and its phase angle has to be known for the control so that $\overrightarrow{I_P}$ could be set aligned with $\overrightarrow{V_g}$ as illustrated in Figure II-3. Therefore, providing an estimate of the grid angle δ_g to the control system of the current is compulsory.

$\overrightarrow{V_g}$ is an external input and the current $\overrightarrow{I_g}$ is known, so $\overrightarrow{V_m}$ can be deduced from (II-2). In case of a change in $\overrightarrow{V_g}$, $\overrightarrow{V_m}$ has to be modified automatically in order to keep a constant grid current in phase and magnitude (and because the active power reference is unchanged). This is the origin of the name "grid-following". In the literature, this type of control is also called "grid-feeding".

In the same way as for the active power, similar control principle in Figure II-4 and Figure II-5 can be applied for the reactive power. In time-domain, the general organization of a grid-following control is given in Figure II-6. It is decomposed in three main parts:

- Average value control of the active and reactive powers. The reactive power loop can be replaced by an RMS voltage loop.
- Estimation of the grid angle.
- Current control.

In Figure II-6 and Figure II-6, the current control is implemented in (abc) and (d-q) frame, respectively. It does not change the general organization. In any case, an estimation of the grid angle is needed either to generate the three-phase sinusoidal current references or to be used in the Park transformation. Note that the active power "P" has been replaced by the instantaneous power "p". To estimate the grid angle, a Synchronous Reference Frame Phase-Locked Loop (SRF-PLL) is often used. The structure of the SRF-PLL is recalled in Figure II-7 [40].

The inputs of the PLL are the three-phase voltage signals $v_{g_{abc}}$, which are sensed at the PCC. The estimated grid frequency $\tilde{\omega}_g$ and angle $\tilde{\theta}_g$ are the outputs of the PLL. The aim of the PLL is to achieve the equality $\theta_g = \tilde{\theta}_g$ in steady state. This is done thanks to the PI controller. The synchronization mechanism and tuning of the PLL is given in Appendix A. For the tuning of the PLL, its response time is mostly chosen between $10\text{ms} \leq t_{r_{PLL}} \leq 100\text{ms}$.

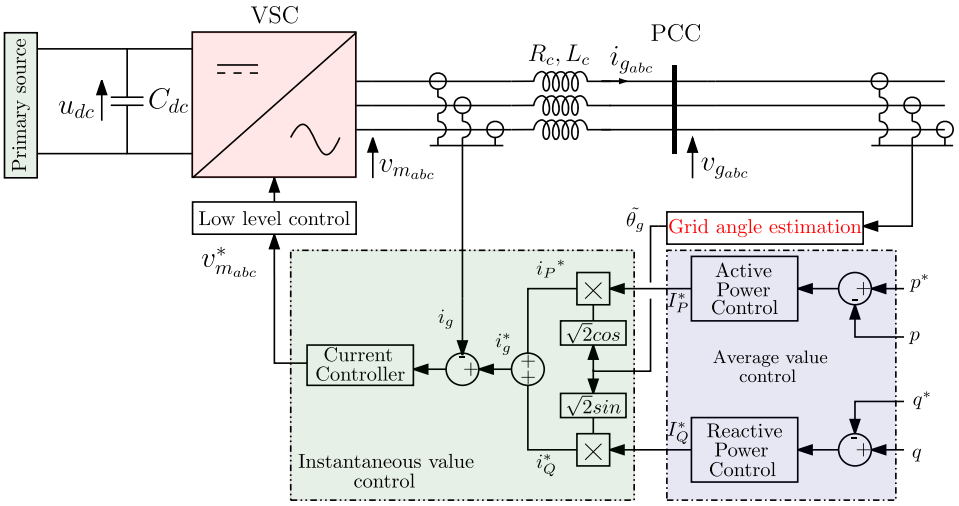

(a) Control in abc frame

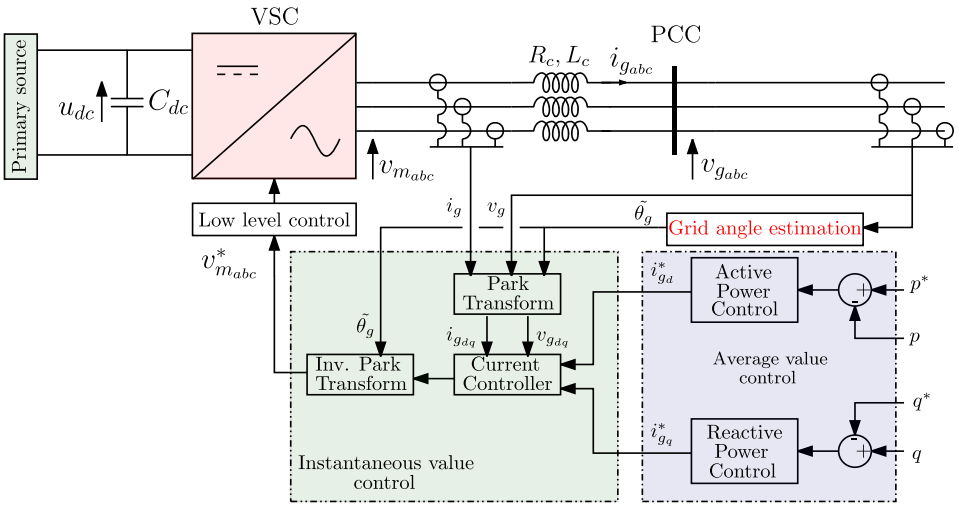

(b) Control in d-q frame

Figure II-6: General principle of the grid-following control.

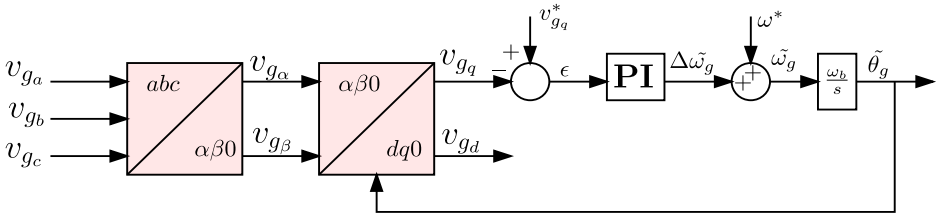

Figure II-7: Structure of SRF-PLL.

Current controller:

To design the current controller, a dynamic model of the AC filter (Figure II-1) is first expressed by considering losses (resistance R_c) in the Synchronous Reference Frame (SRF) in per-unit:

$$\frac{di_{g_d}}{dt} = \frac{\omega_b}{L_c} v_{m_d} - \frac{\omega_b}{L_c} v_{g_d} - \frac{R_c}{L_c} \omega_b i_{g_d} + \omega_g \omega_b i_{g_q} \quad \text{(II- 6)}$$

$$\frac{di_{g_q}}{dt} = \frac{\omega_b}{L_c} v_{m_q} - \frac{\omega_b}{L_c} v_{g_q} - \frac{R_c}{L_c} \omega_b i_{g_q} - \omega_g \omega_b i_{g_d} \quad \text{(II- 7)}$$

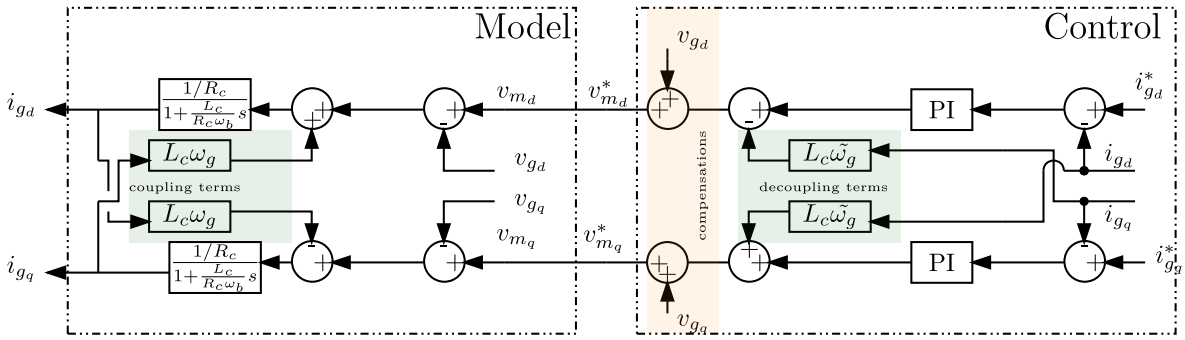

Figure II-8: Grid-following control structure.

Conventionally, the control structure of such system is derived by following a model inversion method, which leads to the control scheme presented in Figure II-8: Grid-following control structure. In addition to the PI controllers, decoupling terms must be implemented to avoid a high transient coupling between i_{g_d} and i_{g_q}. Usually, the grid current control for high power VSCs applications is tuned to achieve its references in around 1-10 ms [40]. The control tuning method is similar to the one used for the SRF-PLL in Appendix A.

Open loop control of powers:

The current references $i^*_{g_{dq}}$ in Figure II-8 can be provided by an outer power control loop. Thanks to the PLL, the grid voltage is assumed to be always aligned with the d-axis ($v_{g_q} = 0$), the powers are expressed by the following equations in the SRF frame:

$$p^* = v_{g_d} i_{g_d} + \underbrace{v_{g_q} i_{g_q}}_{=0} \quad \text{(II- 8)}$$

$$q^* = -v_{g_d} i_{g_q} + \underbrace{v_{g_q} i_{g_d}}_{=0} \quad \text{(II- 9)}$$

By inverting (II-8) and (II-9), the references i^*_{gd} and i^*_{gq} are deduced from the active and reactive power references as shown in Figure II-9.

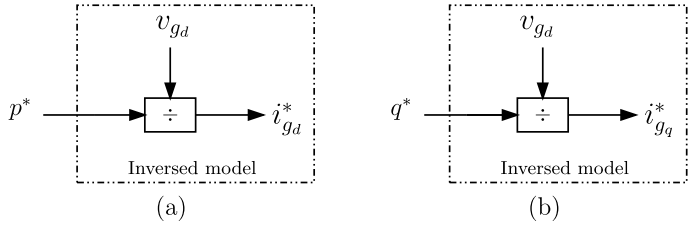

Figure II-9: Power controller for: (a) Active power, (b) Reactive power.

Simulation results:

The performance of this grid-following converter is evaluated through time-domain simulations illustrated in Figure II-10. The system and control parameters are given in Table II-2. The simulation scenario is as follows:

- t=0 s, both active and reactive power references are set zero.
- t= 100 ms, a 0.5 pu step applied to the active power reference.
- t= 300 ms, a 0.5 pu step applied to the reactive power reference.

Table II-2: System and grid-following converter parameters.

Parameter	Value	Parameter	Value
Base power S_b	1 GW	Transformer inductance X_c	0.15 pu
Converter nominal power p_n	1 GW	Transformer resistance R_c	0.005 pu
Base voltage V_b	320 kV	Grid thevenin inductance X_G	0.2 pu
Grid voltage V_e	1 pu	Grid thevenin resistance $R_G = X_G/10$	0.02 pu
Base frequency ω_b in rad/s	314.16	PLL response time $t_{r_{PLL}}$	50 ms
Line to line AC voltage	320 kV	Current controller response time t_{r_i}	5 ms
Ideal DC bus voltage	640 kV		

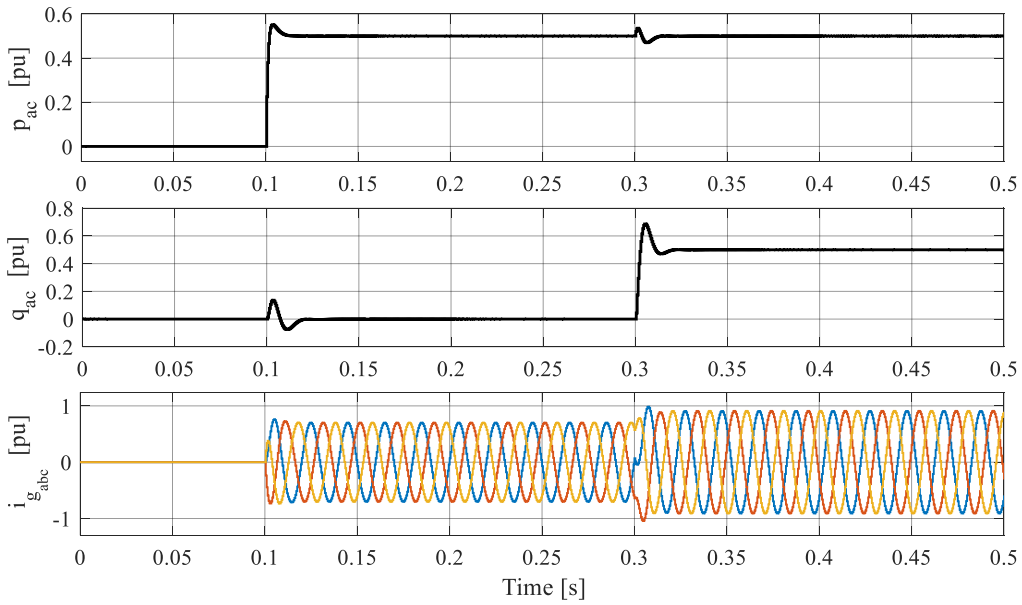

Figure II-10: Time-domain simulation of grid-following control.

Results show that the dynamic responses of the system meet the imposed specifications and the grid-following converter is capable of providing power almost instantaneously.

Aside from the power control loops, other control functions can be implemented to handle the grid services for the AC and DC systems. These outer control structures are summarized in Figure II-11.

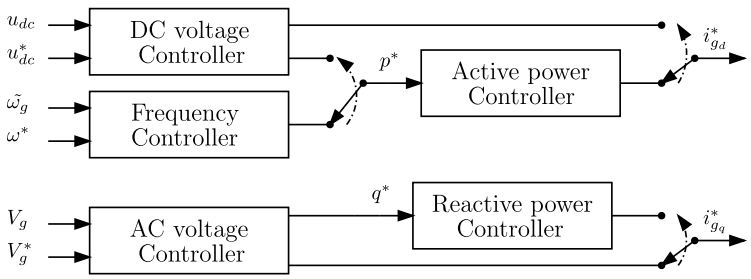

Figure II-11: Grid-following outer controllers.

If a DC voltage controller is implemented, the active current injected to the AC grid i_{g_d} will be calculated in order to keep the DC voltage around its reference value u_{dc}^*. The DC voltage control is a mandatory task that should be handled at least by one of power converters in AC/DC/AC conversion [42].

If the frequency and/or AC voltage controllers are implemented, powers converters become interactive with the AC system. Hence, power converters will adjust their active and reactive power or current in order to maintain the grid frequency and voltage amplitude in acceptable ranges [43].

The VSC based on grid-following control fulfills several functionalities in grid-connected mode, particularly when the AC grid is a stiff. However, its operation under weak grid conditions is one of its weak spots. Small signal stability problem under weak grid conditions [8], inability to provide inherent inertial effect and challenges with synthetic inertia emulation control [5], [7], high voltage ride through problem during post fault operation and transient stability issues [44] limit integrating more grid-following converters to the power system [10]. Discussion on the drawbacks of the grid-following control is out of the scope of this thesis. Grid-forming control, which is known as an emerging solution to deal with the drawbacks of the grid-following control forms the general basis of this thesis.

II.3 Power control with a controlled voltage source (grid-forming principle)

First, this section provides more details on phasor and time-domain modeling of the voltage-controlled converter by considering an open-loop active power control. According to the quasi-static equations introduced previously to calculate the active power ((II-4), (II-5)), two different models in both phasor and time-domain are introduced. Then a closed-loop control is designed to have a more robust active power control.

II.3.1 Open-loop active power control

The electrical model of Figure II-1 including the phasor and time-domain model is recalled in Figure II-12, where the focus is on the active power flow between the modulated voltage $\overrightarrow{V_m}$ and PCC voltage $\overrightarrow{V_g}$. It is assumed that ω_e is constant and equal to 1 pu. In case of any disturbance, the grid frequency ω_g and modulated frequency ω_m face with some transients. However, in steady state $\omega_m = \omega_g = \omega_e = 1$ pu and therefore:

$\theta_m = \omega_b t + \delta_m$, $\theta_g = \omega_b t + \delta_g$.

In all the thesis, the average value of the modulated voltage is supposed to be equal to its reference value in the control v_m^*. Let's define θ_m^* as the angle for v_m^* and $\tilde{\theta}_g$ the estimate of θ_g generated by a PLL, where in steady state: $\tilde{\theta}_g = \theta_g$.

If this estimation is used in the control, the angle reference θ_m^* can be expressed as $\theta_m^* = \tilde{\theta}_g + \psi^*$, where ψ^* is used to control the active power. Figure II-13 shows the implementation of the voltage-controlled converter with a PLL in time-domain.

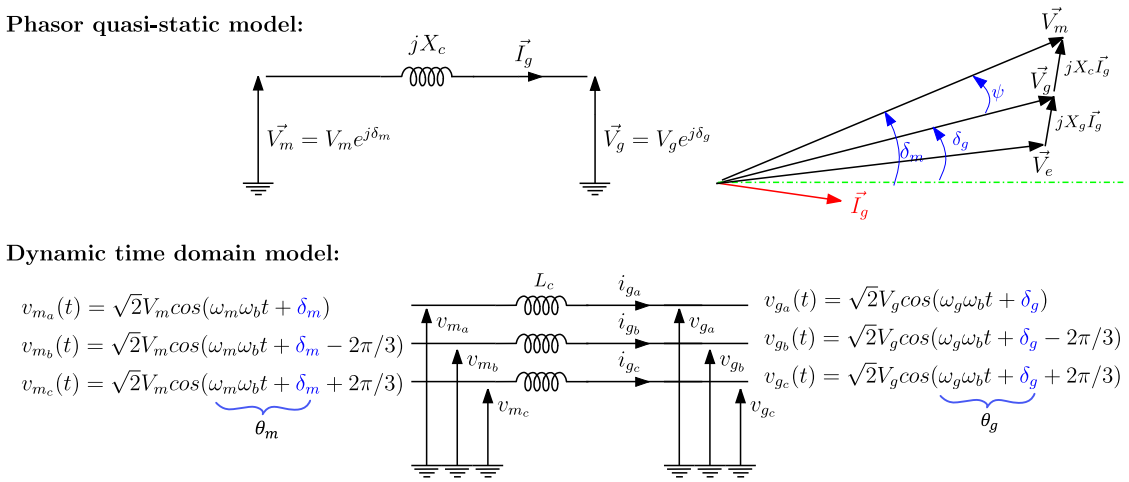

Figure II-12: Phasor and time domain models of the under-study system with a focus on power flow between $\overrightarrow{V_m}$ and $\overrightarrow{V_g}$.

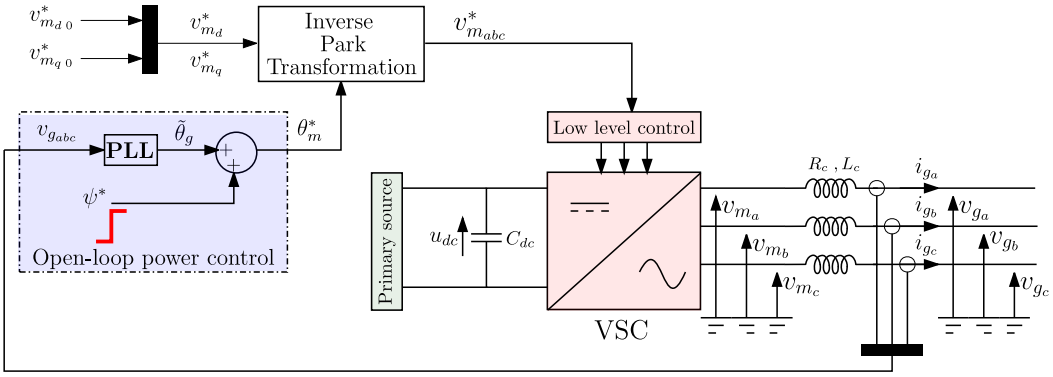

Figure II-13: Time-domain implementation of the voltage-controlled converter with open loop power control using a PLL.

Table II-3: System parameters for the open loop power control with the voltage-controlled converter.

Parameter	Value	Parameter	Value
Base power S_b	1 GW	$v^*_{m_{d0}}$	1 pu
Converter nominal power p_n	1 GW	$v^*_{m_{q0}}$	0 pu
Base voltage V_b	320 kV	Transformer inductance X_c	0.15 pu
Grid voltage V_e	1 pu	Transformer resistance R_c	0.005 pu
Base frequency ω_b in rad/s	314.16	Grid Thevenin inductance X_g	0.1 pu
AC line-to-line voltage	320 kV	Grid Thevenin resistance $R_g = X_g/10$	0.01 pu

Let's apply a small step of $\Delta\psi$ on ψ^*. The phasor quasi-static model of the system implies the following change (a step) in the active power:

$$\Delta P = \frac{V_m V_g}{X_c} sin\ (\Delta\psi\ ) \approx \frac{V_m V_g}{X_c}\Delta\psi \qquad \text{(II- 10)}$$

Considering $\Delta\psi = \frac{\pi}{40}$, the parameters given in Table II-3, PLL response time of 50 [ms] and the quasi-static model in (II-10), it is expected to observe a step of $\Delta P = 0.524$ pu in the active power. $\Delta\psi$ is applied to the converter control at $t = 0.2$ [s]. Figure II-14 shows the active power response of the converter. In steady state, both quasi-static and dynamic models reach the same value. However, the dynamics of the simulated system include some poorly damped poles.

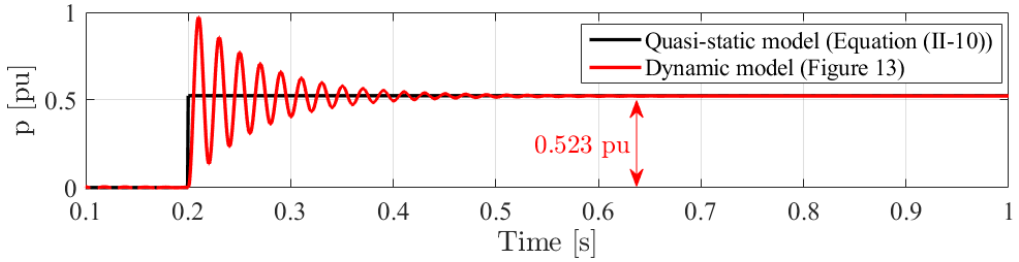

Figure II-14: Active power response with respect to a step in the angle ψ.

In [40] it has been demonstrated that these 50 Hz oscillations are linked with the grid current dynamics ($i_{g_{dq}}$) with two resonant poles $s_{1-2} = -\frac{R_c\omega_b}{L_c} \pm j\omega_g\omega_b$. These modes can be simply calculated by including the grid current dynamics, which results in the following expression:

$$\Delta P \approx \frac{V_m V_g}{X_c} \frac{1}{\left(\frac{1}{\omega_b\omega_g}s+\frac{R_c}{L_c\omega_g}\right)^2+1} \Delta\psi \qquad \text{(II- 11)}$$

It is possible to damp this system by integrating a transient virtual resistor (TVR) in the converter control. As illustrated in Figure II-15, the virtual resistor R_v acts on the magnitude of the modulated voltage in transient as follows:

$$\Delta v^*_{md} = R_v \frac{s}{s+\omega_f} i_{gd} \quad \Delta v^*_{mq} = R_v \frac{s}{s+\omega_f} i_{gq} \qquad \text{(II- 12)}$$

where ω_f is the cut-off frequency of the TVR. The analytical approach to design the TVR is explained in [45].

Considering $\Delta\psi = \frac{\pi}{40}$ [rad], the parameters given in Table II-3, $R_v = 0.09$ pu and $\omega_f = 60$ [rad/s], the same simulation scenario as before is repeated and the active power response of the converter is drawn in Figure II-16. It can be concluded that by including the TVR in the control, the simplified quasi-static model behaves nearly the same as the dynamic model since the oscillatory poles are damped. Therefore, the simplified quasi-static models presented in Figure II-17 can be considered as equivalent to the dynamic model in Figure II-15.

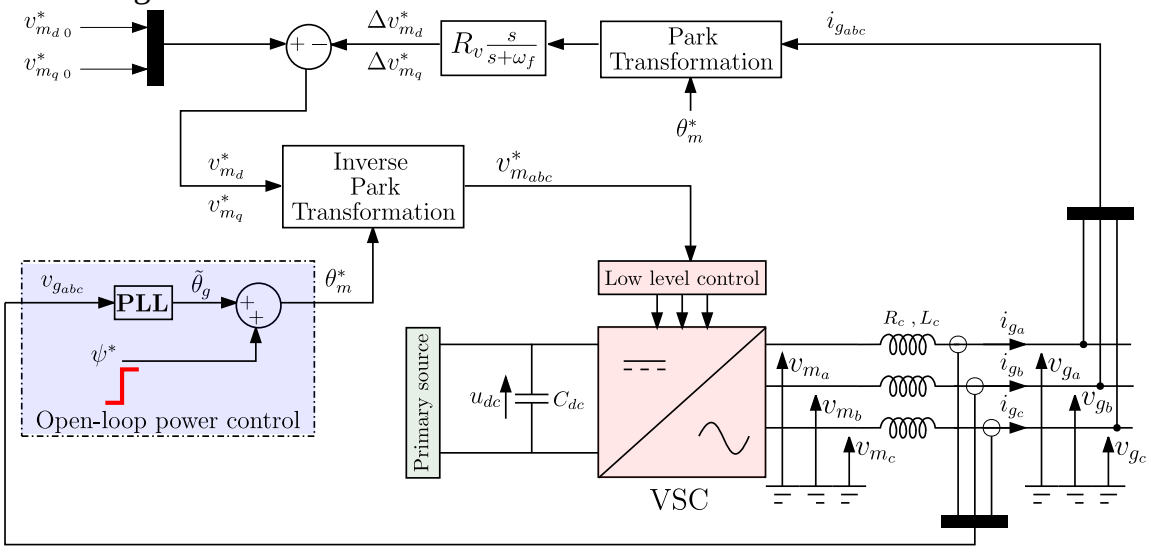

Figure II-15: Time-domain implementation of the voltage-controlled converter with open loop power control using a PLL and transient damping resistor.

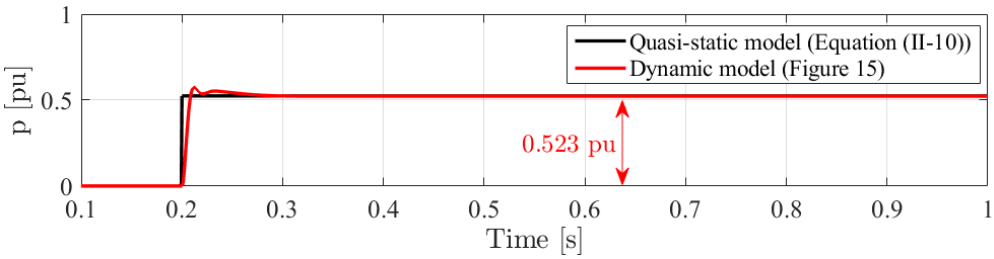

Figure II-16: Active power response with respect to a step in the angle ψ including the TVR.

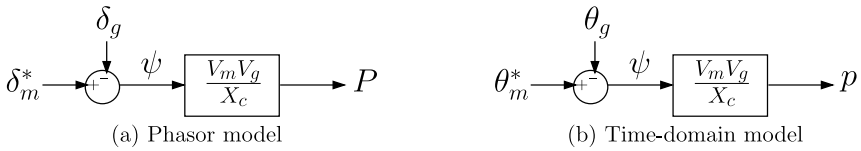

Figure II-17: Simplified models for active power control with a voltage-controlled converter while using a PLL: (a) Phasor model (b) Time-domain model.

If the aim is to remove the PLL from the control, it is still possible to develop an open loop active power control with a different quasi-static model. The electrical circuit of Figure II-1 including the phasor and time domain model is recalled in Figure II-18, where the focus is on the control the active power with the difference of angle between $\overrightarrow{V_m}$ and $\overrightarrow{V_e}$. It is assumed that ω_e is constant and equal to 1 pu. In case of any disturbance, ω_m faces with some transients. However, in steady state $\omega_m = \omega_e = 1$ pu. Therefore, in steady state: $\theta_m = \omega_b t + \delta_m$, $\theta_e = \omega_b t + \delta_e$. Theoretically, if the angle δ_e is known in the control of the converter, then θ_e is also known. By defining the reference angle $\theta_m^* = \theta_e + \rho^*$, Figure II-19 shows the implementation of the voltage-controlled converter without PLL in time-domain where ρ^* is used to control the active power. The angle δ_e is used to initialize the integrator inside the open-loop power controller.

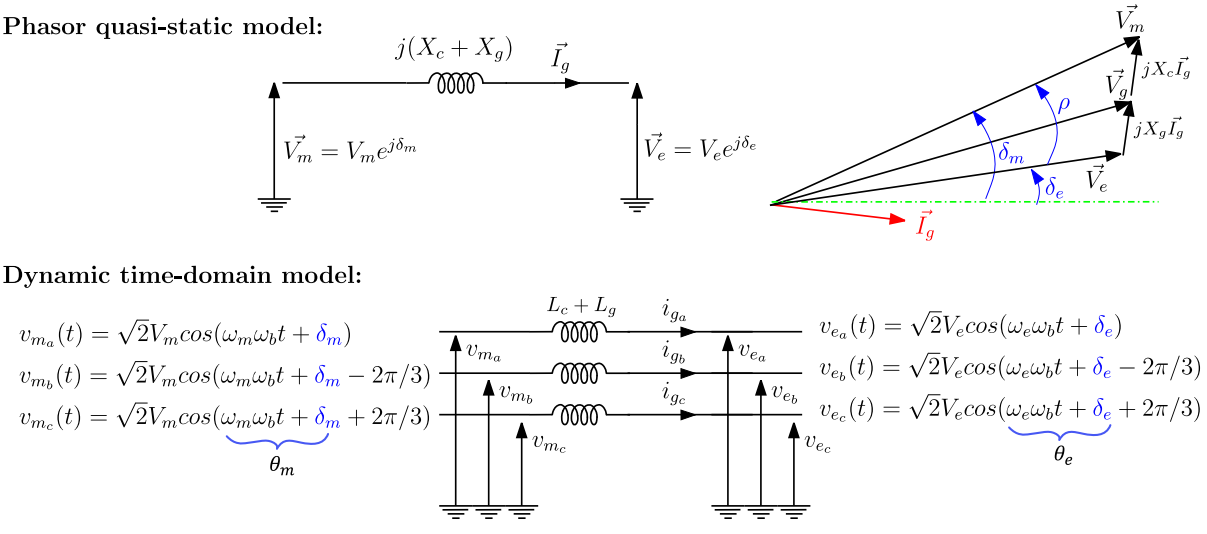

Figure II-18: Phasor and time-domain models of the under-study system with a focus on power flow between $\overrightarrow{V_m}$ and $\overrightarrow{V_e}$.

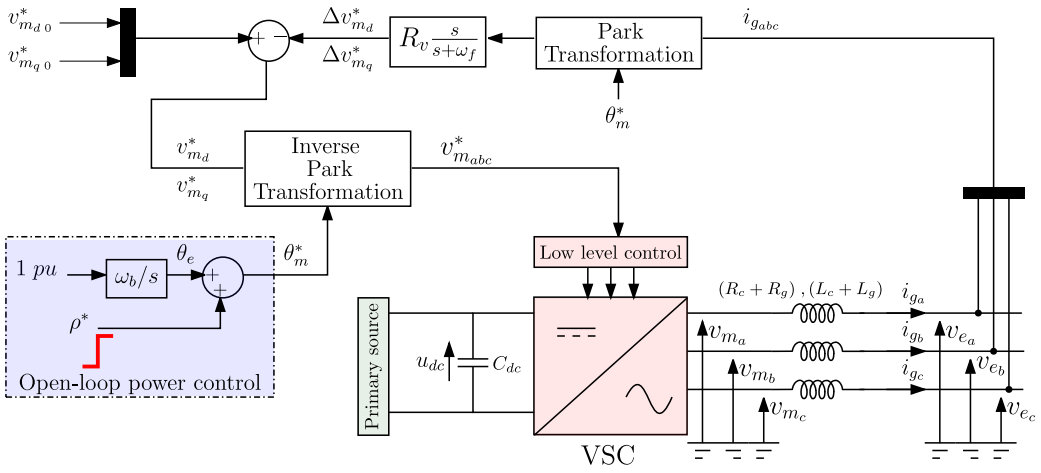

Figure II-19: Time-domain implementation of the voltage-controlled converter with open loop power control without any PLL.

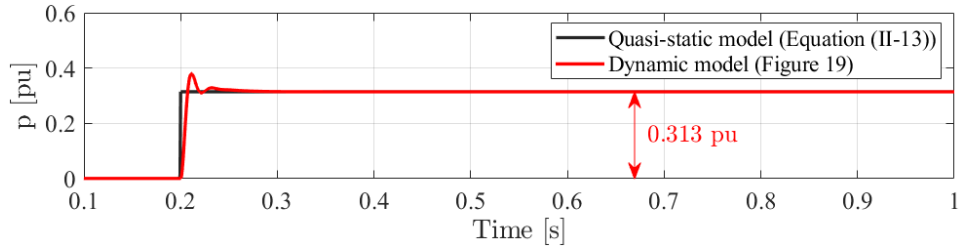

Figure II-20: Active power response with respect to a step in the angle ψ in voltage-controlled converter using a PLL.

In practice, this open-loop control could not be implemented because angle δ_e doesn't exist in a real and it is just a Thevenin equivalent. This simulation allows to define an open loop model, which will be used further. Let's apply a small step of $\Delta\rho$ on ρ^*. The phasor quasi-static model of the system implies following change (a step) in the active power:

$$\Delta P = \frac{V_m V_e}{X_c + X_g} sin\,(\Delta\rho) \approx \frac{V_m V_e}{X_c + X_g}\Delta\rho \qquad \text{(II- 13)}$$

Considering $\Delta\rho = \frac{\pi}{40}$, the parameters given in Table II-3 and the quasi-static model in (II-13), it is expected a step of $\Delta P = 0.314$ pu in the active power. $\Delta\rho$ is applied to the converter control at $t = 0.2$ [s]. Figure II-20 shows the active power response of the converter. It can be confirmed that the behavior of the dynamic model is close to the simplified quasi-static model.

The simplified quasi-static models presented in Figure II-21 can be considered as equivalent to the dynamic model in Figure II-19.

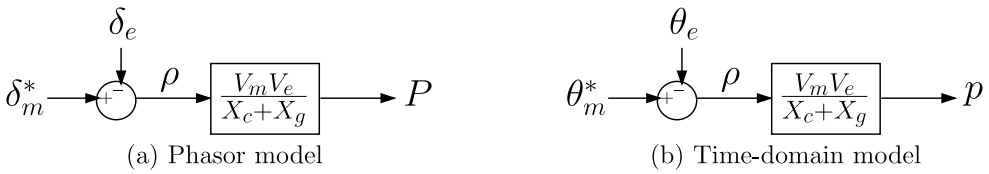

Figure II-21: Simplified models for active power control with a voltage-controlled converter with no PLL: (a) Phasor model (b) Time-domain model.

II.3.2 Closed-loop active power control

Investigation on the open-loop active power control helped to identify and validate the two different quasi-static active power models (i.e., models with/without PLL). The dynamic models including a TVR nearly behave the same as the corresponding quasi-static models. Since this open loop control is not reliable enough, a closed-loop system has to be implemented.

II.3.2.1 Introduction of different types of control

Figure II-22 shows the principle of the closed-loop power control with the voltage source for two cases (i.e., with/without PLL) derived from the simplified quasi-static modeling. The aim of the power control block is to eliminate the steady state error of the active power (i.e., $p^*(t) = p(t)$ in steady state). Depending on which power model is used, different closed-loop power controls can be developed.

Focusing on the PLL-based control, as shown in Figure II-23, any disturbance in the grid angle is instantaneously compensated by the PLL in the control. Hence, a single integrator is enough to eliminate the steady-state active power error. The gain m_c is a control parameter to adjust the response time of the active power.

If the PLL is removed, there will be some differences in the power control. Figure II-24 shows the power control implementation with no PLL using a single integrator. First, the power model has to be changed since the control cannot maintain the angle difference. The angle θ_e as the system disturbance has a ramp shape and it is not compensated in the control. Since the angle ρ is constant in steady state, the reference angle θ_m^* must be a ramp-shaped. Therefore, using a single integrator in the control cannot remove the steady state error of the active power. In fact, in steady state, it yields: $\omega_m = \omega_g = m_p(p^* - p)$ and, this is equivalent to the classical droop control with a frequency droop gain of m_p. Therefore, it can be said that the injected power mandatorily supports the system frequency when implementing a single integrator to the PLL free control scheme.

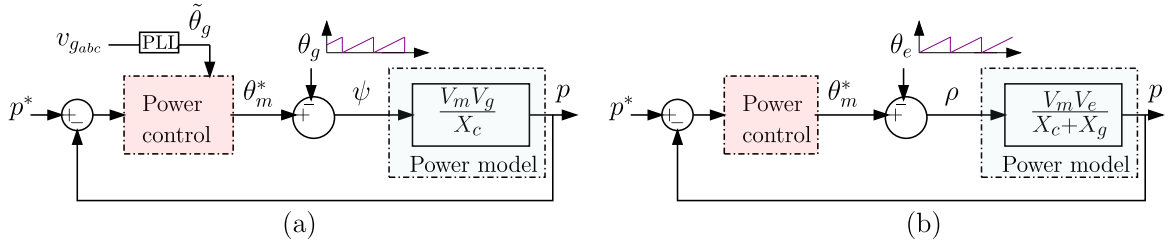

Figure II-22: Principle of the closed-loop power control in voltage-controlled mode (a) model with PLL (b) model without PLL.

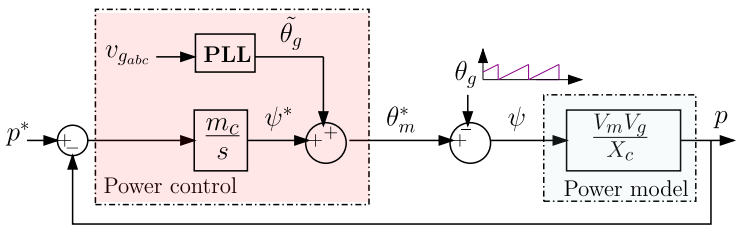

Figure II-23: Power control with a PLL and an integrator in voltage control mode.

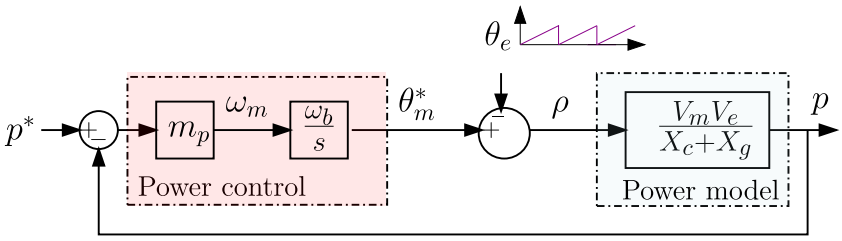

Figure II-24: Power control with no PLL and an integrator in voltage control mode.

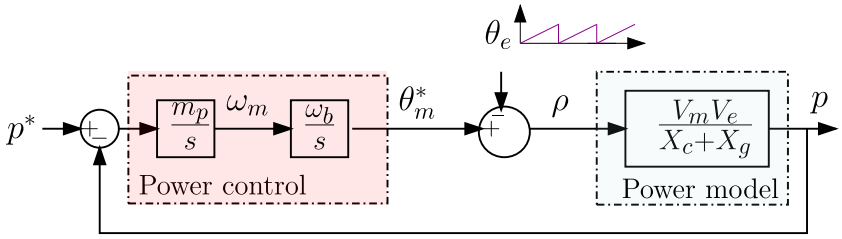

Figure II-25: Power control without PLL in voltage control mode using double integration.

In order to be able to regulate the active power in the PLL free scheme, with no frequency support, a second integration in the control system is needed. Doing so, the frequency support is decoupled from the active power regulation, and it can be implemented in an outer control loop if needed. Figure II-25 illustrates the power control scheme with a double integrator. Undoubtedly, this scheme is a pure oscillator, and a damping effect must be added in the control.

II.3.2.2 Design of the controllers

PLL-based control scheme: The power transfer function of the presented PLL-based control scheme (Figure II-23) is a first order function given by:

$$\frac{p}{p^*} = \frac{1}{\frac{X_c}{m_c V_m V_g} s+1} \qquad \text{(II- 14)}$$

According to this transfer function, by increasing m_c a very fast power response is achievable. This is not a realistic case, since in practice a low-pass filter (LPF) is applied to the power measurement. The aims are to filter the measurement noise and to avoid frequency jump [46]. Here, a filter is applied to the mismatch of the reference power and the measured power that provides the same effect as shown in Figure II-26.

The cut-off frequency of the filter ω_c has to fulfill the following condition to ensure the stable operation of the power converter [45]:

$$\frac{\omega_{gn}.\omega_b}{20} < \omega_c < \frac{\omega_{gn}.\omega_b}{5}, \qquad \text{(II- 15)}$$

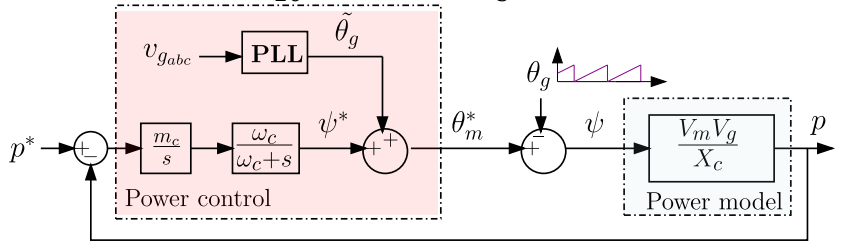

Figure II-26: Power control with a PLL and an integrator in voltage control mode including an LPF.

where ω_{gn} is the nominal grid frequency. Normally, $\omega_c = \frac{\omega_{gn}.\omega_b}{10}$ is chosen in the literature [45]. The closed-loop transfer function is now a second order function given by:

$$\frac{p}{p^*} = \frac{1}{\frac{X_c}{m_c\omega_c V_m V_g}s^2 + \frac{X_c}{m_c V_m V_g}s + 1}. \quad \text{(II- 16)}$$

According to this transfer function, the gain m_c cannot be incautiously increased to get a faster power response, since it results in a high overshoot. A pole map analysis will be presented in section II.4 to highlight this statement. The damping ratio ζ and natural frequency ω_n can be calculated by the following formulas:

$$\zeta = \sqrt{\frac{X_c\omega_c}{4m_c V_m V_g}} \quad , \quad \omega_n = \sqrt{\frac{m_c\omega_c V_m V_g}{X_c}}. \quad \text{(II- 17)}$$

Considering that the voltages V_m in the control and Thevenin equivalent voltage V_e are set to 1 pu, the PCC voltage V_g will be very close to 1 pu (transmission system). Therefore, (II-17) can be further simplified as follows:

$$\zeta = \sqrt{\frac{X_c\omega_c}{4m_c}} \quad , \quad \omega_n = \sqrt{\frac{m_c\omega_c}{X_c}}. \quad \text{(II- 18)}$$

There are two significant comments on the developed PLL-based control scheme. Firstly, the grid impedance X_g did not appear in the active power transfer function. Hence, the active power response of a converter with this kind of control is **independent to the grid impedance variation**. Secondly, since any disturbance in the grid frequency (subsequently in the angle θ_g) is instantaneously compensated by the PLL, this control scheme does not have inertial effect. These points will be assessed the following section.

PLL-free control scheme with IP-controller: For the PLL-free control scheme, the dynamic equation of the control can be expressed as follows:

$$\Delta p(t) = p^*(t) - p(t) = \frac{1}{m_p\omega_b}\frac{d^2\theta_m(t)}{dt^2} = 2H\,\frac{d\omega_m(t)}{dt}. \quad (m_p = \frac{1}{2H}) \quad \text{(II- 19)}$$

Equation (II-19) is equivalent to the well-known swing equation in a synchronous machine [47] except that the damping is neglected. Therefore, the double integration adds an inherent inertial effect to the closed-loop control. The parameter H is the virtual inertia constant and it will be used instead of the gain m_p in the rest of the thesis. The closed-loop transfer function of the PLL-free control scheme is given by:

$$\frac{p}{p^*} = \frac{1}{\frac{2H(X_c+X_g)}{\omega_b V_m V_e}s^2 + 1} \quad \text{(II- 20)}$$

As this system is an oscillator, a damping term must be added to the control. According to Figure II-27, a damping gain k_p is applied to the measured power resulting in a specific proportional-integral controller, named IP-controller in this thesis.

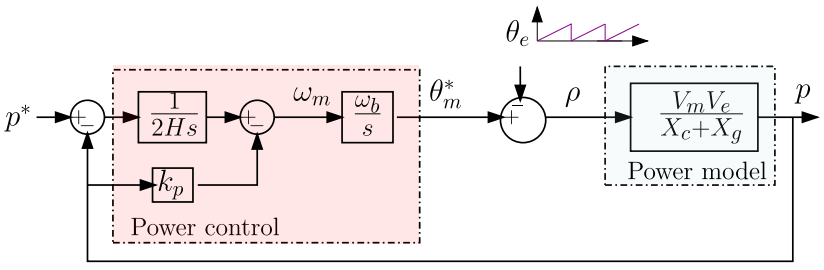

Figure II-27: Power control without PLL in voltage control mode using an IP-controller.

The power transfer function is given by:

$$\frac{p}{p^*} = \frac{1}{\frac{2H(X_c+X_g)}{\omega_b V_m V_e}s^2+2Hk_p s+1} \quad \text{(II- 21)}$$

Considering $V_m = V_e = 1$ p.u, the damping ratio ζ and natural frequency ω_n can be expressed by the following formulas:

$$\zeta = k_p\sqrt{\frac{\omega_b H}{2(X_c+X_g)}} \quad , \quad \omega_n = \sqrt{\frac{\omega_b}{2H(X_c+X_g)}}. \quad \text{(II- 22)}$$

In this control scheme the grid impedance affects the power response. From (II-22), the gains H and k_p can be designed to achieve the desired dynamics of the active power for a given grid impedance. It should be noted that since, in this control, the damping term k_p is rather small (typically between 0.005 to 0.05 pu depending on the grid impedance and desired tuning) and the term "$1/2Hs$" filters the oscillations of the measured power, no additional LPF is needed in the power control loop.

II.4 Dynamic assessment of grid-forming control variants

In this section, the idea of closed-loop active power control with a voltage source, namely grid-forming control, is implemented to a 2-level VSC with an LC filter. The dynamic performance of both PLL-based and IP control schemes is analyzed. It is demonstrated that simplified quasi-static models (presented graphically in Figure II-26 and Figure II-27 and by the power transfer functions in (II-16) and (II-21)) can explain the dominant dynamics of the active power. Afterwards, a parametric analysis is presented, which aims to investigate the impact of some control and system parameters on the active power response. Finally, the inertial support and primary frequency supports as two essential services that can be provided to an AC system by a grid-forming converter are assessed.

II.4.1 Introduction of the grid-forming control implemented on a 2-level VSC

Previously, the way to generate the reference voltage with an ideal VSC has been presented. In case of a 2-level VSC with an LC filter (see Figure II-28), the control must be adjusted in order to take the internal current and voltage loops into account. The LC filter is required to eliminate the high-frequency harmonics caused by the PWM signals. When the LC filter is considered, the active power control is then achieved by acting on the phase of the voltage e_g. Then, this voltage is substituted to v_m in all the previous analysis. Figure II-29 shows the full dynamic model implementation of a grid-forming control on a 2-level VSC. The voltage v_m^* is calculated from the voltage and current control loops [48]. The active power control can be conducted either by the PLL-based control or IP-control.

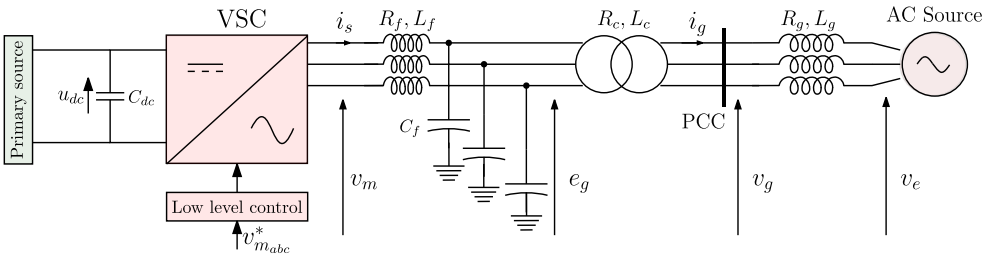

Figure II-28: A 2-level VSC with an LC filter connected to the grid.

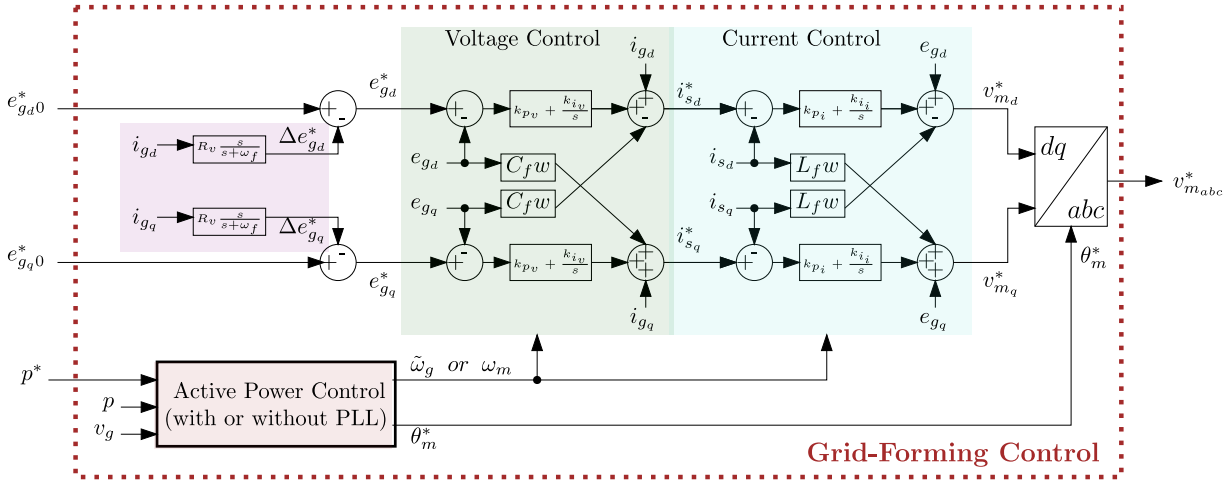

Figure II-29: Full scheme of the grid-forming control for a 2-level VSC.

Table II-4 System and grid-forming converter parameters.

Parameter	Value	Parameter	Value
Base power S_b	1 GW	e^*_{gd0}	1 pu
Converter nominal power p_n	1 GW	e^*_{gq0}	0 pu
Base voltage V_b	320 kV	L_f	0.15 pu
Grid voltage V_e	1 pu	C_f	0.066 pu
Base frequency ω_b in rad/s	314.16	R_f	0.005 pu
AC line-line voltage	320 kV	k_{p_v}	0.52
Transformer inductance X_c	0.15 pu	k_{i_v}	1.16
Transformer resistance R_c	0.005 pu	k_{p_i}	0.73
Grid thevenin inductance X_g	0.333 pu	k_{i_i}	1.19
Grid thevenin resistance $R_g = X_g/10$	0.0333 pu	m_c	1.95
u_{DC}	640 kV	ω_c	31.4 rad/s
n_q	0 pu	PLL response time $t_{r_{PLL}}$	20 ms
R_v	0.09 pu	H	0.796
ω_f	60 rad/s	k_p	0.0483

II.4.2 Validation of the quasi-static models

In order to verify the validity of the simplified quasi-static models presented for the power control in a grid-forming converter, the power response of these models is compared with two cases:

1- The response of the non-linear full dynamic model (Figure II-28 with the control system of Figure II-29).
It should be stated that by proper tuning of inner voltage and current control loops [48] and also the transient damping resistor [40], the corresponding modes become fast enough so that their impact on the dominant dynamic behavior of the system is negligible. The design of the controller has been elaborated in order to avoid

extremely fast poles, which would induce some instabilities for practical applications.

2- The response of the simplified linearized state-space model (derivation method for the state-space model is given in Appendix B).

The system and control parameters are given in Table II-4. Note that the power control loop parameters are tuned to get $\omega_n = 20.2\ rad/s$, $\zeta = 0.777$ for both PLL-based and IP control.

Considering the given parameters, Figure II-30 shows the system poles for both simplified quasi-static and linearized dynamic models. It can be seen that the quasi-static models give a good estimation of the dominant poles. In fact, since the grid current and PLL dynamics are faster than the active power dynamics, the simplified quasi-static and dynamic models behave similarly. Consequently, the analysis of large grids may be done based on a simplified model.

Time domain simulation is performed for all three models. A step is applied to the power reference at t=0.1 s. Figure II-31 validates the simplified quasi-static models in time domain.

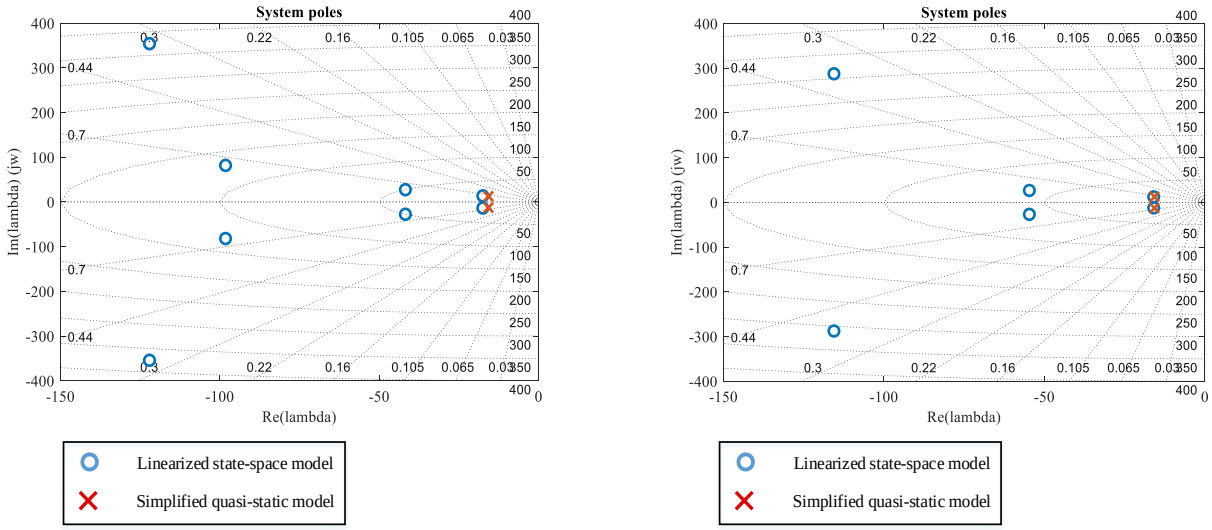

Figure II-30: Validation of quasi-static models by pole analysis: (a) PLL-based control (b) IP control.

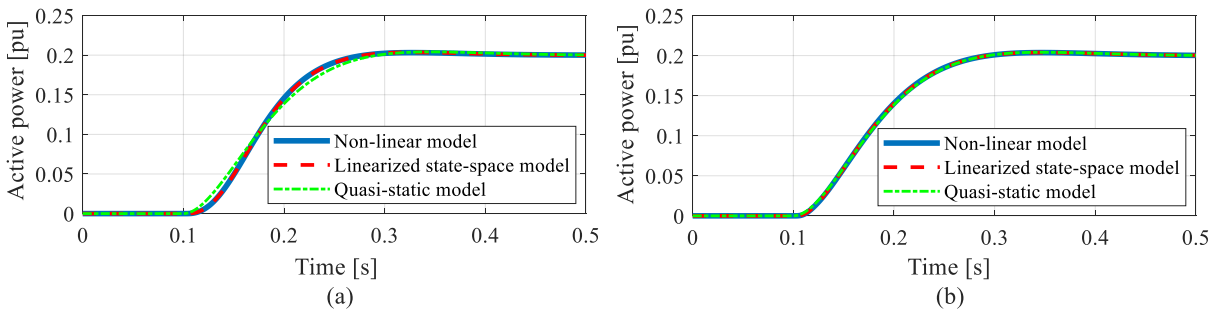

Figure II-31: Validation of quasi-static models by time domain simulation: (a) PLL-based control (b) IP control.

II.4.3 Analysis on parameter variations

Reaching a high controllability level of the grid-forming converters depends on dealing with several factors i.e., dynamics, robustness and stability. In this subsection, the impact of some control and system parameters on the active power dynamic of the presented grid-forming solutions is addressed. The aim is to push these controls to their limits and verify their robust performance.

II.4.3.1 Variation of grid short circuit ratio (SCR)

According to IEEE definition, SCR is the ratio of the available short-circuit current, in amperes, to the load current, in amperes at a particular location [49]. At the PCC, SCR is expressed with respect to the grid impedance (in p.u.) as follows:

$$SCR = \frac{1}{X_g} \qquad \text{(II- 23)}$$

Reference [50] has defined the grid strength as strong, weak or very weak if its SCR is greater than 3, between 2 and 3, or lower than 2, respectively;
Considering the given parameters in Table II-4, Figure II-32 shows the system pole trajectory under a wide range of grid strength for both PLL-based and IP control schemes. From the small signal stability and robustness point of view, both controls show their ability to operate under very weak grid conditions.
As expected from quasi-static consideration the PLL based control keeps the same active power dynamics in both strong and very weak grids, provided that an adequate response time of the PLL is chosen $t_{r_{PLL}} = 20$ [ms]. Therefore, using this control, the grid-forming VSC is a good power injector with nearly constant dynamic behavior independent to the grid impedance.

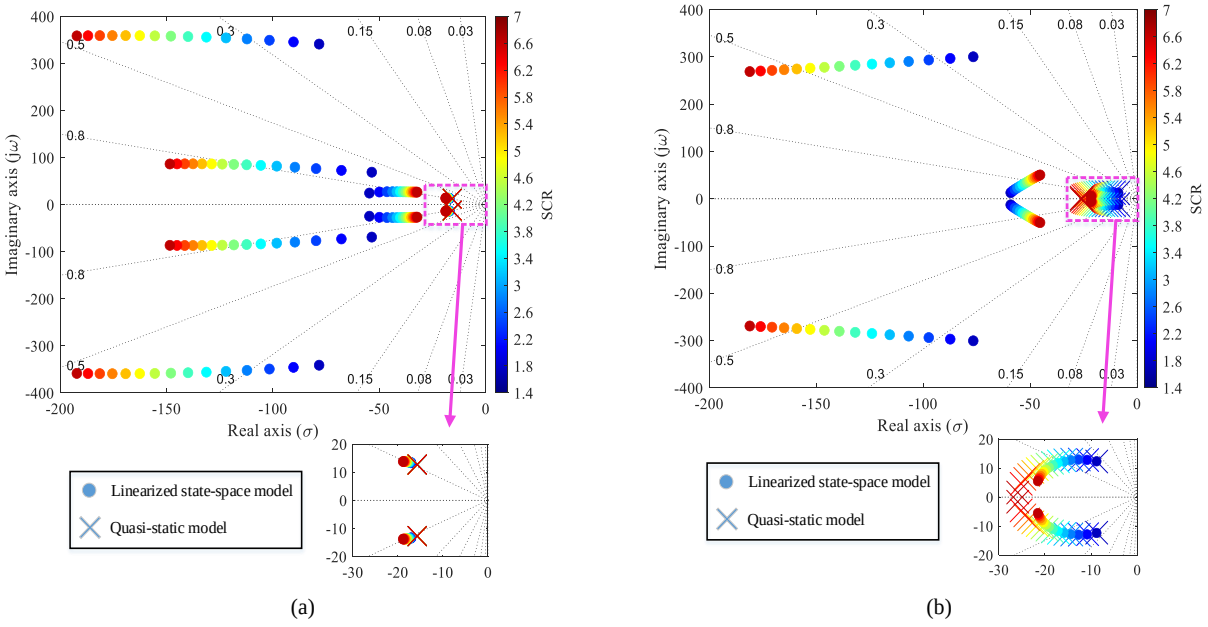

Figure II-32: Validation of quasi-static models by pole map under various SCR: (a) PLL-based control (b) IP control.

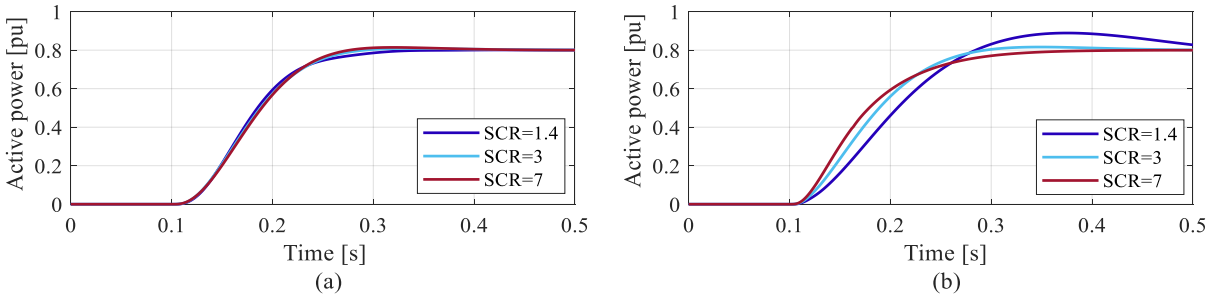

Figure II-33: Dynamic behavior of the active power under various SCR in time domain using nonlinear model: (a) PLL-based control (b) IP control.

The power response of the IP-control based grid-forming is changing with respect to the SCR variation since the quasi-static model depends on the grid impedance. The power response of the developed quasi-static models, again, gives a proper estimate of the dominant modes under SCR variation. Time domain simulations using the nonlinear model of the system, which are presented in Figure II-33, verify these statements. Generally, it can be concluded that the stability is guaranteed on a very wide range of SCR.

Due to the constant power response of the PLL based control scheme under various SCR, it is worthy to check the possibility of reducing its response time to get a faster power response, similarly to the grid-following scheme. In addition, the impact of the PLL response time on the active power dynamics should be examined.

II.4.3.2 Variation of the power loop gain m_c in the PLL based scheme

Considering the given parameters in Table II-4, Figure II-34 shows the system pole trajectory under a wide range of the gain variation in the power control loop of the PLL based control scheme. It can be observed that for $m_c < 1.3$ pu the dominant modes are located on the real axis. Therefore, no overshoot is expected in the system response. Once increasing over the mentioned value, the dominant modes reach a breakaway point on the real axis and some overshoot is expected in the system response. By increasing m_c up to 3.1 pu, the system damping is still acceptable and the quasi-static model is valid. However, this model cannot see the small signal instability that could happen for large values of the m_c (e.g., $m_c \geq 16.9$ p.u). Figure II-35 illustrates the effect of m_c on the active power dynamics of the PLL-based grid-forming control in time domain. For $m_c \leq 3.1$ p.u, the simplified quasi-static model can explain the nonlinear system dynamics. However, for greater gains this model becomes inaccurate and even in extreme cases it cannot explain the instability. The main conclusion of this study is that the power response time of the proposed PLL based grid-forming control is limited to around a minimum of 90 [ms] considering a proper damping.

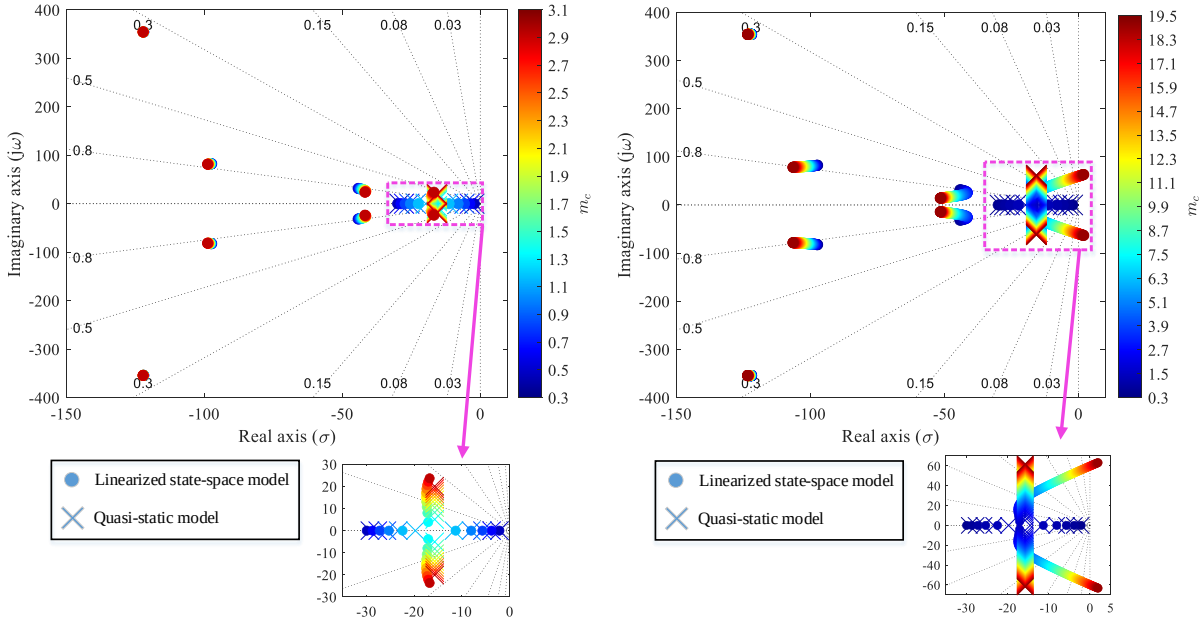

(a) (b)

Figure II-34: System pole trajectory with respect to the power control gain (m_c) variation for the PLL-based scheme - (a) $0.3 \leq m_c \leq 3.1$ (b) $0.3 \leq m_c \leq 19.5$.

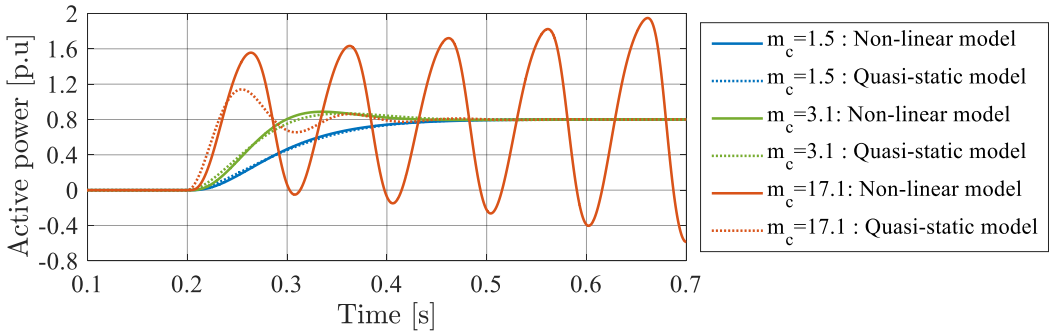

Figure II-35: Dynamic behavior of the active power under variation of m_c for both quasi-static and dynamic models of the PLL based grid-forming control.

II.4.3.3 Variation of the PLL response time in the PLL based scheme

Considering the given parameters in Table II-4, Figure II-36 shows the system pole trajectory under a wide range of the PLL response time variation in the PLL based control scheme. It can be observed that for all the system modes stay in the stable region; however, there is an alteration in the system dominant modes.

For $5 \leq t_{r_{PLL}} \leq 50$ [ms] the dominant modes are λ_1 and λ_2 (the same as dominant modes given in Figure II-30, which are linked with the active power control loop. The quasi-static model that was developed based on the assumption, in which the PLL is fast enough to reject the grid angle disturbance, is valid for the aforementioned range of the PLL response time.

By increasing the PLL response time, the PLL interacts with the power control loop and affect the dominant dynamics of the power. Still the system is stable; however, the simplified quasi-static model is not able to explain the system dynamics. Figure II-37 illustrates the effect of PLL response time variation on the active power dynamics of the PLL-based grid-forming control in time domain, which validates the presented statements.

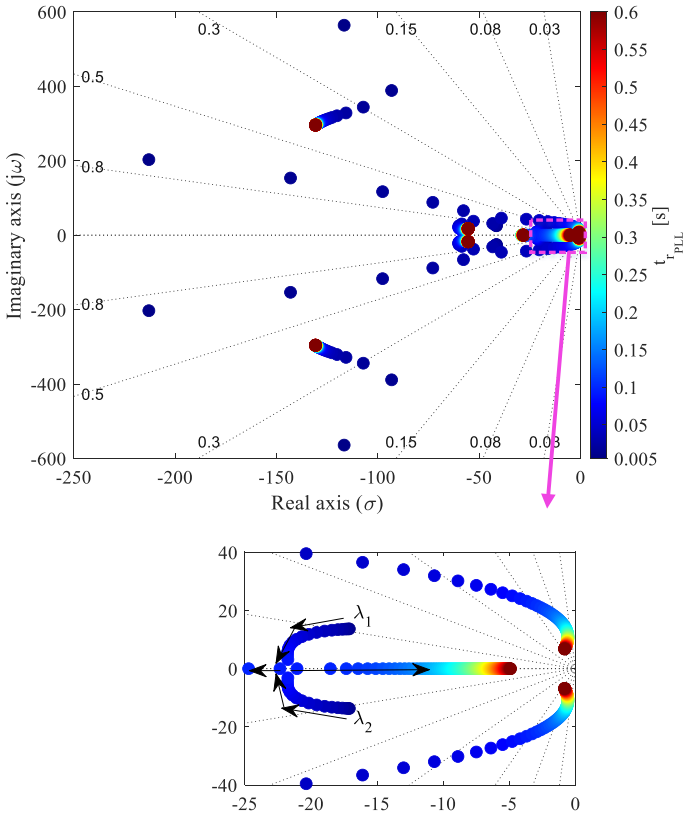

Figure II-36: System pole trajectory with respect to the PLL response time variation for the PLL-based scheme.

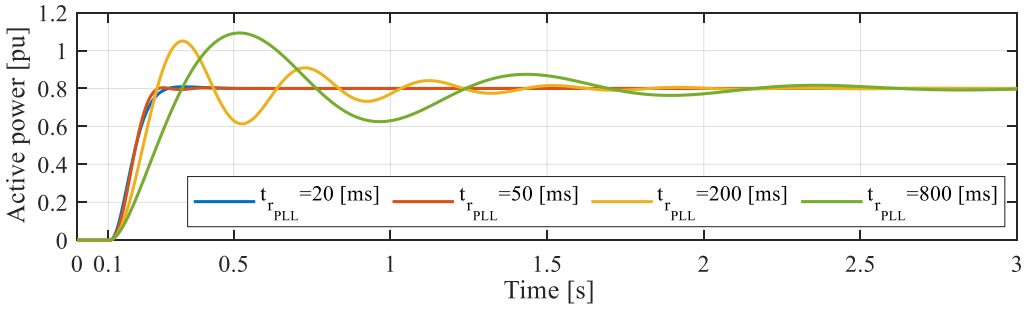

Figure II-37: Dynamic behavior of the active power under variation of the PLL response time in the PLL based grid-forming control.

II.4.4 Inertial effect and frequency support

In the previous subsections, the VSC was connected to an infinite bus, where the frequency is assumed to be constant. In this section, the frequency is not constant anymore. The goal is to study the dynamic behavior of the VSC and its interoperability with a more realistic AC system. Apart from the synchronization and constant power injection, the converter must be able to contribute to the stability needs of the AC system. Therefore, each converter could be asked to regulate its own frequency so they can converge to same value in the steady state. This functionality is ensured by a primary frequency control, also called $p - \omega$ droop control. However, because of the power control dynamics, the primary frequency control does not allow an instantaneous compensation of the power imbalance. Thus, power converters are also asked to ensure an inertial support. The inertial support based on the grid-forming VSCs has been widely discussed in these last years, which leads to the development of new control

method, so-called virtual synchronous generator (VSG) [51], [52], virtual synchronous machine (VSM) [47], [53], or Synchronverter [20], [54]. They have been proposed to mimic the swing equation of synchronous generators, and also their electrical dynamics. With a good energy management, power converters can use their energy stored on the DC side to provide the equivalent kinetic energy of a synchronous generators, and therefore, provide inertia to the system. In this subsection, a systemic approach has been proposed in order to explain theoretically and in a simple manner the dynamic behavior of the VSC with two proposed strategies connected to a variable frequency AC system.

II.4.4.1 System description

Figure II-38 presents a VSC connected to an AC system formed by a linear resistive load P_{load} and an equivalent variable frequency AC grid. The dynamic performance of the proposed grid-forming controls will be analyzed. An outer droop control loop may be implemented to allow a frequency support from the VSC.

The equivalent AC grid consists of an AC voltage source in series with its impedance (R_g, L_g), which is driven by a model representing the frequency dynamic of a synchronous machine. It consists of a swing equation and a lead lag filter, which stands for a simplified model of the turbine [55]. A governor is added to support the grid frequency. The notations used in this subsection are given in the following lines:

For the VSC:

- p and p^{SI} are the active power calculated from the converter side in per-unit and SI, respectively.
- ω_m is the modulated frequency of the converter.
- L_c, R_c is the connection impedance.
- S_{b1} is the rated power of the VSC chosen as its base power.
- R is the outer droop control gain.

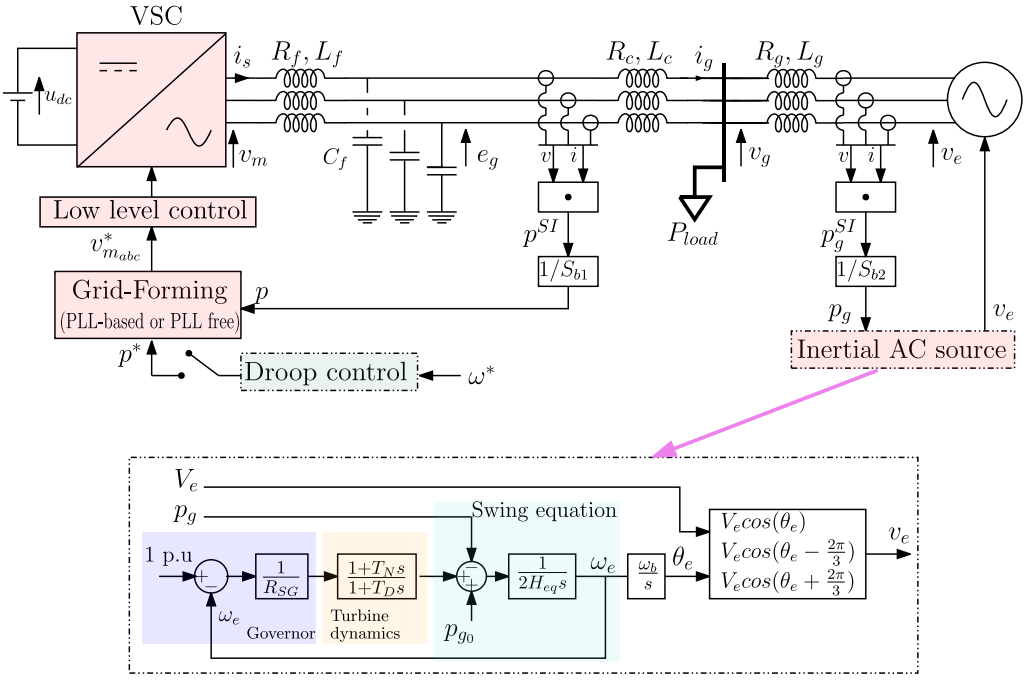

Figure II-38: AC voltage controlled VSC connected to an equivalent AC grid with variable frequency.

For the equivalent AC grid:

- p_g and p_g^{SI} are the active power calculated from the grid side in per-unit and SI, respectively.
- ω_e is the modulated frequency of the grid.
- L_g, R_g is the connection impedance.
- S_{b2} is the rated power of the equivalent AC grid chosen as its base power.
- R_{SG} is the droop control gain.
- $H_{eq}, T_N, T_D, \omega_{e_n}$ are the equivalent inertia constant, the lead time constant, the lag time constant and nominal grid frequency, respectively.

At the PCC:

- ω_g is the frequency at the load level.
- P_{load} is the instantaneous power of the load in SI and : $p_g^{SI} + p^{SI} = P_{load}$

The grid case in Figure II-38 is used to analyze the active power and frequency dynamics for the two introduced grid-forming control strategies in response to a load change.

II.4.4.2 PLL-based control: Dynamic analysis of the variable-frequency system

First, a small-signal analytic model of the system in Figure II-38 is built. The idea is to achieve a qualitative dynamic analysis of this system in order to have a physical explanation of the active power and frequency behavior when the converter is controlled via PLL-based scheme. It is assumed that the outer droop is disabled.

When a load change is applied, the grid frequency variation $\Delta\omega_g$, which results in the grid angle variation $\Delta\theta_g$ is compensated almost instantaneously in the control by the PLL, and thus, $\Delta p^{SI} = 0$. Hence, $\Delta p_g^{SI} = S_{b_2}\Delta p_g = \Delta P_{load}$. The expression of Δp_g in the variable frequency AC grid model is:

$$\Delta p_g = -\left[2H_{eq}s + \frac{1}{R_{SG}}\left(\frac{1+T_N s}{1+T_D s}\right)\right]\Delta\omega_e \qquad \text{(II- 24)}$$

Therefore, the grid frequency dynamics with respect to a load change in the described system can be assessed by the following second order transfer function:

$$\Delta\omega_e = -\frac{1}{S_{b_2}}\frac{R_{SG}(1+T_D s)}{\left(1+(T_N+2H_{eq}R_{SG})s+2H_{eq}R_{SG}T_D s^2\right)}\Delta P_{load} \qquad \text{(II- 25)}$$

The damping ratio and natural frequency of (II-25) are given by:

$$\zeta = \frac{1}{2}\frac{T_N+2H_{eq}R_{SG}}{\sqrt{2H_{eq}R_{SG}T_D}}, \qquad \omega_n = \sqrt{\frac{1}{2H_{eq}R_{SG}T_D}} \qquad \text{(II- 26)}$$

Equation (II-26) indicates the parameters influencing the grid frequency dynamics. Let us focus on the impact of the equivalent inertia constant H_{eq}:

- The decrease of the inertia constant results in an increase of the damping and leads to an increase of the natural frequency.
- The increase of the natural frequency results in a faster frequency response.

Table II-5: Variable frequency AC system and VSC control parameters.

Parameter	Value	Parameter	Value
VSC base power S_{b_1}	1 GW	C_f	0.066 pu
AC grid base power S_{b_2}	1 GW	R_f	0.005 pu
Base voltage V_b	320 kV	k_{pv}	0.52
Grid voltage V_e	1 pu	k_{iv}	1.16
Base frequency ω_b in rad/s	314.16	k_{p_i}	0.73
AC line-line voltage	320 kV	k_{i_i}	1.19
Transformer inductance X_c	0.15 pu	m_c	1.95
Transformer resistance R_c	0.005 pu	ω_c	31.4 rad/s
Grid thevenin inductance X_g	0.15 pu	PLL response time $t_{r_{PLL}}$	20 ms
Grid thevenin resistance $R_g = X_g/10$	0.005 pu	H	5 s
u_{DC}	640 kV	k_p	0.01
n_q	0 pu	ω^*	1 pu
R_v	0.09 pu	R	0.04 pu
ω_f	60 rad/s	R_{SG}	0.04 pu
$e^*_{g_{d0}}$	1 pu	H_{eq}	5 s
$e^*_{g_{q0}}$	0 pu	T_N	1 s
L_f	0.15 pu	T_D	2 s

The inertia constant also has an impact on the rate of change of frequency (RoCoF). The RoCoF value for a load step ($\Delta P_{load}/s$) is determined using the well-known "initial value problem" [56] as follows:

$$RoCoF = |\lim_{s\to\infty} s^2 \Delta\omega_e f_b| = \frac{1}{S_{b_2}} \frac{\Delta P_{load} f_b}{2H_{eq}} \quad \text{(II- 27)}$$

The steady state frequency variation $\Delta\omega_{e_{ss}}$ with respect to the load step ($\Delta P_{load}/s$) is determined using the well-known "final value problem" [56] as follows:

$$\Delta\omega_{e_{ss}} = |\lim_{s\to 0} s\Delta\omega_e(s)| = -\frac{1}{S_{b_2}} R_{SG} \Delta P_{load} \quad \text{(II- 28)}$$

In order to verify the validity of the simplified linear model presented in (II-25), this theoretical model is compared with the nonlinear model using time domain simulation. The variable frequency AC system and VSC control parameters are given in Table II-5.

Initially, there is no power exchange in the system ($p_g = p = P_{load} = 0$). A step of 200 MW (0.2 pu) is applied to the load at *t*=1 s. Since the frequency support from VSC is not active, it is expected all this power is supplied from the grid. Moreover, the frequency dynamics should respect the simplified model given in (II-25). According to (II-27) and (II-28), $RoCoF = 1$ Hz/s and $\Delta\omega_{e_{ss}} = -0.008$ pu should be achieved in this simulation study. As shown in Figure II-39, the response of simplified theoretical model matches the nonlinear model response. Some slight differences in fast transient after the load disturbance can be noticed, which are mainly linked to the PLL and the grid current dynamics as well as to the resistive part of the impedances.

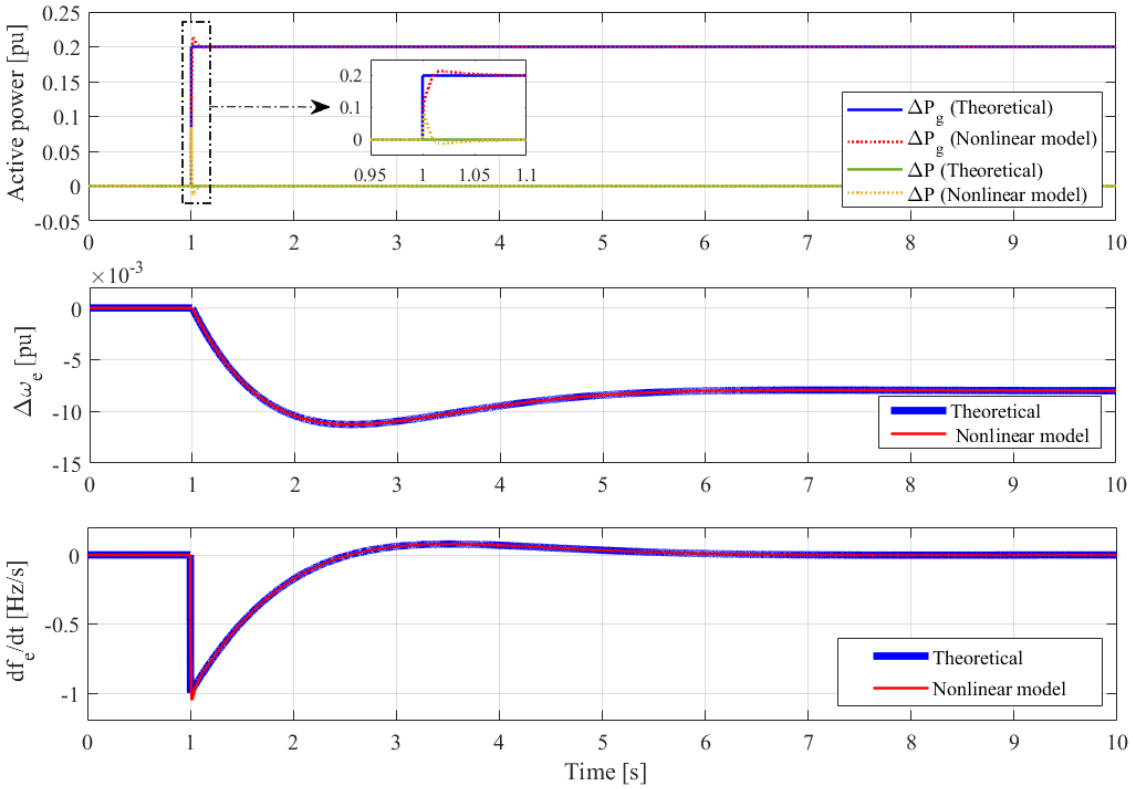

Figure II-39: Frequency and power dynamics with respect to a load change (PLL-based control).

II.4.4.3 IP control: Dynamic analysis of the variable-frequency system

Same as previously, the grid case in Figure II-38 implementing the IP control grid-forming on the VSC is used to analyze the active power and frequency dynamics. In this case, when a load change is applied to the PCC, there is the grid frequency variation $\Delta\omega_g$, which results in the grid angle variation $\Delta\theta_g$. Since this angle variation is not compensated in the control contrary to the PLL based scheme, $\Delta p \neq 0$. The VSC power variation in small signal can be expressed with respect to the internal modulated frequency as follows (according to Figure II-27):

$$\Delta p = -\frac{2Hs}{1+2Hk_{ps}}\Delta\omega_m \qquad \text{(II- 29)}$$

As highlighted by (II-29), an expression of $\Delta\omega_m$ with respect to the other parameters is required. The active power flow between the VSC/Load and the grid/Load in small signal is given by two following expressions:

$$\Delta p = K_c\left(\Delta\delta_m - \Delta\delta_g\right) = K_c\frac{\Delta\omega_m - \Delta\omega_g}{s}\omega_b \qquad \text{(II- 30)}$$

$$\Delta p_g = K_g\left(\Delta\delta_e - \Delta\delta_g\right) = K_g\frac{\Delta\omega_e - \Delta\omega_g}{s}\omega_b \qquad \text{(II- 31)}$$

where $K_c = \frac{E_g V_g}{X_c}$ and $K_g = \frac{V_e V_g}{X_g}$. Replacing $\Delta\omega_g$ obtained from (II-30) to (II-31):

$$\Delta\omega_m = \Delta\omega_e + \left(\frac{\Delta p}{K_c} - \frac{\Delta p_g}{K_g}\right)\frac{s}{\omega_b} \qquad \text{(II- 32)}$$

At the PCC: $p_g^{SI} + p^{SI} = P_{load}$. Since Δp is imposed by the grid-forming control, the active power delivered by the equivalent source in small signal is (in pu):

$$\Delta p_g = \frac{\Delta P_{load}}{S_{b_2}} - \frac{S_{b_1}\Delta p}{S_{b_2}} \qquad \text{(II- 33)}$$

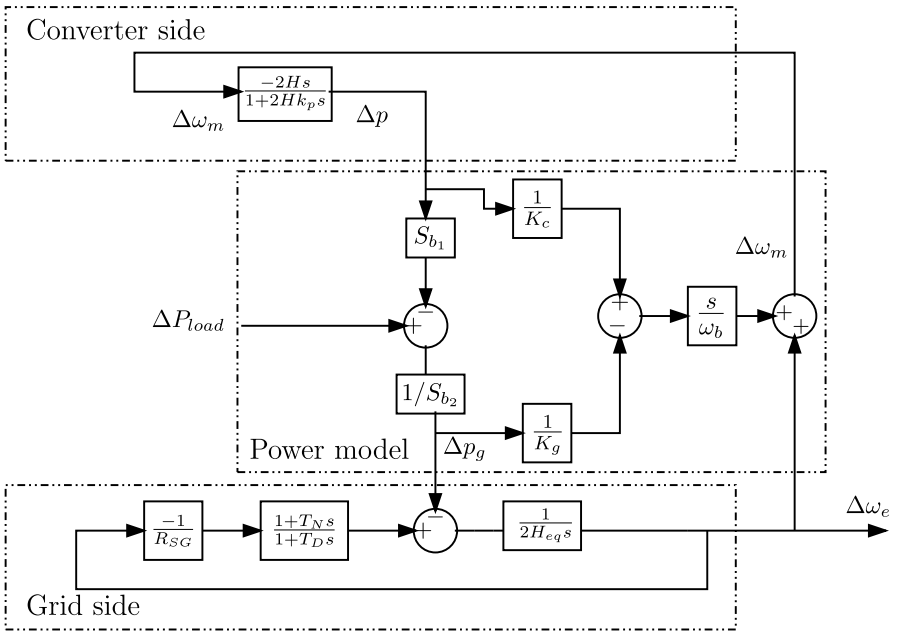

Figure II-40: Block diagram representation of the studied system for analysis of the active power and frequency dynamics (IP-control).

Merging (II-29), (II-24), (II-32) and (II-33), the block diagram of Figure II-40 can represent the overall system. This is a 4th order model and it can be further simplified by neglecting the damping term in the VSC control ($k_p = 0$) and considering $\Delta\omega_m = \Delta\omega_e$. The resulting model, which is a second order, is depicted in the left-hand side of Figure II-41. This simplified model can be equivalently re-shaped to highlight the contribution of the VSC inertial support to the grid frequency as show in the right-hand side of Figure II-41. From this demonstration and in the viewpoint of frequency dynamics studies, it can be concluded that the power converter based on IP control grid-forming scheme is seen as a synchronous machine in the grid side. From Figure II-41, the transfer function of the grid frequency with respect to the load change is deduced:

$$\frac{\Delta\omega_e}{\Delta P_{load}} = -\frac{1}{S_{b_2}} \frac{R_{SG}(1+T_D s)}{1+\left(2R_{SG}\left(H_{eq}+H\frac{S_{b_1}}{S_{b_2}}\right)+T_N\right)s+2R_{SG}T_D(H_{eq}+H\frac{S_{b_1}}{S_{b_2}})s^2} \qquad \text{(II- 34)}$$

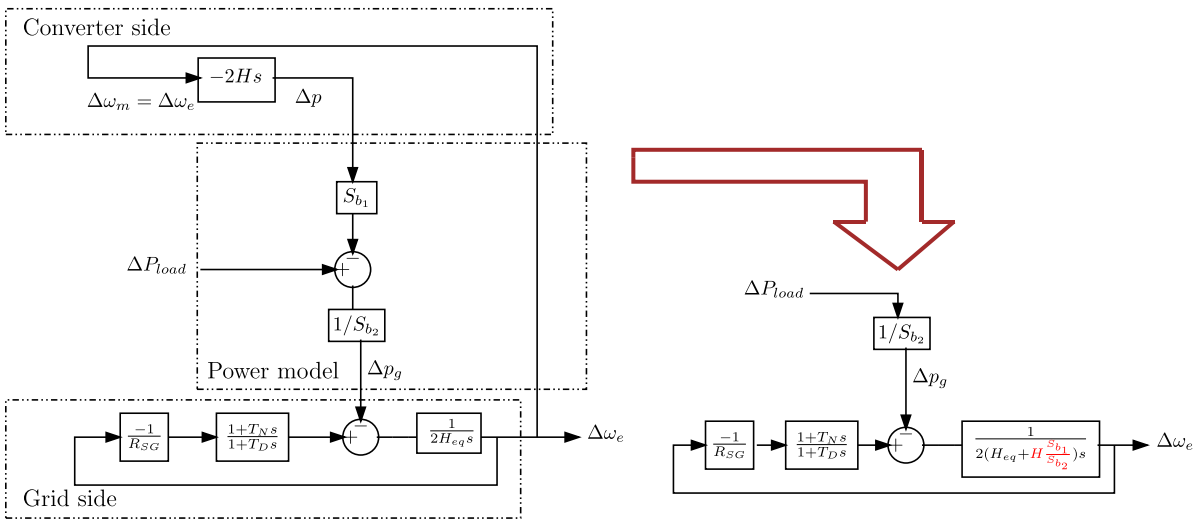

Figure II-41: Simplified block diagram for analysis of the active power and frequency dynamics (IP-control).

The damping ratio and natural frequency of (II-34) are given by:

$$\zeta = \frac{1}{2}\frac{2R_{SG}\left(H_{eq}+H\frac{S_{b_1}}{S_{b_2}}\right)+T_N}{\sqrt{2R_{SG}T_D\left(H_{eq}+H\frac{S_{b_1}}{S_{b_2}}\right)}}, \qquad \omega_n = \sqrt{\frac{1}{2R_{SG}T_D\left(H_{eq}+H\frac{S_{b_1}}{S_{b_2}}\right)}} \qquad \text{(II- 35)}$$

The RoCoF value for a load step ($\Delta P_{load}/s$) is determined as follows:

$$RoCoF = |\lim_{s\to\infty} s^2 \Delta\omega_e f_b| = \frac{1}{S_{b_2}}\frac{\Delta P_{load} f_b}{2\left(H_{eq}+H\frac{S_{b_1}}{S_{b_2}}\right)} \qquad \text{(II- 36)}$$

Comparing (II-36) with (II-27), it can be clearly seen that the inertia contribution by the IP control based VSC has reduced the RoCoF. The steady state frequency variation $\Delta\omega_{e_{ss}}$ with respect to the load step is the same as (II-28). To confirm the validity of the presented theoretical approach, similar time domain simulations as before (considering the system and control parameters given in Table II-5) are performed. Initially, there is no power exchange in the system ($p_g = p = P_{load} = 0$). A step of 200 MW (0.2 pu) is applied to the load at t=1 s. Figure II-42 shows the results of this case study. It can be seen that the response of the linearized fourth order model is matches to the nonlinear model. With the simplified second order model, there are some differences in transient mainly due to the assumption of $\Delta\omega_m = \Delta\omega_e$. However, this model can simply explain the dominant response of the system. According to (II-36), $RoCoF = 0.5$ Hz/s, which is improved compared to the results with the PLL-based control (Figure II-39).

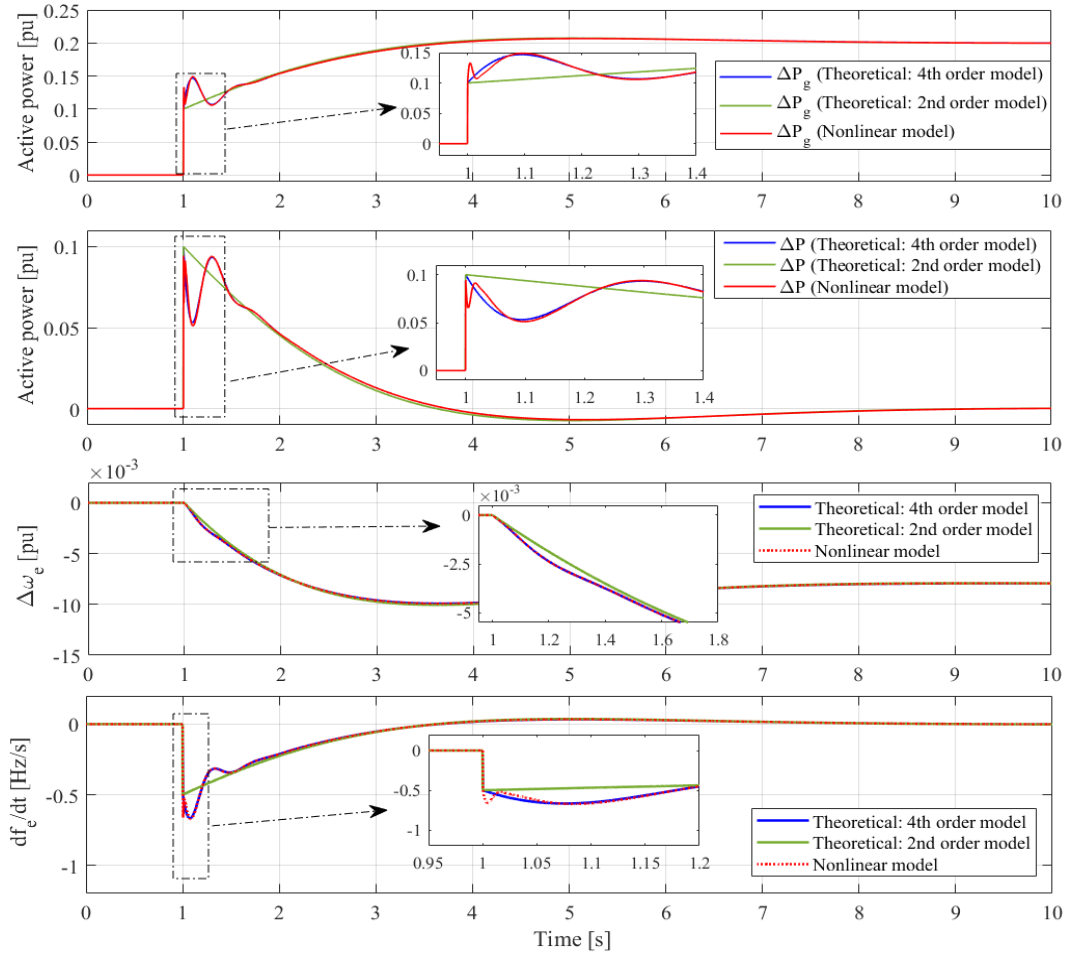

Figure II-42: Frequency and power dynamics with respect to a load change (IP-control).

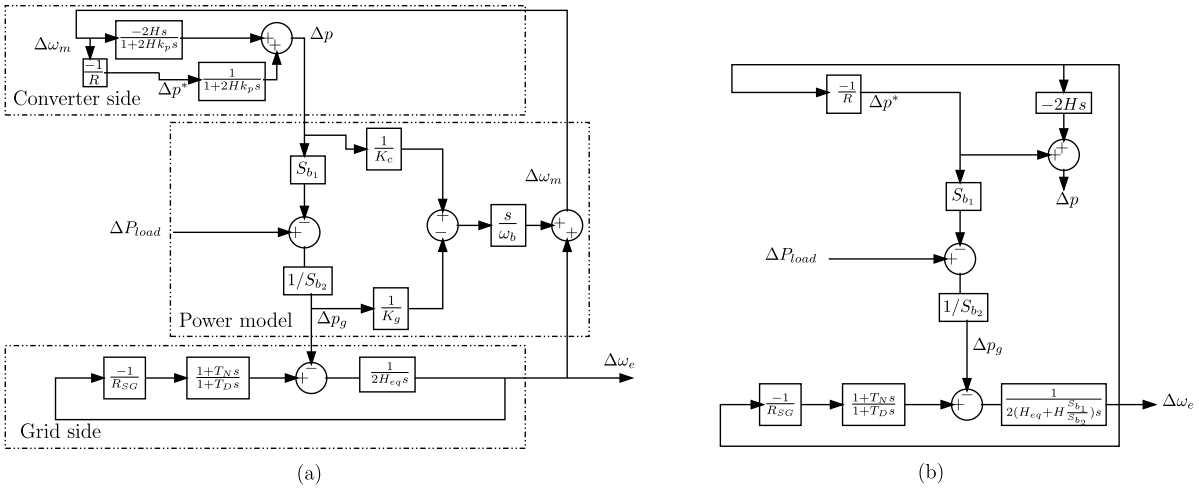

Figure II-43: Block diagram representation of the studied system for analysis of the active power and frequency dynamics (PLL-based control): (a) 4th order model (b) simplified 2nd order model.

II.4.4.4 Effect of the outer droop control loop on the frequency dynamics

In the previous study, the VSC was not participating in the frequency support and thus, only the grid was supplying the load in steady state. In order to support the grid frequency, a droop control is introduced in the VSC. Its equation is given by:

$$(\omega^* - \omega_m)\frac{1}{R} = p^* \qquad \text{(II- 37)}$$

where ω^* is the VSC frequency setpoint fixed at 1 pu. In small signal:

$$-\Delta\omega_m \frac{1}{R} = \Delta p^* \qquad \text{(II- 38)}$$

Taking into account previously presented modeling approach and considering the outer droop control for the IP- control based VSC, Figure II-43 presents the 4th order block diagram the overall system. Like before, neglecting the VSC damping term ($k_p = 0$) and assuming $\Delta\omega_m = \Delta\omega_e$, a simplified second order model shown in Figure II-43 is obtained.

Based on the second order mode, the transfer function of the grid frequency with respect to the load change is deduced:

$$\frac{\Delta\omega_e}{\Delta P_{load}} = -\frac{1}{S_{b_2}} \frac{RR_{SG}(1+T_D s)}{(R+R_{SG}\frac{S_{b_1}}{S_{b_2}})+\left(2RR_{SG}\left(H_{eq}+H\frac{S_{b_1}}{S_{b_2}}\right)+RT_N+R_{SG}\frac{S_{b_1}}{S_{b_2}}T_D\right)s+2RR_{SG}T_D(H_{eq}+H\frac{S_{b_1}}{S_{b_2}})s^2} \qquad \text{(II- 39)}$$

The damping and the natural frequency of (II-39) are given by:

$$\zeta = \frac{1}{2}\frac{RS_{b_2}T_N+R_{SG}S_{b_1}T_D+2(H_{eq}+H\frac{S_{b_1}}{S_{b_2}})RR_{SG}S_{b_2}}{\sqrt{2(H_{eq}+H\frac{S_{b_1}}{S_{b_2}})T_D RR_{SG}S_{b_2}(R_{SG}S_{b_1}+RS_{b_2})}}, \quad \omega_n = \sqrt{\frac{R_{SG}S_{b_1}+RS_{b_2}}{2(H_{eq}+H\frac{S_{b_1}}{S_{b_2}})T_D RR_{SG}S_{b_2}}} \qquad \text{(II- 40)}$$

Equation (II-40) states that the outer droop control increases the system damping and makes the frequency response faster. The RoCoF value for a load step ($\Delta P_{load}/s$) is the same as (II-36). This simply means that enabling the frequency support for the VSC has no effect on the RoCoF. The steady state frequency variation $\Delta\omega_{e_{ss}}$ with respect to the load step ($\Delta P_{load}/s$) is determined as follows:

$$\Delta\omega_{e_{ss}} = |\lim_{s\to 0} s\Delta\omega_e(s)| = -(\frac{RR_{SG}}{R_{SG}S_{b_1}+RS_{b_2}})\Delta P_{load} \qquad \text{(II- 41)}$$

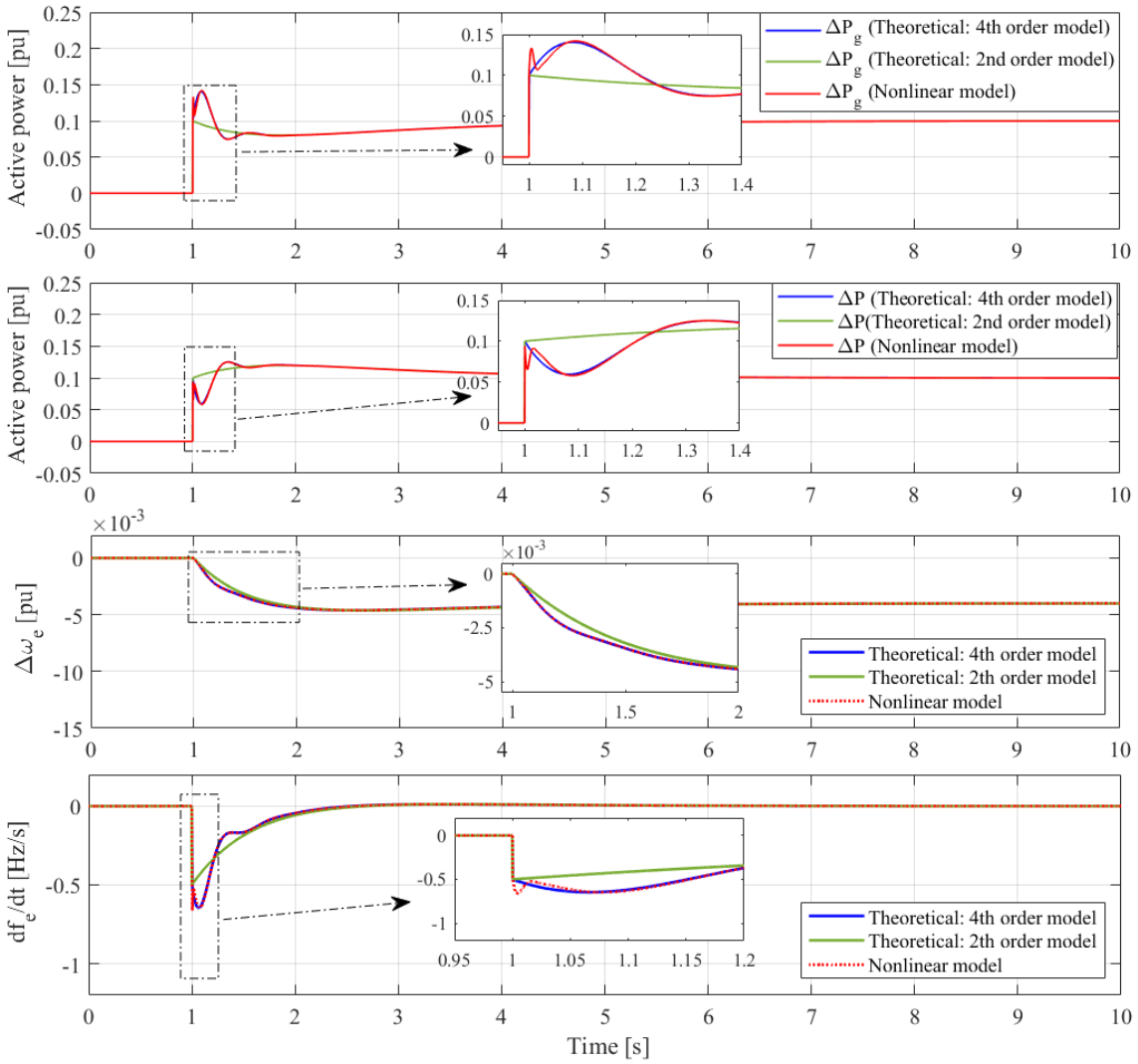

Figure II-44: Frequency and power dynamics with respect to a load change while enabling the frequency support of the VSC (IP-control).

Comparing (II-41) and (II-28), it is concluded that the steady state frequency variation is reduced when enabling the frequency support of the VSC. Applying the same load change scenario as before, Figure II-44 confirms the validity of the presented models and highlights the simultaneous inertia provision and frequency support contribution by the VSC.

II.5 Classification of grid-forming control schemes

Until here, two different control schemes (PLL-based and IP control) to generate the internal angle required for grid-forming implementation on VSCs were proposed. This section gathers four fundamentally different grid-forming control variants and classify them according to their capabilities/functionalities.

II.5.1 Equivalence of IP control and VSM

From the original formulation, it is possible to modify the IP control scheme proposed in Figure II-27 in order to reveal a VSM like formulation. Focusing on the active power flow:

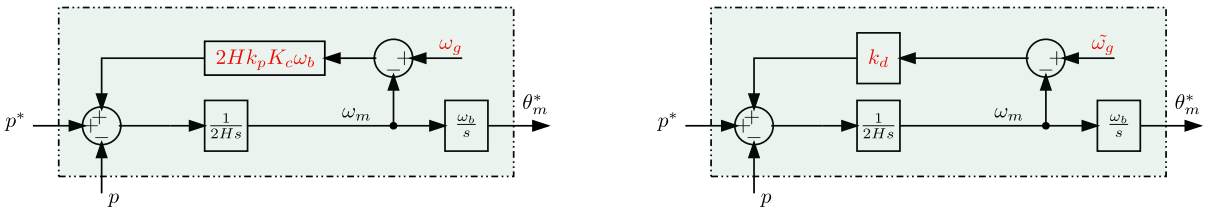

(a) Modified formulation of the PI controller. (b) VSM scheme.

Figure II-45: Equivalence between VSM and IP-control.

$$p = \frac{V_m V_g}{X_c}\frac{(\omega_m - \omega_g)\omega_b}{s} = K_c\frac{(\omega_m - \omega_g)\omega_b}{s}, \quad \text{(II- 42)}$$

The internal frequency from the IP-control is expressed as:

$$\omega_m = \frac{1}{2Hs}(p^* - p) - k_p p \quad \text{(II- 43)}$$

Replacing the term $k_p p$ in (II-43) by (II-42) yields:

$$\omega_m = \frac{1}{2Hs}(p^* - p) - \frac{k_p K_c(\omega_m - \omega_g)\omega_b}{s} \quad \text{(II- 44)}$$

Equation (II-44) can be re-written as follows:

$$2Hs.\omega_m = p^* - p + 2Hk_pK_c(\omega_g - \omega_m)\omega_b \quad \text{(II- 45)}$$

This new mathematical formulation of the internal frequency is graphically illustrated in Figure II-45. It has to be emphasized that this control cannot be implemented like that. It is just another way to present the control in order to show its similarity with the VSM presented in Figure II-45. Although the general organization is similar, there is a fundamental difference since the estimation of the grid frequency $\tilde{\omega}_g$ (provided by a PLL) needed in the VSM [57] is replaced with the grid frequency ω_g itself.

II.5.2 Derivation of other grid-forming variants

From the PLL-based control, it is possible to derive two other variants, which have been already studied in the literature [40], [58]. Considering the control given in Figure II-46, the information from the PLL has been moved to obtain another variant of the grid-forming schemes. The estimate of the grid angle is not used anymore but only the estimate of the grid frequency. The active power is still under control but not with the same dynamics.

For this control scheme, the differential equation that relates the internal frequency ω_m to the active power can be written as follows:

$$\frac{1}{m_p\omega_c}\frac{d\omega_m(t)}{dt} = p^*(t) - p(t) + \frac{1}{m_p}\left(\omega_m(t) - \tilde{\omega}_g(t)\right) \quad \text{(II- 46)}$$

Equation (II-46) is equivalent to the one for the VSM (can be derived from Figure II-45). By identification, the equivalent inertia constant and damping factor are found as follow:

$$H = \frac{1}{2m_p\omega_c} \quad , \; k_d = \frac{1}{m_p} \quad \text{(II- 47)}$$

Therefore, this scheme is capable of providing an inertial effect. In [58] it has been demonstrated that the power response of this control is sensible to the SCR variation. Frequency support is an optional task and it can be implemented in an outer loop.

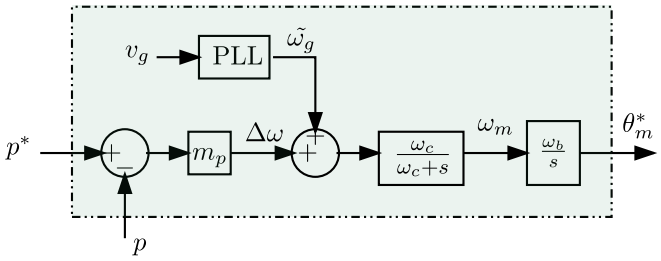

Figure II-46: Grid-forming control with a PLL, where the PLL is used to provide an estimate of the grid frequency.

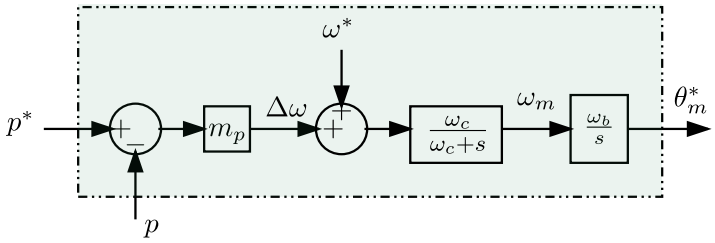

Figure II-47: Grid-forming scheme based on the classical droop control.

If the estimated frequency by the PLL is replaced by a frequency setpoint ω^* (it is generally the grid nominal frequency) another grid-forming variant is attained which is illustrated in Figure II-47. In [40], [59], it has been shown that:

$$\omega_g(t) - \omega^* = m_p(p^*(t) - p(t)) \quad \text{(II- 48)}$$

This last formula is equivalent to the classical droop control with the frequency droop gain of m_p. This scheme is equivalent to the VSM implementation (with equivalent parameters in (II-47)) in which, no PLL is used as demonstrated in [40]. The power response of this control is sensible to the SCR variation. In this control, the frequency support is a compulsory task of the control and therefore, there is no possibility to limit the amount power that participates in the frequency support. This might be a big issue for the sources that are connected to this kind of converter. This problem does not exist in PLL based schemes or IP-control where the frequency support is implemented in an outer control loop decoupled from the power regulation task. It should be noted that since m_p is the droop gain and it cannot be chosen freely, the design of the desired inertia constant is linked to the value of ω_c. To have a high inertia support (e.g., $H = 5$ [s]), the corresponding value of ω_c is small and it is out of the range given in (II-15). This reduction in the filter cut-off frequency results in power oscillations. Therefore, an additional damping (e.g., a derivative action on the measured active power [60]) has to be utilized to mitigate these oscillations.

Based on the provided content, Table II-6 presents four different classes of grid-forming control schemes along with the summary of their features.

Table II-6: Classification of grid-forming control schemes.

Type	Scheme (s)	Features
Type A	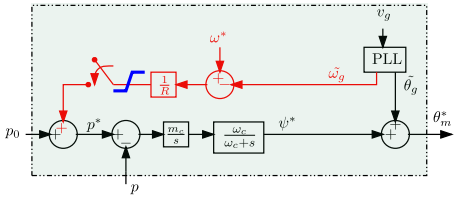	- A PLL is required to provide an estimate of the grid angle to the control. - The active power response is not sensible to the SCR variation. - This scheme has no inherent inertial effect - The frequency support is optional and it can be implemented in an outer loop, decoupled from the power regulation task. - It is possible to limit the additional power served for the frequency support.
Type B	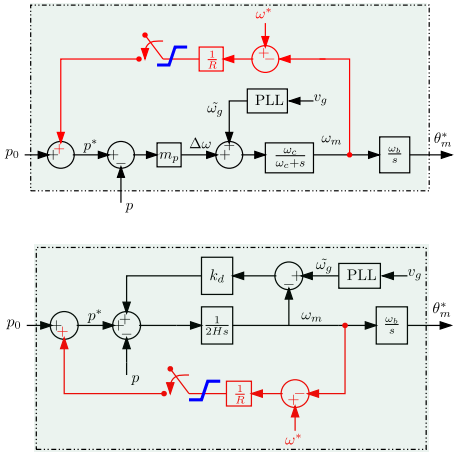	- A PLL is required to provide an estimate of the grid frequency to the control. - These schemes are equivalent considering: $H = \frac{1}{2m_p\omega_c}, k_d = \frac{1}{m_p}$ - Their active power response is sensible to the SCR variation. - These schemes have inherent inertial effect. - The frequency support is optional and it can be implemented in an outer loop, decoupled from the power regulation task. - It is possible to limit the additional power served for the frequency support.
Type C	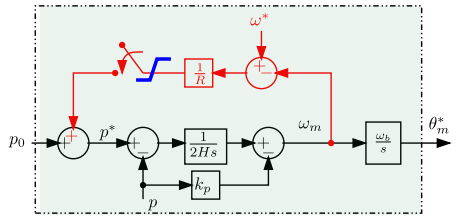	- Similar to Type B with no PLL. The equivalent damping term is: $k_p = \frac{k_d}{2HK_c\omega_b}$
Type D	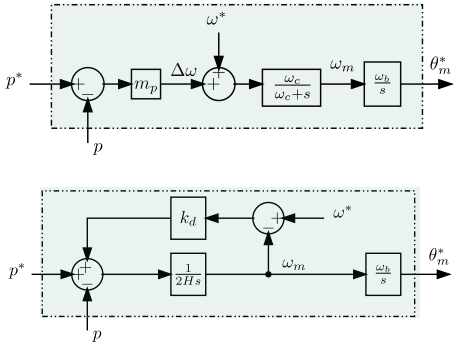	- No PLL is required. - These schemes are equivalent considering: $H = \frac{1}{2m_p\omega_c}, k_d = \frac{1}{m_p}$ - Their active power response is sensible to the SCR variation. - These schemes have inherent inertial effect. However, an additional damping term (e.g., a derivative action on the measured power) is required to have a damped power response while asking for inertia service. - The frequency support is a compulsory task of the control and $m_p = \frac{1}{k_d}$ is the droop gain. - Since the power regulation and frequency support tasks are fully coupled in a single control loop, it is not possible to limit the additional power served for the frequency support.

II.6 Conclusions

In this chapter the fundamental of active power control in a power electronic converter, where it can behave as either current source or voltage source, from the AC grid point of view, was explained. Focusing on the voltage source behavior that is the origin of grid-forming control, two different solutions, namely PLL-based and IP-control, were developed based on quasi-static models to regulate the active power of a simplified VSC with no LC filter. In the next step, the grid-forming schemes were implemented to a 2-level VSC with LC filter. In this case, it was demonstrated that the quasi-static models give a good estimate of the system dominant modes, and therefore they can be used to simply explain the system dynamics and to tune the active power response of the grid-forming converters. Consequently, the analysis of large grids may be done based on the simplified models.

From the small-signal stability and robustness point of view, the studied grid-forming controls in this chapter show their ability to operate under very weak grid conditions, which is much superior compared to the grid-following control. Moreover, the ancillary services such as inertial response and frequency support can be appropriately provided to the AC grid.

Chapter III: Current Limitation and Transient Stability

In the previous chapter, the presented analyses were related to the normal operation of the power converter. Due to the voltage-source behavior of a grid-forming converter, some extreme faults that may happen in the power grids such as short circuit, heavy load connection, line-tripping/reclosing and voltage phase jump can cause overcurrent in the converter [61]. Compared to synchronous generators (SGs) that can support up to seven times over their rated current, power converters can only cope with few percent of overcurrent (typically 20%) Therefore, the overcurrent protection requires a specific attention [62].

Many control strategies have been proposed for grid-forming converters in order to limit the current during large transients [63]–[65]. One strategy is to limit the current with a current saturation algorithm (CSA). In practice, this technique is implemented on the generated current reference of the converters by saturating the reference current during over current period [65], [66]. Another well-known current limiting strategy is based on a virtual impedance (VI) that emulates the effect of an impedance when the current exceeds its rated value [62], [67], [68]. This method has shown its effectiveness to limit the current transients in case of various events while keeping the voltage source nature of the power converter.

Once the fault is cleared, the post-fault synchronization is of highest importance. Indeed, an unstable behavior when the overcurrent protection is disabled would lead to an unavoidable trip from the main grid for safety purposes [44]. However, in future power systems, all different power sources have to cope with various events and guarantee the stability. In this context, the transient stability of the system is defined as the ability of the power converter to stably recover its equilibrium point after fault clearing. This aspect has been studied in [69], [70] while neglecting the current limitation. However, as mentioned in [66], [71], the current limitation has a large impact on the transient stability.

In [72], [73], the transient stability of the grid-forming converters including the VI is investigated. In [72], the transient stability of a droop-based virtual synchronous generator in case of a 30% grid voltage sag is studied in two steps. First, the VI is not taken into account. Based on that, a theoretical approach relying on the Lyapunov's direct method to predict the critical clearing time (CCT) is developed. Then, when including a constant VI, it has been demonstrated that the stability region becomes more limited. In [73], a method for critical clearing angle (CCA) and CCT calculation in case of a bolted fault while limiting the current with a VI is proposed. To improve the CCA and CCT, authors in [72], [73] propose to decrease the power reference with respect to the AC voltage magnitude. An alternative solution that consists to increase the inertia constant with respect to the AC voltage magnitude is suggested in [74]. Referring to [40], the management of the power reference or inertia constant with respect to the voltage magnitude is mainly effective when the voltage magnitude is decreasing as in case of a voltage sag. However, in the case of a voltage phase shift, which is a very likely event, these solutions are useless.

Considering the effect of a CSA on the transient stability, only few research have been done. Authors in [66], [75] have determined a stability criterion based on CCA for

an inertia-less droop-controlled VSC in case of a voltage sag. Then, in [66] a stability enhanced P-f droop control scheme is presented to improve the transient stability of the VSC by modifying the frequency setpoint through the quadrature voltage component of the Park frame. In [66] and [75], the priority of the saturated current reference has been given to the d-axis component, so the converter injects the current aligned with the d-axis during the fault. To the best of our knowledge, the impact of the current reference priority (i.e., the current reference angle) has not been justified and its impact on the transient stability has not been highlighted.

Based on the presented literature review, the aims of this chapter are:

1- Presenting a general overview of current limitation strategies including VI and CSA for grid-forming converters.
2- Post-fault synchronization of the grid-forming converter while considering a CSA as current limiting strategy.
3- Investigation of the impact of the current reference angle on the transient stability.

III.1 Overview of current limitation methods for grid-forming applications

Figure III-1 shows two general control schemes to implement the current limitation on the IP-controlled grid-forming VSC: the VI and the CSA. Both algorithms are recalled in the following subsections.

III.1.1 Virtual impedance

The idea behind the VI is to virtually add an extra impedance (voltage drop proportional to the overcurrent) during the overcurrent period in order to reduce the modulated voltage amplitude by the converter and accordingly limit the output current. To this end, the voltage setpoints e'^{*}_{gdq0} drop e^{*}_{gdq0} to as follow:

$$e^{*}_{gd0} = e'^{*}_{gd0} - \delta e_{gd} \quad , \quad \delta e_{gd} = R_{VI} i_{sd} - X_{VI} i_{sq} \qquad \text{(III- 1)}$$

$$e^{*}_{gq0} = e'^{*}_{gq0} - \delta e_{gq} \quad , \quad \delta e_{gq} = R_{VI} i_{sq} + X_{VI} i_{sd} \qquad \text{(III- 2)}$$

where X_{VI} and R_{VI} are the reactance and resistance of the VI, respectively.

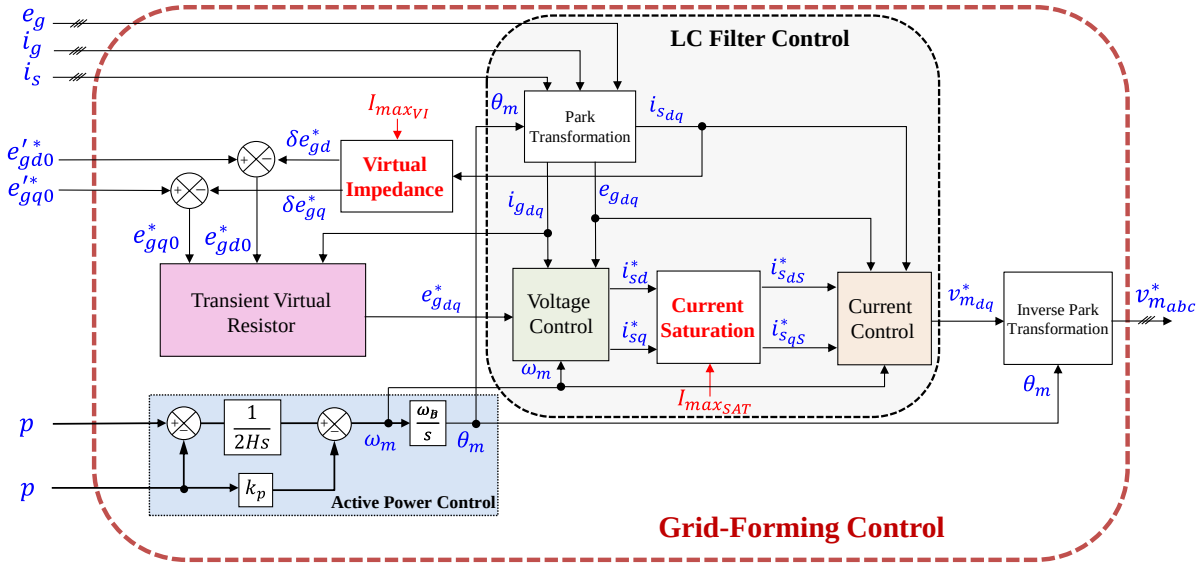

Figure III-1: Implementation of VI and CSA on a 2-level VSC with grid-forming control.

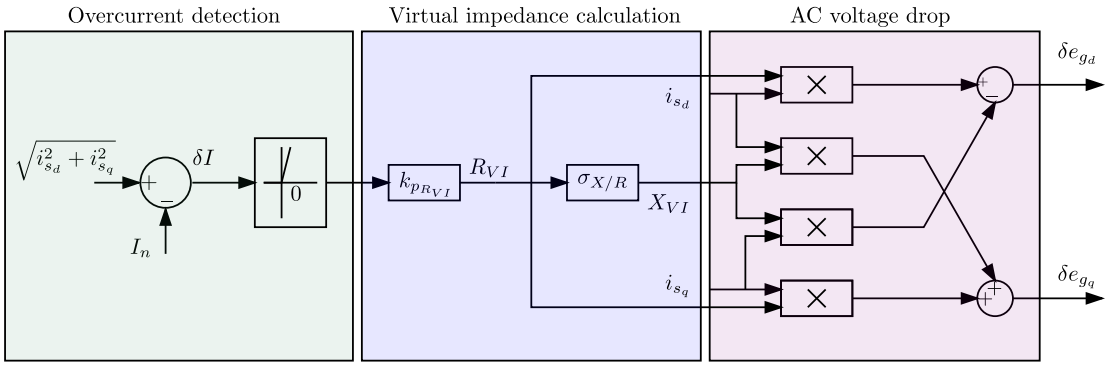

Figure III-2: VI implementation principle.

The design of the VI is based on the worst-case scenario, which in this study, is a three-phase short circuit at the PCC. Figure III-2 shows the conventional implementation of the VI [67], [76], [77]. According to this implementation, the VI is activated only when the current exceeds its nominal value $I_n = 1$ p.u. Otherwise, it is disabled. The VI components are determined by the following expressions:

$$X_{VI} = \begin{cases} k_{p_{R_{VI}}} \sigma_{X/R} \delta I & if \;\; \delta I > 0 \\ 0 & if \;\; \delta I \leq 0 \end{cases} \quad \text{(III- 3)}$$

$$R_{VI} = X_{VI}/\sigma_{X/R} \quad \text{(III- 4)}$$

where $\delta I = I_s - I_n$. The parameters $k_{p_{RVI}}$ and $\sigma_{X/R}$ are defined respectively as the virtual impedance proportional gain and the virtual impedance ratio. The parameter $k_{p_{R_{VI}}}$ is tuned to limit the current magnitude to a suitable level $I_{max_{VI}}$ in case of a bolted fault, while $\sigma_{X/R}$ ensures a good system dynamics during the overcurrent and keeps a higher X/R ratio [67].

To calculate the parameter $k_{p_{R_{VI}}}$, the single-phase equivalent static representation of the 2-level VSC for a fault that occurs at the PCC is considered and illustrated in Figure III-3. Neglecting the transformer resistance, the following expression in per-unit gives the voltage and current relationship during the fault period:

$$E'_g = I_{max_{VI}} \sqrt{R_{VI}^2 + (\omega_0 L_{VI} + \omega_0 L_c)^2} \quad \text{(III- 5)}$$

where E'_g is the magnitude of the voltage that is controlled by the converter, ω_0 is the fundamental frequency in per-unit and L_{VI} is the virtual inductance at the fundamental frequency. By solving (III-3), (III-4) and (III-5) with respect to the $k_{p_{R_{VI}}}$:

$$k_{p_{R_{VI}}} = \frac{-b + \sqrt{b^2 - 4ac}}{2a} \quad \text{(III- 6)}$$

with, $a = \left(I_{max_{VI}} - I_n\right)^2 (1 + \sigma_{X/R}^2)$, $b = 2\sigma_{X/R} \omega_0 L_c (I_{max_{VI}} - I_n)$, $c = (\omega_0 L_c)^2 - \frac{E_g'^2}{I_{max_{VI}}^2}$.

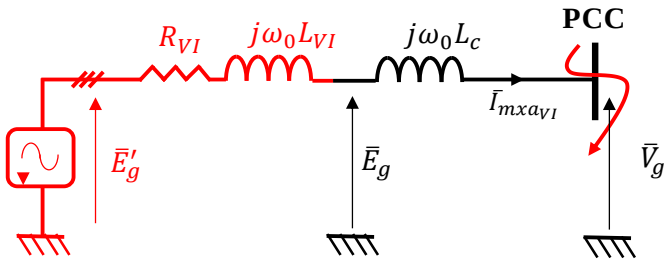

Figure III-3: Single-phase static representation of the VSC with the VI in case of a fault at the PCC.

III.1.2Current reference saturation

The other current limiting method is based on saturating the current reference generated in the cascaded control structure of the VSC. One solution is to saturate the d-axis current component to the maximum current magnitude, the q-axis current component is then deduced [75]:

$$\begin{cases} i_{s_{dS}}^{*} = min(I_{max_{SAT}}, |i_{s_d}^{*}|) \\ i_{s_{qS}}^{*} = min(\sqrt{I_{max_{SAT}}^{2} - {i_{s_{dS}}^{*}}^{2}}, |i_{s_q}^{*}|) \end{cases} \quad \text{(III- 7)}$$

where, $I_{max_{SAT}}$ stands for the maximum allowable current magnitude of the converter, whereas $i_{s_{dqS}}^{*}$ denotes the saturated d-q currents. With this solution, the current vector is sliding along a parallel of the q-axis in the Park frame during the overcurrent situation.

A second possibility is to limit the current magnitude I_S^* without giving any priority to the direct current $i_{s_d}^{*}$ or to the quadratic one $i_{s_q}^{*}$. It is done by reducing both current components in the Park frame in such a way that the current vector is on the perimeter of a circle whose radius equals the maximum current magnitude. This strategy is described as:

$$\begin{cases} i_{s_{dqS}}^{*} = i_{s_{dq}}^{*} & if \ \sqrt{i_{s_d}^{2} + i_{s_q}^{2}} \leq I_{max_{SAT}} \\ i_{s_{dS}}^{*} = I_{max_{SAT}} cos[arctan\left(\frac{i_{s_q}^{*}}{i_{s_d}^{*}}\right)] & if \ \sqrt{i_{s_d}^{2} + i_{s_q}^{2}} > I_{max_{SAT}} \\ i_{s_{qS}}^{*} = I_{max_{SAT}} sin[arctan\left(\frac{i_{s_q}^{*}}{i_{s_d}^{*}}\right)] & if \ \sqrt{i_{s_d}^{2} + i_{s_q}^{2}} > I_{max_{SAT}} \end{cases} \quad \text{(III- 8)}$$

To validate the performance of both current limiting strategies, it is assumed that the 2-level VSC is connected to an infinite bus (See Figure II-28) and a three-phase bolted fault at $t = 3$ [s] is applied to the PCC. The operating point is $p^* = 0.9$ p.u. The control and system parameters are listed in Table III-1. For these parameters and based on (III-6): $k_{p_{RVI}} = 0.6724 \ p.u.$

Table III-1 System and control parameters.

$P_n = S_b$	1 GW	ω_f	60 rad/s
ω_b	314.16 rad/s	k_{pi}	0.73 p.u
$L_g = 10R_g$	0.1 p.u	k_{ii}	1.19 p.u
L_c	0.15 p.u	k_{pv}	0.52 p.u
R_c	0.005 p.u	k_{iv}	1.16 p.u
C_f	0.066 p.u	$I_{max_{SAT}}$	1.2 p.u
L_f	0.15 p.u	$I_{max_{VI}}$	1.2 p.u
R_f	0.005 p.u	$\sigma_{X/R}$	5
u_{dc}	640 kV	I_n	1 p.u.
u_{ac}	320 kV	$k_{p_{RVI}}$	0.6724 p.u
$e_{g_{d0}}^{\prime *}$	1 p.u	H	5 s
$e_{g_{q0}}^{\prime *}$	0 p.u	k_p	0.007
R_v	0.09 p.u		

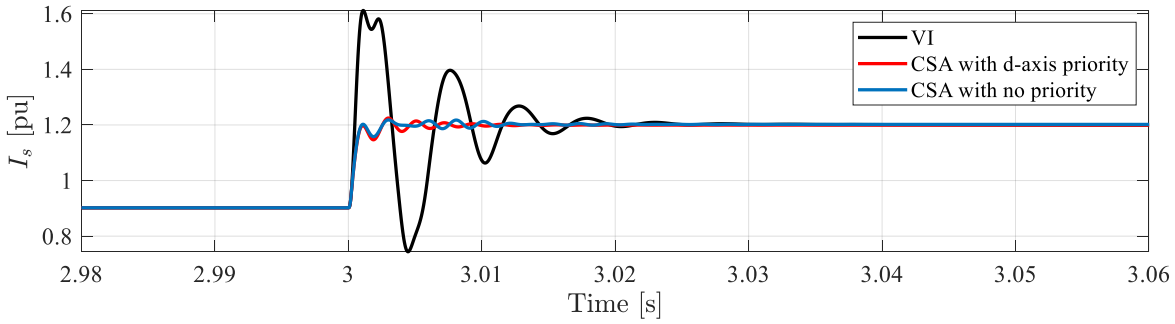

Figure III-4: dynamics of the VSC current during a symmetrical three-phase fault.

Figure III-4 presents the simulation results. It can be seen that both VI and CSA strategies effectively limit the VSC current to the maximum allowable value (1.2 pu) in steady state. The CSA has a better performance in limiting the current during the first milliseconds after the fault, while for the VI strategy, an overcurrent during the first 20 milliseconds is observed. The reason is the slower behavior of the VI due to its indirect action for limiting the current. In [71] a comparative study between the CSA and VI strategies in case of a three-phase short circuit is performed and a hybridized approach is proposed to improve the dynamic performance of the system.

III.2 Post-fault synchronization of a grid-forming converter considering current reference saturation as current limiting strategy

Once the fault is cleared (i.e., three-phase bolted fault), the power converter has to be able to resynchronize with the AC grid by only using local measurements. Post-fault synchronization and transient stability problem of the grid-forming converters considering the VI as current limiting strategy is extensively studied in the literature. The aim of this section is to analyze the transient stability of the grid forming converters facing with two different types of balanced faults (i.e., three phase short-circuit fault and phase-shift), while including the current reference saturation in the control. This topic has not been much discussed in the literature.

III.2.1 Phasor model for transient stability studies

When analyzing the transient stability problem caused by the power control loop, the inner control loops can be neglected because of their faster response time [66], [69]. Neglecting the internal loops dynamics (i.e., the dynamics of the cascaded voltage and current control loops), a classical phasor model is proposed in Figure III-5, where only the voltage e_g is considered at the converter side. In steady state, it is represented by a complex quantity $\overrightarrow{E_g}$. The magnitude is supposed to be 1 pu and the angle is δ_m, which is linked with θ_m : $\theta_m(t) = \omega_m t + \delta_m$.

The vector $\overrightarrow{V_e}$ represents the voltage vector at the grid side, the magnitude is 1 [pu] and the phase angle is δ_e. By neglecting the resistance, Figure III-5 illustrates the corresponding phasor diagram in the normal operation mode (unsaturated current operation mode). The vector $\overrightarrow{E_g}$. (in blue) is the controlled vector that is supposed to be aligned with the d-axis. The current vector $\overrightarrow{I_g}$ (in green) is a consequence of this operation mode. The well-known expression of the power can be written in steady state

as follows:

$$P = \frac{E_g V_e}{X_c + X_g} sin(\delta_m - \delta_e) = P_{max} sin\delta, \qquad \text{(III- 9)}$$

where $\delta = \delta_m - \delta_e$ denotes the power angle, $P_{max} = E_g V_e/(X_c + X_g)$.
During some transient times, the current may increase over the maximum current of the converter. To limit the current, the following CSA is proposed:

$$\begin{cases} i^*_{s_{dS}} = i^*_{s_d}\ ,\ i^*_{s_{qS}} = i^*_{s_q} & if \quad \sqrt{i^2_{s_d} + i^2_{s_q}} \le I_{max_{SAT}} \\ i^*_{s_{dS}} = I_{max_{SAT}}\ cos\ (-\phi) & if \quad \sqrt{i^2_{s_d} + i^2_{s_q}} > I_{max_{SAT}} \\ i^*_{s_{qS}} = I_{max_{SAT}}\ sin\ (-\phi) \end{cases} \qquad \text{(III- 10)}$$

In saturated operation mode, it is possible to draw a new phasor diagram as illustrated in Figure III-6. In the proposed CSA, the magnitude of $\overrightarrow{I_g}$ is set to $I_{max_{SAT}}$ and however, its angle ϕ can be chosen freely (with reference to the d-axis) by the control. This point makes a distinction between the proposed CSA and the one with d-axis priority in (III-7) or the one with no priority in (III-8). In fact, the choice of priority has not been justified in the literature and its impact on the stability has not been analyzed. In the following sub-sections, the effect of this choice on the transient stability of the grid-forming converter under various events is investigated.

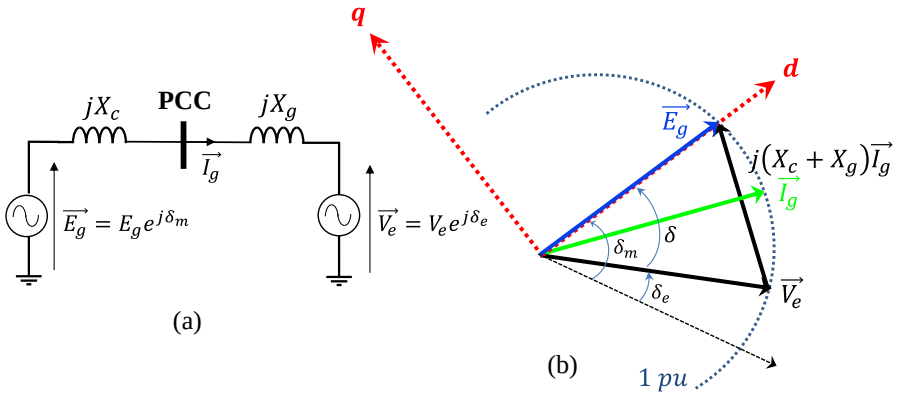

Figure III-5: (a)- Single-phase equivalent circuit of the VSC, (b)- Phasor diagram in voltage control mode.

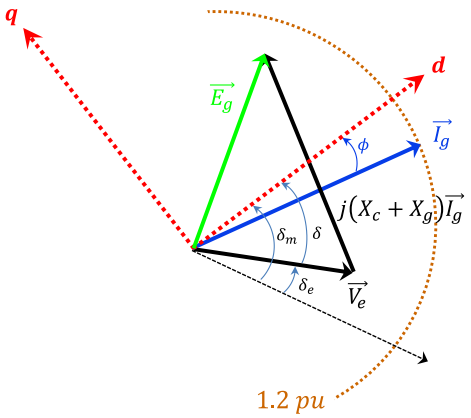

Figure III-6: Phasor diagram of the VSC in saturated current operation mode.

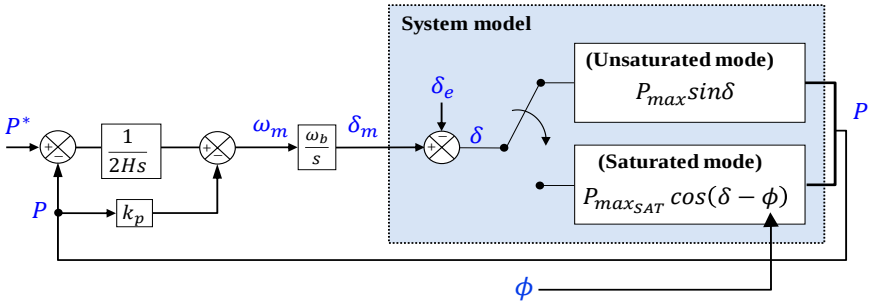

Figure III-7 Large signal model including the dynamic control for transient analysis.

Since the voltage vector $\overrightarrow{E_g}$ is not under control, it becomes a consequence in the saturated current control mode. Hence, the active power is now calculated with the grid voltage $\overrightarrow{V_e}$ and the controlled vector $\overrightarrow{I_g}$ as follows [66], [75]:

$$P = V_e I_{max_{SAT}}\, cos(\delta_e - (\delta_m - \phi)) = P_{max_{SAT}}\, cos(\delta - \phi) \qquad \text{(III- 11)}$$

where $P_{max_{SAT}} = V_e I_{max_{SAT}}$. According to (III-9) and (III-11), the large signal model of the grid-forming converter for both unsaturated and saturated current operation modes is illustrated in Figure III-7.

III.2.2 Transient stability analysis in case of a voltage sag

In this subsection, the transient stability of the grid-forming converter in case of a voltage sag is studied. First, a specific case considering a 100% voltage sag at the PCC is investigated. The aims of this study are to simply explain the operation mechanism of the VSC under this event, to derive the critical clearing angle (CCA) and critical clearing time (CCT) formulas and to investigate the impact of an optimal calculation of the saturated current angle ϕ on the transient stability. After that, a generic case of voltage sag is considered.

III.2.2.1 Analysis of the operation under a 100% voltage sag

Figure III-8 describes the operation mechanism of the grid-forming VSC subjected to a bolted fault. Initially the converter is operating in normal condition and the initial operating point is (δ_0, P^*):

- Phase 1: The voltage drops to zero, resulting in an increase of the current, which is limited by the CSA, and a decrease of the active power. According to the control described in Fig. 5, the angle δ increases untill δ_c , which is defined as the clearing angle (moving from the operating point ‘a’ to ‘b’).
- Phase 2: The fault is cleared; the CSA is activated and the operating point jumps to the point (c) located on the saturated $P-\delta$ curve.
- Phase 3: The active power is higher than its setpoint, however, the angle δ is still increasing untill the point (d) due to the inertial effect.
- Phase 4: Once the converter frequency becomes lower than the grid frequency, the angle starts to decrease until reaching the operating point (e), which is the intersection point of the saturated and unsaturated $P-\delta$ curves.
- Phase 5: At the operating point (e), the CSA is deactivated and the system switches back to the voltage control mode. The angle decreases until the equilibrium point (a), where $P = P^*$.

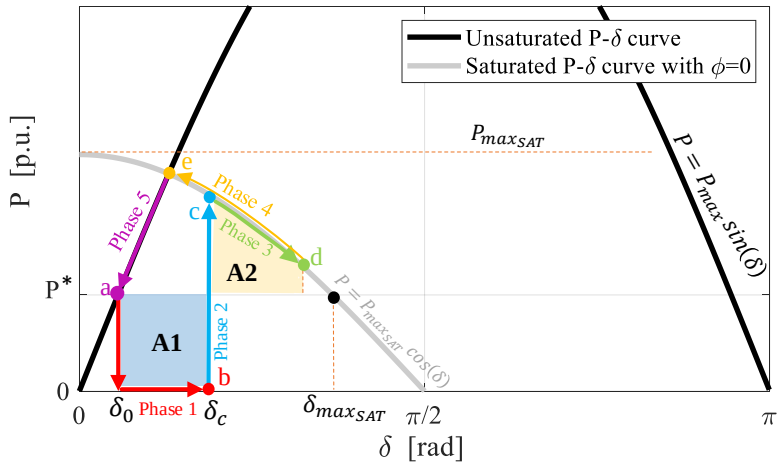

Figure III-8 Operation mechanism of the VSC under 100% voltage sag.

For a given δ_c, the system remains stable as long as the areas A_1 and A_2 are equal. The stability limit is reached when $\delta_c = \delta_{cc}$, which is called the "critical clearing angle (CCA)" δ_{cc}. Under this condition, the internal angle reaches to its maximum value $\delta_{max_{SAT}}$ after the fault clearance.

$$\delta_{max_{SAT}} = acos\left(\frac{P_0}{P_{max_{SAT}}}\right) \qquad \text{(III- 12)}$$

It should be mentioned that during phase 1 to 4, the voltage control (see Figure III-1) might generate some current references over the maximum value $I_{max_{SAT}}$. Hence, an anti-windup method has to be implemented. When reaching point e, the voltage control starts to decrease the current references and the system switches to Phase 5.

The use of equal are criterion here is similar to a synchronous machine. From the physical point of view, the internal frequency of the converter is just a signal obtained by a simplified model of the rotating shaft. During the fault (surface A1), where is no power exchange, the internal frequency increases. This effect is virtual. However, once the fault is cleared and the voltage is recovered (surface A2) the converter delivers a real power to the grid.

III.2.2.2 Critical clearing time calculation

The critical clearing angle is calculated by considering equal surfaces A_1 and A_2:

$$\int_{\delta_0}^{\delta_{cc}} P^*\, d\delta \;=\; \int_{\delta_{cc}}^{\delta_{max_{SAT}}} (P_{max_{SAT}}\cos(\delta) \;- P^*)\, d\delta$$

$$\Rightarrow \delta_{cc} = asin\left(\frac{P^*\left(\delta_0 - \delta_{max_{SAT}}\right)}{P_{max_{SAT}}} + si\,n\left(\delta_{max_{SAT}}\right)\right), \qquad \text{(III- 13)}$$

where $\delta_0 = \text{asin}\,(\frac{P^*(X_c+X_g)}{E_g V_e})$. In order to calculate the critical clearing time (CCT) t_{cc}, the expression of the angle δ during the phase 1 is needed. According to the control system (Figure III-7) and considering a fault condition (P=0), it can be written:

$$\delta(t) = \frac{\omega_b P^*}{4H} t^2 + \delta_0 \qquad (\delta_0 \leq \delta \leq \delta_{cc}) \qquad \text{(III- 14)}$$

Hence, the CCT can be expressed as:

$$t_{cc} = 2\left(\sqrt{\frac{H(\delta_{cc}-\delta_0)}{\omega_b P^*}}\right) \quad \text{(III- 15)}$$

Equation (III-15) clearly demonstrates the effect of the initial operating point and inertial effect on the CCT. Two large assumptions have been used to obtain the expression of the critical clearing time:

1- The effect of the damping is negligible.
2- The quasi-static model is valid enough even during large transient phenomena.

The validity of these assumptions is demonstrated in the following lines through dynamic simulations.

The system and control parameters are given in the Table III-1. Note that an anti-windup is adopted to the PI regulators in the voltage control loop (see Appendix C) [40]. Considering the given parameters in Table III-1, the CCT predicted from (III-15) and the one observed from the time-domain simulations are compared in Table III- 2 for different operating points. One can notice a small error between both CCTs. This error is due to the damping effect as it is mentioned in [78].

Taking $P^* = 1\ pu$ as an illustrative example, Figure III-9 shows the simulation results with two different fault durations of $t_{f1} = t_{cc} = 38\ ms$ and $t_{f2} > t_{cc}$ $(45\ ms)$. As expected, if the clearing time is lower or equal to the CCT, the internal angle of the VSC stably recovers its equilibrium point, otherwise it diverges and the system loses the synchronism.

In order to investigate the impact of the inertia constant on the accuracy of (III-15), another case study with $H = 1.25$ [s] is examined. To have a fair comparison, the damping ratio ζ of the active power response should be the same for different inertia constants. As it is demonstrated in [74], the damping ratio is proportional to $k_p\sqrt{H}$. Therefore, the controller gain k_p is set to 0.014 [pu]. Table III- 3 summarizes the obtained CCT for various operating points. It can be seen that the accuracy of the predicted CCT is slightly reduced compared to the case with $H = 5$ [s] (in Table III- 2). In fact, when the inertial effect is negligible, the angle δ right after the phase 2, shown in Figure III-8, tends to be decreased immediately. This makes the critical clearing angle δ_{cc} closed to the maximum allowable angle $\delta_{max_{SAT}}$ and therefore, a different formula for the CCT can be derived without using the equal area criterion as it has been already studied in [71].

In any case, the obtained value of the critical clearing time is quite small. Next subsection proposes to set the current reference angle in order to increase this critical clearing time.

Table III- 2: Results of the CCT determination.

	$\boldsymbol{\phi = 0}$ $\boldsymbol{H = 5\ s, k_p = 0.007}$	
$\boldsymbol{P_0}$	Predicted CCT by (III-15)	CCT in simulation
1 pu	41 ms	38 ms
0.9 pu	69 ms	63 ms
0.8 pu	99 ms	91 ms
0.7 pu	133 ms	120 ms
0.6 pu	173 ms	157 ms
0.5 pu	221 ms	204 ms

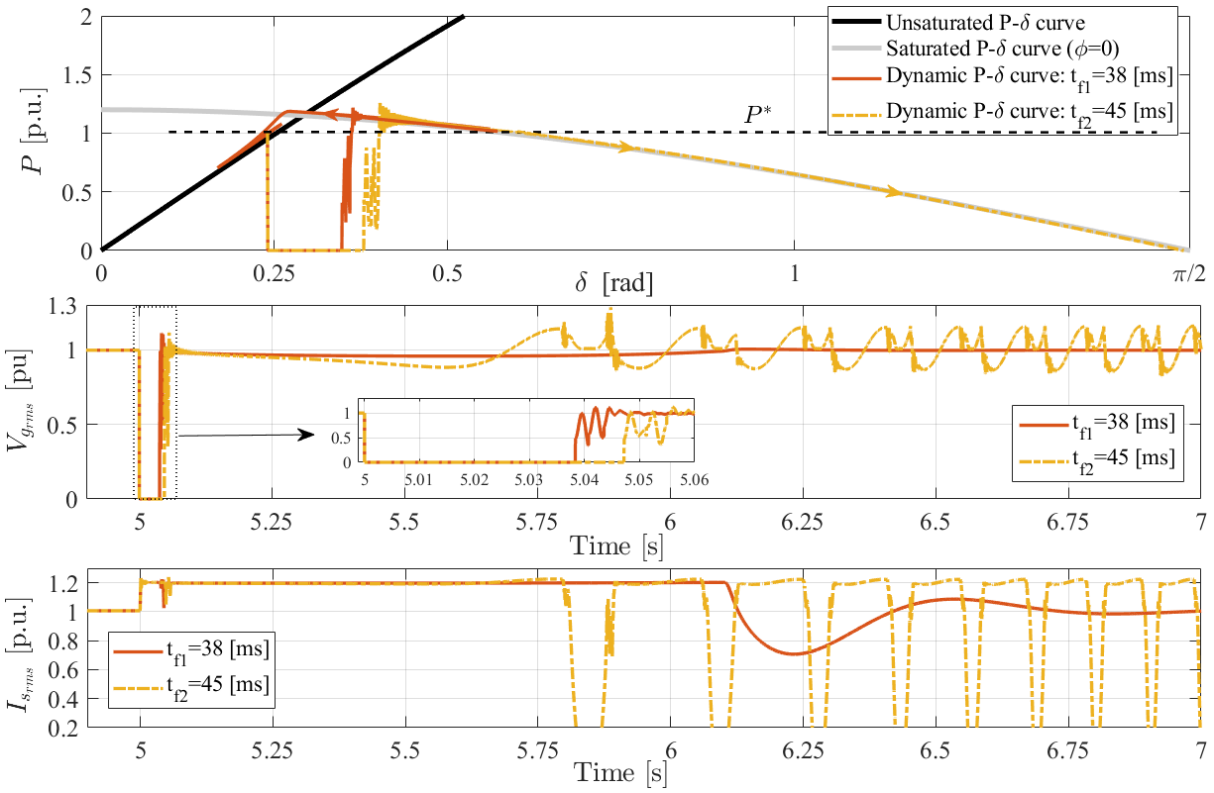

Figure III-9: Simulation results in case of a 100% voltage sag with different fault time durations.

Table III- 3: Results of the CCT determination for a small inertia constant.

	$\boldsymbol{\phi = 0}$ $\boldsymbol{H = 1.25\ s, k_p = 0.014}$	
$\boldsymbol{P^*}$	Predicted CCT by (III-15)	CCT in simulation
1 pu	20 ms	17 ms
0.9 pu	34 ms	28 ms
0.8 pu	50 ms	44 ms
0.7 pu	67 ms	58 ms
0.6 pu	86 ms	78 ms
0.5 pu	110 ms	98 ms

III.2.2.3 Impact of the saturated current angle ϕ on transient stability

From (III-15), two control parameters namely the power setpoint (P^*) and inertia constant (H) affect the transient stability of the VSC. As pointed out in [72] the transient stability of grid-forming converters can be enhanced by reducing the active power reference during grid voltage sags. References [73] and [74] have demonstrated that increasing the inertia constant in case of a voltage sag also improves the transient stability.

The angle ϕ is a new control degree of freedom that has not been exploited in the literature to enhance the transient stability of the grid-forming VSCs. As shown in (III-11), the angle ϕ has an influence on the expression of the active power. When applying a positive angle, the quasi-static $P - \delta$ curve in the saturated current operation mode is shifted to the right side as illustrated in Figure III-10. In this condition, the maximum angle that converter can reach is given by:

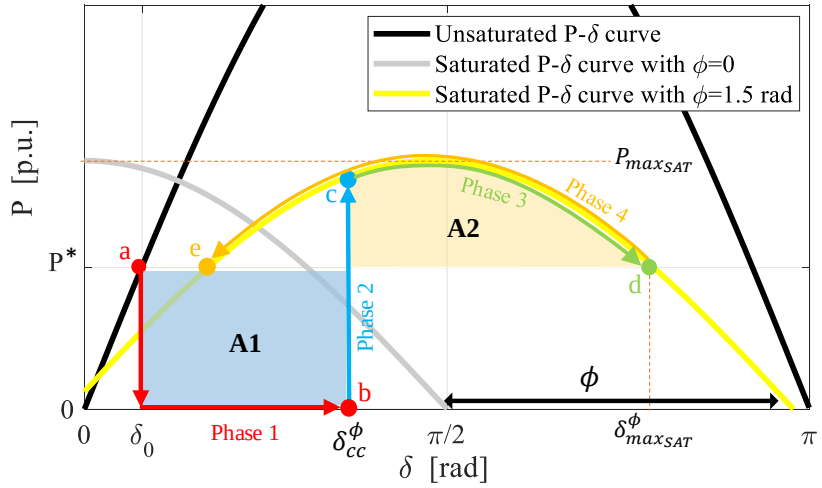

Figure III-10 Operation mechanism of the VSC under a 100% voltage sag by including $\phi = 1.5$ rad.

$$\delta^{\phi}_{max_{SAT}} = acos\left(\frac{P^*}{P_{max_{SAT}}}\right) + \phi \qquad \text{(III- 16)}$$

Using equal area criterion in this condition, the following expression for the CCA and CCT are obtained:

$$\delta^{\phi}_{cc} = asi\,n\left(\frac{P^*\left(\delta_0 - \delta^{\phi}_{max_{SAT}}\right)}{P_{max_{SAT}}} + si\,n\left(\delta^{\phi}_{max_{SAT}} - \phi\right)\right) + \phi \qquad \text{(III- 17)}$$

$$t^{\phi}_{cc} = 2\left(\sqrt{\frac{H\left(\delta^{\phi}_{cc} - \delta_0\right)}{\omega_b P^*}}\right) \qquad \text{(III- 18)}$$

Comparing to (III-13) and (III-15), (III-17) and (III-18) demonstrate that the CCA and CCT are increased with respect to the increase of ϕ giving more time for clearing the fault while ensuring a stable restoration.

However, the parameter ϕ could not be incautiously chosen. Referring to Figure III-10 and focusing on the "Phase 4", where the operating point moves from (d) to (e), in this particular situation the internal angle is locked at the operating point (e) located in the saturated $P - \delta$ curve since P reaches P^* In other word, the system cannot switch back to the voltage control mode. Therefore, the choice of ϕ is constrained by the ability of the VSC to switch from the saturated current control mode to the voltage control mode. Consequently, ϕ_{opt} is defined as the optimal shift of saturated $P - \delta$ curve that allows at once a transient stability enhancement and a post-fault recovering to the voltage control mode. The rightness of the analysis proposed in this subsection is validated through time domain simulations in the next subsection.

III.2.2.4 Optimal calculation of the saturated current angle ϕ

In order to avoid the internal angle being locked in the saturated current mode during the re-synchronization phase, the maximum value of ϕ can be calculated in such a way that the operating points 'a' and 'e' in Fig. 9 are matched. Hence:

$$\phi \leq acos\left(\frac{P^*}{P_{max_{SAT}}}\right) + asin\left(\frac{P^*}{P_{max}}\right) \qquad \text{(III- 19)}$$

The value ϕ obtained by (III-19) is the maximum allowable shift in the saturated quasi-static characteristic that guarantees the ability of the converter to switch back to the voltage control mode and a better transient stability compared to the case in with $\phi = 0$. According to (III-19), the maximum value of ϕ depends on the initial power setpoint and grid impedance. By defining the grid impedance based on the short circuit ratio (SCR) of the grid as: $SCR = (1/X_g)$, the optimal value of ϕ can be obtained by solving the following optimization problem:

$$\begin{cases} \phi_{opt} = min\left\{\phi = acos\left(\frac{P^*}{P_{max_{SAT}}}\right) + asin\left(\frac{P^*}{P_{max}}\right)\right\} \\ constraints: \quad 0 \le P^* \le 1 \\ SCR_{min} \le SCR \le SCR_{max} \end{cases} \quad \text{(III- 20)}$$

To solve this problem, it is possible to simply draw a surface that relates ϕ to the SCR and P^* as shown in Figure III-11. It can be seen that for a wide range of SCR and various initial operating powers, the maximum value of ϕ that satisfies the constraints is around 0.8 radian. Therefore, $\phi_{opt} = 0.8$ [rad] is considered as the optimal value. It should be mentioned that SCR = 1.2 corresponds to the minimum grid impedance that allows the VSC to transfer 1 pu active power (according to (III-9)).

Considering the given parameters in Table III-1 and the initial power setpoint of $P^* = 1$ pu, Fig. 10 shows the simulation results with two different values of ϕ. In case that $\phi = \phi_{opt}$, the theoretical value of CCT is $t_{cc} = 96$ [ms], which is higher than the CCT in the case of $\phi = 0$. As it can be seen, the system, switches back to the voltage control mode approximatively in 1200 [ms] after the beginning of the transient. If $\phi = 1.5$ [rad] ($\phi > \phi_{opt}$), the system remains stable and $P = P^*$ in steady-state. However, the angle reaches a new operating point, which is higher than the pre-fault value δ_0. Consequently, the VSC remains operating in the saturated current mode, as shown by the curve of the current $I_{s_{rms}}$, and the voltage in no longer under control. This verifies the presented claims in subsection III.2.2.3.

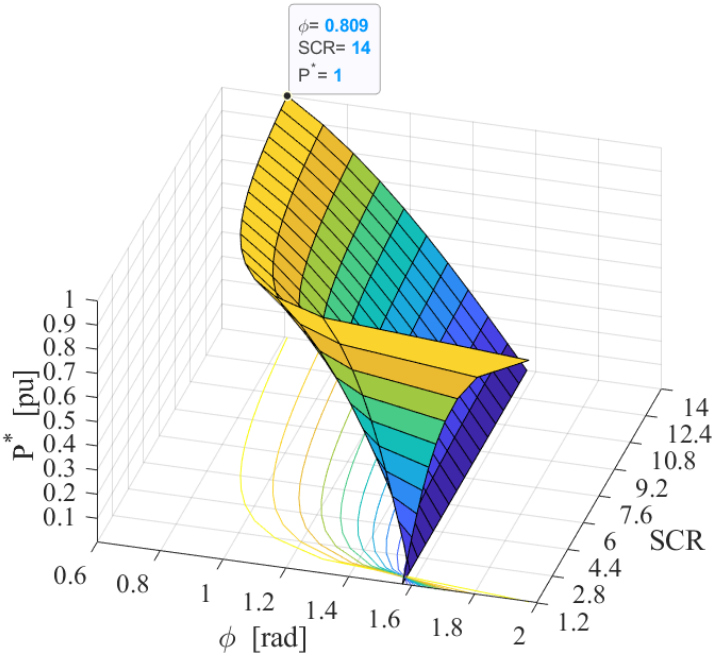

Figure III-11: The angle ϕ with respect to the variation of SCR and power setpoint.

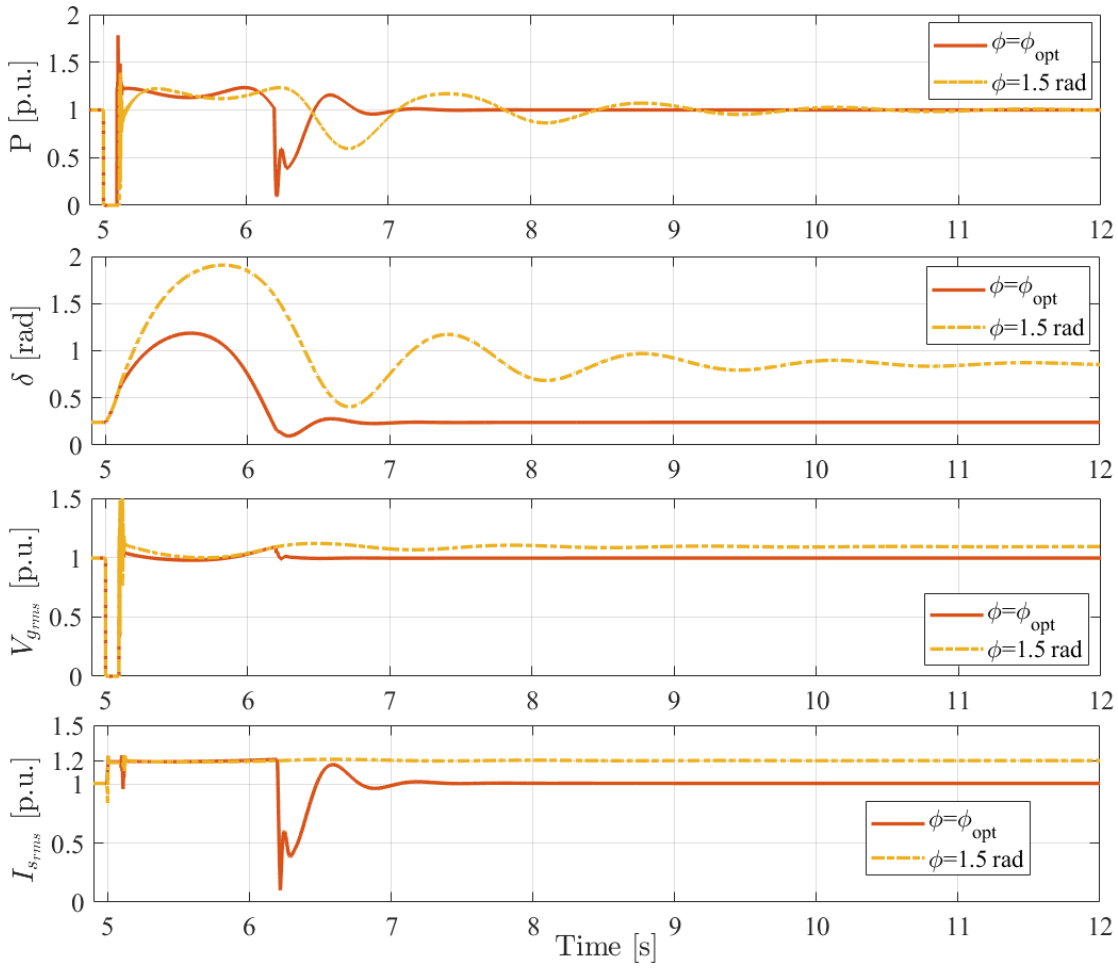

Figure III-12: Effect of including ϕ in the control on transient stability in case of a 100% voltage sag.

Table III-4 presents the CCT values while including the current angle shift for different power setpoints. These results confirm that the proposed method can enhance the transient stability and (III-18) gives a satisfactory accuracy in the anticipated CCT.

Table III-4: Results of the CCT determination considering $\phi = \phi_{opt}$.

	$\boldsymbol{\phi = \phi_{opt}}$ $\boldsymbol{H = 5\ s, k_p = 0.007}$	
$\boldsymbol{P^*}$	Predicted CCT by (III-18)	CCT in simulation
1 pu	96 ms	94 ms
0.9 pu	135 ms	130 ms
0.8 pu	175 ms	164 ms
0.7 pu	217 ms	204 ms
0.6 pu	266 ms	247 ms
0.5 pu	325 ms	304 ms

III.2.2.5 Impact of the saturated current angle ϕ on transient stability in case of a generic voltage sag

In order to validate that the proposed transient stability enhancement method with the current reference angle is effective in more general cases, a given voltage drop (ΔV) in the grid voltage is considered as follows:

$$\Delta V = 1 - V_{e_{drop}} \qquad \text{(III- 21)}$$

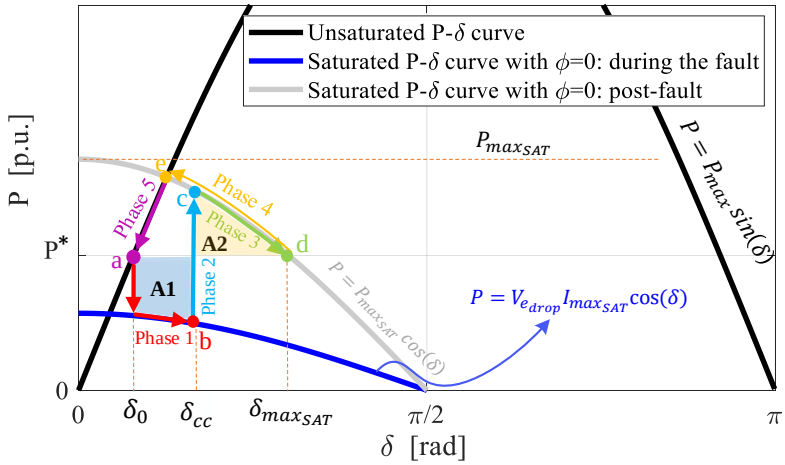

Figure III-13: Operation mechanism of the VSC under a generic voltage sag with $\phi = 0$.

Considering $\phi = 0$, the quasi-static expression of the active power during the fault is:

$$P = V_{e_{drop}} I_{max_{SAT}} cos(\delta) \qquad \text{(III- 22)}$$

Figure III-13 shows the operation mechanism of the grid-forming VSC subjected to a generic voltage sag. The various phases are the same as previously. The only difference is that during the fault (Phase 1), some amount of active power is exchanged with the grid by the VSC that can be determined with (III-22). According to the large signal model presented in Figure III-7, this injection of the power during the fault reduces the divergence speed of the angle δ. Therefore, it is expected that the CCT in this case is higher than the one with a 100% voltage drop.

If $\phi = \phi_{opt}$, the quasi-static expression of the active power during the fault is updated to:

$$P = V_{e_{drop}} I_{max_{SAT}} cos\,(\delta - \phi_{opt}) \qquad \text{(III- 23)}$$

Figure III-14 shows the operation mechanism of the grid-forming VSC subjected to a generic voltage sag with optimally shifted saturated $P - \delta$ curves. Since the maximum allowable angle is increased in this case ($\delta^{\phi}_{max_{SAT}} > \delta_{max_{SAT}}$), it is expected to get a higher CCT. Having in mind that the optimal value of ϕ is based on matching the intersection point of the unsaturated $P - \delta$ curve and saturated one during the post-fault, since the saturated curve in the post fault (yellow curve) is not affected by the magnitude of the voltage drop, the optimal value of ϕ remains unchanged.

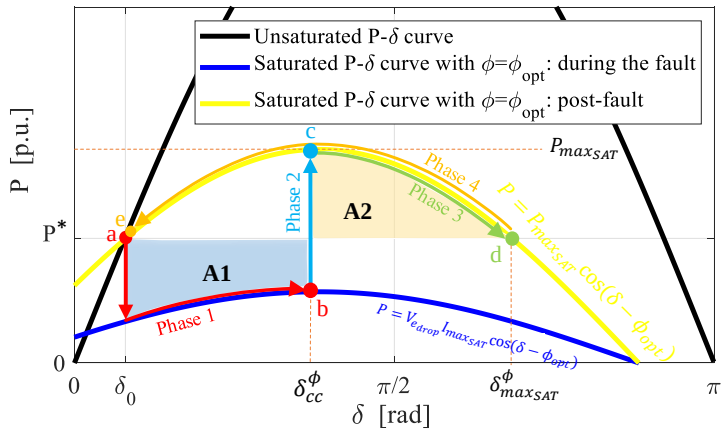

Figure III-14: Operation mechanism of the VSC under a generic voltage sag with $\phi = \phi_{opt}$.

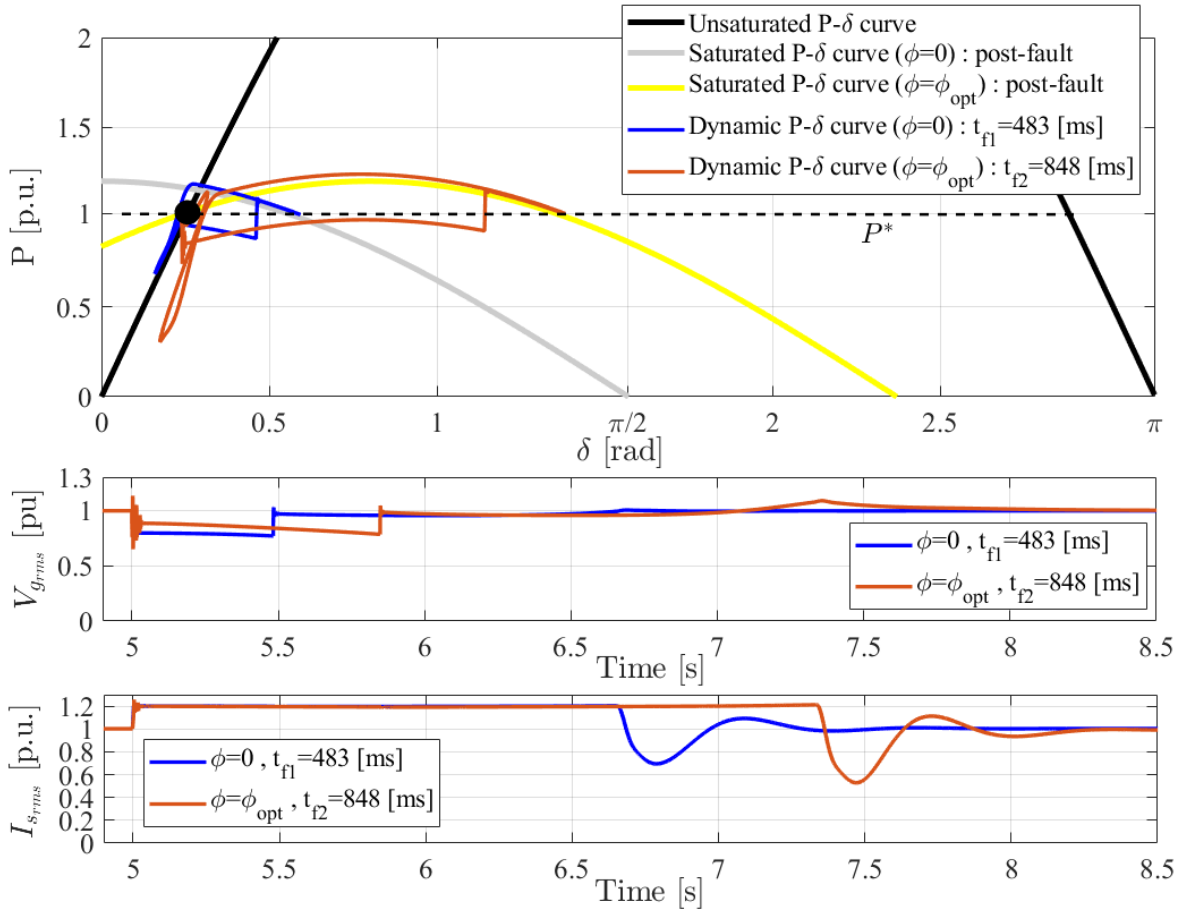

Figure III-15: Simulation results in case of a 20% grid voltage sag.

Considering the given parameters in Table III-1, and taking $P^* = 1\,pu$ as an illustrative example, Figure III-15 shows the simulation results for a 20% grid voltage sag. The fault time durations (t_{f1} , t_{f2}) are equal to CCTs (t_{cc1} , t_{cc2}) in each case. It can be seen that the proposed optimal setting of the saturated current angle increases the CCT and the dynamic simulations are matched to the described operation phases in quasi-static state.

III.2.2.6 Experimental validation

The aim of this section is to validate experimentally the theoretical developments. The experimental bench is illustrated in Figure III-16. The 2-Level VSC (1) is supplied by an ideal 600V DC voltage source (4) and connected to a high bandwidth AC amplifier (5) through an LCL filter (3) as depicted in Figure III-17. Table III-5 presents the mockup parameters. The amplifier is used to emulate the AC system (i.e., 300V ph-ph) as well as to generate the events discussed in this work (i.e., 100% voltage sag emulating a 3-phase bolted fault). The 2-Level VSC is controlled with a dSPACE dS1005 (2) with a 40 μs time step. The switching frequency of the converter is $f_{sw} = 10$kHz.
Two test cases are performed:

- A 100 % voltage sag considering $\phi = 0$.
- A 100 % voltage sag considering $\phi = \phi_{opt}$.

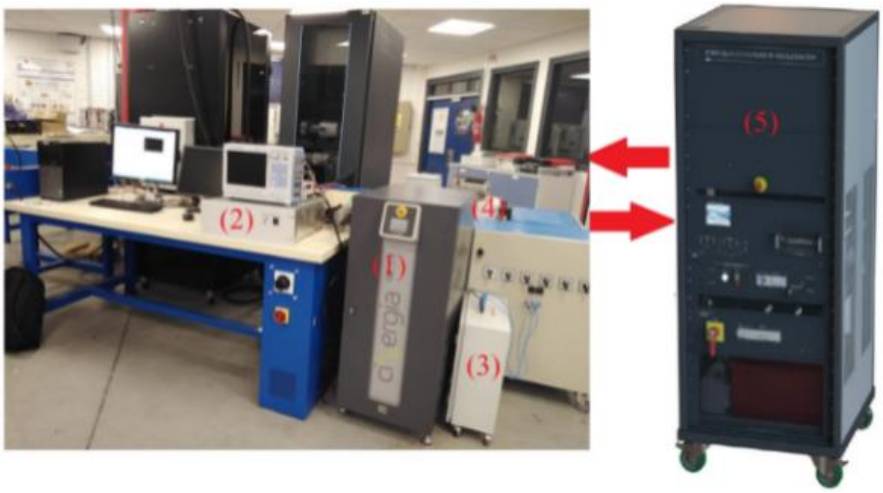

Figure III-16: Mockup presentation.

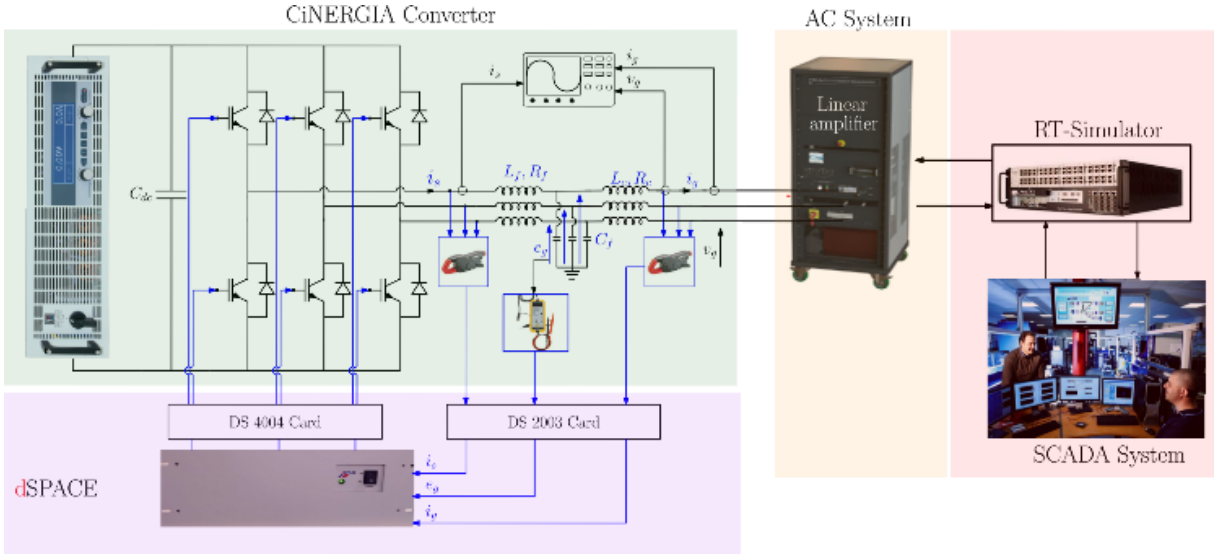

Figure III-17: Functional scheme.

Table III-5: Mockup parameters.

S_n	5,625 kVA	L_f	10.9mH
I_n	10 A	L_c	10.9mH
f_n	50 Hz	C_f	9.2 μF

- A 100% voltage sag considering $\phi = 0$:

Initially, $P^* = 0.6$ [p.u]. Subsequently, a 100 % voltage sag with the duration of 200 [ms] is applied to the system. According to Table II when $\phi = 0$, the CCT obtained from the simulation is 157 [ms]. Hence, it is expected that the system cannot be operating stably under this fault duration.

Figure III-18 shows the output power, voltage and current of the VSC in response to the fault. It can be clearly seen that the VSC losses the synchronism and it becomes unstable.

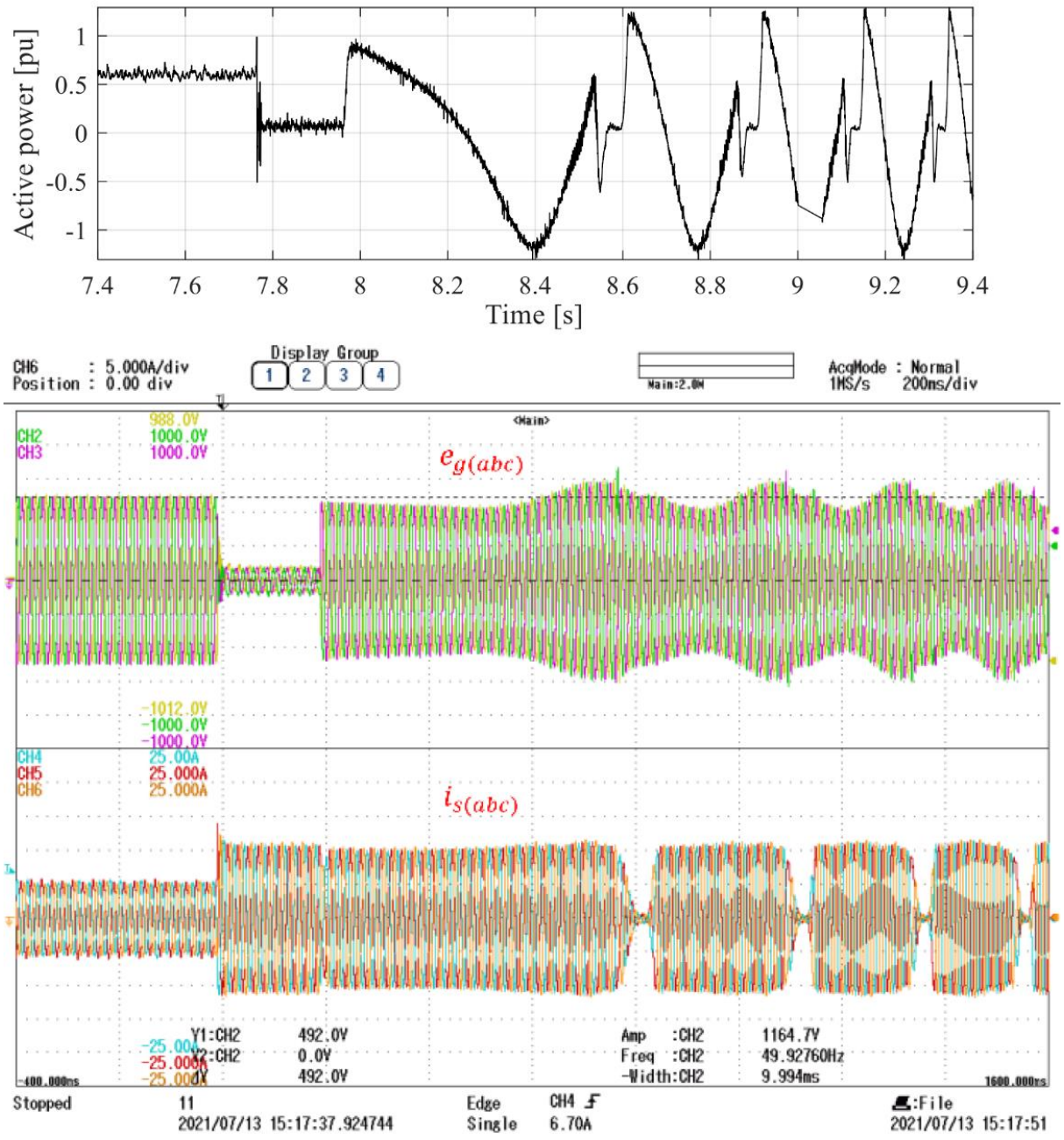

Figure III-18: Response to a 100 % voltage sag with the duration of 200 [ms] considering $\phi = 0$.

- A 100% voltage sag considering $\phi = \phi_{opt}$:

As in the previous case, the active power reference P^* is set to 0.6 [p.u] and a 100 % voltage sag with the duration of 200 [ms] is applied to the system. According to Table III-4, when $\phi = \phi_{opt}$ the CCT obtained from the simulation is 247 [ms]. Hence, it is expected that the VSC does not lose the synchronism and recovers the initial operating point stably. Figure III-19 demonstrates the stable performance of the VSC under this scenario, which confirms the effectiveness of the proposed method.

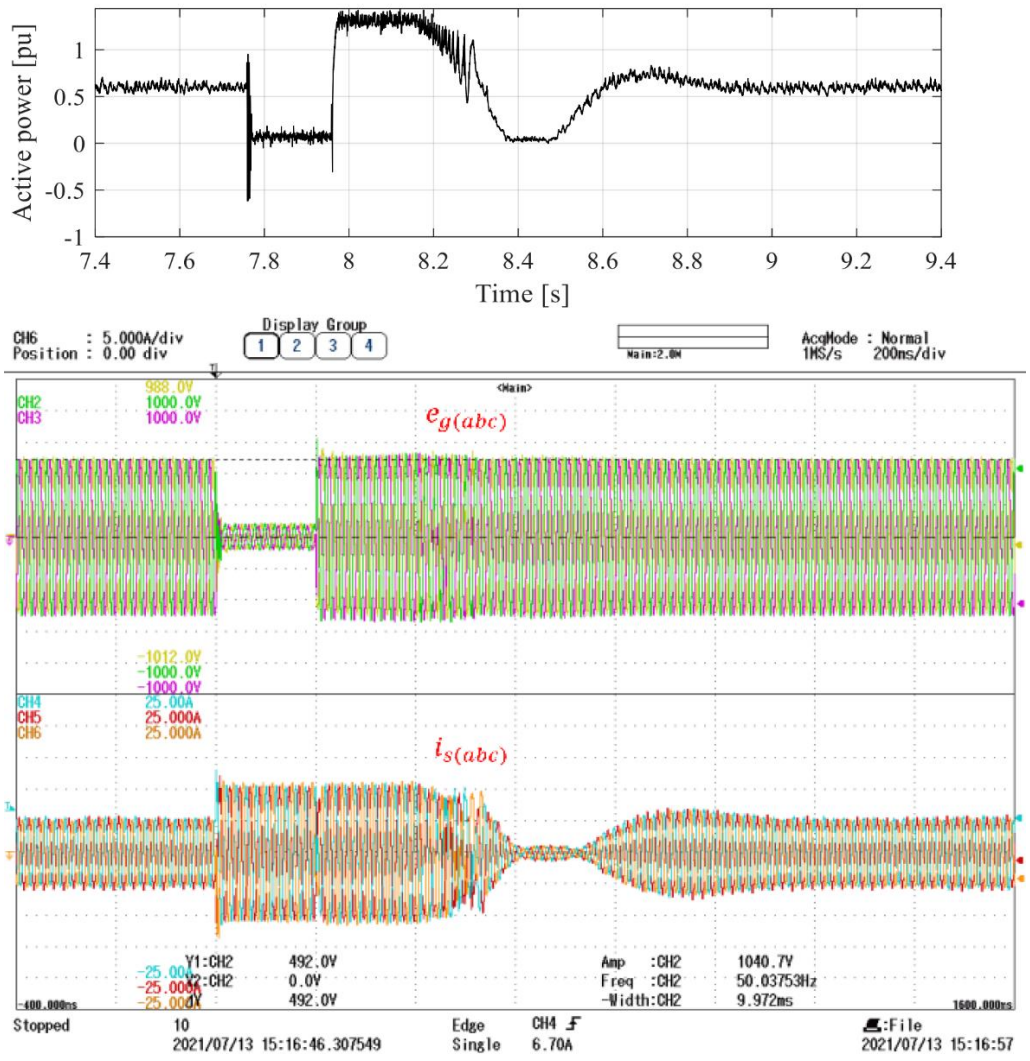

Figure III-19: Response to a 100 % voltage sag with the duration of 200 [ms] considering $\phi = \phi_{opt}$.

III.2.3Transient stability analysis in case of a phase shift

Another large event, which can happen in the grid, is a line tripping/reclosing. Due to the large grid impedance variation, it results in a phase shift [75]. The stability of the VSC has to be analyzed, especially in case of weak grid conditions. To analyze this effect, a small benchmark is studied (see Figure III-20). Depending on the K_2 breaker position, the short circuit ratio is $SCR_1 = \frac{1}{X_{g1}}$ or $SCR_2 = \frac{X_{g1}+X_{g2}}{X_{g1}.X_{g2}}$. As previously, the different phases are described with the help of some curves derived from the quasi-static models.

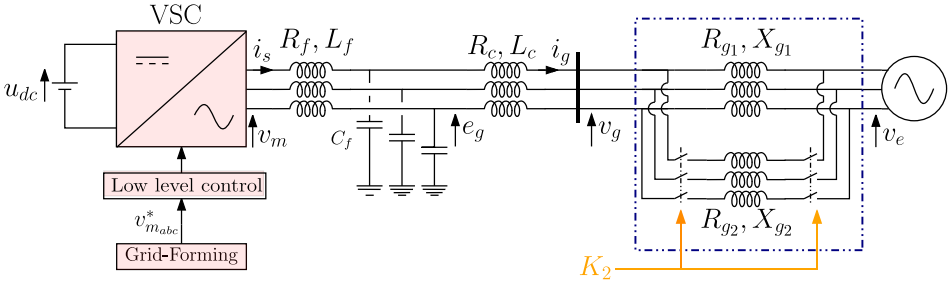

Figure III-20: Studied system with a line tripping/reclosing scenario.

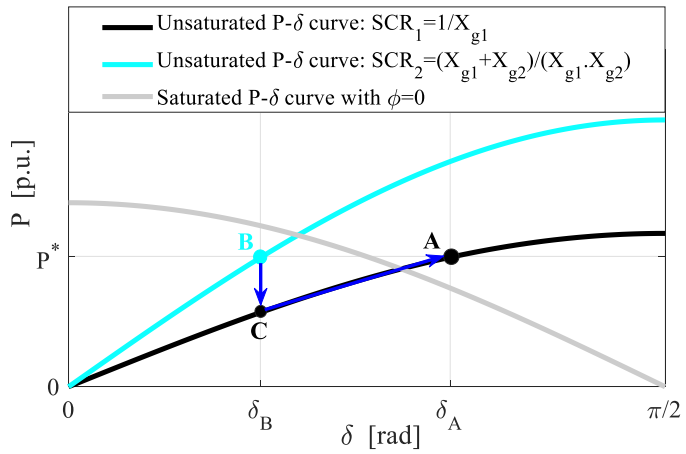

Figure III-21: Operation mechanism of the VSC in case of line tripping under low SCR.

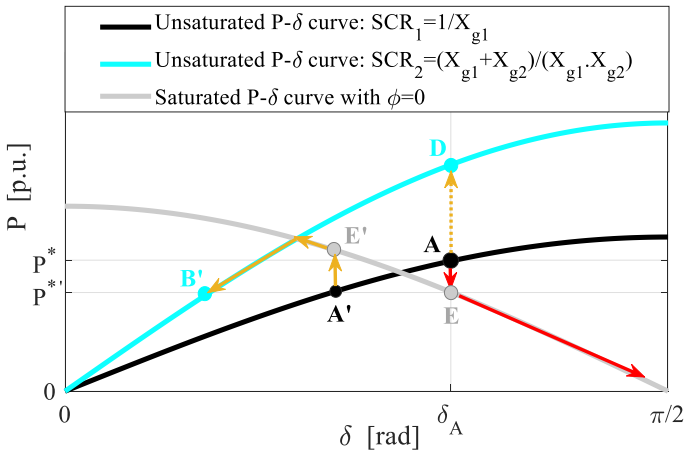

Figure III-22 Operation mechanism of the VSC in case of line reclosing under low SCR.

Considering the line-tripping scenario, according to Figure III-21, the VSC is initially operating at the point B located on the light blue curve with $SCR = SCR_2$. When the second line is tripped, the operating point suddenly moves to the other curve with $SCR = SCR_1$ (black curve) while keeping the same angle (point C) and then the angle increases to reach the point A where the initial operating power is recovered. It should be mentioned that in this scenario, since the connection impedance suddenly increases, the current is initially dropped and then incrementally reaches to the value corresponding to P^*, the CSA is not activated.

Considering the line-reclosing scenario, according to Figure III-22, the VSC is initially operating at the point A. When connecting the second line, it is expected that the operating point jumps to the other curve with $SCR = SCR_2$ (light blue curve) while keeping the same angle (operating point D). However, reclosing the line activates the CSA due to a sudden decrease of the connection impedance and therefore, the operating point moves to the saturated curve to limit the current (operating point E). At this point, the active power is smaller than its setpoint. Therefore, the angle δ diverges and the VSC loses the synchronism. Actually, the instability issue caused by a line reclosing is linked to the location of the initial operating point with respect to the saturated curve in the $P - \delta$ plane. If the initial operating power is located above the saturated quasi-static $P - \delta$ curve, then the system loses the synchronism as explained previously. If the initial

operating point is below the saturated curve (A'), the operating point moves to E', whose corresponding power is higher than the initial power setpoint. Therefore, the angle decreases to reach its new equilibrium point (B').

According to the coordinates of the initial operating point with respect to the saturated curve, the following constraints on the initial angle and therefore on the initial power setpoint can be derived to guarantee a stable line reclosing:

$$\begin{cases} P^* \leq V_e I_{max_{SAT}} \cos(\delta_0) \\ P^* = P_{max_1} \sin(\delta_0) \end{cases} \quad \text{(III- 24)}$$

where $P_{max_1} = \frac{E_g V_e}{X_c + \frac{1}{SCR_1}}$ Therefore:

$$\delta_0 \leq atan\left(\frac{I_{max_{SAT}}\left(X_c + \frac{1}{SCR_1}\right)}{E_g}\right), \quad \text{(III- 25)}$$

$$P^* \leq P_{max_1} \sin\left(atan\left(\frac{I_{max_{SAT}}\left(X_c + \frac{1}{SCR_1}\right)}{E_g}\right)\right) \quad \text{(III- 26)}$$

Using the proposed shifting of the saturated curve to the right side of the $P - \delta$ plane, (III-26) is updated to:

$$P^* \leq P_{max_1} \sin\left(atan\left(\frac{I_{max_{SAT}}\left(X_c + \frac{1}{SCR_1}\right)}{E_g - \left(I_{max_{SAT}}\left(X_c + \frac{1}{SCR_1}\right)\right).\sin\phi}.\cos\phi\right)\right) \quad \text{(III- 27)}$$

By setting $\phi = \phi_{opt}$ in (III-25), Figure III-23 demonstrates the capability of the VSC to deal with the line-reclosing for the full range of initial power setpoint ($0 \leq P^* \leq 1$) under very low grid impedances.

To verify the correctness of the presented analysis, we consider $P^* = 1$ [pu], $SCR_1 = 1.2$, $SCR_2 = 2.4$ and simulate the line reclosing. In this situation, according to Figure III-24, if $\phi = 0$, it is expected that the VSC loses the synchronism, while if $\phi = \phi_{opt}$, it stably shifts to a new operating point. It can be seen that with the proposed setting of the angle ϕ, the VSC can stably deal with the phase shift.

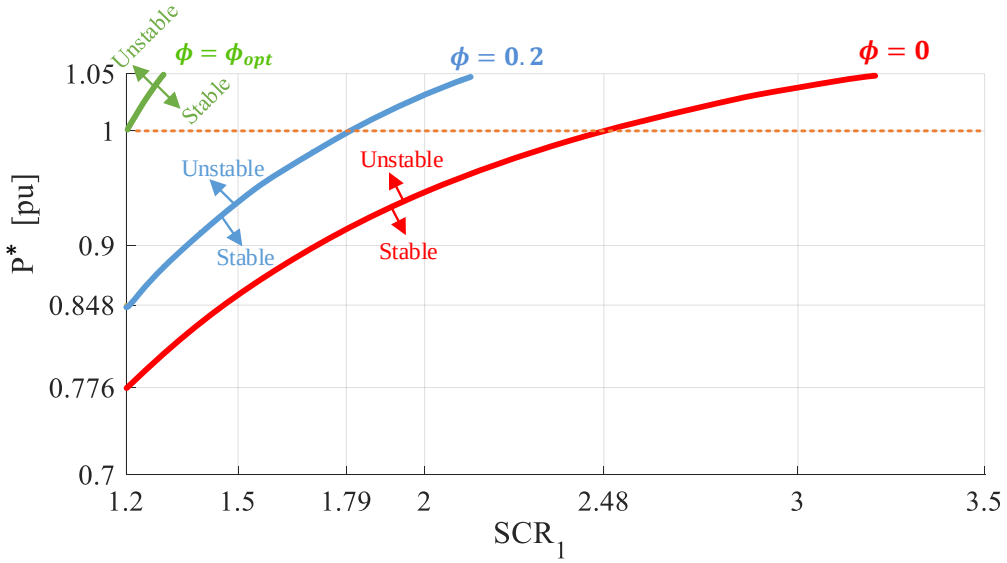

Figure III-23: Effect of shifting the saturated quasi-static $P - \delta$ curve on the stability region in case of a line reclosing.

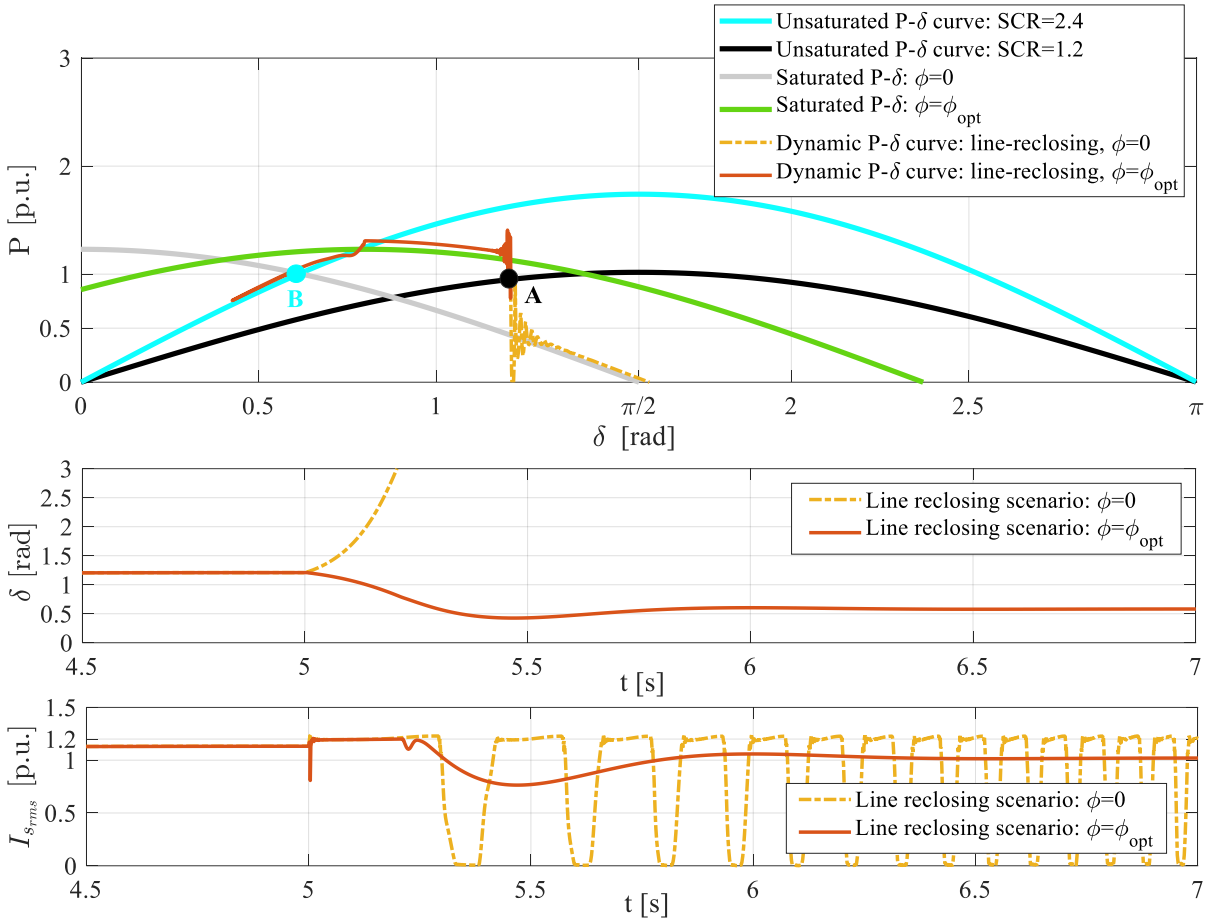

Figure III-24: Dynamic simulation of the line-reclosing under low SCR.

III.2.4Combination of several control degrees of freedom

As mentioned before, the inertia constant is a degree of freedom in the control that could be modified during the saturated operation mode to increase the CCT. The proposed solution in (III-28) consists in modifying the inertia constant with respect to the AC voltage reference at the PCC:

$$H_{mod} = \frac{H}{1-\Delta V} \qquad \text{(III- 28)}$$

where $\Delta V = E_g^* - E_g$. In normal operation mode, $\Delta V = 0$ and $H_{mod} = H$. During the fault, the PCC voltage magnitude E_g drops and ΔV has a positive value, which results in reduction of the power set-point. Fig. 13 indicates the simulation results of a 100% voltage sag considering the parameters given in Table III-1 and initial operating point of $P^* = 1$ pu. The CCT is enhanced to 80 [ms] by modifying the inertia constant during the transient (compared to Figure III-9 where the CCT was 38 [ms]).

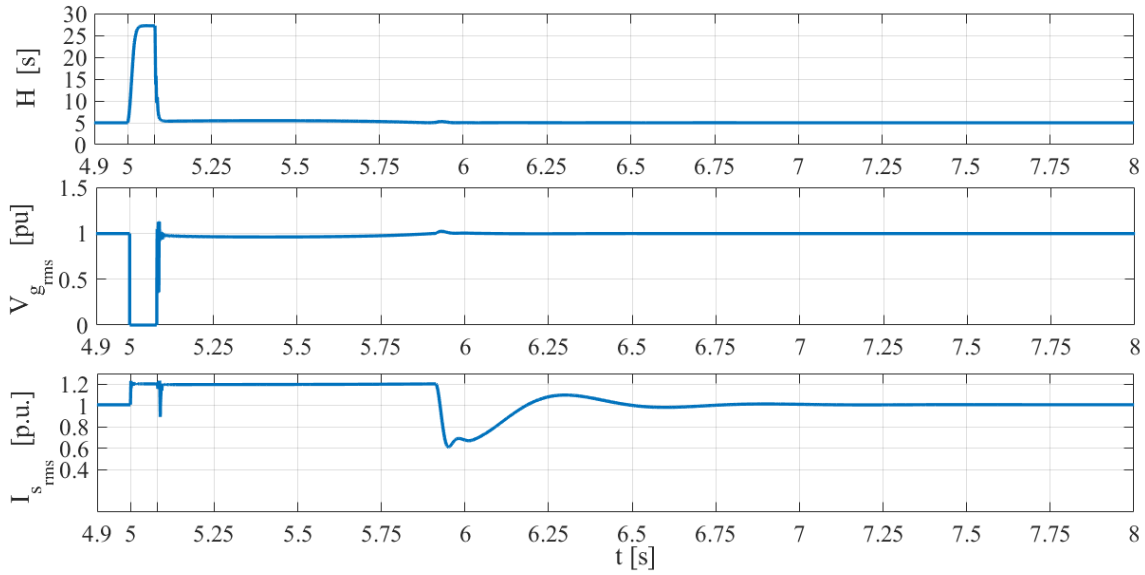

Figure III-25: Effect of modifying the inertia constant on transient stability.

In order to get a better performance and increase the CCT, several degrees of freedom in the control could be utilized simultaneously. Figure III-26 Shows the results where a combination of inertia constant modification and inclusion of the optimal value of ϕ is considered. Thanks to this hybridization, the CCT is increased to 253 [ms]. Summarizes the CCT values for the proposed hybridization considering various initial operating points.

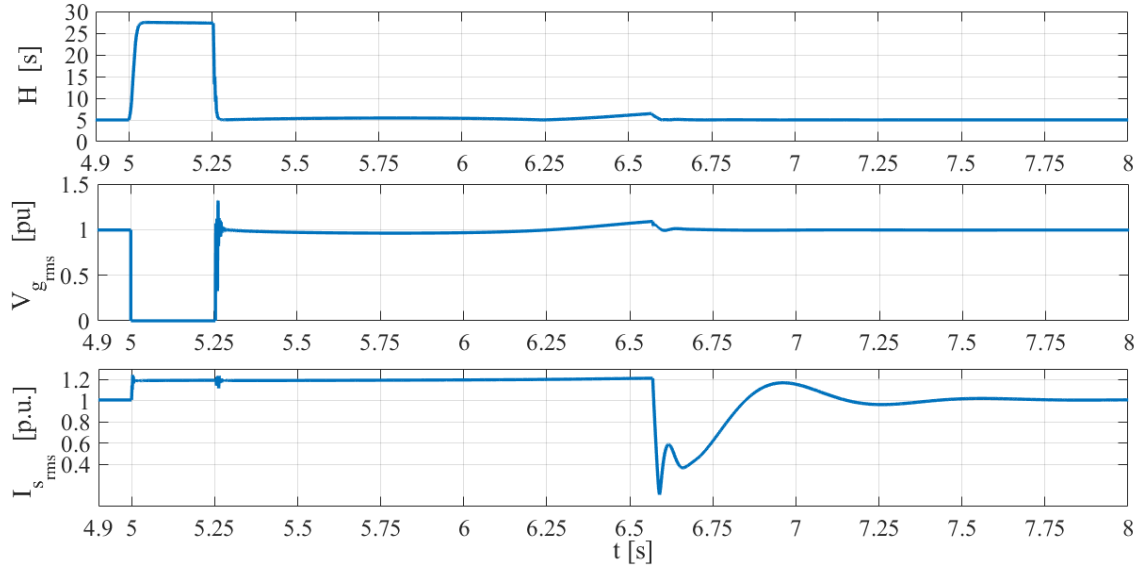

Figure III-26: Results when combining two control degrees of freedom.

Table III-6: CCT in case of combination of two control degrees of freedom for transient stability enhancement.

P* [pu]	0.5	0.6	0.7	0.8	0.9	1
CCT [ms]	684	564	470	390	322	253

III.3 Conclusions

In chapter, the current limitation of grid-forming converters with two different strategies (i.e., VI and CSA) was briefly discussed. Then, the transient stability of the converter embedding a current saturation algorithm as the control limiting strategy was investigated. In case of large grid disturbances, the converter switches to the saturated current control mode. According to the active power expression in this control mode, a new degree of freedom was identified, which is the angle of the saturated current reference. Thanks to the derived formulas for the critical clearing angle and critical clearing time in case of a voltage sag event, the impact of this angle on the transient stability was investigated and its optimal value was calculated. It was also demonstrated that this optimal value enhances the stability margin in case of a phase shift event. It was demonstrated that this angle has a better positive effect in the case of a phase shift than for a voltage sag. This is explained by the fact that the proposed method does not prevent the power angle deviation caused by the power mismatch in the power control loop during the fault.

The overall idea was to promote some simple methods to improve the performance of this kind of control. Of course, some more advanced controls can be found in the literature, but it seems important to use all the possible control degrees of freedom in order to push these methods to their limit and evaluate in which cases more advanced control can really bring some better performance. Another possibility was to use a combination of the proposed solution with an additional transient management of the inertia constant that would result in a higher system performance.

Chapter IV: Grid-forming control of a modular multi-level converter

The MMC has become the preferred converter topology for high-power applications such as high voltage direct current (HVDC) transmission systems. The MMC control has been widely studied in the literature mostly with the grid-following scheme in the high-level control [79], [80]. With the recent interest of using grid-forming control schemes for providing ancillary services to the power system, it is expected to adapt these kinds of controls to MMCs that will have a major share of power converters in the future power systems.

The VSC-MMCs contain internal capacitors in each submodule, which require some internal loops to control the energy. A main question to answer for the MMC is about a potential interaction between the grid-forming control and the energy closed-loop control, which are used in the MMC control. In this chapter, firstly the effect of internal energy control of the MMC on the general dynamic behavior of the system with a grid-forming control is studied. Then, the possibility of explaining the dynamic behavior of the MMC with a simplified equivalent 2-level VSC is studied. After that, the current limitation and transient stability problems, which were studied for the 2-level VSC configuration in previous chapter, are extended to the MMC structure. Finally, by including the DC side model, an HVDC interconnection with grid-forming control is studied. The challenges ahead of the HVDC interconnections with grid-forming control operation for virtual inertia emulation is addressed and a solution based on integrating a storage device to the DC link is proposed to stabilize the system.

IV.1 Recall on the MMC model

A three-phase MMC is constituted by the series connection of N sub-modules (SMs) with independent capacitors C to build one arm of the converter as indicated in Figure IV-1. In HVDC applications, N can be of several hundreds. The SMs in each arm are connected to an inductive filter (L_{arm}, R_{arm}) whose aim is to limit the derivative of current in case of a DC short-circuit. Depending on the MMC application and its topology, different types of SMs can be used. Among all the SM circuit configurations, the half-bridge topology has been widely applied in the MMC-HVDC applications. This is due to the presence of only two switches in the SM, which results in a lower number of components and higher efficiency [81]. Hereafter, the MMC based on the half-bridge SM is considered since the losses are regarded as the first priority in MMC-HVDC applications. Two identical arms are connected, one to the upper and the other to lower DC-side, respectively, to form one leg for each phase $j = [a, b, c]$. Thanks to its modularity, the converter allows generating a sinusoidal output AC voltage. The absence of the LC filter leads to cost saving compared to the conventional 2-Level converter.

Given the large number of SMs, it is necessary to find a model to design the different high-level controllers (current, energy). Assuming that the SM voltages are equal and balanced, a simplified “arm averaged model”, that has been developed for several years [81], can be used. This model is represented in Figure IV-1 for the lower arm of the phase “c”.

Based on this representation, each arm is modelled as a controllable voltage source with a modulation index m_{u/l_j} (m_{u/l_j} is defined as the ratio of the active SMs number in the upper/lower arm of the phase j divided by the total number of SMs in the corresponding arm of the phase j) and an equivalent voltage $v_{Ctot\,u/l_j}$ across the equivalent capacitor C_{tot}. The modulated voltages v_u and v_l as well as the current for each arm j are expressed as follow:

$$v_{u_j} = m_{u_j} v_{Ctot\,u_j}\,,\ v_{l_j} = m_{l_j} v_{Ctot\,l_j} \tag{IV- 1}$$

$$i_{Ctot\,u_j} = m_{u_j} i_{u_j}\,,\ i_{Ctot\,l_j} = m_{l_j} i_{l_j} \tag{IV- 2}$$

The currents and voltages of the equivalent capacitor are related by the following expressions:

$$i_{Ctot\,u_j} = C_{tot}\frac{d}{dt}(v_{Ctot\,u_j})\,,\ i_{Ctot\,l_j} = C_{tot}\frac{d}{dt}(v_{Ctot\,l_j}) \tag{IV- 3}$$

By applying the Kirchhoff's voltage law (KVL), following equations can be obtained for each phase of the MMC:

$$\frac{u_{dc}}{2} = v_{u_j} + L_{arm}\frac{di_{u_j}}{dt} + R_{arm} i_{u_j} + L_c\frac{di_{g_j}}{dt} + R_c i_{g_j} + v_{g_j}\,, \tag{IV- 4}$$

$$\frac{u_{dc}}{2} = v_{l_j} + L_{arm}\frac{di_{l_j}}{dt} + R_{arm} i_{l_j} - L_c\frac{di_{g_j}}{dt} - R_c i_{g_j} - v_{g_j}\,, \tag{IV- 5}$$

where v_{g_j} is the voltage at the PCC and i_{g_j} is the grid current. In order to have a decoupled control on the inner dynamics, the DC and AC part of the above equations can be extracted by adding and subtracting (IV-4) and (IV-5), respectively:

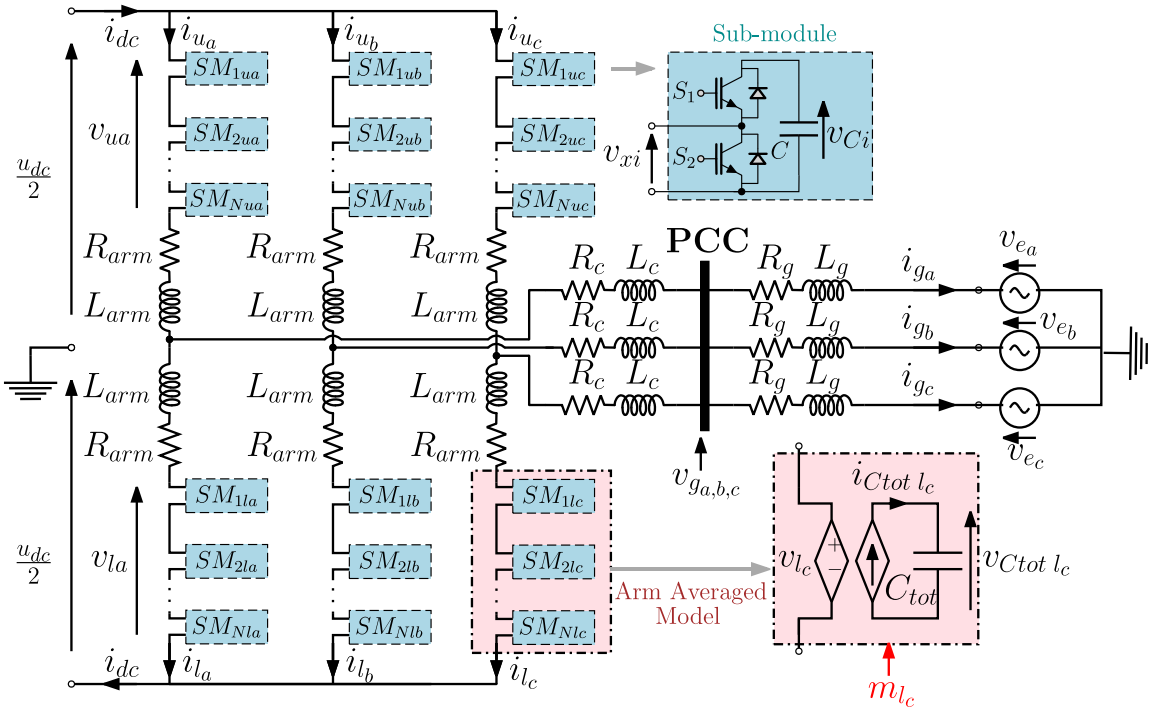

Figure IV-1: MMC topology with arm averaged model representation.

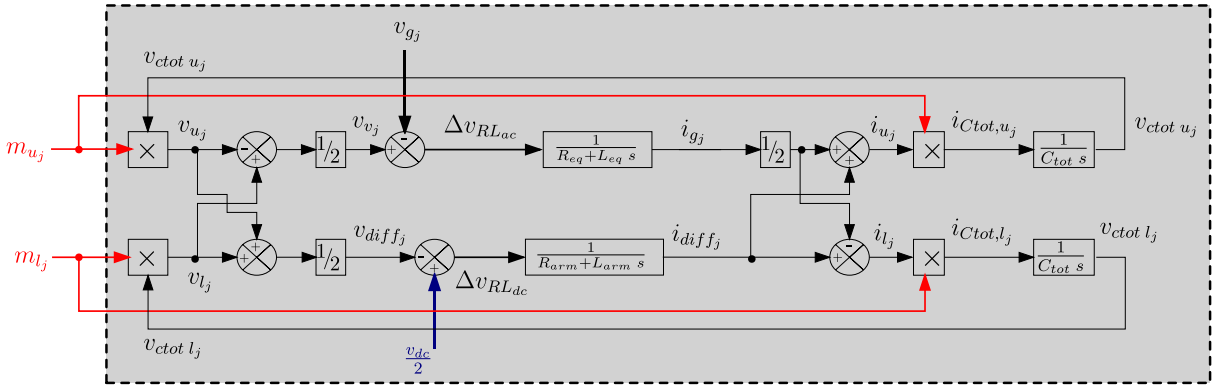

Figure IV-2: MMC model representation in (abc) frame.

$$\frac{u_{dc}}{2} - v_{diff_j} = L_{arm}\frac{di_{diff_j}}{dt} + R_{arm}i_{diff_j}\,, \tag{IV- 6}$$

$$v_{v_j} - v_{g_j} = L_{eq}\frac{di_{g_j}}{dt} + R_{eq}i_{g_j}\,, \tag{IV- 7}$$

where $L_{eq} = \frac{2L_c+L_{arm}}{2}$ and $R_{eq} = \frac{2R_c+R_{arm}}{2}$. The currents $i_{diff_j} \triangleq \frac{i_{u_j}+i_{l_j}}{2}$ are the common-mode currents of the MMC and the voltages $v_{diff_j} \triangleq \frac{v_{u_j}+v_{l_j}}{2}$ are the modulated voltages driving the common-mode currents. The voltage $v_{v_j} \triangleq \frac{v_{l_j}-v_{u_j}}{2}$ is the external voltage that drives the AC grid current $i_{g_j} = i_{u_j} - i_{l_j}$.

Based on (IV-3), (IV-6) and (IV-7), the system contains 11 state variables: 6 voltages across the equivalent capacitors, 3 common-mode currents and 2 independent grid currents. The obtained equations are represented in the block diagram model of Figure IV-2.

The objectives of the control law are:

1- Controlling the common-mode currents $i_{diff_{abc}}$ to suppress the internal circulating current, and thereby, avoiding unwanted oscillations on the DC side [80], [82].
2- Controlling the exchange of energy between arms and phases to guaranty an equipartition of the internal energy of the MMC [79].
3- Controlling the power exchange between AC and DC sides.

The two first objectives have been widely discussed in the literature and they have been achieved through different control strategies so-called circulating current suppression controller (CCSC) [83], Energy-based control and improved CCSC with DC energy management [79], [80]. All these control strategies have been applied for MMCs operating as current sources to meet the third control objective. However, few research have been focused on the VSC-MMC controlled as a voltage source. The first examples of studying the utilization of the grid-forming control for the MMC have been published in [84], [85] with the aim of providing virtual inertia and frequency support for an MMC-based HVDC terminal. More recently, in [86] a VSM-based grid-forming control of MMC in order to provide an inertia support to the grid has been examined with a laboratory demonstration. Authors in [87] have presented an evaluation of different inertia emulation strategies with grid-forming control based on a laboratory-scale prototype of a point-to-point HVDC transmission system with MMC.

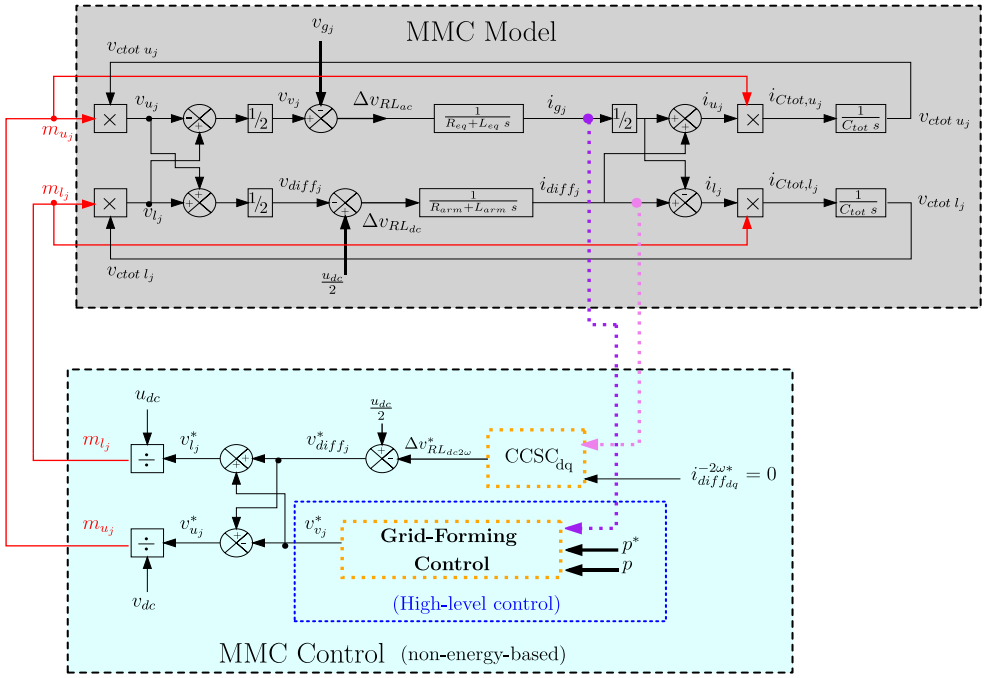

Figure IV-3: General structure of the non-energy-based grid-forming MMC control.

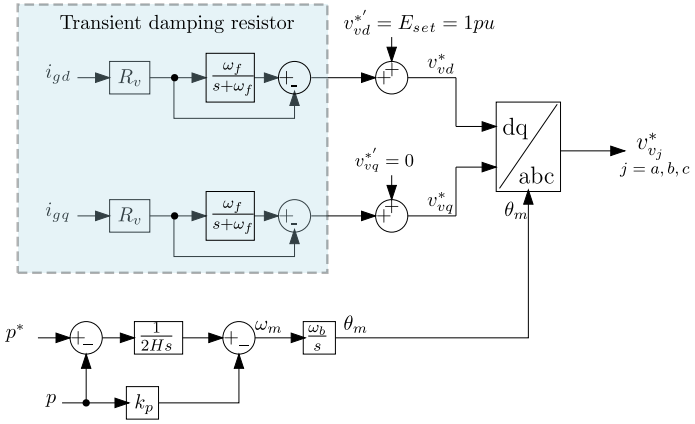

Figure IV-4: IP-control based grid-forming scheme for generating the external voltage references of the MMC.

In these previous publications on the grid-forming MMC, the internal energy of the MMC is not controlled. The main question to answer in this case is about a potential interaction between the grid-forming control and the closed-loop energy control, which are used in the MMC control. A comparative study regarding the dynamic behavior of the MMC with grid-forming control either with or without controlling the MMC internal energy can be helpful to answer this question.

IV.2 Grid-forming MMC control overview

Contrary to the 2-Level VSCs, MMCs are able to generate a nearly perfect modulated voltage waveform if the number of sub-modules is high (e.g., 400 SMs). Hence, the MMC can be simply controlled according to its physical voltage source nature without a need for additional regulation loops for the AC voltage control. In other words, the outer control strategy can be used to directly provide the AC voltage $v_{v_j}^*$ references. The outer control strategy in this chapter is the grid-forming control based on the IP-controller. The other references needed to be generated in the control are the modulated

voltages driving the common-mode currents $v^*_{diff_j}$. These references are generated by two different approaches i.e., non-energy-based and energy-based control. In the following, the non-energy-based and energy-based controls strategies are adopted for common-mode currents control.

IV.2.1 Non-energy-based grid-forming control

The non-energy-based control strategies are based on the inner current controllers, which produce the voltage references $v^*_{diff_j}$ for the modulators. In this concept, a CCSC strategy is widely used in the literature. Figure IV-3 illustrates the general structure of the non-energy-based grid-forming MMC control. The CCSC is a classical current control loop whose aim is to eliminate the second harmonic component of the circulating current, which has a large influence on the system losses and voltage ripple of the capacitors. Therefore, a Park transform at $-2\omega_g$ is utilized. More details about the CCSC are given in [88]. The IP-control based grid-forming scheme that generates the external voltage reference $v^*_{v_j}$ is recalled in Figure IV-4.

IV.2.2 Energy-based grid-forming control

To have a full control of the MMC dynamics and the stored energy in the system, the energy-based control has been developed. Figure IV-5 illustrates the general structure of the energy-based grid-forming MMC control. It can be seen that unlike the non-energy-based control, in which the common-mode currents are not fully controlled and only their second harmonic component is suppressed, here the common-mode currents are fully controlled with three PI controllers (one for each phase). The parameters of these PI controllers are classically designed with respect to a desired response time of the transfer function $i_{diff_j}/i^*_{diff_j}$ [81].

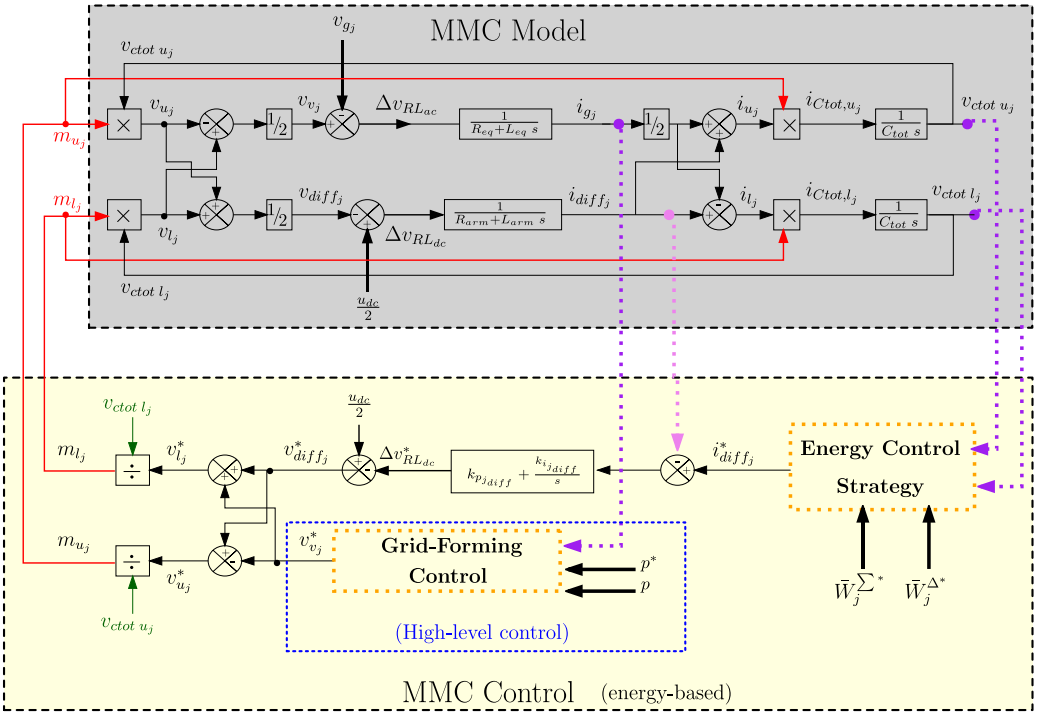

Figure IV-5: General structure of the energy-based grid-forming MMC control.

The common-mode currents references are generated from an energy control strategy that includes a feedback control loop on the capacitor voltage in each arm. By considering the equivalent arm capacitors as the main energy storage elements in the MMC, the stored energy in upper/lower arm ($W_{Ctot\,u/l_j}$) can be calculated as:

$$\frac{dW_{Ctot\,u/l_j}}{dt} = v_{Ctot\,u/l_j} i_{Ctot\,u/l_j} \quad \text{(IV- 8)}$$

Based on (IV-1) and (IV-2) $v_{u_j} = m_{u_j} v_{Ctot\,u_j}$, $v_{l_j} = m_{l_j} v_{Ctot\,l_j}$:

$$v_{Ctot\,u/l_j} i_{Ctot\,u/l_j} = v_{u/l_j} i_{u/l_j} \quad \text{(IV- 9)}$$

By expressing v_{u/l_j} and i_{u/l_j} with respect to the external voltage and common-mode voltage/current, following equations are obtained for the MMC energy in upper/lower arm:

$$\frac{dW_{Ctot\,u_j}}{dt} = v_{Ctot\,u_j} i_{Ctot\,u_j} = v_{u_j} i_{u_j} = \left(v_{diff_j} - v_{v_j}\right)\left(i_{diff_j} + \frac{i_{g_j}}{2}\right) \quad \text{(IV- 10)}$$

$$\frac{dW_{Ctot\,l_j}}{dt} = v_{Ctot\,l_j} i_{Ctot\,l_j} = v_{l_j} i_{l_j} = \left(v_{diff_j} + v_{v_j}\right)\left(i_{diff_j} - \frac{i_{g_j}}{2}\right) \quad \text{(IV- 11)}$$

In [81] it has been demonstrated that a simple and decoupled control of the stored energy can be achieved by defining the energy variables as follow:

Per-phase energy sum (W_j^{Σ}):

$$W_j^{\Sigma} = W_{Ctot\,u_j} + W_{Ctot\,l_j} = \frac{1}{2} C_{tot} \left(v_{ctot\,u_j}^2 + v_{ctot\,l_j}^2\right) \quad \text{(IV- 12)}$$

Per-phase energy difference (W_j^{Δ}):

$$W_j^{\Delta} = W_{Ctot\,u_j} - W_{Ctot\,l_j} = \frac{1}{2} C_{tot} \left(v_{ctot\,u_j}^2 - v_{ctot\,l_j}^2\right) \quad \text{(IV- 13)}$$

The per-phase energy sum mainly comprises a DC and a double frequency component $2\omega_g$. The per-phase energy difference mainly comprises an oscillation with fundamental component ω_g [89]. To control the energy stored per MMC arm while ensuring the energy balance between the upper and lower arm, both W_j^{Σ} and W_j^{Δ} have to be controlled. The control task is to master only the average value of both previously defined energy variables. The reference of the average energy sum $\bar{W}_j^{\Sigma^*}$ is set to 1 pu, while $\bar{W}_j^{\Delta^*} = 0$.

By considering an AC (with the fundamental grid frequency) and a DC part in the common-mode current (i.e. $i_{diff_j} = i_{diff_j}^{ac} + i_{diff_j}^{dc}$), the variation in the average value of the energy variables ($\bar{W}_j^{\Sigma}$, $\bar{W}_j^{\Delta}$) are expressed as follow [81], [90]:

$$\frac{d\bar{W}_j^{\Sigma}}{dt} \approx v_{dc} i_{diff_j}^{dc} - \frac{1}{3} p \quad \text{(IV- 14)}$$

$$\frac{d\bar{W}_j^{\Delta}}{dt} \approx -2 < i_{diff_j}^{ac} v_{g_j} >_T , \quad \text{(IV- 15)}$$

where p is the total injected AC power of the MMC. The average value of the per-phase energy sum and per-phase energy difference are controlled through the DC and AC component of the common-mode current, respectively. For controlling $\bar{W}_j^{\Sigma}$, as depicted in Figure IV-6, three independent PI controllers are implemented. The $\bar{W}_j^{\Sigma}$ is obtained with a notch filter tuned at the frequency $2\omega_g$. The output of this control loop gives the reference for the DC component of the common-mode current.

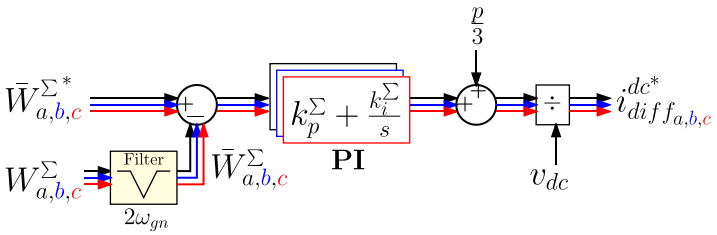

Figure IV-6: Scheme of the per-phase energy sum control.

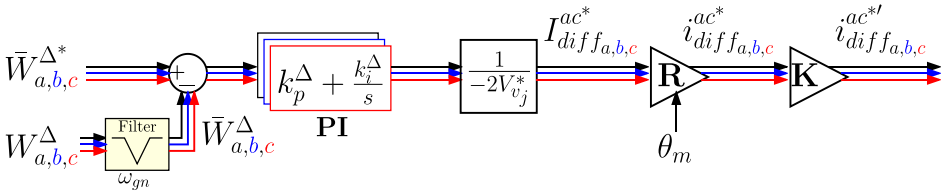

Figure IV-7: Scheme of the per-phase energy difference control.

The energy difference control is shown in Figure IV-7, generates the reference for the AC component of the common-mode current. The matrix **R** (given in (IV-16)) forms a three-phase AC current system using the internal time-domain angle θ_m, which is produced by the grid-forming control. The frequency of this three-phase system in steady state is equal to the grid nominal frequency ω_{gn}. The matrix **K** (given in (IV-17)) is used to cancel the sum of the AC differential component in order to mitigate this AC component in the DC current during transient. More details about this control can be found in [91]. It should be mentioned that for the energy difference control, constant amplitude of the AC voltage V_g is usually used, while in this thesis, the reference of the modulated voltage amplitude V_v^* will be used instead of V_g.

$$\boldsymbol{R} = \begin{bmatrix} cos(\theta_m) & 0 & 0 \\ 0 & cos(\theta_m - \frac{2\pi}{3}) & 0 \\ 0 & 0 & cos(\theta_m + \frac{2\pi}{3}) \end{bmatrix} \quad \text{(IV- 16)}$$

$$\boldsymbol{K} = \begin{bmatrix} 1 & -\frac{1}{2} & -\frac{1}{2} \\ -\frac{1}{2} & 1 & -\frac{1}{2} \\ -\frac{1}{2} & -\frac{1}{2} & 1 \end{bmatrix} \quad \text{(IV- 17)}$$

IV.3 A comparative study between the grid-forming controlled MMC and 2-level VSC in normal voltage control mode

In this section, a comparative study on the dynamic behavior of a grid-forming MMC and a 2-level VSC under normal operation mode in connection to an infinite bus is presented. Three different cases are considered as illustrated in Figure IV-8.

- First case: non-energy-based MMC (Figure IV-8): the switches S1 and S2 are set to the position “a”.
- Second case: energy-based MMC (Figure IV-8): the switches S1 and S2 are set to the position “b”.
- Third case: simplified 2-level VSC (Figure IV-8): since the dominant dynamics in this study are decisive, it is not needed to take the LC filter into account (see chap.2). Therefore, a simplified 2-level VSC with an equivalent connection impedance to the MMC ($Z_{eq} = R_{eq} + jX_{eq}$) is used.

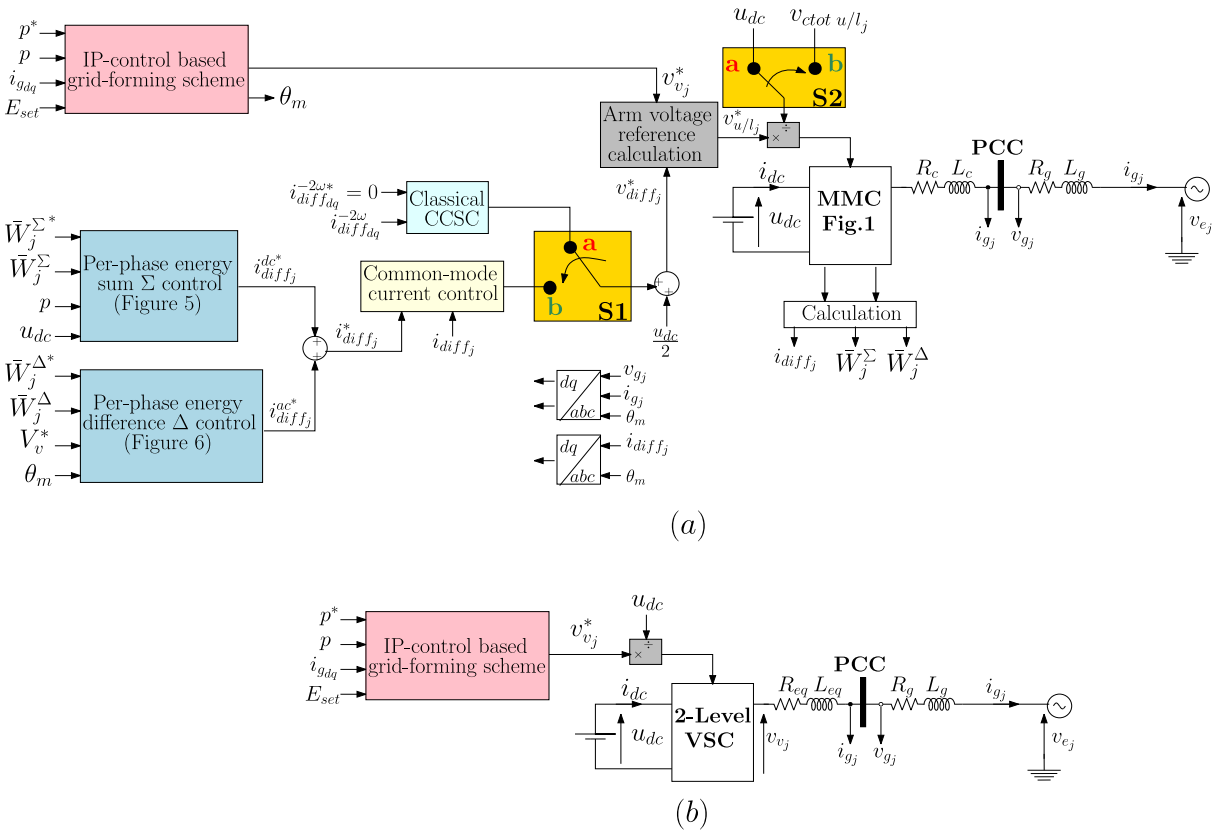

Figure IV-8: General structures for implementing various case studies on: (a) MMC (b) Equivalent 2-level VSC.

To tune the PI controllers of the various control loops in Figure IV-8, we consider following response times: 5 ms for the CCSC, 5 ms for the common-mode current control loop, 100 ms for the per-phase energy sum and 200 ms for the per-phase energy difference. The value of the arm capacitors is determined from the MMC equivalent static inertia. This electrostatic inertia, named H_c, is given in (IV-18). The H_c factor is around 40 ms for a high power MMC [92]. The system parameters are given in Table IV-1.

$$H_c = \frac{6*\frac{1}{2}*C_{tot}*u_{dc}^2}{p_n} \quad \text{(IV- 18)}$$

Table IV-1: System and control parameters.

Parameter	Value	Parameter	Value
Base power S_b	1 GW	E_{set}	1 pu
Converter nominal power p_n	1 GW	L_{arm}	0.18 pu
Base voltage V_b	320 kV	R_{arm}	0.005 pu
Grid voltage V_e	1 pu	C_{tot}	32.552 μF
Base frequency ω_b in rad/s	314.16	Transformer inductance X_c	0.15 pu
Grid nominal frequency ω_{gn}	1 pu	Transformer resistance R_c	0.005 pu
AC line-line voltage	320 kV	u_{DC}	640 kV
Grid thevenin inductance X_g	0.1 pu	$k_{p_{diff}}$	0.17
Grid thevenin resistance $R_g = X_g/10$	0.01 pu	$k_{i_{diff}}$	103.1
H	5 s	k_p^{Σ}	3.36
k_p	0.015	k_i^{Σ}	72
R_v	0.09 pu	k_p^{Δ}	1.68
ω_f	60 rad/s	k_i^{Δ}	18

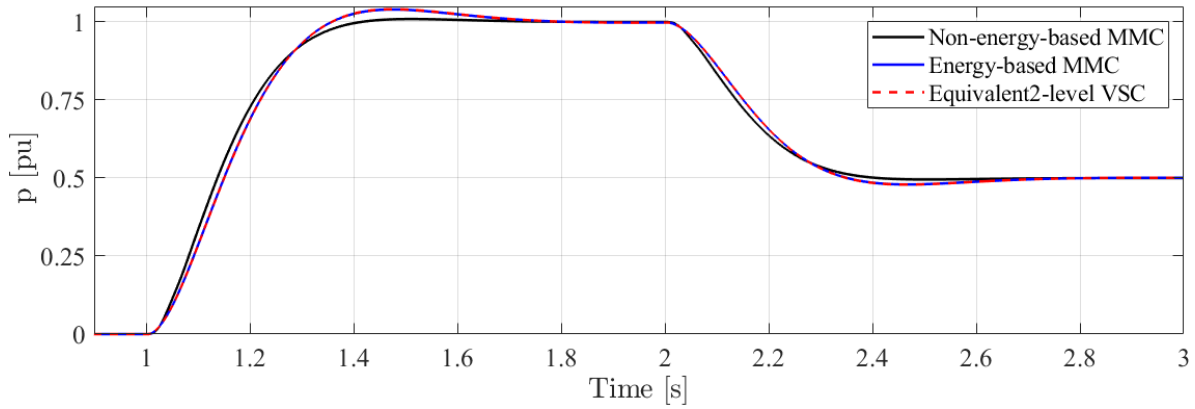

Figure IV-9: Active power responses.

Two steps are applied to the active power reference of the power converter including 1 pu at $t = 1\ s$ and -0.5 pu at $t = 2\ s$. Figure IV-9 shows the active power response of the power converter for different cases. It can be seen that the grid-forming control is properly implemented to the MMC, and the dynamics of the power response are quite well-damped. The power response of the energy-based MMC is perfectly matched to the equivalent 2-level VSC, however for the non-energy-based MMC a slight difference is observed. Therefore, it seems that there is an interaction between the power control and energy control in the MMC.

To ensure this fact, the per-phase energy sum and per-phase energy difference and their average values for the non-energy-based MMC are presented in Figure IV-10. It is validated that the per-phase energy sum a double frequency component $2\omega_g$, while the per-phase energy difference includes an oscillation with fundamental component ω_g. It can be clearly seen that although the average value of the stored energy in non-energy based MMC is stabilized naturally, however the energy level is not controlled at 1 pu. The results for the energy-based MMC are given in Figure IV-11. In this case, the average value of the energy sum is under control.

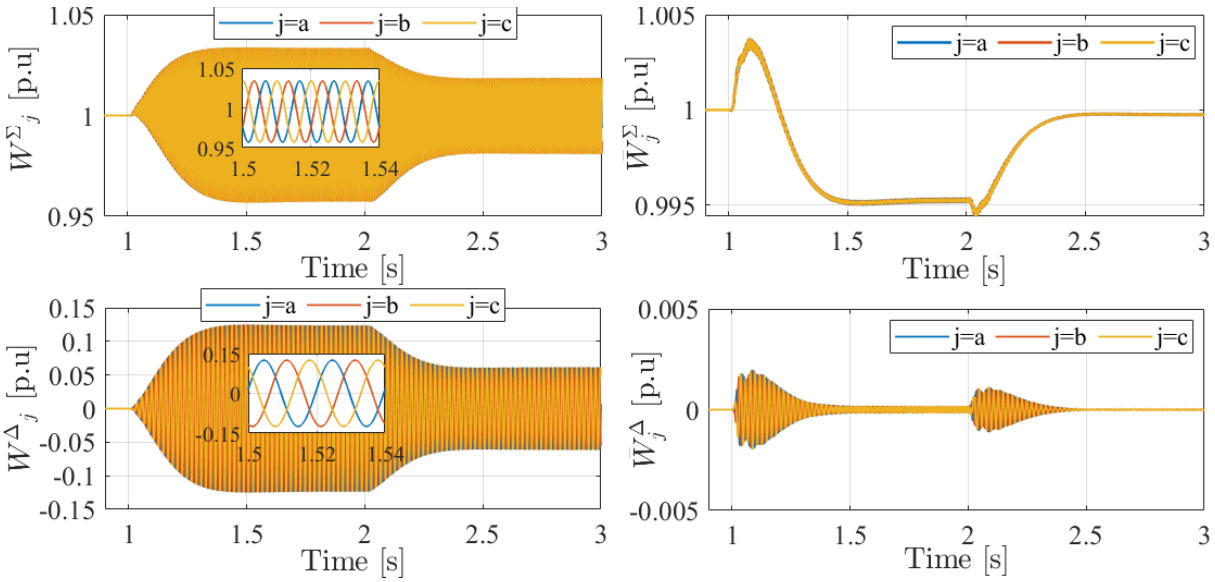

Figure IV-10: Per-phase energy sum and energy difference in non-energy-based MMC.

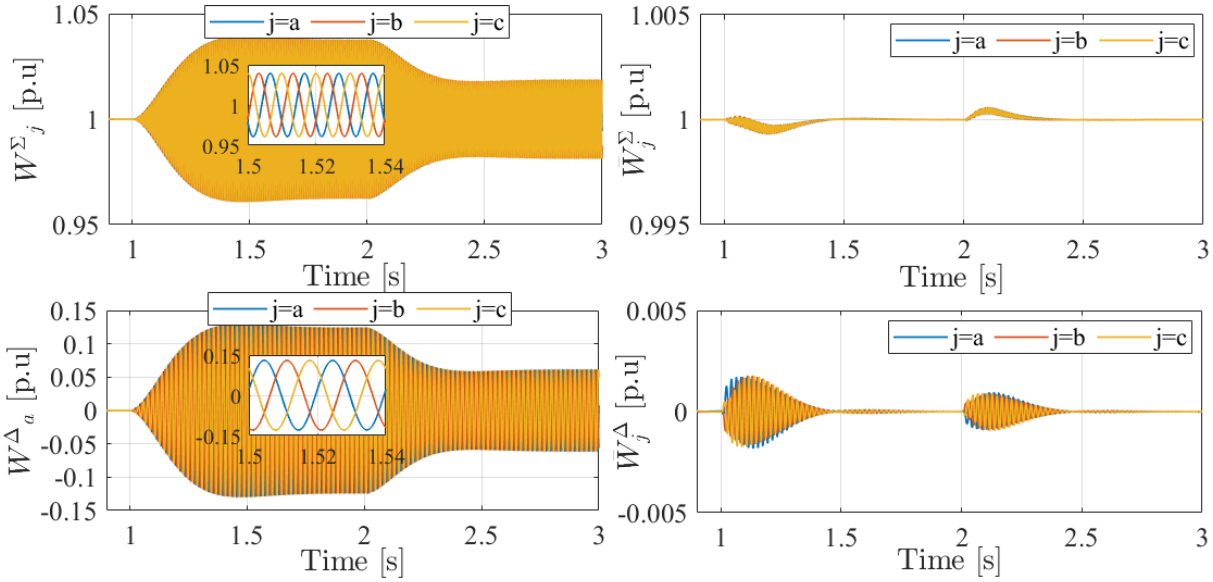

Figure IV-11: Per-phase energy sum and energy difference in energy-based MMC.

In order to find the origin of this difference, it is usefull to have a look to the phasor angle δ_m of the modulated external voltage, which is ilustrated in Figure IV-12. It can be observed that the behaviour of the angle is different in non-energy-based MMC. As it has been already seen, the active power reached 1 pu in steady-state. However, the converter based on the non-energy-based MMC transfers the same amount of active power with a lower voltage angle. By ignoring the resistances, a simple static consideration of the equivalent circuit depicted in Figure IV-8 gives the relation between the active power and voltage angle of the power converter as follows:

$$P = \frac{V_v.V_e}{X_{eq}+X_g} sin(\delta_m) \qquad \text{(IV- 19)}$$

According to (IV-19), for the non-energy-based MMC, the magnitude of the external voltage V_v must be higher to inject 1 pu active power with a lower angle that is confirmed in Figure IV-12. Although the reference value of this voltage is set to $E_{set} = 1\ pu$ in the control, the MMC with a non-energy-based control is not tracking the set-point in steady-state. The reason why non-energy-based MMC has a different dynamic behavior compared to the energy-based MMC and equivalent VSC is linked to the control of the modulated external voltage. In order to justify this result, a focus should be put on the general structure of the MMC control that is presented in Figures IV-3 and IV-5.

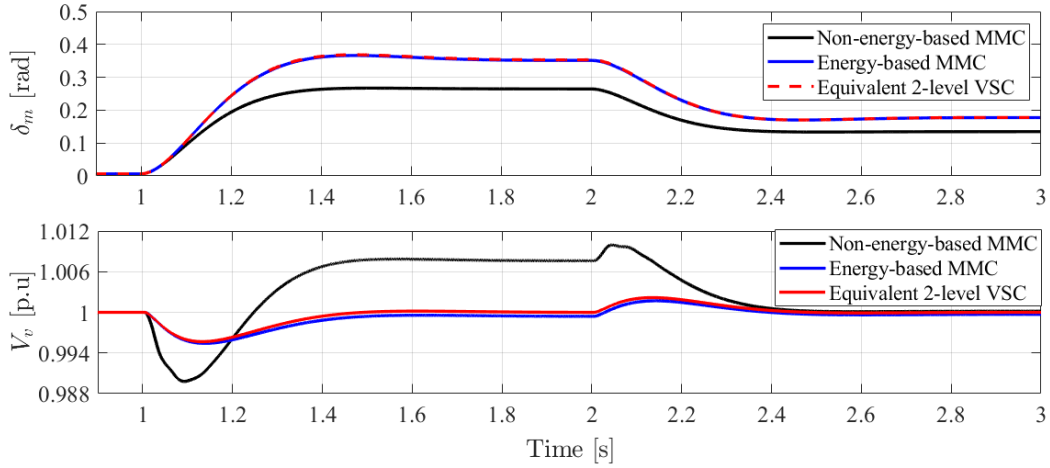

Figure IV-12: Phase and magnitude of the modulated external voltage v_v.

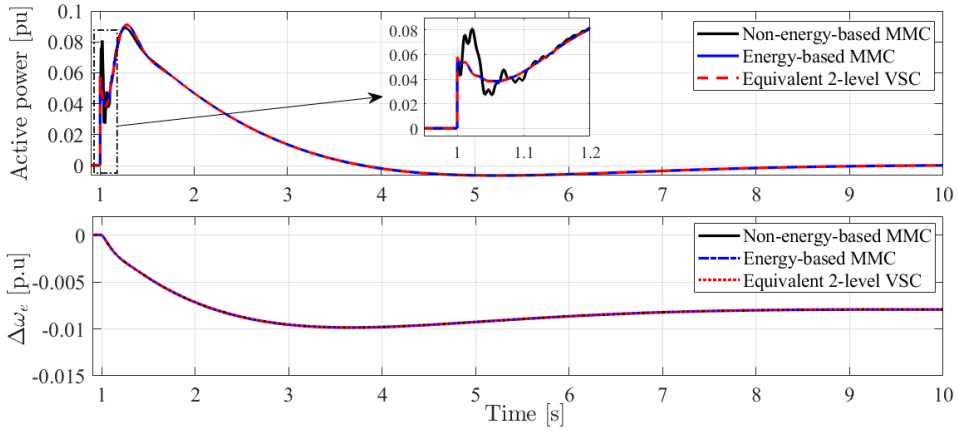

Figure IV-13: Frequency and power dynamics with respect to a load change.

It can be seen that the obtained voltages v^*_{u/l_j} are divided to different voltages (i.e., $v_{Ctot\,u/l_j}$ and u_{dc}) to obtain the modulation indices. Contrary to the energy-based control, since the capacitor voltages are not sensed in the non-energy-based control, the only possibility to obtain the modulation indices is to divide the voltage voltages v^*_{u/l_j} to u_{dc}, which is a constant value. This is not a strict adherence to the principle of the model inversion in control system design. Therefore, the voltage magnitude in the non-energy-based scheme is not under control. In the equivalent VSC, as it is shown in Figure IV-8, since there is no internal capacitor, the external voltage reference is divided to v_{dc} in order to obtain the modulation indices. In this case, since the DC bus voltage is generally kept very closed to its nominal value, the model inversion is met. That is why the energy-based MMC has similar dynamic behavior as the equivalent VSC.

In order to investigate the inertia provision capability of the grid-forming MMC, the converter is connected to the variable frequency grid described in Chapter 2 (Subsection II.4.4, Figure II-38). Initially, there is no power exchange in the system ($p_g = p = P_{load} = 0$). A step of 200 MW (0.2 pu) is applied to the load at t=1 s. Figure IV-13 shows the results of this case study. It can be seen that both energy-based and non-energy based MMC provide nearly the same inertial support to the grid. However, there are some small differences during the first 100 [ms] after the disturbance.

Figure IV-14 and Figure IV-15 demonstrate the internal energy dynamics of the MMC for both energy-based and non-energy-based MMC. Obviously, the non-energy-based MMC is unable to keep the energy level stored in the converter in steady state.

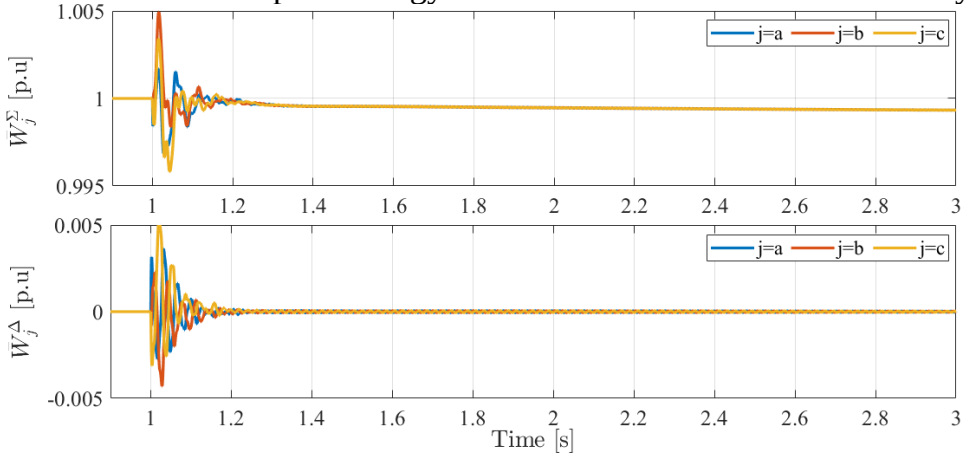

Figure IV-14: Average of energy sum and energy difference in non-energy-based MMC with respect to the load change.

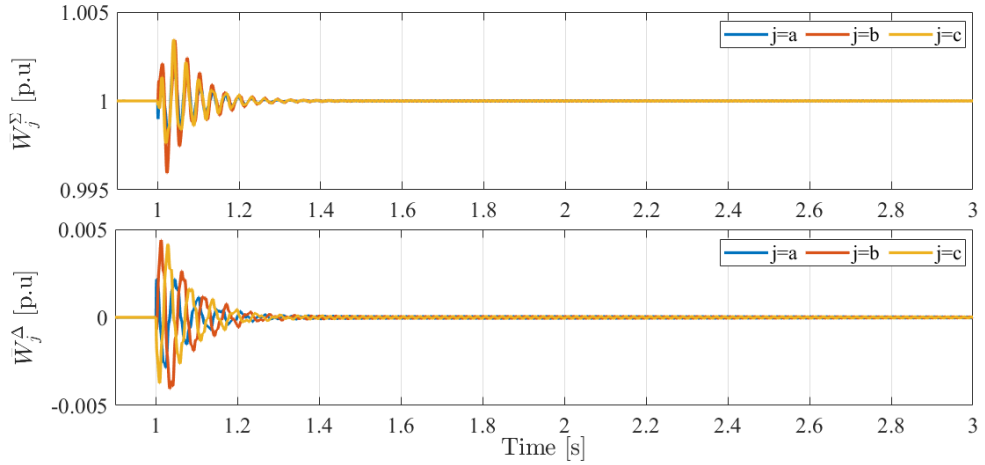

Figure IV-15: Average of energy sum and energy difference in energy-based MMC with respect to the load change.

To sum up, it has been demonstrated that the stored energy in the MMC interacts with the active power response when the internal energy is not controlled. Moreover, it has been highlighted that the dynamic behavior of the active power in an energy-controlled MMC is similar to an equivalent 2-level VSC. This means that in the studies where the focus is on the dynamic behavior of the power converters at the AC side with no specific consideration about the DC bus and internal energy of the converter, a 2-level VSC can be used instead of MMC that results in reducing the complexity of the analysis.

IV.4 Current limitation and transient stability

IV.4.1 Current limitation

Similar to the 2-level VSC, two general approaches (i.e., VI and CSA) can be utilized to limit the MMC current. The current limitation strategies are implemented to grid-forming control, which generates the external voltage of the MMC as shown in Figure IV-16. The structure of internal energy control for energy-based MMC and CCSC for the non-energy based MMC are independent to the AC current limitation and, therefore, they remain unchanged.

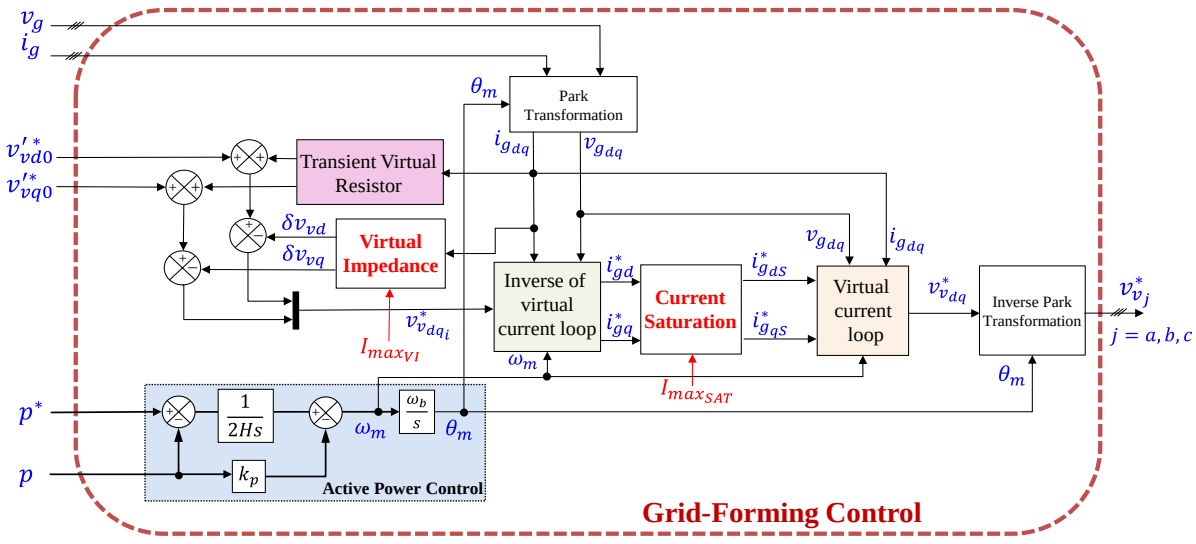

Figure IV-16: Implementation of VI and CSA on the MMC with grid-forming control.

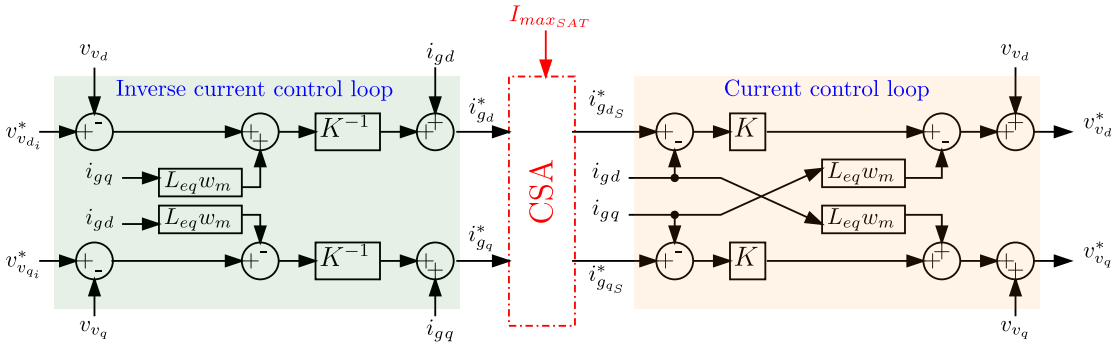

Figure IV-17: Implementation of a fictitious current control loop and its inverse to generate the current reference in the MMC.

The design of the VI is the same as Chapter 3, with the difference that in MMC the equivalent inductance $L_{eq} = L_c + \frac{L_{arm}}{2}$ is replaced with L_c in the equations (III- 5) and (III- 6). Hence, the gain $k_{p_{R_{VI}}}$ is smaller than the one designed for the 2-level VSC.

The current saturation cannot be directly implemented to MMC, since the external voltage is directly imposed by the control and there is no current loop. An idea that is initiated in [93] could be used to add a fictitious current loop and its inverse to the control as shown in Figure IV-16. This allows saturating the generated current reference only when it exceeds its maximum allowable magnitude. Let us recall the conventional d-q current control formulation:

$$v^*_{v_{dq}} = \left(i^*_{g_{dqS}} - i_{g_{dq}}\right) C(s) \pm L_{eq}\omega_m i_{g_{qd}} + v_{g_{dq}} \qquad \text{(IV- 20)}$$

where $C(s)$ is the current controller. The trick of the threshold current control consists in reversing (IV-20):

$$i^*_{g_{dq}} = \left(v^*_{v_{dq_i}} \mp L_{eq}\omega_m i_{g_{qd}} - v_{g_{dq}}\right) C(s)^{-1} + i_{g_{dq}} \qquad \text{(IV- 21)}$$

By paying attention to the red and green terms, important conclusions can be achieved:

- If $i^*_{g_{dq}} = i^*_{g_{dqS}}$, then (IV-20) and (IV-21) are compensated and their effect is cancelled and so, $v^*_{v_{dq}} = v^*_{v_{dq_i}}$.
- If $i^*_{g_{dq}} \neq i^*_{g_{dqS}}$, consequently the current loop in (IV-20) is activated and the converter moves to the current control mode, where $v^*_{v_{dq}}$ are calculated to achieve the desired current references $i^*_{g_{dqS}}$. Figure IV-17 demonstrate this idea with control blocks.

Actually, by implementing the CSA, $i^*_{g_{dq}}$ is equal to $i^*_{g_{dqS}}$ if the current is lower than the maximum allowable current $I_{max_{SAT}}$. Otherwise, the current is saturated to protect the converter against overcurrent, and thus, the converter moves from a voltage source to a current source. To achieve a perfect compensation between (IV-20) and (IV-21) in the unsaturated mode, the choice of $C(s)$ is very important. The controller has to be a proportional one ($C(s) = K$) in order to be able to easily invert the control.

Assuming that the current saturation mode is enabled, the threshold current loop is activated (i.e., the converter is controlled as a current injector) and the resistances are neglected, the closed-loop transfer function of the current loop is expressed as follows:

$$\frac{i_{g_{dq}}}{i^*_{g_{dq}}} = \frac{1}{1+\tau s} \qquad \text{(IV- 22)}$$

where, $\tau = \frac{L_{eq}}{K\omega_b}$. The current loop controller is set to $K = 1.2$ pu (it results in 1.9 [ms] response time for the current control loop), which ensure acceptable dynamics and negligible steady state error in the current. To implement the CSA, the proposed strategy explained in Chapter 3 can be used. The CSA is recalled in the following equation:

$$\begin{cases} i_{g_{dS}}^{*} = i_{g_d}^{*}\ ,\ i_{g_{qS}}^{*} = i_{g_q}^{*} & if \quad \sqrt{i_{g_d}^2 + i_{g_q}^2} \leq I_{max_{SAT}} \\ i_{g_{dS}}^{*} = I_{max_{SAT}}\ cos\ (-\phi) & if \quad \sqrt{i_{g_d}^2 + i_{g_q}^2} > I_{max_{SAT}} \\ i_{g_{qS}}^{*} = I_{max_{SAT}}\ sin\ (-\phi) & \end{cases} \qquad \text{(IV- 23)}$$

To validate the performance of both current limiting strategies, it is assumed that MMC is connected to an infinite bus and a three-phase bolted fault at t= 3 [s] is applied to the PCC. The operating point is $p^{*} = 0.9$ p.u. Considering the control and system parameters given in Table IV-1 and the VI and CSA parameters given in Table IV-2, Figure IV-18 presents the simulation results.

Focusing on the dynamic performance of the VI (black and blue curves), an overcurrent during the first 20 milliseconds is observed for both energy-based and non-energy-based MMC. The CSA has a better performance in limiting the current during the first milliseconds after the fault. This performance is similar to the results already obtained for the 2-level VSC. It can be also seen that when the internal energy of the MMC is not controlled, some damped 50 Hz oscillations appear in the converter current. In terms of current limiting, the energy-based MMC with CSA shows the best dynamic performance.

It should be noted that among these four case studies, the non-energy-based MMC with the VI (black curve) has a steady state error in the limited current. This is because the MMC keeps its voltage source behavior in the current limitation phase, while trying to limit the current with the external voltage v_v that is not perfectly under control (as explained in section IV-3).

Table IV-2: VI and CSA parameters.

$I_{max_{VI}}$	1.2 p.u	$I_{max_{SAT}}$	1.2 p.u
$\sigma_{X/R}$	5	K	1.2 p.u
I_n	1 p.u.	ϕ	0 rad
$k_{p_{R_{VI}}}$	0.5851 p.u		

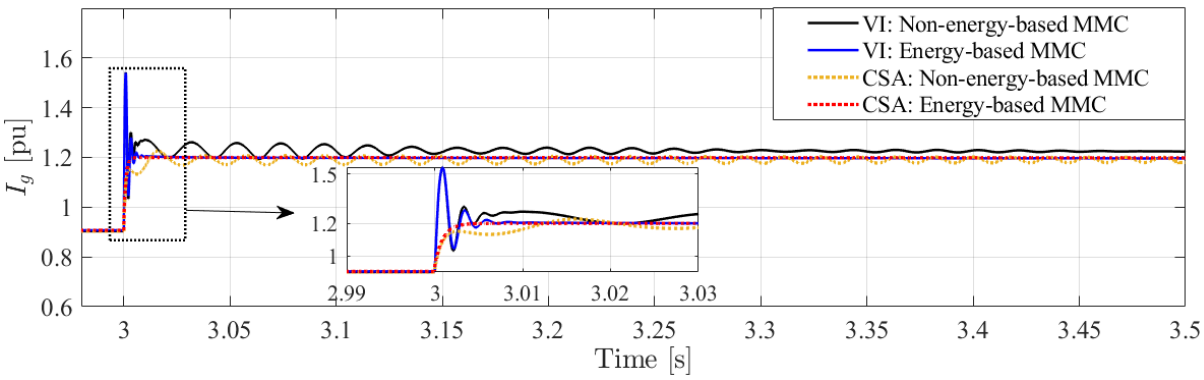

Figure IV-18: Dynamics of the MMC current during a symmetrical three-phase fault.

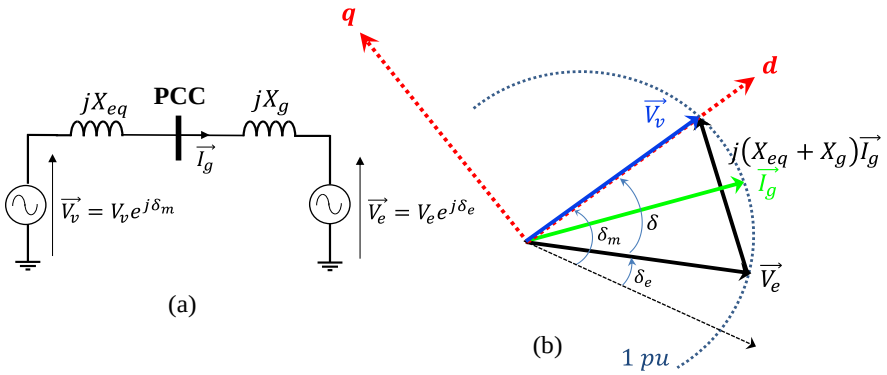

Figure IV-19: (a)- Single-phase equivalent circuit of the MMC, (b)- Phasor diagram in voltage control mode.

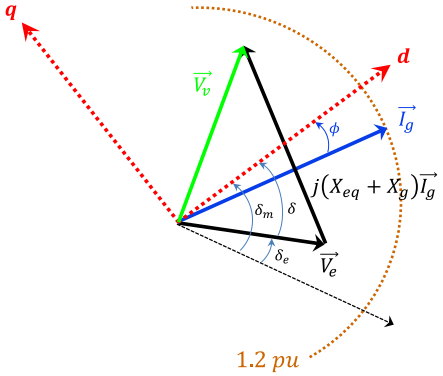

Figure IV-20: Phasor diagram of the MMC in saturated current operation mode.

IV.4.2 Transient stability analysis in case of a 100% voltage sag

For the sake of brevity, the post fault synchronization and transient stability is extended to the MMC structure only for the case of 100% voltage sag. Similar to the Chapter 3, it is assumed that the CSA is implemented to protect the converter against overcurrent. The classical single-phase equivalent circuit and its corresponding phasor model of Figure IV-1 in the normal operation mode (unsaturated current operation mode) is drawn in Figure IV-19 . The vector $\overrightarrow{V_v}$. (in blue) is the controlled vector that is supposed to be aligned with the d-axis. The current vector $\bar{I}_g$ (in green) is a consequence of this operation mode. The well-known expression of the power can be written in steady state as follows:

$$P = \frac{V_v V_e}{X_{eq}+X_g} sin(\delta_m - \delta_e) = P_{max}^{MMC} sin\delta, \qquad \text{(IV- 24)}$$

where $\delta = \delta_m - \delta_e$ denotes the power angle, $P_{max}^{MMC} = V_v V_e/(X_{eq} + X_g)$.

During some transient times, the current may increase over the maximum current of the converter. To limit the current, the CSA in (IV-23) is activated and the MMC moves to the saturated mode. In this operation mode, it is possible to draw a new phasor diagram, as illustrated in Figure IV-20, where the voltage vector $\overrightarrow{V_v}$ is not under control anymore. The MMC operated as a current injector with the control vector of $\overrightarrow{I_g}$. Same as previous chapter, in the proposed CSA, the magnitude of $\overrightarrow{I_g}$ is set to $I_{max_{SAT}}$ and however, its angle ϕ can be chosen freely (with reference to the d-axis) by the control.

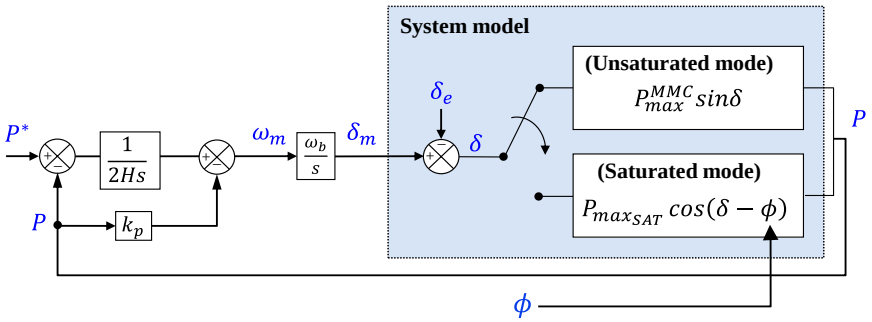

Figure IV-21: Large signal model of the MMC including the dynamic control for transient analysis.

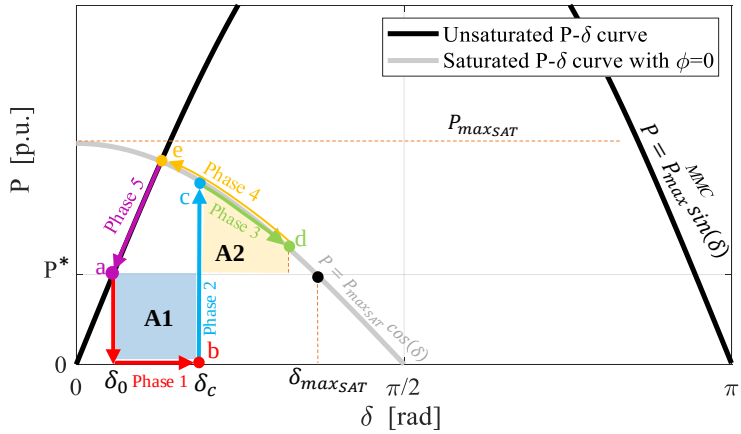

Figure IV-22: Operation mechanism of the MMC under 100% voltage sag.

The active power is calculated with the grid voltage $\overrightarrow{V_e}$ and the controlled vector $\overrightarrow{I_g}$ as follows:

$$P = V_e I_{max_{SAT}} \, cos(\delta_e - (\delta_m - \phi)) = P_{max_{SAT}} \, cos(\delta - \phi) \qquad \text{(IV- 25)}$$

where $P_{max_{SAT}} = V_e I_{max_{SAT}}$. According to (IV-24) and (IV-25), the large signal model of the grid-forming MMC for both unsaturated and saturated current operation modes is illustrated in Figure IV-21.

It can be seen that the only difference in large signal modeling of MMC for transient stability analysis compared to the 2-level VSC is the quasi-static expression of the active power in unsaturated voltage control mode, where P_{max} is replaced with P_{max}^{MMC}.
Figure IV-22 describes the operation mechanism of the grid-forming MMC subjected to a bolted fault. All the five phases are the exact same as Chapter 3. The only difference that slightly changes the calculations is the quasi-static curve in unsaturated mode.

Following formulation based on the quasi-static considerations and the use of equal area criterion is obtained for the initial angle δ_0, angle stability limit $\delta_{max_{SAT}}$, critical clearing angle δ_{cc} and critical clearing time t_{cc}:

$$\delta_0 = asin\left(\frac{P^*}{P_{max}^{MMC}}\right) \qquad \text{(IV- 26)}$$

$$\delta_{max_{SAT}} = acos\left(\frac{P^*}{P_{max_{SAT}}}\right) \qquad \text{(IV- 27)}$$

$$\delta_{cc} = asin\left(\frac{P^*\left(\delta_0 - \delta_{max_{SAT}}\right)}{P_{max_{SAT}}} + sin\left(\delta_{max_{SAT}}\right)\right) \qquad \text{(IV- 28)}$$

$$t_{cc} = 2\left(\sqrt{\frac{H(\delta_{cc} - \delta_0)}{\omega_b P^*}}\right) \qquad \text{(IV- 29)}$$

IV.4.2.1 Energy-based MMC

The energy-based MMC properly controls the modulated external voltage in unsaturated mode. Therefore, it is expected that the quasi-static consideration in this mode is valid. Considering the given parameters in Table IV-1, Table IV-2, $H = 5s$ and $k_p = 0.01$, the CCT predicted from (IV-29) and the one observed from the time-domain simulations are compared in Table IV-3 for different operating points. One can notice a small error between both CCTs due to the damping effect as it was also observed with the 2-level VSC before. Taking $P^* = 1\,pu$ as an illustrative example, Figure IV-23 shows the simulation results with two different fault durations of $t_{f1} = t_{cc} = 29\,ms$ and $t_{f2} > t_{cc}$ $(35\,ms)$. As expected, if the clearing time is lower or equal to the CCT, the internal angle of the MMC stably recovers its equilibrium point, otherwise it diverges and the system loses the synchronism.

Table IV-3: Results of the CCT determination for energy-based MMC.

	$\boldsymbol{\phi = 0}$ $\boldsymbol{H = 5s\,, k_p = 0.01}$	
$\boldsymbol{P^*}$	Predicted CCT by (IV-29)	CCT in simulation
1 pu	31 ms	29 ms
0.9 pu	59 ms	56 ms
0.8 pu	90 ms	85 ms
0.7 pu	125 ms	116 ms
0.6 pu	165 ms	156 ms
0.5 pu	214 ms	202 ms

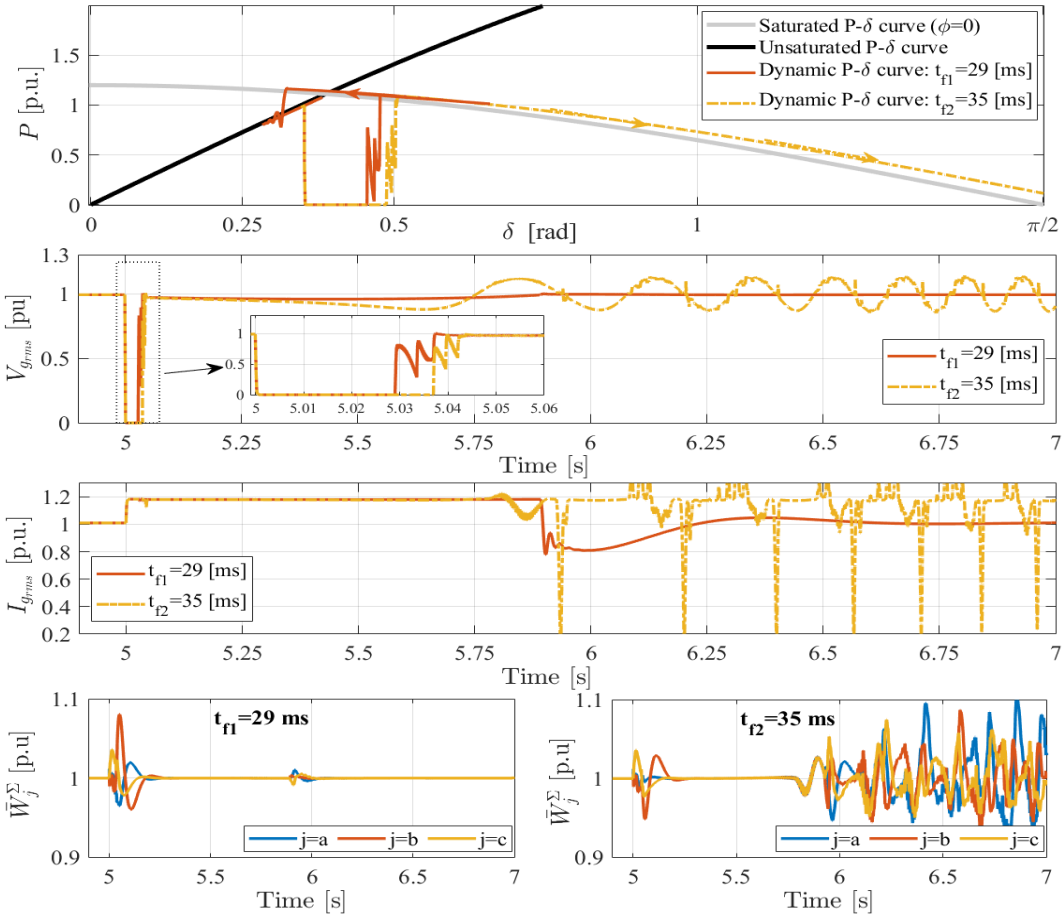

Figure IV-23: Simulation results in case of a 100% voltage sag with different fault time durations for the energy-based MMC.

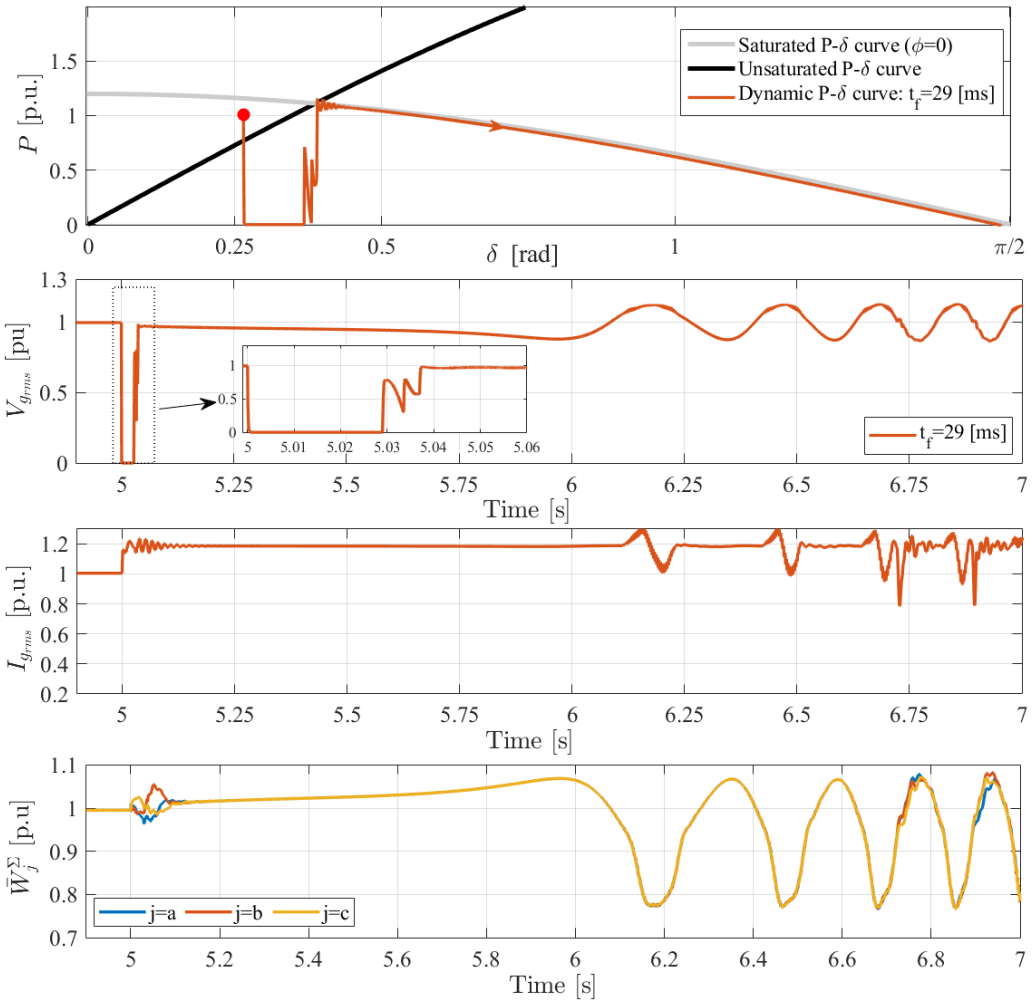

Figure IV-24: Simulation results in case of a 100% voltage sag with 29 [ms] durations for the non-energy-based MMC.

IV.4.2.2 Non-energy-based MMC

Having in mind that in non-energy-based MMC control the external voltage v_v is not ideally controlled, the converter operation point in unsaturated mode does not follow the quasi-static $P-\delta$ curve. Considering the same parameters as the previous simulation study and the fault duration of $t_f = 29\,ms$, shows that non-energy-based MMC cannot achieve the same performance as the energy-based MMC and it becomes unstable. It can be clearly seen that the initial operating point is not located on the unsaturated $P-\delta$ curve before the disturbance. As the result, the previous stability analysis cannot be extended to an MMC with no internal energy control.

IV.4.2.3 Impact of the saturated current angle ϕ on transient stability

Similar to Chapter 3, shifting the saturated quasi-static $P-\delta$ curve to the right side thanks to the angle ϕ can increase the angle stability limit $\delta^{\phi}_{\max_{SAT}}$ and therefore, the CCA and CCT. Following formulation based on the quasi-static considerations and the use of equal area criterion is obtained for the MMC structure:

$$\delta^{\phi}_{max_{SAT}} = acos\left(\frac{P^*}{P_{max_{SAT}}}\right) + \phi \qquad \text{(IV- 30)}$$

$$\delta_{cc}^{\phi} = asi\,n\left(\frac{P^*\left(\delta_0 - \delta_{max_{SAT}}^{\phi}\right)}{P_{max_{SAT}}} + si\,n\left(\delta_{max_{SAT}}^{\phi} - \phi\right)\right) + \phi \qquad \text{(IV- 31)}$$

$$t_{cc}^{\phi} = 2\left(\sqrt{\frac{H\left(\delta_{cc}^{\phi} - \delta_0\right)}{\omega_b P^*}}\right) \qquad \text{(IV- 32)}$$

Comparing to (IV-28) and (IV-29), (IV-31) and (IV-32) demonstrate that the CCA and CCT are increased with respect to the increase of ϕ giving more time for clearing the fault while ensuring a stable restoration.

The optimal value of ϕ that guarantees the ability of the converter to switch back to the voltage control mode and a better transient stability compared to the case in with $\phi = 0$ is obtained by solving the following optimization problem:

$$\begin{cases} \phi_{opt} = min\left\{\phi = acos\left(\frac{P^*}{P_{max_{SAT}}}\right) + asin\left(\frac{P^*}{P_{max}^{MMC}}\right)\right\} \\ constraints: \quad 0 \le P^* \le 1 \\ SCR_{min} \le SCR \le SCR_{max} \end{cases} \qquad \text{(IV- 33)}$$

To solve this problem, it is possible to simply draw a surface that relates ϕ to the SCR and P^* as shown in Figure IV-25. It can be seen that for a wide range of SCR and various initial operating power, the maximum value of ϕ that satisfies the constraints is around 0.93 radian. Therefore, $\phi_{opt} = 0.93$ [rad] is considered as the optimal value. It should be mentioned that SCR = 1.32 corresponds to the minimum grid impedance that allows the MMC to transfer 1 pu active power (according to (IV-24)).

Considering the energy-based MMC with initial power setpoint of $P^* = 1$ pu and $\phi = \phi_{opt}$, the CCT predicted from (IV-32) and the one observed from the time-domain simulations are compared in Table IV-4 for different operating points. These results confirm that the proposed use of the saturated current angle can enhance the transient stability and (IV-32) gives a satisfactory accuracy in the anticipated CCT.

Taking $P^* = 1\,pu$ as an illustrative example, Figure IV-26 shows the simulation results with the fault durations of $t_f = t_{cc} = 97\,ms$. As expected, the MMC stably recovers its equilibrium point after in the post-fault.

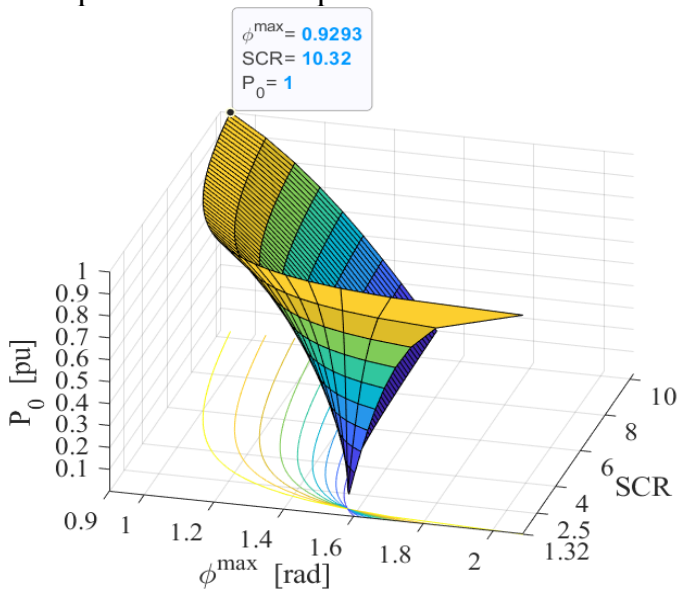

Figure IV-25: The angle ϕ with respect to the variation of SCR and power setpoint.

Table IV-4: Results of the CCT determination for energy-based MMC with optimum ϕ.

	$\boldsymbol{\phi = 0.93\,rad}$ $\boldsymbol{H = 5s\,, k_p = 0.01}$	
$\boldsymbol{P^*}$	Predicted CCT by (IV-32)	CCT in simulation
1 pu	97 ms	97 ms
0.9 pu	137 ms	133 ms
0.8 pu	178 ms	170 ms
0.7 pu	223 ms	214 ms
0.6 pu	273 ms	262 ms
0.5 pu	334 ms	319 ms

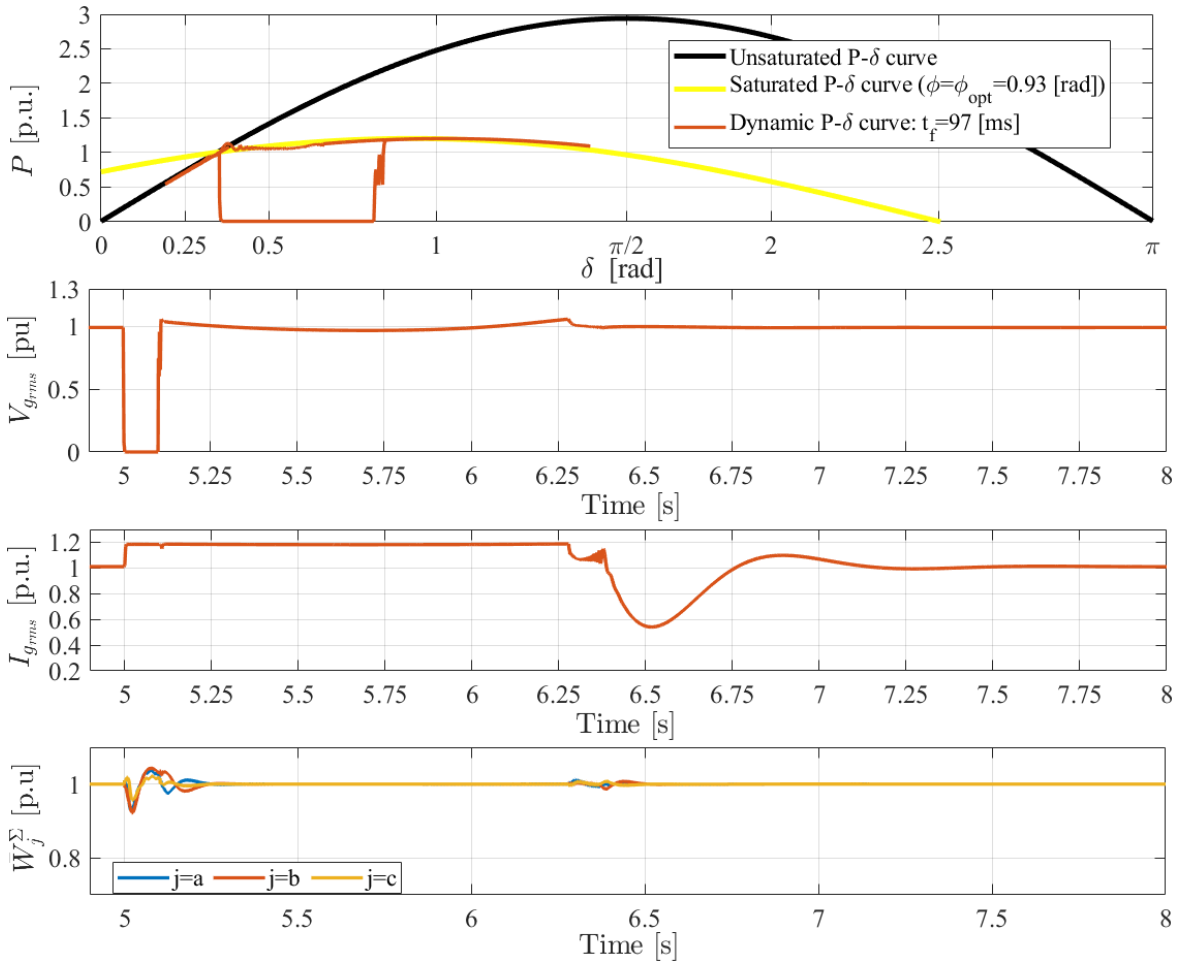

Figure IV-26: Effect of including $\phi = \phi_{opt}$ in the control on transient stability in case of a 100% voltage sag.

Up to here, the obtained results show that the grid-forming control can be successfully implemented to the MMC configuration. In normal voltage control mode of the MMC, the dynamic behavior of the MMC nearly same as an equivalent 2-level VSC. If the internal energy of the MMC is controlled, the dynamic behavior is identical. In case of large disturbances, the role of energy control becomes more important. The conducted studies demonstrated that only with energy-based control MMC it is possible to develop a similar approach as the 2-level VSC for transient stability analysis.

As the MMC plays a key role in developing HVDC transmission system, next section is dedicated to the studies on controlling an MMC-HVDC link interconnecting two AC areas with the aim of virtual inertia provision, considering the grid-forming implementation at the converter substations.

IV.5 Grid-forming control of an HVDC system interconnecting two AC grids

Several publications have proposed to utilize voltage source converter (VSC) HVDC systems for providing virtual inertia. Many of the proposed control methods are based on grid-following control concept and they use the frequency derivative (i.e., *df/dt* or RoCoF) to synthetize the inertial response. Such strategies can be easily integrated with conventional VSC control loops, but they rely on a PLL for the synchronization with the grid and to estimate the *df/dt*. However, under weak grid condition, in addition to difficulties with estimating effectively the *df/dt*, there are stability issues reported in the literature [94], [95].

The use of a grid forming control in an HVDC converter is interesting for the grid to which it is connected due to the inertial effect that can be inherently embedded in the control. Most of the previous publications on grid-forming control for HVDC applications have studied the implementation and control system performance for an individual converter terminal [58], [96]. By implementing the grid-forming control in both substations, the impact of inertial support on the frequency dynamics needs to be assessed. Focusing on the case of two AC grids interconnected with an HVDC link, the HVDC interconnector consists of two converter stations. One of the stations has to manage the active power flow, while the other station controls the DC bus voltage. If a grid-forming converter to bring an inertial effect controls the DC bus, this may induce some instability issues.

Until now, this topic has not been widely studied in the literature, except for some examples in [25], [97]. Author in [25], by implementing the VSM-based control in both stations have demonstrated that it is possible to stabilize the system. However, integrating the feature of DC voltage regulation requires a slower performance for the DC controller and possibly increased DC-side capacitive energy storage.

In this section, first a non-ideal DC bus model is added to the previous converter modeling in order to include the DC bus dynamics. Then, several studies are conducted on a single grid-forming converter substation to assess its dynamic performance while providing inertial service and DC voltage control. The challenges ahead of the control system are highlighted. Finally, a full model of an HVDC interconnection including both converter substations is developed and the requirements for providing inertia to both AC sides of the link, while having proper dynamics in the DC bus is discussed.

IV.5.1 Inclusion of DC bus dynamics

In the first step, only one side of the HVDC link is accurately modelled. For the sake of simplicity, an equivalent 2-level VSC is used, as it has been shown already that it behaves similarly to an MMC (see Figure IV-8). As shown in Figure IV-27, the VSC 1 is connected to and equivalent AC grid and a load in ZONE 1. For the other side of the link, it is simply assumed that the active power is assimilated to a 20 [ms] first order model via a controllable current source. In the DC link, the charging time of the DC capacitors at each substation is considered to be 40 [ms] [92].

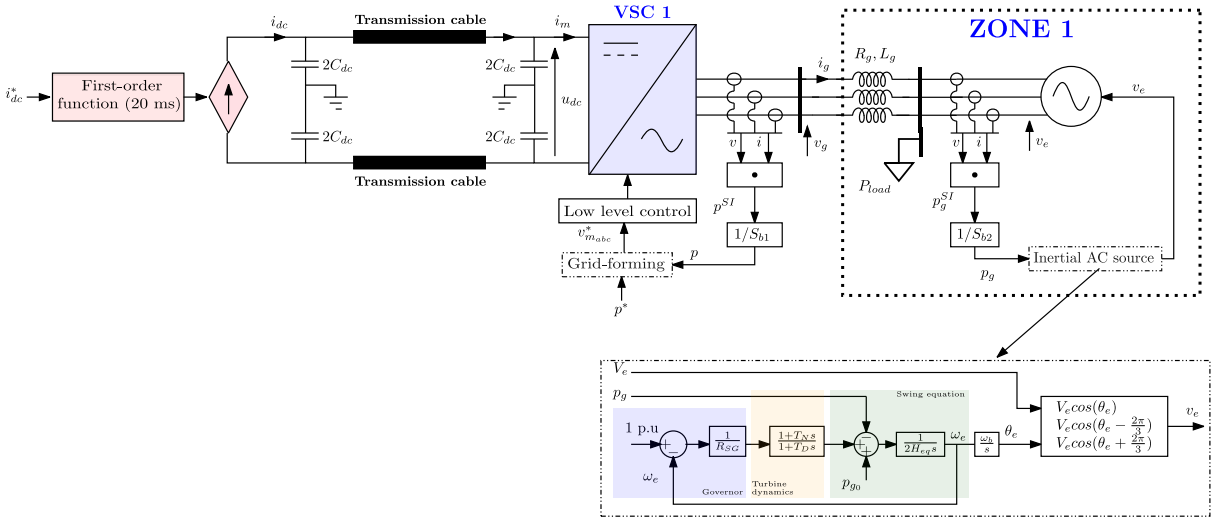

Figure IV-27: Scheme of the HVDC link including the DC link and one converter substation.

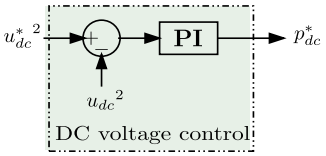

Figure IV-28: Scheme of the DC voltage controller.

Table IV-5: System and control parameters.

AC grid			
$P_n = S_{b_3} = S_{b_4}$	1000 MW	H_{eq}	5 s
V_b	320 kV	R	0.04 p.u.
V_e	1 p.u.	T_N	1 s
$L_g = 10R_g$	0.1 p.u.	T_D	2 s
ω_b	314.16 rad/s		
DC bus and DC controller			
u_{dc}	640 kV	L_{cable}	0.5 mH/km
C_{dc}	0.1953 mF	C_{cable}	8.6 nF/km
R_{cable}	0.02568 Ω /km	DC controller response time	150 ms
Grid-forming converters (equivalent 2-level)			
L_{eq}	0.24 p.u.	**PLL-based inertia less scheme:**	
R_{eq}	0.0075 p.u.	m_c	1.95 p.u.
IP- control scheme:		ω_c	31.4 rad/s
H	5 s	PLL response time	20 ms
k_p	0.01 p.u.		

The DC cooper cables with an area of 1000 [mm^2], a total distance of 500 [km] is modeled with a PI connection (R_{cable}, L_{cable} C_{cable}) [98]. The DC voltage control is performed by a PI-controller, as illustrated in Figure IV-28, and its design is based on the classical tuning considering a desired response time for the DC voltage regulation (see Appendix D).

IV.5.1.1 DC bus control with a current injector

The aim of this study is to assess the DC bus dynamics, while providing inertia to the AC grid. In this scenario, the required power is absorbed from a current injector placed at the DC link. Hence, the output of the DC voltage controller (p_{dc}^*) is divided by the

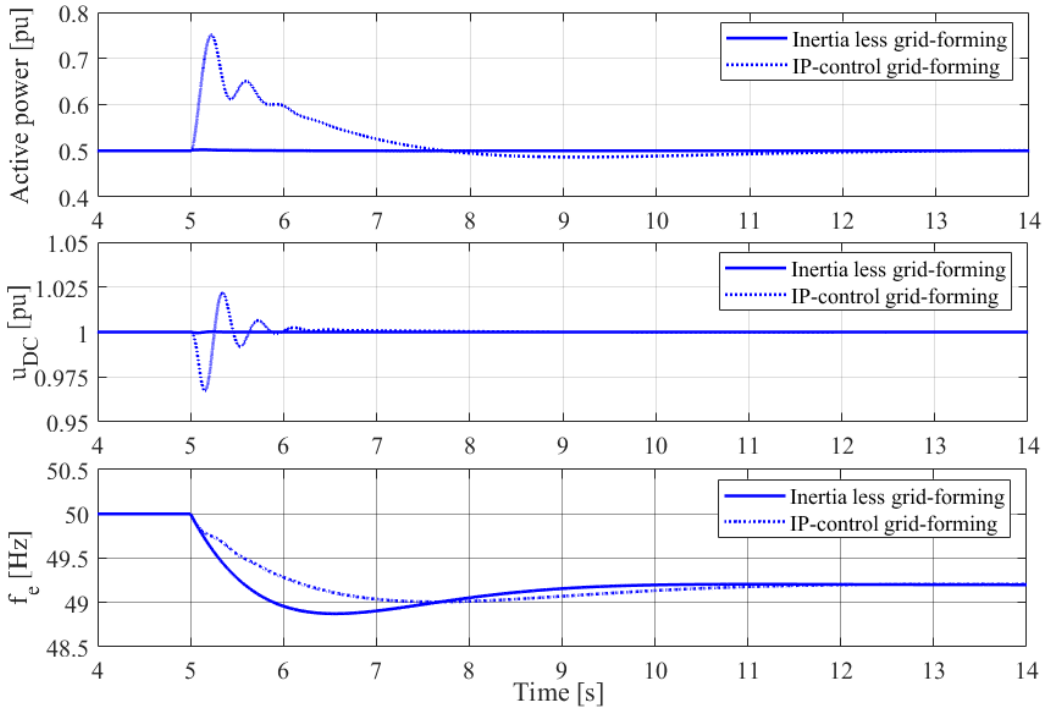

Figure IV-29: Active power of VSC 1, DC bus voltage and grid frequency in case of a load change at ZONE 1.

constant u_{dc}^* to get i_{dc}^*. Then i_{dc}^* is passed through a first-order function in order to inject i_{dc} to the DC link and keep the DC voltage level. The VSC 1 is controlled either with the PLL-based inertia-less grid-forming scheme (introduced in Chapter 2) or with the IP-control grid-forming strategy that provide inertial effect. The system and control parameters are given in Table IV-5.

Initially, 500 MW of power (0.5 p.u) is transferred from the VSC 1 to ZONE 1. At t=5 [s] a step of 0.4 [pu] is applied to the load in order to modify the frequency. Figure IV-29 shows the active power injected by the VSC 1, DC bus voltage and grid frequency. When the VSC 1 is controlled with IP-control grid-forming strategy, it can provide the inertial response to improve the frequency dynamics, while the DC bus voltage level remains in the acceptable range (0.95 pu $\leq u_{DC} \leq 1.05$ pu). As expected, the inertia-less grid-forming strategy is nearly insensitive to the disturbance.

IV.5.1.2 DC bus control with grid-forming converter

In this scenario, it is assumed that the VSC 1 is controlled with IP-control grid forming strategy with virtual inertia emulation capability. Simultaneously, this converter is controlling the DC bus voltage. Therefore, the output of the DC voltage controller (p_{dc}^*) is directly imposed to the power reference of the VSC 1 p^* as illustrated in Figure IV-30. Since the DC bus control is the outermost control loop, it should be slower than the power control loop to avoid interactions and possible instability. First, we keep the same DC bus control response time as before (i.e., 150 [ms]) and start with a small inertial constant in order to have a fast power control loop. Then, the inertia constant is increased as much as possible. It should be noted that by changing the value of inertia, the damping ratio of the active power response is kept always to $\zeta = 0.7$ in our control tuning. Therefore, the damping term k_p is updated with respect to the different choices for inertia constant.

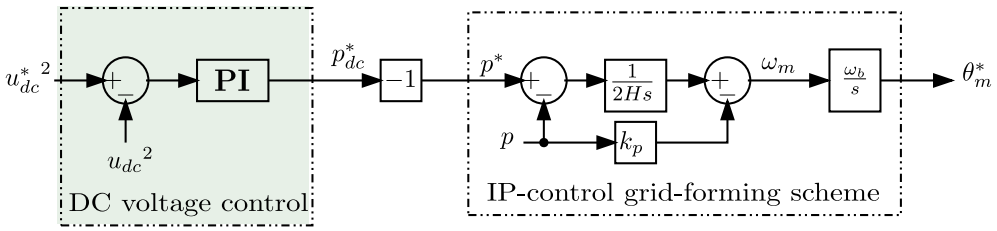

Figure IV-30: DC bus control integrated to the control of grid-forming VSC.

Same as previously, 500 MW of power (0.5 p.u) is transferred from the VSC 1 to ZONE 1. At t=5 [s] a step of 0.4 [pu] is applied to the load. Figure IV-31 demonstrates the active power response of the VSC1 and DC bus voltage corresponding to this event. It can be seen that with $H = 0.25$ [s], which is quite a small value and it results in a fast power control, the responses are well damped. If the aim is to provide the inertial support, a bigger inertia constant is needed. This result shows that by increasing the inertia constant over 0.41 [s], there is a risk of instability due to the interaction between the power control loop and DC voltage control loop.

A primitive idea to avoid these interactions is to slowdown the DC bus regulation. Therefore, in the next simulation study presented in Figure IV-32, the DC control response time is increased to 400 [ms]. From this figure, it can be observed that with higher inertia constant, the responses are well damped but with a larger deviation in the power and DC voltage.

In fact, there is a fundamental contradiction between the inertial support provision and DC bus voltage control. Focusing on the curves of active power and DC bus voltage, right after the disturbance, the VSC1 tends to inject power rapidly due to its inertial effect. At the same time, since the DC bus voltage is dropping, the DC voltage controller tries to reduce the power setpoint of VSC1 to maintain the DC bus level. Hence, these two actions introduce two opposite effects and neither the DC bus is controlled within the acceptable range, nor a proper inertial support is provided. It can be seen that by choosing a bigger inertia constant, the frequency Nadir is not improved due to this contradiction.

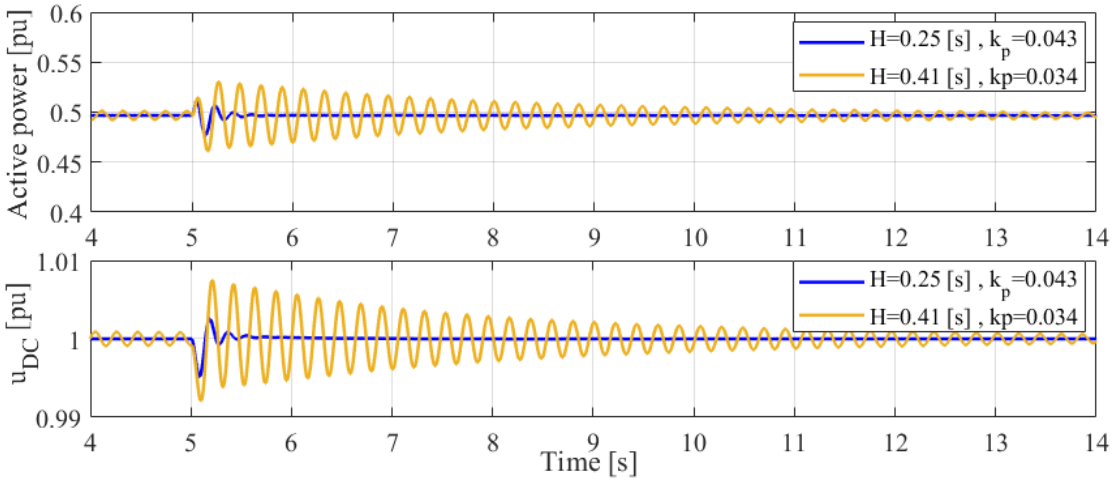

Figure IV-31: Active power of VSC1 and DC bus voltage in case of load change in ZONE 1 considering a fast DC bus regulation (150 [ms] response time).

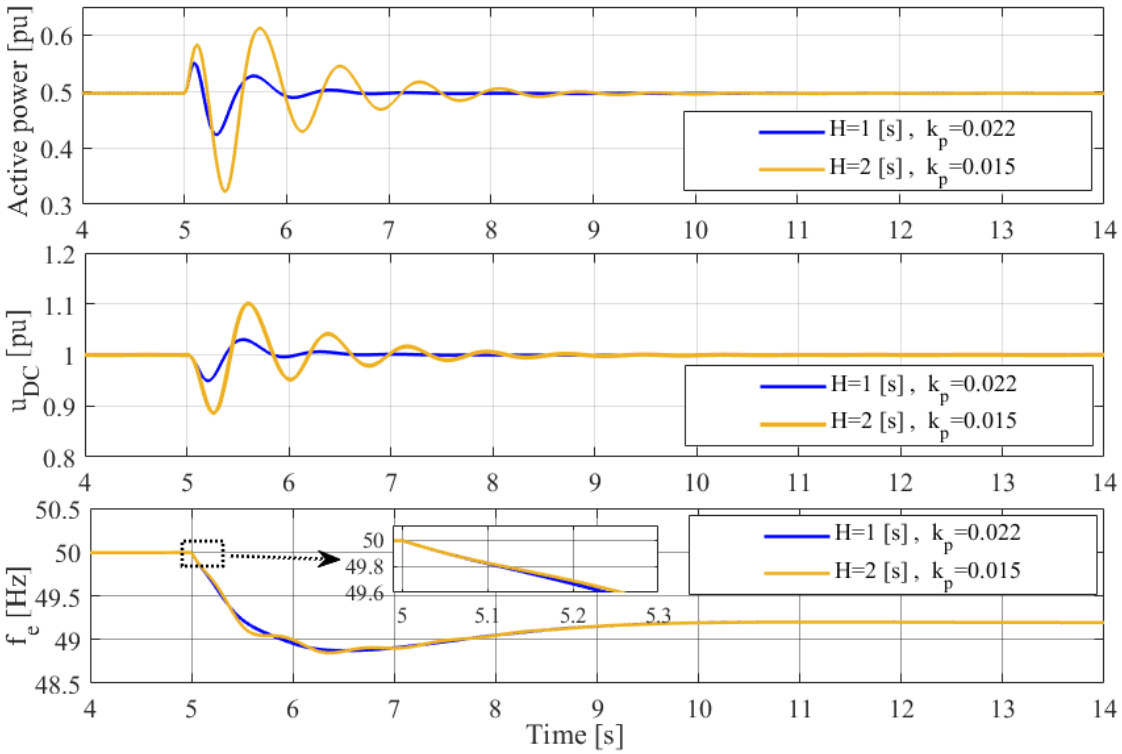

Figure IV-32: Active power of VSC1, grid frequency and DC bus voltage in case of load change in ZONE 1 considering a slower DC bus regulation (400 [ms] response time).

To sum up, when asking for the DC bus voltage regulation and inertial support simultaneously from a single converter at an HVDC substation, two different conditions arise:

- If the DC voltage control loop is fast in order to achieve an adequate regulation of the DC voltage, the inertial effect must be very small in order to avoid the interactions between the internal loop (power control loop) and the external one (DC voltage control loop).
- In order to be able to increase the inertia constant in power control loop, the DC voltage control loop must be slower. In this case, the contradiction between the inertial support and DC voltage control prevents the DC voltage to be well-controlled and also to have a proper inertial effect.

IV.5.2 Control of an HVDC interconnection with grid-forming control at both substations

In this section, an HVDC link with two converter substations is fully modeled. As shown in Figure IV-33, one of the stations has to manage the active power flow (VSC 2), while the other station controls the DC bus voltage (VSC 1). The ZONE 2 is fully symmetrical to the ZONE 1. According to the previous discussion on the conflict of simultaneous DC bus control and inertial effect, the control of VSC 1 is based on the PLL-based inertia less grid-forming strategy with $m_c = 7.85$ [pu], $\omega_c = 31.14$ [rad/s] to avoid any contradictory effect. The VSC 2 is controlled with the IP-control grid-forming strategy with $H = 5\ s$ and $k_p = 0.01$. The response time of the DC bus voltage controller is 150 [ms].

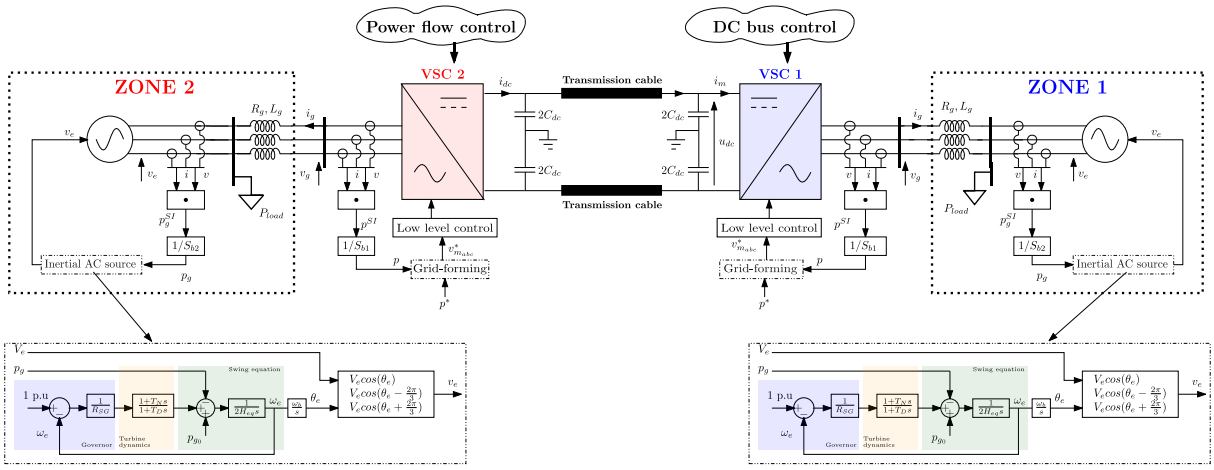

Figure IV-33: Full model of the studied HVDC interconnection.

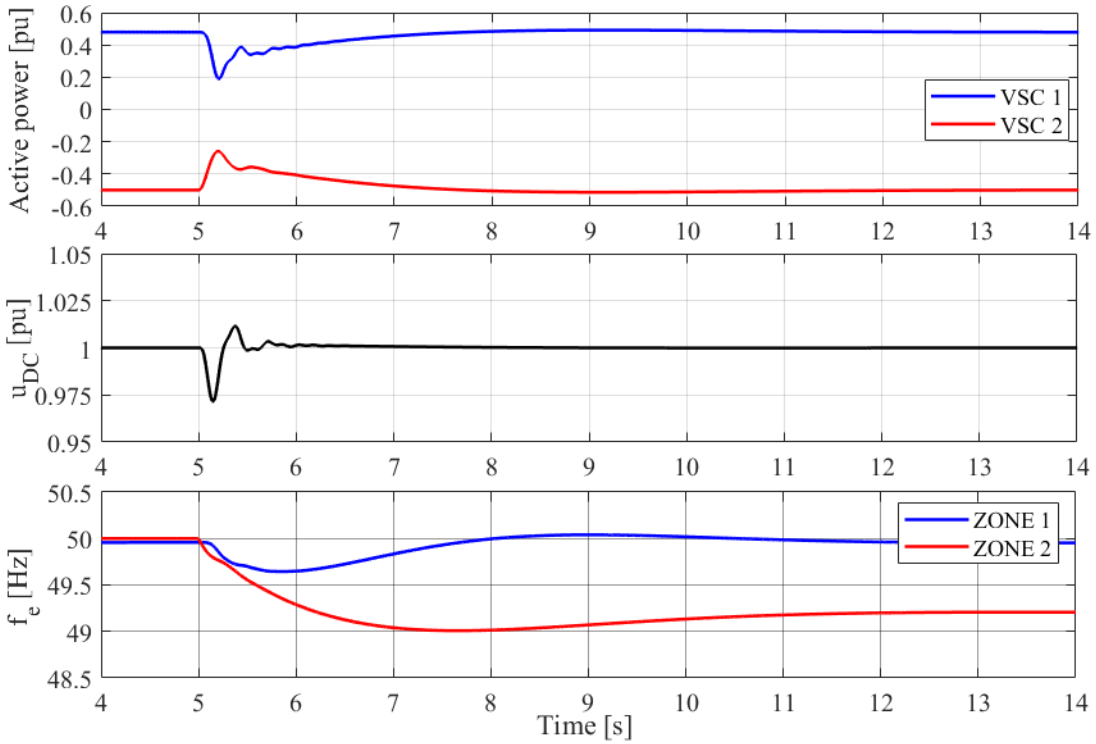

Figure IV-34: Active power of VSCs, frequencies and DC bus voltage in case of load change in ZONE 2.

Initially, 0.5 pu of active power is transferred from the ZONE 2 to ZONE 1. At t=5 [s] a step of 0.4 [pu] is applied to the load at ZONE 2. Figure IV-34 shows the active power responses at VSC1 and VSC2 substations, DC bus voltage and frequencies in each zone. It can be seen that the grid-forming VSC 2 is participating to the frequency regulation of ZONE 2 thanks to its inertial response by injecting active power during transient. This transient power is absorbed from the ZONE 1 through VSC1. The DC bus voltage is also kept within an acceptable range.

In the previous study, it is possible to support the frequency of ZONE 2 by activating the droop control in VSC 2. Considering the droop gain of 4% for VSC 2, a similar load change scenario at ZONE 2 is repeated. Simulation results are presented in Figure IV-35. It can be seen that the additional steady-state power that is injected from ZONE 1 to ZONE 2 has improved the steady-state frequency response in ZONE 2.

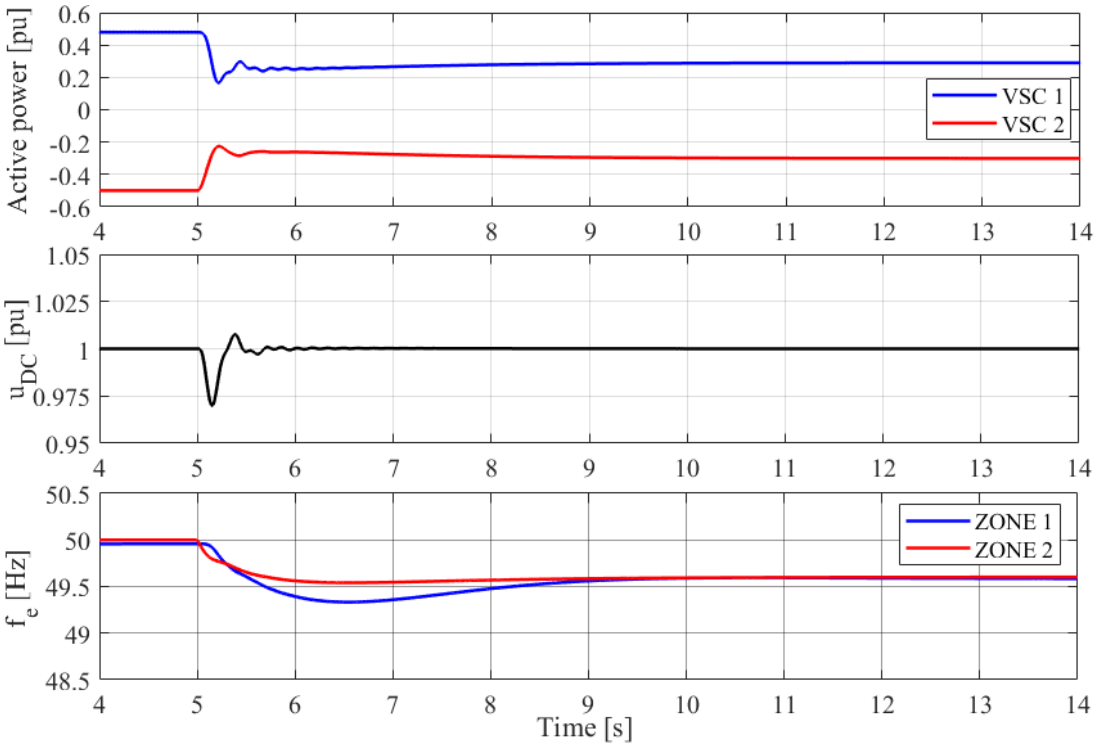

Figure IV-35: Active power of VSCs, frequencies and DC bus voltage in case of load change in ZONE 2 considering the frequency support by VSC 2.

The obtained results demonstrated that it is possible to control an HVDC link with two grid-forming converters at both substations. However, due to the contradiction between DC voltage control and inertial effect, the substation that controls the DC bus voltage has to be inertia-less. There is a similar contradictory effect between the DC voltage control and frequency support. Therefore, the substation that controls the DC bus cannot provide virtual inertia or frequency support for the area to which it is connected.

If the aim is to have an identical inertia support in both sides of an HVDC interconnection (which could be an essential need especially if the HVDC link connects two AC grids managed by different TSOs), the DC bus voltage needed be decoupled from inertia emulation task. One option is to add a third converter to the DC link. In this case, the DC voltage control task is given to this new converter and two existing converters will be providing the inertial support. Since the DC voltage is controlled by injecting/absorbing the active power to/from the DC link, an energy storage device is required to be integrated to the additional converter.

IV.5.3 Integration of a storage device to the DC bus

There are different storage system technologies including super capacitor [99], battery energy storage system (BESS) [100] and flywheel energy storage system (FESS) [98] that can be used for this application (see Figure IV-36). For the first two cases, a DC/DC step-up converter is needed to adapt the DC voltage levels. The FESS is considered as a rotating mass that stores some energy and it can be driven either by a permanent magnet synchronous generator (PMSM) or by an induction machine (IM) [98]. Therefore, an AC/DC converter is essential to connect the FESS to the DC bus of an HVDC interconnection.

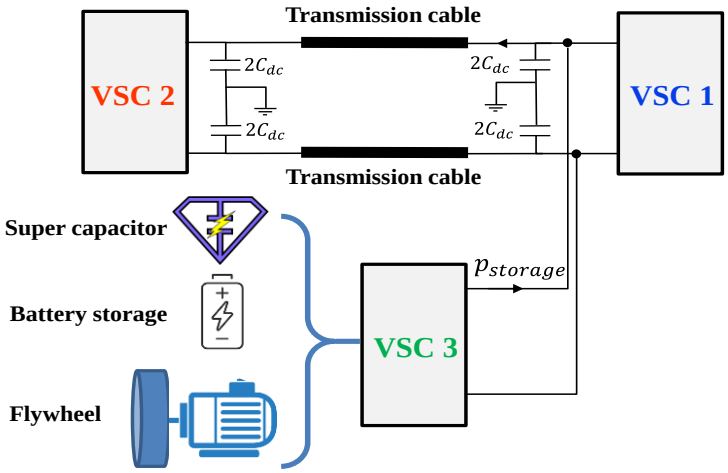

Figure IV-36: Various energy storage systems that could be integrated to the DC bus of an HVDC interconnection.

It should be noted that the comparison of investment and operational costs for different storage systems (installed either in the DC link of an HVDC interconnection or in the AC side (such as synchronous condenser)) is out of the scope of this work. The main purpose is to highlight that an HVDC link with grid-forming control in both substations for the aim of inertia provision is facing physical challenges that could be solved by, for example, integrating a storage device to the DC bus.

In this thesis, a FESS is used to support the DC bus of an HVDC interconnection, so that the two HVDC substation can take the required energy for the inertial support provision from the FESS. It should be mentioned that the main aim of this section is not evaluating the detailed modeling and control of an FESS, which has been widely studied in the literature [98], [101], [102], but giving an idea about how to size this kind of system. Hence, a simplified model of a rotating mass to derive an equivalent flywheel rotational speed is utilized.

IV.5.3.1 Simplified model for a FESS

Considering that the required power to regulate the DC bus voltage is p_{DC}^{*} (in per-unit) and is given by the DC voltage controller, the output of the DC voltage controller is proposed to be divided to two components (see Figure IV-37).

- One transient component that is sent to the FESS
- The other component is transmitted to the VSC1. It represents the steady-state component.

The two components are calculated by some first-order filters with the time constant of τ. The sum of both components is one. The chosen value for the parameter τ determines how much power is injected/absorbed from the FESS during transient. In steady-state, the VSC 1 controls the DC bus voltage. According to Figure IV-37, a simple rotating mass model is used to derive the flywheel speed. The flywheel power reference p_{fly}^{*} is given by:

$$p_{fly}^{*} = p_{DC} \cdot \frac{P_n}{P_{n_{fly}}}, \tag{IV-34}$$

where, P_n and $P_{n_{fly}}$ are the nominal power of the HVDC interconnection and the FESS, respectively. The flywheel speed can be derived from the well-known swing equation:

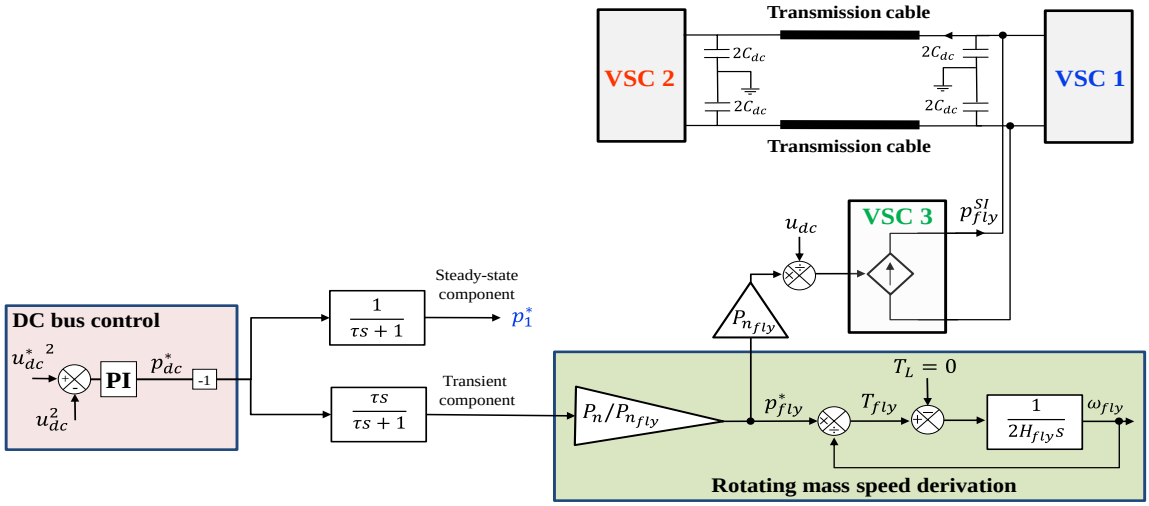

Figure IV-37: A simplified model of a FESS integrated to the DC bus of an HVDC interconnection.

$$T_{fly} - T_L = 2H_{fly}\frac{d(\omega_{fly})}{dt}, \tag{IV-35}$$

where, $T_{fly} = P_{fly}^*/\omega_{fly}$ is the flywheel torque, T_L is the load torque that is zero and H_{fly} is the rotational inertia of the flywheel.

IV.5.3.2 Sizing of the storage system

In order to have a proper control of the DC bus voltage, the AC power variation Δp at each substation needs to be well supported by the storage system. This means that, ideally, FESS has to be sized according to the maximum AC power variation ΔP_{max}. Focusing on the dynamic equation of the IP-control scheme adopted to VSC1/VSC2 ($\Delta p^* = 0$):

$$\Delta\omega_m = -\left[\frac{1}{2Hs} + k_p\right]\Delta p \tag{IV-36}$$

If the damping term k_p is neglected:

$$\Delta p = -\frac{2H}{f_0}\frac{d(\Delta f_m)}{dt}, \tag{IV-37}$$

where f_m is the internal frequency of the VSC in Hertz. The term $\frac{d(\Delta f_m)}{dt}$ is known as the rate of change of frequency (RoCoF). Considering that the maximum RoCoF is an available information (e.g., by transmission system operators (TSOs)). For a given maximum RoCoF, the maximum power variation is obtained by:

$$\Delta P_{max} = -\frac{2H}{f_0}RoCoF_{max}. \tag{IV-38}$$

ΔP_{max} determines the size of the FESS. If the damping term is not negligible:

$$\Delta P_{max} = -\frac{2H}{f_0}RoCoF_{max} - 2Hk_p\frac{d(\Delta p)}{dt} \tag{IV-39}$$

Considering an AC load connection that causes a positive power variation during first few seconds of transient and a negative RoCoF, the first term of (IV-39) is positive and its second term is negative. Therefore, the power variation is less than expected due to the damping term. The same analysis in case of an AC load shedding implies that the damping effect reduces the injected power corresponds to a given RoCoF in transient. Therefore, the sizing of the FESS according to (IV-38) induces a bit of oversizing depending on the tuning of the IP-control-based grid-forming converter at each HVDC substation.

IV.5.3.3 Simulation results

- Load step in Zone 2:

As an illustrative example, assuming that $RoCoF_{max} = -1.5$ [Hz/s], and $H = 5$ [s], then according to (IV-38) the maximum power variation is $\Delta P_{max} = 0.3$ p.u. Therefore, the FESS is sized to the same value ($P_{n_{fly}} = 300$ [MW]). The flywheel inertia is $H_{fly} = 5$ [s] and the DC voltage control response time is 150 [ms]. In the simulation environment, initially, 500 MW of power is transferring from the ZONE 2 to ZONE 1. A step of 0.4 [p.u.] is applied to the load in ZONE 2 at t=5 [s] in order to reach $RoCoF_{max} = -1.5$ [Hz/s]. The damping ratio of the both grid-forming VSC 1 and VSC 2 is $\zeta = 0.7$.

The results of this case study are given in Figure IV-38 for two different values of τ. In both cases, can be seen that the maximum power variation of VSC 2 (red curves) is less than the theoretical value due to the damping effect. The DC bus is well controlled and the frequency behavior is the same in ZONE 2 (same frequency nadir (49 [Hz])).

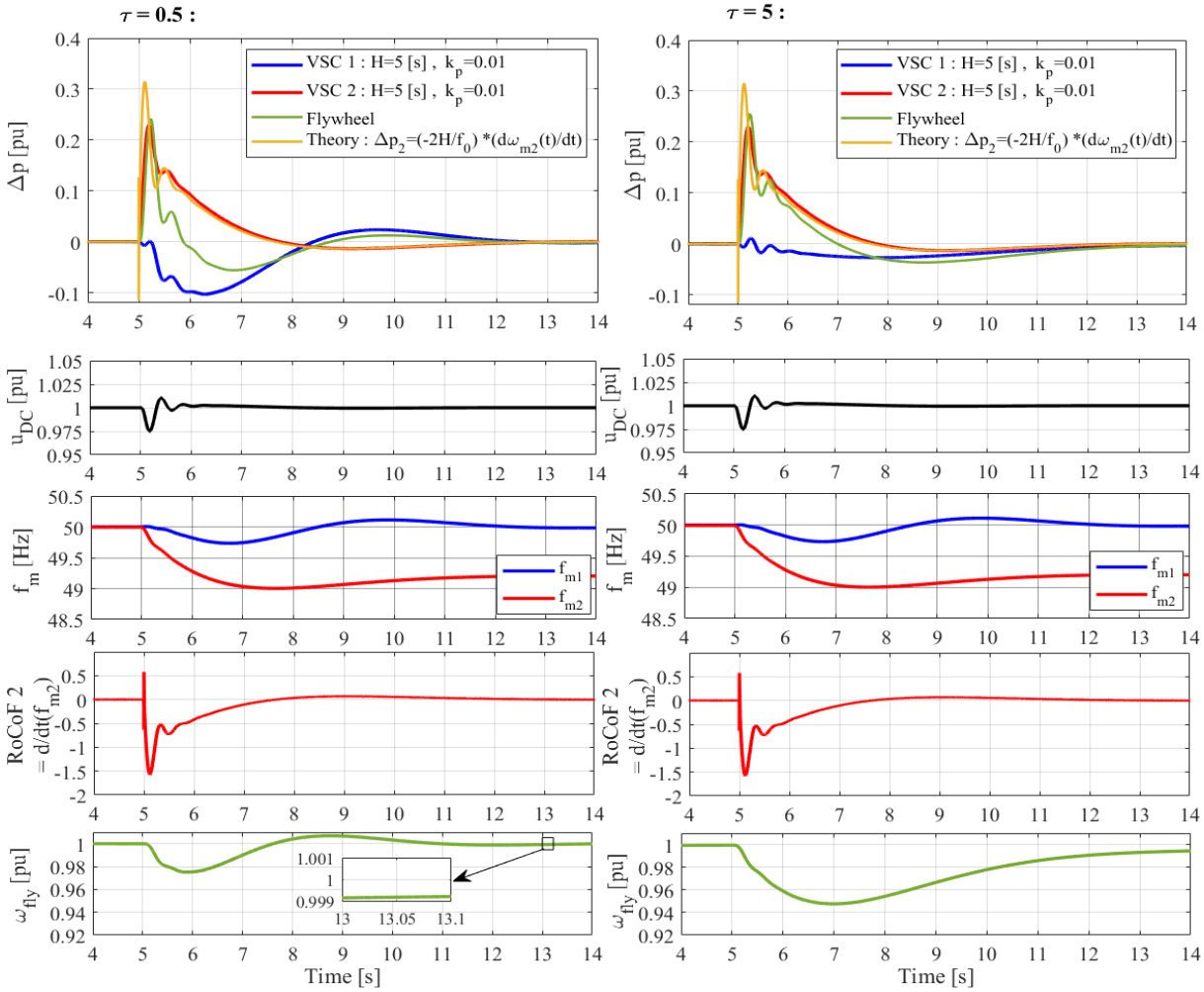

Figure IV-38: Responses to the load disturbance in ZONE 2 considering the damping ratio of $\zeta = 0.7$ for both substations.

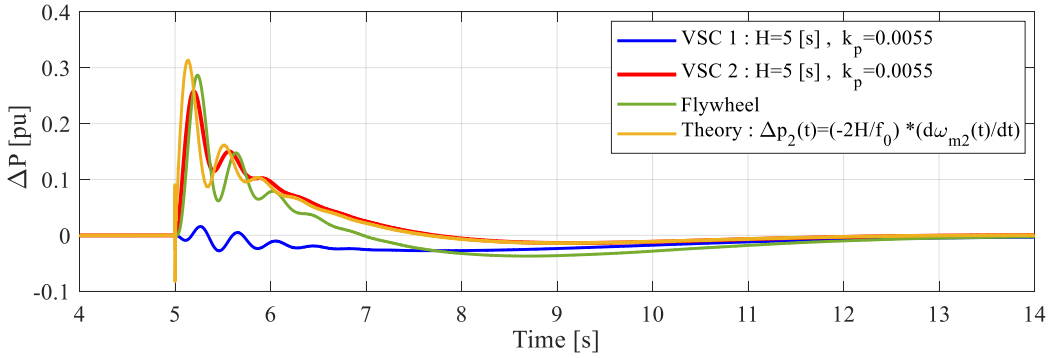

Figure IV-39: Power responses to the load disturbance in ZONE 2 considering the damping ratio of $\zeta = 0.5$ for both substations.

In fact, the power needed for providing inertial effect, with the classical shape, to the ZONE 2 is absorbed from both FESS and ZONE 1. The difference is that when using a bigger τ the participation of the FESS to the supplied power is enhanced. Hence, the active power variation curve of the FESS in this case is much closer to the one for VSC 2 and the power variation of VSC 1 become closer to zero. Clearly, more energy is absorbed from the FESS and its speed drops more. A slow speed regulator can be implemented to recover the flywheel speed to its nominal value. The flywheel's maximum transient power is higher than the VSC 2. This is due to a delay induced by the DC control response time. It is noted that the maximum power provided by the FESS is slightly less than the expected theoretical value.

In order to see the impact of damping on the proposed sizing of the FESS, the same study as previously is performed with a low damping ratio of $\zeta = 0.5$ at each substation ($\tau = 5$). In this case, as shown in Figure IV-39, the peak power of VSC 2 and, accordingly, the FESS is increased. However, the FESS maximum transient power is still slightly less that the theoretical value. The obtained results highpoint the proposed simple idea to size the FESS integrated to an HVDC interconnection based on a maximum RoCoF.

It should be mentioned that in previous examples, where the inertia support provided by HVDC substations is based on $H = 5$ [s], the calculated size of the FESS is quite large (0.3 p.u.). If the HVDC owner tends to utilize a smaller storage system for inertia provision, the maximum transient AC power needs to be reduced and this can be done by reducing the inertia constant of the substations. For instance, assuming: $RoCoF_{max} = -1.5$ [Hz/s], and $H = 2.5$ [s], then according to (IV-37) the maximum power variation is $\Delta P_{max} = 0.15$ p.u. Therefore, the FESS is sized 0.15 p.u.

- Load step in Zone 1:

Contrary to the previous study where the tuning of τ did not affect the inertial response provided by the VSC 2 to ZONE 2, in this case since the VSC 1 is also participating in the DC bus voltage control, its active power and accordingly its provided inertial response to ZONE 1 is affect by the value of τ. Since the dynamics of VSC 2 are nearly decoupled from the DC bus voltage, the only source of power to support the ZONE 1 frequency is the FESS.

Considering the previous simulation parameters ($RoCoF_{max} = -1.5$ [Hz/s], $H = 5$ [s], $H_{fly} = 5$ [s], $\zeta = 0.7$, DC voltage control response time = 150 [ms]), initially, 500 MW of power is transferred from the ZONE 2 to ZONE 1. A step of 0.4 [p.u.] is applied

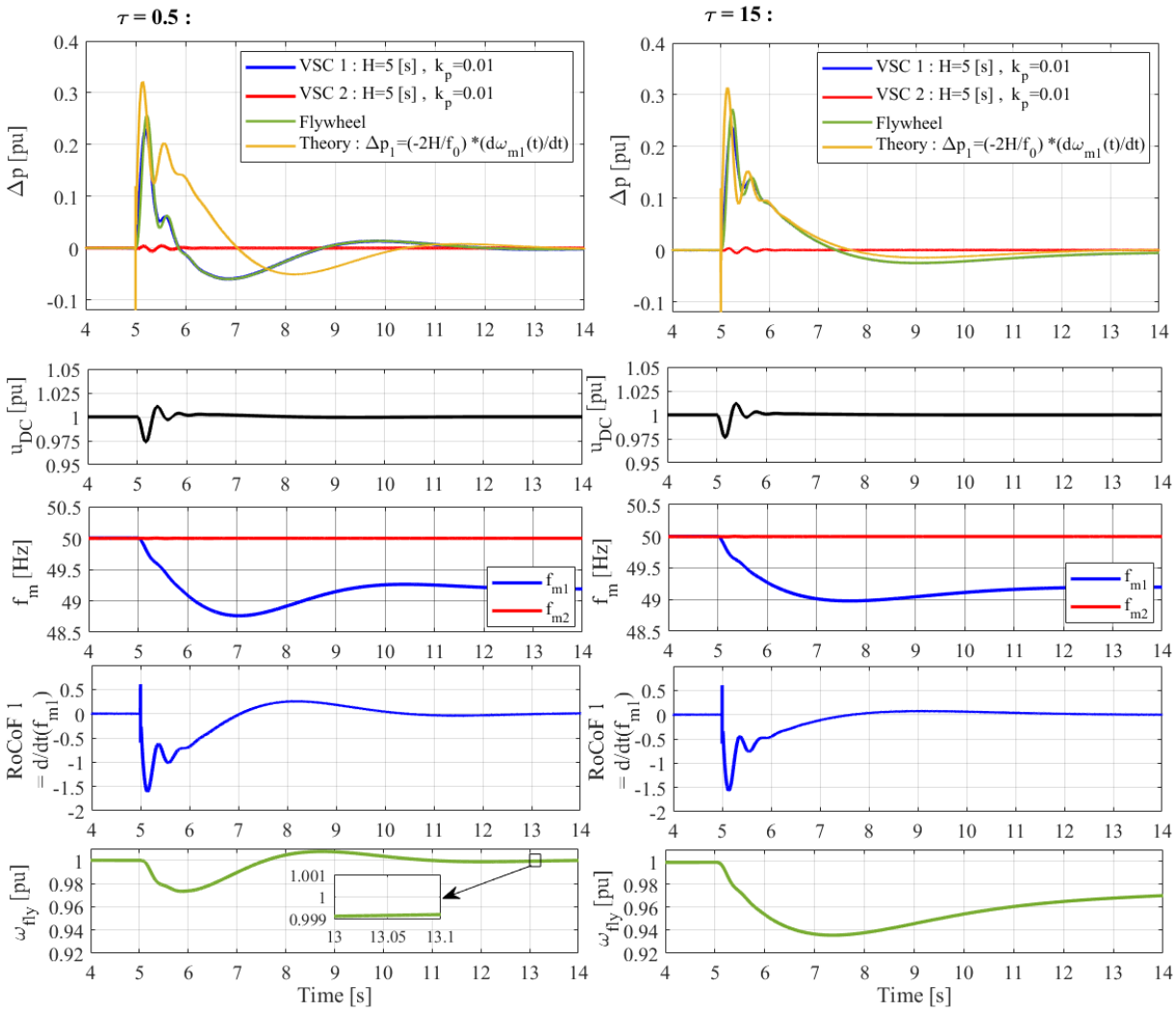

Figure IV-40: Responses to the load disturbance in ZONE 1.

to the load in ZONE 1 at t=5 [s]. The results of this case study are given in Figure IV-40 for two different values of τ. It can be clearly seen that with a small value of τ, there is not a proper participation of the FESS in providing the active power to support the frequency at ZONE 1. Therefore, the frequency nadir is lower than the previous cases (49 [Hz]). Once asking for more energy from the FESS by selecting $\tau = 15$, the classical active power shape corresponds to the inertial effect is obtained. In this case, the flywheel speed drops more. The frequency nadir in ZONE 1 is improved.

IV.6 Conclusions

This chapter investigated the dynamic performance of a grid-forming MMC. It was demonstrated that the stored energy in the MMC interacts with the active power response when the internal energy is not controlled. Moreover, it was highlighted that the dynamic behavior of the active power in an energy-controlled MMC is similar to an equivalent 2-level VSC not only in normal voltage control operation mode, but also when the MMC switches to the current control mode in response to the grid faults. In summary, all the dynamic studies conducted in previous chapters (Chapter 2 and 3) can

be generalized to an MMC topology. In the last part of the chapter, the inertia provision by an HVDC interconnection was evaluated. It was demonstrated that by controlling one HVDC substation with the inertia-less grid-forming converter (that controls the DC bus voltage) and controlling the other substation with high inertia grid-forming control (that manages the power flow through the HVDC link), it is possible to stabilize the system and have a proper inertial effect only in one side. However, if the aim is to have an identical inertial support at both substations, there is a conflicting effect between the inertia emulation and DC bus control. In this case, it was shown that neither the DC link is controlled very well, nor a proper inertial support is provided. To solve this issue, it was proposed to integrate a FESS to the HVDC link in order to control the DC bus voltage, so that the two substations can provide the inertial support straightforwardly. Finally, a simplified approach to size the FESS was proposed.

Chapter V: General conclusions and future works

V-I General conclusions

The rapid development of intermittent renewable generation and HVDC links yields a significant increase in the penetration rate of the power electronic converters in transmission systems. This modifies the foundation of today's power system operation and control. In this scenario, some grid-connected converters should act as AC voltage sources. These converters require different control laws in order to respond to the system needs, and to allow a stable operation during large disturbances. This thesis focuses on the grid-forming control principle used for power electronic converters connected to a transmission system. The key elements of this work are the development of some fundamental explanations of the grid-forming concept, which help to identify several control variants, as well as the protection algorithms. In the following, the main chapter conclusions are summarized:

1- Chapter 2 presents the fundamental of active power control in a power electronic converter with a voltage source behavior. From that, two different solutions, namely PLL-based and IP-control, are proposed and the corresponding quasi-static models are developed in order to explain their dominant dynamics. It is demonstrated that several other grid-forming variants could be derived from the proposed approach and they can be classified in four fundamentally different groups. From the small-signal stability and robustness point of view, the studied grid-forming controls in this chapter show their ability to operate under very weak grid conditions. Moreover, the ancillary services such as inertial response and frequency support can be appropriately provided to the AC grid.

2- Chapter 3 deals with the current limitation and transient stability of the grid-forming converters. Two general approaches for the current limitation that are virtual impedance and reference current saturation are addressed. It is highlighted that the choice of the current limiting strategy influences the performance of the grid-forming converter in terms of resynchronization to the AC grid after a large disturbance. A comprehensive analysis on the post-fault synchronization of the grid-forming converter while embedding a current reference saturation strategy is then provided. The impact of the current reference angle on the transient stability is investigated. In case of a balanced voltage sag, analytical formulas to estimate the critical clearing angle and critical clearing time while considering different values of the current reference angle are derived. It is demonstrated that the choice of this angle is constrained by the ability of the power converter to switch back to the voltage control mode. Based on that, its optimal value that enhances the transient stability and allows a switching from the saturated current control mode to the voltage control mode is calculated. Thereafter, the effectiveness of this optimal choice to guarantee the stability in case of a phase shift caused by a line re-closing event is verified.

3- Chapter 4 mainly covers the extension of the dynamic studies, which are conducted on a 2-level VSC topology in previous chapter, to an MMC topology. It is demonstrated that the dynamic behavior of an MMC with internal energy control is similar to an equivalent 2-level VSC, not only in normal voltage control operation mode, but also when the MMC switches to the current control mode in response to the grid faults. This is helpful to simplify the analysis by avoiding several MMC dynamics that are not dominant. According to this conclusion, by considering a simplified equivalent 2-level VSC, an HVDC link interconnecting two AC areas is modeled in order to assess the inertia provision by controlling the HVDC converters with the grid-forming strategy. It is shown that the grid-forming converter can provide the inertia if it is not responsible for the DC bus voltage control. This is due to a fundamental conflict between both control tasks. If the aim is to have an identical inertial support at both substations, it is proposed to integrate a storage element to the HVDC link to control the DC bus voltage so that the two substations can provide the inertial support straightforwardly.

V-II Recommendations for future works

Below is the orientation of some timely topics to continue this work and explore further:

- Impact of different types of loads on the control performance: studies on different kinds of loads such as motor loads and non-linear loads are missing from this work. Actually, non-linear loads induce harmonics, which may affect the control performances.

- Unbalance conditions: this aspect has not been studied in this PhD. Recently a new research work from SINTEF, which is one of the academic participants in the HVDC inertia provision project, is published where this topic is discussed. In this work, beside the fact that a VSM-based grid-forming control is used for the synchronization and active power control, a current control loop considering a virtual impedance is implemented to regulate the converter current (introduced as the current controlled VSM or CCVSM). Existence of a current control loop in grid-forming control may modify slightly its performance under normal voltage control operation mode; however, it can have a major impact under unbalance conditions. A similar virtual current loop could be added to the proposed grid-forming strategies in this thesis and the control performance for a group of various standard unbalanced scenarios should be assessed.

- Current limitation: this point is a significant challenge under unbalanced grid conditions that could be considered in the future works.

- Transient stability: the proposed method to enhance the transient stability in Chapter 3 is based on using a constant optimal value of the saturated current reference angle. It is worthy to investigate on the dynamic management of this angle, more specifically with respect to the grid voltage recovery behavior after the fault. Moreover, the effect of using different current limiting strategies (i.e.

current saturation algorithm and virtual impedance) on transient stability in case of various grid events should be compared.

- Multi-converter environment: extension of the conducted studies to a multi-converter connected to the same AC system is missing from this work.

- HVDC link with grid-forming control: the challenge is when both sides of the HVDC interconnection need a high inertial support. In this case, an additional source of energy is required. From the academic and industrial point of view, what kind of storage capacity should be integrated to an HVDC interconnection in near future is still a matter of debate. Depending on the advancement of technology, three solutions including a FESS driven by a machine and connected with an AC/DC converter to the DC bus, a BESS connected by as DC/DC converter to the DC bus and, integrating super for example inside the MMC submodules could be considered and studied. Of course, avoiding new investments and using the capacity of the current system as much as possible is always a priority. Hence, developing more advanced control strategies to handle this problem with minimum costs is an open issue. The studies on this topic could be extended to multi-terminal DC (MTDC) systems.

References:

[1] B. Kroposki *et al.*, "Achieving a 100% Renewable Grid: Operating Electric Power Systems with Extremely High Levels of Variable Renewable Energy," *IEEE Power Energy Mag.*, vol. 15, no. 2, pp. 61–73, Mar. 2017.

[2] S. K. Chaudhary, R. Teodorescu, and P. Rodriguez, "Wind Farm Grid Integration Using VSC Based HVDC Transmission - An Overview," in *IEEE Energy2030*, 2008.

[3] W. Zappa, M. Junginger, and M. van den Broek, "Is a 100% renewable European power system feasible by 2050?," *Appl. Energy*, vol. 233–234, pp. 1027–1050, Jan. 2019.

[4] E. Rokrok, M. Shafie-khah, and J. P. S. Catalão, "Review of primary voltage and frequency control methods for inverter-based islanded microgrids with distributed generation," *Renew. Sustain. Energy Rev.*, vol. 82, pp. 3225–3235, 2018.

[5] A. Ulbig, T. S. Borsche, and G. Andersson, "Impact of low rotational inertia on power system stability and operation," *IFAC Proc. Vol.*, vol. 19, pp. 7290–7297, 2014.

[6] ENTSO-E, "High Penetration of Power Electronic Interfaced Power Sources (HPoPEIPS)," [Online] Available: https://consultations.entsoe.eu/system-development/entso-e-connection-codes-implementation-guidance-d-3/, 2017.

[7] P. Tielens, P. Henneaux, and S. Cole, "Penetration of renewables and reduction of synchronous inertia in the European power system – Analysis and solutions," Advanced System Studies for Energy Transition (ASSET) project, [Online] Available: https://asset-ec.eu/wp-content/uploads/2018/12/EC_EUES_4NT_0631748_000_01_NTE.pdf, 2018.

[8] A. Adib, B. Mirafzal, X. Wang, and R. Blaabjerg, "On stability of voltage source inverters in weak grids," *IEEE Access*, vol. 6, pp. 4427–4439, Jan. 2018.

[9] G. Denis, "From grid-following to grid-forming: The new strategy to build 100 % power-electronics interfaced transmission system with enhanced transient behavior," PhD thesis, Ecole Centrale de Lille, Nov., 2017.

[10] Y. Wang, V. Silva, and M. Lopez-Botet-zulueta, "Impact of high penetration of variable renewable generation on frequency dynamics in the continental Europe interconnected system," *IET Renew. Power Gener.*, vol. 10, no. 1, pp. 10–16, Jan. 2016.

[11] K. Visscher and S. W. H. De Haan, "Virtual synchronous machines (VSG'S) for frequency stabilisation in future grids with a significant share of decentralized generation," in *CIRED Seminar 2008: SmartGrids for Distribution*, 2008.

[12] J. Rocabert, A. Luna, F. Blaabjerg, and P. Rodríguez, "Control of power converters in AC microgrids," *IEEE Trans. Power Electron.*, vol. 27, no. 11, pp. 4734–4749, 2012.

[13] Y. Lin *et al.*, "Research Roadmap on Grid-Forming Inverters," Technical Report, National Renewable Energy Laboratory (NREL), , 2020. [Online] Available: https://www.nrel.gov/docs/fy21osti/73476.pdf.

[14] ENTSO-E, "Grid-Forming Capabilities : Towards System Level Integration," Technical Report, March, 2021. [Online] Available: https://eepublicdownloads.entsoe.eu/clean-documents/RDC%20documents/210331_Grid%20Forming%20Capabilities.pdf.

[15] P. Unruh, M. Nuschke, P. Strauß, and F. Welck, "Overview on grid-forming inverter control methods," *Energies*, vol. 13, no. 10, 2020.

[16] R. Rosso, X. Wang, M. Liserre, X. Lu, and S. Engelken, "Grid-Forming Converters: Control Approaches, Grid-Synchronization, and Future Trends—A Review," *IEEE Open J. Ind. Appl.*, vol. 2, pp. 93–109, Apr. 2021.

[17] K. De Brabandere, B. Bolsens, J. Van den Keybus, A. Woyte, J. Driesen, and R. Belmans, "A voltage and frequency droop control method for parallel inverters," *IEEE Trans. Power Electron.*, vol. 22, no. 4, pp. 1107–1115, Jul. 2007.

[18] L. Zhang, L. Harnefors, and H. Nee, "Power-Synchronization Control of Grid-

Connected Voltage-Source Converters," *IEEE Trans. Power Syst.*, vol. 25, no. 2, pp. 809–820, 2010.
[19] L. Harnefors, M. Hinkkanen, U. Riaz, F. M. M. Rahman, and L. Zhang, "Robust analytic design of power-synchronization control," *IEEE Trans. Ind. Electron.*, vol. 66, no. 8, pp. 5810–5819, Aug. 2019.
[20] Q. C. Zhong and G. Weiss, "Synchronverters: Inverters that mimic synchronous generators," *IEEE Trans. Ind. Electron.*, vol. 58, no. 4, pp. 1259–1267, Apr. 2011.
[21] S. D'Arco and J. A. Suul, "Virtual synchronous machines - Classification of implementations and analysis of equivalence to droop controllers for microgrids," *2013 IEEE Grenoble Conf. PowerTech, POWERTECH 2013*, no. June 2013, 2013.
[22] A. J. Roscoe *et al.*, "A VSM (virtual synchronous machine) convertor control model suitable for RMS studies for resolving system operator/owner challenges," in *15th Wind Integration Workshop*, 2016.
[23] M. Ndreko, S. Rüberg, and W. Winter, "Grid forming control scheme for power systems with up to 100% power electronic interfaced generation: A case study on Great Britain test system," *IET Renew. Power Gener.*, vol. 14, no. 8, pp. 1268–1281, 2020.
[24] C. Arghir, T. Jouini, and F. Dörfler, "Grid-forming control for power converters based on matching of synchronous machines," *Automatica*, vol. 95, pp. 273–282, 2018.
[25] F. Palombi, L. Piegari, S. D'Arco, A. G. Endegnanew, and J. A. Suul, "Impact on Power System Frequency Dynamics from an HVDC Transmission System With Converter Stations Controlled as Virtual Synchronous Machines," in *2019 IEEE Milan PowerTech*, 2019, pp. 1–6.
[26] J. Chen, M. Liu, F. Milano, and T. O'Donnell, "100% Converter-Interfaced generation using virtual synchronous generator control: A case study based on the irish system," *Electr. Power Syst. Res.*, vol. 187, p. 106475, Oct. 2020.
[27] P. Marinakis and N. Schofield, "Grid Forming Control for Power Systems with up to 100% Inverter Based Generation," *9th Renew. Power Gener. Conf. (RPG Dublin Online 2021)*, pp. 143–148, 2021.
[28] H. M. A. Antunes, S. M. Silva, D. I. Brandao, A. A. P. Machado, and R. V. Ferreira, "A fault-tolerant grid-forming converter applied to AC microgrids," *Int. J. Electr. Power Energy Syst.*, vol. 121, p. 106072, Oct. 2020.
[29] O. Schömann *et al.*, "Experience with Large Grid-Forming Inverters on Various Island and Microgrid Projects," *4th Int. Hybrid Power Syst. Work.*, no. May, pp. 0–4, 2019.
[30] A. Roscoe *et al.*, "Response of a grid forming wind farm to system events, and the impact of external and internal damping," *IET Renew. Power Gener.*, vol. 14, no. 19, pp. 3908–3917, 2020.
[31] A. Roscoe *et al.*, "Practical experience of providing enhanced grid forming services from an onshore wind park," *19th Wind Integr. Work.*, 2020.
[32] "Gamesa Electric at La Plana Hybrid Pilot Plant - Gamesa Electric." [Online]. Available: https://www.gamesaelectric.com/gamesa-electric-at-siemens-gamesas-la-plana-hybrid-pilot-plant/.
[33] Siemens Gamesa, "Siemens Gamesa hybrid solutions Leading the way to a renewables powered future ," in *4 th International Hybrid Power Systems Workshop*, 2019.
[34] "OSMOSE Project." [Online]. Available: https://www.osmose-h2020.eu/.
[35] "OSMOSE Project - WP3: Grid Forming for the synchronization of large power systems by multi-service hybrid storage." [Online]. Available: https://www.osmose-h2020.eu/project-overview/wp3/.
[36] "OSMOSE Project - WP3 - Deliverable D3.3 : Analysis of the synchronization capabilities of BESS power converters." [Online]. Available: https://www.osmose-h2020.eu/wp-content/uploads/2022/03/OSMOSE-D3.3-Analysis-of-the-

synchronisation-capabilities-of-BESS-power-converters.pdf.
[37] “Fluence, Siemens and Litgrid Partner on Baltics’ First Storage as Transmission Pilot Project.” [Online]. Available: https://blog.fluenceenergy.com/fluence-siemens-litgrid-partner-baltics-first-storage-as-virtual-transmission-pilot-project.
[38] “ENTSO-E: TYNDP 2018.” [Online]. Available: https://tyndp.entsoe.eu/tyndp2018/.
[39] “HVDC Inertia Provision Project.” [Online]. Available: https://www.sintef.no/en/projects/2017/hvdc-inertia-provision/.
[40] T. Qoria, “Grid-forming control to achieve a 100% power electronics interfaced power transmission systems,” PhD thesis, HESAM Université, École Nationale Supérieure d’Arts et Métiers, November, 2020.
[41] J. J. Grainger and W. D. Stevenson, *Power system analysis*. New York: McGraw-Hill, 1994.
[42] J. Freytes, P. Rault, F. Gruson, F. Colas, and X. Guillaud, “Dynamic impact of MMC controllers on DC voltage droop controlled MTDC grids,” *2016 18th Eur. Conf. Power Electron. Appl. EPE 2016 ECCE Eur.*, Oct. 2016.
[43] N. R. Ullah, T. Thiringer, and D. Karlsson, “Voltage and transient stability support by wind farms complying with the E.ON netz grid code,” *IEEE Trans. Power Syst.*, vol. 22, no. 4, pp. 1647–1656, Nov. 2007.
[44] European Union, “Commission Regulation (Eu) 2016/631,” *Off. J. Eur. Union*, no. 14 April 2016, p. 68, 2016.
[45] A. T. Qoria, Q. Cossart, C. Li, and X. Guillaud, “MIGRATE Project, WP3 - Control and Operation of a Grid with 100 % Converter-Based Devices, Deliverable 3 . 2 : Local control and simulation tools for large transmission systems,” 2019.
[46] S. D’Arco, J. A. Suul, and O. B. Fosso, “Automatic Tuning of Cascaded Controllers for Power Converters Using Eigenvalue Parametric Sensitivities,” *IEEE Trans. Ind. Appl.*, vol. 51, no. 2, pp. 1743–1753, 2015.
[47] S. D’Arco and J. A. Suul, “Equivalence ofVirtual Synchronous Machines and Frequency-Droops for Converter-Based MicroGrids,” *IEEE Trans. Smart Grid*, vol. 5, no. 1, pp. 394–395, 2014.
[48] T. Qoria, F. Gruson, F. Colas, X. Guillaud, M. S. Debry, and T. Prevost, “Tuning of cascaded controllers for robust grid-forming voltage source converter,” *20th Power Syst. Comput. Conf. PSCC 2018*, pp. 1–7, 2018.
[49] IEEE Power and Energy Society, “IEEE Recommended Practice and Requirements for Harmonic Control in Electric Power Systems,” *IEEE Stand.*, 2014.
[50] IEEE Power Engineering Society, *IEEE Guide for Planning DC Links Terminating at AC Locations Having Low Short-Circuit Capacities*. ISBN 1-55937-936-7, 1997.
[51] J. Driesen and K. Visscher, “Virtual synchronous generators,” *IEEE Power Energy Soc. 2008 Gen. Meet. Convers. Deliv. Electr. Energy 21st Century, PES*, 2008.
[52] J. Liu, Y. Miura, and T. Ise, “Comparison of Dynamic Characteristics between Virtual Synchronous Generator and Droop Control in Inverter-Based Distributed Generators,” *IEEE Trans. Power Electron.*, vol. 31, no. 5, pp. 3600–3611, May 2016.
[53] M. Yu *et al.*, “Use of an inertia-less Virtual Synchronous Machine within future power networks with high penetrations of converters,” *19th Power Syst. Comput. Conf. PSCC 2016*, Aug. 2016.
[54] R. Rosso, J. Cassoli, G. Buticchi, S. Engelken, and M. Liserre, “Robust Stability Analysis of LCL Filter Based Synchronverter Under Different Grid Conditions,” *IEEE Trans. Power Electron.*, vol. 34, no. 6, pp. 5842–5853, Jun. 2019.
[55] Z. Li, C. Zang, P. Zeng, H. Yu, S. Li, and J. Bian, “Control of a grid-forming inverter based on sliding-mode and mixed H2/H∞ control,” *IEEE Trans. Ind. Electron.*, vol. 64, no. 5, pp. 3862–3872, May 2017.

[56] W. E. Boyce, R. C. DiPrima, and D. B. Meade, *Boyce's elementary differential equations and boundary value problems*. 11th Edition, WILEY, 2017.
[57] S. D'Arco, J. A. Suul, and O. B. Fosso, "A Virtual Synchronous Machine implementation for distributed control of power converters in SmartGrids," *Electr. Power Syst. Res.*, vol. 122, pp. 180–197, 2015.
[58] E. Rokrok, T. Qoria, A. Bruyere, B. Francois, and X. Guillaud, "Classification and dynamic assessment of droop-based grid-forming control schemes: Application in HVDC systems," *Electr. Power Syst. Res.*, vol. 189, p. 106765, Dec. 2020.
[59] E. Rokrok, T. Qoria, A. Bruyere, B. Francois, and X. Guillaud, "Effect of Using PLL-Based Grid-Forming Control on Active Power Dynamics under Various SCR," *IECON Proc. (Industrial Electron. Conf.*, vol. 2019-October, pp. 4799–4804, Oct. 2019.
[60] T. Qoria, F. Gruson, F. Colas, G. Denis, T. Prevost, and X. Guillaud, "Inertia effect and load sharing capability of grid forming converters connected to a transmission grid," in *15th IET International Conference on AC and DC Power Transmission (ACDC 2019)*, 2019, pp. 79 (6 pp.)-79 (6 pp.).
[61] I. Sadeghkhani, M. E. H. Golshan, J. M. Guerrero, and A. Mehrizi-Sani, "A Current Limiting Strategy to Improve Fault Ride-Through of Inverter Interfaced Autonomous Microgrids," *IEEE Trans. Smart Grid*, vol. 8, no. 5, pp. 2138–2148, Sep. 2017.
[62] G. Denis, T. Prevost, M.-S. Debry, F. Xavier, X. Guillaud, and A. Menze, "The Migrate project: the challenges of operating a transmission grid with only inverter-based generation. A grid-forming control improvement with transient current-limiting control," *IET Renew. Power Gener.*, vol. 12, no. 5, pp. 523–529, 2018.
[63] D. Gros and F. Dorfler, "Projected grid-forming control for current-limiting of power converters," *57th Annu. Allert. Conf. Commun. Control. Comput. Allert.*, pp. 326–333, 2019.
[64] A. Tayyebi, D. Grob, A. Anta, F. Kupzog, and F. Dorfler, "Frequency Stability of Synchronous Machines and Grid-Forming Power Converters," *IEEE J. Emerg. Sel. Top. Power Electron.*, vol. 8, no. 2, pp. 1004–1018, 2020.
[65] M. G. Taul, X. Wang, P. Davari, and F. Blaabjerg, "Current Limiting Control with Enhanced Dynamics of Grid-Forming Converters during Fault Conditions," *IEEE J. Emerg. Sel. Top. Power Electron.*, vol. 8, no. 2, pp. 1062–1073, 2020.
[66] L. Huang, H. Xin, Z. Wang, L. Zhang, K. Wu, and J. Hu, "Transient Stability Analysis and Control Design of Droop-Controlled Voltage Source Converters Considering Current Limitation," *IEEE Trans. Smart Grid*, vol. 10, no. 1, pp. 578–591, Sep. 2017.
[67] A. D. Paquette and D. M. Divan, "Virtual Impedance Current Limiting for Inverters in Microgrids With Synchronous Generators," *IEEE Trans. Ind. Appl.*, vol. 51, no. 2, pp. 1630–1638, Mar. 2015.
[68] T. Qoria *et al.*, "Tuning of AC voltage-controlled VSC based linear quadratic regulation," in *2019 IEEE Milan PowerTech*, 2019.
[69] H. Wu and X. Wang, "Design-oriented transient stability analysis of grid-connected converters with power synchronization control," *IEEE Trans. Ind. Electron.*, vol. 66, no. 8, pp. 6473–6482, Aug. 2019.
[70] D. Pan, X. Wang, F. Liu, and R. Shi, "Transient Stability of Voltage-Source Converters with Grid-Forming Control: A Design-Oriented Study," *IEEE J. Emerg. Sel. Top. Power Electron.*, vol. 8, no. 2, pp. 1019–1033, Jun. 2020.
[71] T. Qoria, F. Gruson, F. Colas, X. Kestelyn, and X. Guillaud, "Current limiting algorithms and transient stability analysis of grid-forming VSCs," *Electr. Power Syst. Res.*, vol. 189, p. 106726, Dec. 2020.
[72] Z. Shuai, C. Shen, X. Liu, Z. Li, and Z. John Shen, "Transient angle stability of virtual synchronous generators using lyapunov's direct method," *IEEE Trans. Smart Grid*, vol.

10, no. 4, pp. 4648–4661, 2019.
[73] T. Qoria, F. Gruson, F. Colas, G. Denis, T. Prevost, and X. Guillaud, “Critical Clearing Time Determination and Enhancement of Grid-Forming Converters Embedding Virtual Impedance as Current Limitation Algorithm,” *IEEE J. Emerg. Sel. Top. Power Electron.*, vol. 8, no. 2, pp. 1050–1061, Jun. 2020.
[74] T. Qoria, E. Rokrok, A. Bruyere, B. Francois, and X. Guillaud, “A PLL-Free Grid-Forming Control with Decoupled Functionalities for High-Power Transmission System Applications,” *IEEE Access*, pp. 1–1, Oct. 2020.
[75] H. Xin, L. Huang, L. Zhang, Z. Wang, and J. Hu, “Synchronous Instability Mechanism of P-f Droop-Controlled Voltage Source Converter Caused by Current Saturation,” *IEEE Trans. Power Syst.*, vol. 31, no. 6, pp. 5206–5207, Nov. 2016.
[76] I. Erlich *et al.*, “New Control of Wind Turbines Ensuring Stable and Secure Operation Following Islanding of Wind Farms,” *IEEE Trans. Energy Convers.*, vol. 32, no. 3, pp. 1263–1271, Sep. 2017.
[77] X. Lu, J. Wang, J. M. Guerrero, and D. Zhao, “Virtual-impedance-based fault current limiters for inverter dominated AC microgrids,” *IEEE Trans. Smart Grid*, vol. 9, no. 3, pp. 1599–1612, May 2018.
[78] P. Kundur, N. Balu, and M. Lauby, *Power system stability and control*. New York: McGraw-hill, 1994.
[79] S. Samimi, F. Gruson, P. Delarue, F. Colas, M. M. Belhaouane, and X. Guillaud, “MMC Stored Energy Participation to the DC Bus Voltage Control in an HVDC Link,” *IEEE Trans. Power Deliv.*, vol. 31, no. 4, pp. 1710–1718, Aug. 2016.
[80] J. Freytes *et al.*, “Improving Small-Signal Stability of an MMC With CCSC by Control of the Internally Stored Energy,” *IEEE Trans. Power Deliv.*, vol. 33, no. 1, pp. 429–439, Feb. 2018.
[81] S. Samimi, “Modélisation et Commande des Convertisseurs MMC en vue de leur Intégration dans le Réseau Electrique,” PhD thesis, ECOLE CENTRALE DE LILLE, 2016.
[82] Q. Tu, Z. Xu, and L. Xu, “Reduced Switching-frequency modulation and circulating current suppression for modular multilevel converters,” *IEEE Trans. Power Deliv.*, vol. 26, no. 3, pp. 2009–2017, Jul. 2011.
[83] W. Tang, D. Jiang, R. Yin, Y. Wang, and Y. Zhou, “A novel CCSC for circulating current suppression in modular multilevel converters,” *IEEE Power Energy Soc. Gen. Meet.*, vol. 2016-November, Nov. 2016.
[84] C. Verdugo, J. I. Candela, and P. Rodriguez, “Grid support functionalities based on modular multilevel converters with synchronous power control,” in *2016 IEEE International Conference on Renewable Energy Research and Applications, ICRERA 2016*, 2017, pp. 572–577.
[85] O. D. Adeuyi *et al.*, “Frequency support from modular multilevel converter based multi-terminal HVDC schemes,” in *IEEE Power and Energy Society General Meeting*, 2015, vol. 2015-September.
[86] S. D’Arco, G. Guidi, and J. A. Suul, “Operation of a Modular Multilevel Converter Controlled as a Virtual Synchronous Machine,” in *2018 International Power Electronics Conference (IPEC-Niigata 2018 -ECCE Asia)*, 2018, pp. 782–789.
[87] S. D’Arco, T. T. Nguyen, and J. A. Suul, “Evaluation of Virtual Inertia Control Strategies for MMC-based HVDC Terminals by P-HiL Experiments,” *IECON Proc. (Industrial Electron. Conf.*, vol. 2019-Octob, pp. 4811–4818, 2019.
[88] G. Bergna *et al.*, “An energy-based controller for HVDC modular multilevel converter in decoupled double synchronous reference frame for voltage oscillation reduction,” *IEEE Trans. Ind. Electron.*, vol. 60, no. 6, pp. 2360–2371, 2013.

[89] S. Samimi, F. Gruson, P. Delarue, and X. Guillaud, “Synthesis of different types of energy based controllers for a modular multilevel converter integrated in an HVDC link,” *IET Semin. Dig.*, vol. 2015, no. CP654, pp. 1–7, 2015.
[90] P. Delarue, F. Gruson, and X. Guillaud, “Energetic macroscopic representation and inversion based control of a modular multilevel converter,” in *2013 15th European Conference on Power Electronics and Applications, EPE 2013*, 2013.
[91] K. Shinoda, J. Freytes, A. Benchaib, J. Dai, H. Saad, and X. Guillaud, “Energy Difference Controllers for MMC without DC Current Perturbations,” in *2nd International Conference on HVDC (HVDC2016 - CIGRE)*, 2016.
[92] F. Gruson *et al.*, “Design, implementation and testing of a Modular Multilevel Converter,” *EPE J. (European Power Electron. Drives Journal)*, vol. 27, no. 4, pp. 153–166, 2017.
[93] L. Zhang, L. Harnefors, and H.-P. Nee, “Power-Synchronization Control of Grid-Connected Voltage-Source Converters,” *IEEE Trans. Power Syst.*, vol. 25, no. 2, pp. 809–820, May 2010.
[94] J. Zhu, C. D. Booth, G. P. Adam, A. J. Roscoe, and C. G. Bright, “Inertia emulation control strategy for VSC-HVDC transmission systems,” *IEEE Trans. Power Syst.*, vol. 28, no. 2, pp. 1277–1287, 2013.
[95] E. Rakhshani and P. Rodriguez, “Inertia Emulation in AC/DC Interconnected Power Systems Using Derivative Technique Considering Frequency Measurement Effects,” *IEEE Trans. Power Syst.*, vol. 32, no. 5, pp. 3338–3351, Sep. 2017.
[96] M. Guan, W. Pan, J. Zhang, Q. Hao, J. Cheng, and X. Zheng, “Synchronous Generator Emulation Control Strategy for Voltage Source Converter (VSC) Stations,” *IEEE Trans. Power Syst.*, vol. 30, no. 6, pp. 3093–3101, Nov. 2015.
[97] R. Aouini, B. Marinescu, K. Ben Kilani, and M. Elleuch, “Synchronverter-Based Emulation and Control of HVDC Transmission,” *IEEE Trans. Power Syst.*, vol. 31, no. 1, pp. 278–286, Jan. 2016.
[98] M. I. Daoud, A. M. Massoud, A. S. Abdel-Khalik, A. Elserougi, and S. Ahmed, “A Flywheel Energy Storage System for Fault Ride Through Support of Grid-Connected VSC HVDC-Based Offshore Wind Farms,” *IEEE Trans. Power Syst.*, vol. 31, no. 3, pp. 1671–1680, May 2016.
[99] M. Farhadi and O. Mohammed, “Energy Storage Technologies for High-Power Applications,” *IEEE Trans. Ind. Appl.*, vol. 52, no. 3, pp. 1953–1962, May 2016.
[100] J. Guo, D. Jiang, Y. Zhou, P. Hu, Z. Lin, and Y. Liang, “Energy storable VSC-HVDC system based on modular multilevel converter,” *Int. J. Electr. Power Energy Syst.*, vol. 78, pp. 269–276, Jun. 2016.
[101] F. Díaz-González, A. Sumper, O. Gomis-Bellmunt, and F. D. Bianchi, “Energy management of flywheel-based energy storage device for wind power smoothing,” *Appl. Energy*, vol. 110, pp. 207–219, 2013.
[102] G. Cimuca, S. Breban, M. M. Radulescu, C. Saudemont, and B. Robyns, “Design and control strategies of an induction-machine-based flywheel energy storage system associated to a variable-speed wind generator,” *IEEE Trans. Energy Convers.*, vol. 25, no. 2, pp. 526–534, 2010.

Appendices

Appendix A

Clarke transformation:

Let's consider $\mathbf{f_{abc}} = [f_a \quad f_b \quad f_c]$ is a rotating vector in three-phase abc stationary frame. This vector can be expressed in the two-phase $\alpha\beta$ stationary frame as follows:

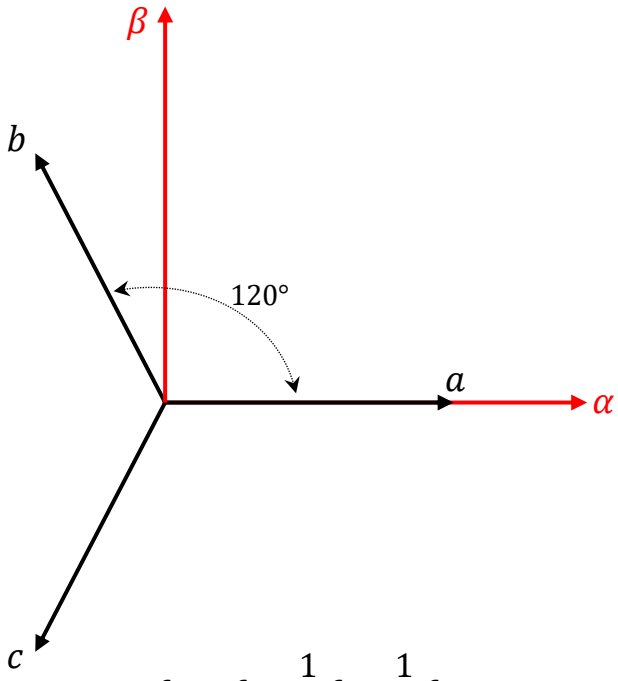

$$f_\alpha = f_a - \frac{1}{2}f_b - \frac{1}{2}f_c$$

$$f_\beta = 0f_a + \frac{\sqrt{3}}{2}f_b - \frac{\sqrt{3}}{2}f_c$$

$$\begin{bmatrix} f_\alpha \\ f_\beta \end{bmatrix} = K.\begin{bmatrix} 1 & -\frac{1}{2} & -\frac{1}{2} \\ 0 & \frac{\sqrt{3}}{2} & -\frac{\sqrt{3}}{2} \end{bmatrix}.\begin{bmatrix} f_a \\ f_b \\ f_c \end{bmatrix}$$

When going from a 3-phase to a 2-phase system, the total vector length need to be adapted by 2/3 to get the same length in both systems. Therefore: $K = \frac{2}{3}$.

$$T_{abc-\alpha\beta} = \frac{2}{3}.\begin{bmatrix} 1 & -\frac{1}{2} & -\frac{1}{2} \\ 0 & \frac{\sqrt{3}}{2} & -\frac{\sqrt{3}}{2} \end{bmatrix}$$

The classical Clarke transform is not power invariant, i.e., the instantaneous power of the variables calculated in the $\alpha\beta$ frame is not the same as the power calculated in the natural coordinate reference frame. The power invariant version of the $\alpha\beta$ transform is as follows:

$$T_{abc-\alpha\beta} = \sqrt{\frac{2}{3}} \cdot \begin{bmatrix} 1 & -\frac{1}{2} & -\frac{1}{2} \\ 0 & \frac{\sqrt{3}}{2} & -\frac{\sqrt{3}}{2} \end{bmatrix}$$

Park transformation:

Park transformation takes the vector $\mathbf{f_{\alpha\beta}} = [f_\alpha \quad f_\beta]$ along the stationary frame $\alpha\beta$ and transforms it into a two-phase synchronous frame:

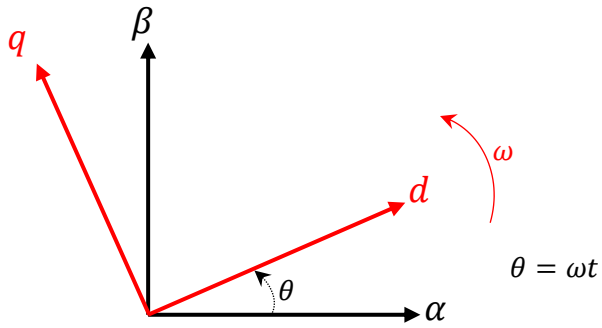

$$f_d = f_\alpha cos\theta + f_\beta sin\theta$$
$$f_q = -f_\alpha sin\theta + f_\beta cos\theta$$

$$\rightarrow \quad \begin{bmatrix} f_d \\ f_q \end{bmatrix} = \begin{bmatrix} cos\theta & sin\theta \\ -sin\theta & cos\theta \end{bmatrix} \cdot \begin{bmatrix} f_\alpha \\ f_\beta \end{bmatrix}$$

Amplitude invariant abc to dq transformation:

$$\begin{bmatrix} f_d \\ f_q \end{bmatrix} = \frac{2}{3} \cdot \begin{bmatrix} cos\theta & sin\theta \\ -sin\theta & cos\theta \end{bmatrix} \begin{bmatrix} 1 & -\frac{1}{2} & -\frac{1}{2} \\ 0 & \frac{\sqrt{3}}{2} & -\frac{\sqrt{3}}{2} \end{bmatrix} \begin{bmatrix} f_a \\ f_b \\ f_c \end{bmatrix}$$

$$\begin{bmatrix} f_d \\ f_q \end{bmatrix} = \frac{2}{3} \cdot \begin{bmatrix} \cos\theta & \cos(\theta - \frac{2\pi}{3}) & \cos(\theta + \frac{2\pi}{3}) \\ -sin\theta & -\sin(\theta - \frac{2\pi}{3}) & -\sin(\theta + \frac{2\pi}{3}) \end{bmatrix} \begin{bmatrix} f_a \\ f_b \\ f_c \end{bmatrix}$$

The inverse transformation from the dq frame to the abc frame:

$$\begin{bmatrix} f_a \\ f_b \\ f_c \end{bmatrix} = \begin{bmatrix} \cos\theta & -\sin\theta \\ \cos(\theta - \frac{2\pi}{3}) & -\sin(\theta - \frac{2\pi}{3}) \\ \cos(\theta + \frac{2\pi}{3}) & -\sin(\theta + \frac{2\pi}{3}) \end{bmatrix} \begin{bmatrix} f_d \\ f_q \end{bmatrix}$$

Power invariant abc to dq transformation:

$$\begin{bmatrix} f_d \\ f_q \end{bmatrix} = \sqrt{\frac{2}{3}}.\begin{bmatrix} \cos\theta & \cos\left(\theta - \frac{2\pi}{3}\right) & \cos\left(\theta + \frac{2\pi}{3}\right) \\ -sin\theta & -\sin\left(\theta - \frac{2\pi}{3}\right) & -\sin\left(\theta + \frac{2\pi}{3}\right) \end{bmatrix}\begin{bmatrix} f_a \\ f_b \\ f_c \end{bmatrix}$$

The inverse transformation from the dq frame to the abc frame:

$$\begin{bmatrix} f_a \\ f_b \\ f_c \end{bmatrix} = \sqrt{\frac{2}{3}}.\begin{bmatrix} \cos\theta & -\sin\theta \\ \cos\left(\theta - \frac{2\pi}{3}\right) & -\sin\left(\theta - \frac{2\pi}{3}\right) \\ \cos\left(\theta + \frac{2\pi}{3}\right) & -\sin\left(\theta + \frac{2\pi}{3}\right) \end{bmatrix}\begin{bmatrix} f_d \\ f_q \end{bmatrix}$$

Synchronization mechanism in a PLL:

The structure of the SRF-PLL is recalled in the following figure:

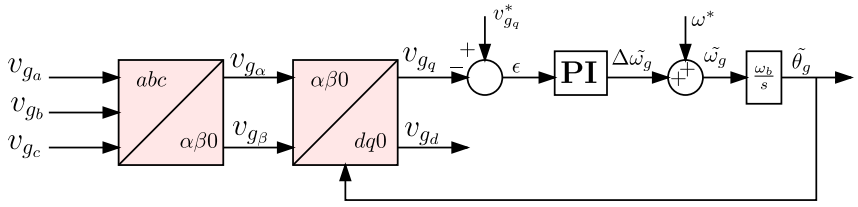

The inputs of the PLL are the three-phase voltage signals $v_{g_{abc}}$, which are sensed at the PCC. They can be expressed, in per-unit, by the following equation:

$$\begin{bmatrix} v_{g_a} \\ v_{g_b} \\ v_{g_c} \end{bmatrix} = \begin{bmatrix} V_g\, cos(\theta_g) \\ V_g\, cos\left(\theta_g - \frac{2\pi}{3}\right) \\ V_g cos\left(\theta_g + \frac{2\pi}{3}\right) \end{bmatrix}$$

The grid voltage signals are converted to two-phase stationary reference frame signals v_{g_α} and v_{g_β}, which are given by:

$$\begin{bmatrix} v_{g_\alpha} \\ v_{g_\beta} \end{bmatrix} = \sqrt{\frac{2}{3}}\begin{bmatrix} 1 & -\frac{1}{2} & -\frac{1}{2} \\ 0 & \frac{\sqrt{3}}{2} & -\frac{\sqrt{3}}{2} \end{bmatrix}\begin{bmatrix} v_{g_a} \\ v_{g_b} \\ v_{g_c} \end{bmatrix} = \sqrt{\frac{3}{2}}\begin{bmatrix} V_g cos\left(\theta_g\right) \\ V_g sin(\theta_g) \end{bmatrix}$$

v_{g_α} and v_{g_β} are directly fed into the next function which is $\alpha\beta$ to dq rotating reference frame transformation matrix with time-domain angle of $\tilde{\theta}_g$. This later is given by:

$$\begin{bmatrix} v_{g_d} \\ v_{g_q} \end{bmatrix} = \underbrace{\begin{bmatrix} cos\left(\tilde{\theta}_g\right) & sin(\tilde{\theta}_g) \\ -sin\left(\tilde{\theta}_g\right) & cos(\tilde{\theta}_g) \end{bmatrix}}_{\boldsymbol{R}(\tilde{\theta}_g)}\begin{bmatrix} v_{g_\alpha} \\ v_{g_\beta} \end{bmatrix} = \sqrt{\frac{3}{2}}\begin{bmatrix} V_g cos\left(\theta_g - \tilde{\theta}_g\right) \\ V_g sin\left(\theta_g - \tilde{\theta}_g\right) \end{bmatrix}$$

The aim of the PLL is to achieve the equality $\theta_g = \tilde{\theta}_g$ in steady state. Doing so yields:

$$\begin{bmatrix} v_{g_d} \\ v_{g_q} \end{bmatrix} = \sqrt{\frac{3}{2}} \begin{bmatrix} V_g \\ 0 \end{bmatrix}$$

In order to meet this last formula, the PI-controller used in the PLL has to regulate v_{g_q} to its reference $v_{g_q}^* = 0$ in the steady state. The output of the controller is the estimated grid frequency $\tilde{\omega}_g$. The estimated phase angle $\tilde{\theta}_g$ is then derived by the integration of $\tilde{\omega}_g$:

$$\tilde{\theta}_g = \omega_b \int \tilde{\omega}_g \, dt$$

The system is nonlinear because of the rotational matrix $\mathbf{R}(\tilde{\theta}_g)$. By assuming a small difference between the grid phase angle and the estimated one, the nonlinearity can be neglected i.e., $cos\,(\theta_g - \tilde{\theta}_g) \approx 1$ and $sin\,(\theta_g - \theta_{est}) \approx (\theta_g - \tilde{\theta}_g)$. Based on this assumption, following figure describes both linear and nonlinear models for the PLL:

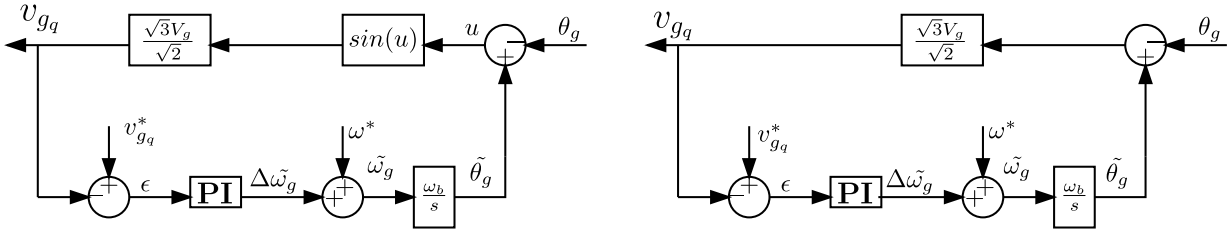

(a) Nonlinear model (b) Linearized model

Thanks to the linearized model, the transfer function of the SRF-PLL is expressed as follows:

$$\frac{v_{gq}}{v_{gq}^*} = \frac{1 + \frac{k_{p_{PLL}}}{k_{i_{PLL}}} s}{1 + \frac{k_{p_{PLL}}}{k_{i_{PLL}}} s + \frac{1}{k_{i_{PLL}} \omega_b} s^2}$$

where $k_{p_{PLL}}$ and $k_{i_{PLL}}$ are the proportional control gain and integrator gain of the PI controller, respectively. The characteristic polynomial of the closed-loop system $\Delta(s) = 1 + \frac{k_{p_{PLL}}}{k_{i_{PLL}}} s + \frac{1}{k_{i_{PLL}} \omega_b} s^2$ determines the natural frequency ω_n and damping ratio ζ and as follow:

$$\omega_n = \sqrt{k_{i_{PLL}} \omega_b} \quad , \quad \zeta = \frac{k_{p_{PLL}} \omega_b}{2\omega_n}$$

Typically, the value of damping ratio is set to 0.7 to achieve a 5% overshoot and or set to1 to have no overshoot. The response time of the PLL $t_{r_{PLL}}$ is obtained by:

$$t_{r_{PLL}} = \begin{cases} \frac{3}{\omega_n} & if \ \zeta = 0.7 \\ \frac{5}{\omega_n} & if \ \zeta = 1 \end{cases}$$

Appendix B

Building-block approach to obtain the state-space model:

This method is used to derive the state matrix of a system for the goal of small-signal stability analysis. The system is first split to so-called "building-blocks" and all the equations including differential, algebraic and output equations are written at the building block level. Then, by using the coupling equations all building blocks are assembled to form the whole system. In this stage, all the equations that describe the system are available. Finally, thanks to the Jacobian matrix, the system equations are linearized around a specific operating point and the state matrix can be derived.

In the following, the application of the system Jacobian matrix in calculating the state matrix is briefly explained and then an example of using building-block method to derive the state-space model of a two-level VSC with grid-forming control is presented.

Let's suppose that x is the state vector, y is the algebraic variables vector, u is the input vector and z is the output vector. The whole system equations can be written as follow:

$$\dot{x} = f(x, y, u)$$
$$0 = g(x, y, u)$$
$$z = h(x, y, u).$$

Linearization of the abovementioned equations results in:

$$\Delta\dot{x} = A\Delta x + B\Delta y + C\Delta u$$
$$0 = D\Delta x + E\Delta y + F\Delta u$$
$$\Delta z = G\Delta x + H\Delta y + K\Delta u$$

where:

$$A = \frac{\partial f}{\partial x} \qquad B = \frac{\partial f}{\partial y} \qquad C = \frac{\partial f}{\partial u}$$

$$D = \frac{\partial g}{\partial x} \qquad E = \frac{\partial g}{\partial y} \qquad F = \frac{\partial g}{\partial u}$$

$$G = \frac{\partial h}{\partial x} \qquad H = \frac{\partial h}{\partial y} \qquad K = \frac{\partial h}{\partial u}$$

Jacobian matrix is then defined as follows:

$$J = \begin{bmatrix} A & B & C \\ D & E & F \\ G & H & K \end{bmatrix}$$

On the other hand, the state-space model is expressed as:

$$\Delta\dot{x} = A_{ss}x + B_{ss}u$$
$$\Delta z = C_{ss}x + D_{ss}u$$

The aim is to derive the state matrix of a system A_{ss} from the Jacobian matrix. To do so, the following relation is used:

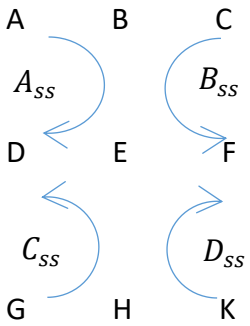

$$A_{ss} = A - BE^{-1}D = \frac{\partial f}{\partial x} - \frac{\partial f}{\partial y}\left(\frac{\partial g}{\partial y}\right)^{-1}\frac{\partial g}{\partial x}$$

The same approach can be used to obtain B_{ss}, C_{ss} and D_{ss}.

Example:

Following figure shows the general scheme of the studied VSC with grid-forming control. In this simple example, there are three building blocks including: 1- GRD (grid), 2- VSC01 and 3- power control strategy (PCS01). The grid is modeled with an ideal voltage source in series with the Thevenin equivalent impedance. The VSC is modeled with a controllable voltage source and a transformer.

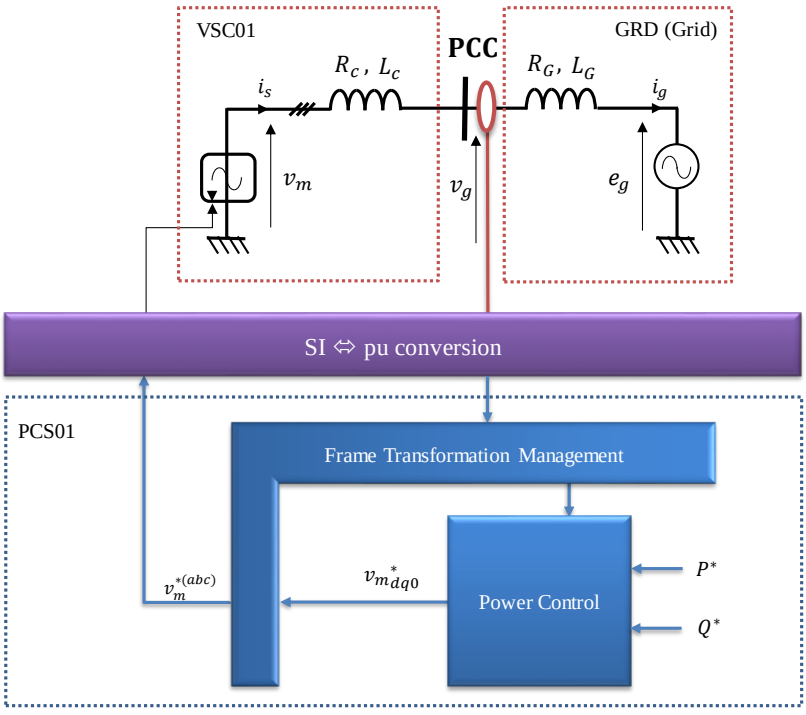

Balding-block representation of the grid-forming.

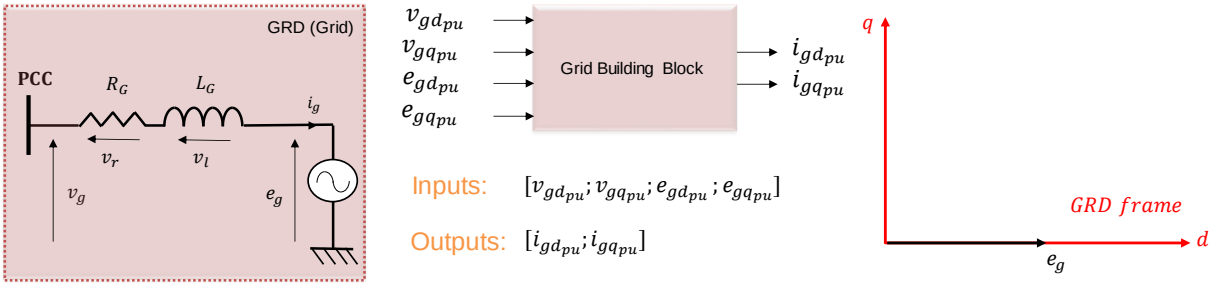

Grid building block presentation.

GRD building block:

The equations that describe this building block need to be written. Note that all the equations for this building block and all other building blocks are expressed in per-unit system and they are written in the synchronous reference frame. In order to put all the system equations in a same frame, the voltage of the ideal source e_g is consider as the reference. Therefore, in SI we obtain two differential equations as well as two algebraic equations:

$$\frac{di_{gd}}{dt} = \frac{1}{L_g} v_{ld} + \omega_g L_g i_{gq}$$
$$\frac{di_{gd}}{dt} = \frac{1}{L_g} v_{ld} + \omega_g L_g i_{gq}$$
$$0 = -v_{ld} + v_{pccd} - R_g i_{gd} - v_{gd}$$
$$0 = -v_{lq} + v_{pccq} - R_g i_{gq} - v_{gq}$$

In per-unit system, we obtain:

$$\frac{di_{gd_{pu}}}{dt} = \frac{\omega_B \sqrt{3}}{L_{G_{pu}}} v_{ld_{pu}} + \omega_{g_{pu}} \omega_B i_{gq_{pu}}$$
$$\frac{di_{gq_{pu}}}{dt} = \frac{\omega_B \sqrt{3}}{L_{G_{pu}}} v_{lq_{pu}} - \omega_{g_{pu}} \omega_B i_{gd_{pu}}$$
$$0 = -v_{ld_{pu}} + v_{gd_{pu}} - \frac{1}{\sqrt{3}} R_{G_{pu}} i_{gd_{pu}} - e_{gd_{pu}}$$
$$0 = -v_{lq_{pu}} + v_{gq_{pu}} - \frac{1}{\sqrt{3}} R_{G_{pu}} i_{gq_{pu}} - e_{gq_{pu}}$$

The grid building block is expressed in a Matlab script as follows:

```
%% GRD : Grid building block

% inputs : [GRD_vgd_pu GRD_vgq_pu GRD_egd_pu GRD_egq_pu]
% outputs : [GRD_igd_pu GRD_igq_pu]

% states : [GRD_igd_pu GRD_igq_pu]
% algebraic variables : [GRD_vld_pu GRD_vlq_pu]

% symbolic definition:

syms GRD_Lg_pu_s GRD_Rg_pu_s GRD_wB_s GRD_wg_pu_s
syms GRD_igd_pu_s GRD_igq_pu_s
syms GRD_vgd_pu_s GRD_vgq_pu_s GRD_egd_pu_s GRD_egq_pu_s GRD_vld_pu_s GRD_vlq_pu_s


% Differential equations:

GRD_DIF01 = (sqrt(3)*GRD_wB_s)*(GRD_vld_pu_s/GRD_Lg_pu_s)+GRD_wg_pu_s*GRD_wB_s*GRD_igq_pu_s;
GRD_DIF02 = (sqrt(3)*GRD_wB_s)*(GRD_vlq_pu_s/GRD_Lg_pu_s)-GRD_wg_pu_s*GRD_wB_s*GRD_igd_pu_s;

% Algebraic equations:

GRD_ALG01 = -GRD_vld_pu_s+GRD_vgd_pu_s-(1/sqrt(3))*GRD_Rg_pu_s*GRD_igd_pu_s-GRD_vgd_pu_s;
GRD_ALG02 = -GRD_vlq_pu_s+GRD_vgq_pu_s-(1/sqrt(3))*GRD_Rg_pu_s*GRD_igq_pu_s-GRD_vgq_pu_s;

% Output equations:

GRD_OUT01 = GRD_igd_pu_s;
GRD_OUT02 = GRD_igq_pu_s;

% Putting all equations and variables in GRD matrices:

GRD_difEquations = [GRD_DIF01 GRD_DIF02];
GRD_algEquations = [GRD_ALG01 GRD_ALG02];
GRD_outEquations = [GRD_OUT01 GRD_OUT02];

GRD_difVariables = [GRD_igd_pu_s GRD_igq_pu_s];
GRD_algVariables = [GRD_vld_pu_s GRD_vlq_pu_s];
GRD_inputs = [GRD_vgd_pu_s GRD_vgq_pu_s GRD_vgd_pu_s GRD_vgq_pu_s];
```

VSC01 building block:

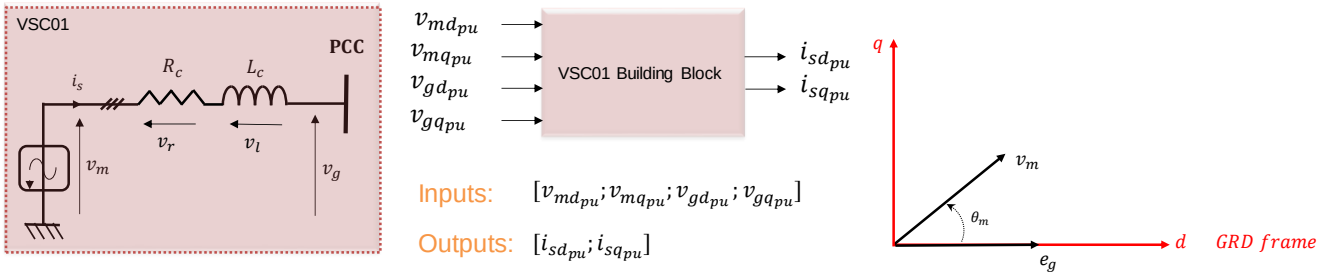

VSC01 building block presentation.

The VSC01 building block consists of a controlled voltage source that controls v_m and a simplified model of transformer connected to PCC. It should be noted that all the system equations are written in a common frame which is the grid frame. Similar to the

grid building block, we obtain two differential equations as well as two algebraic equations in per-unit as follows:

$$\frac{di_{sd_{pu}}}{dt} = \frac{\omega_B\sqrt{3}}{L_{c_{pu}}} v_{ld_{pu}} + \omega_{g_{pu}}\omega_B i_{sq_{pu}}$$

$$\frac{di_{sq_{pu}}}{dt} = \frac{\omega_B\sqrt{3}}{L_{c_{pu}}} v_{lq_{pu}} - \omega_{g_{pu}}\omega_B i_{sd_{pu}}$$

$$0 = -v_{ld_{pu}} + v_{md_{pu}} - \frac{1}{\sqrt{3}} R_{c_{pu}} i_{sd_{pu}} - v_{gd_{pu}}$$

$$0 = -v_{lq_{pu}} + v_{mq_{pu}} - \frac{1}{\sqrt{3}} R_{c_{pu}} i_{sq_{pu}} - v_{gq_{pu}}$$

The VSC01 building block is expressed in a Matlab script follows:

```
%% VSC01: Voltage Source Converter 01

% inputs : [VSC01_vmd_pu VSC01_vmq_pu VSC01_vgd_pu VSC01_vgq_pu]
% outputs : [VSC01_isd_pu VSC01_isq_pu]

% states : [VSC01_isd_pu VSC01_isq_pu]
% algebraic : [VSC01_vld_pu_s VSC01_vlq_pu_s]

% Symbolic definition:
syms VSC01_vmd_pu_s VSC01_vmq_pu_s VSC01_isd_pu_s VSC01_isq_pu_s
syms VSC01_vgd_pu_s VSC01_vgq_pu_s VSC01_wB_s VSC01_wg_pu_s
syms VSC01_vld_pu_s VSC01_vlq_pu_s VSC01_Lc_pu_s VSC01_Rc_pu_s

% Differential equation:

VSC01_DIF01 =
(sqrt(3)*VSC01_wB_s)*(VSC01_vld_pu_s/VSC01_Lc_pu_s)+VSC01_wg_pu_s*VSC01_wB_s*VSC01_isq_pu_s;

VSC01_DIF02 =
(sqrt(3)*VSC01_wB_s)*(VSC01_vlq_pu_s/VSC01_Lc_pu_s)-VSC01_wg_pu_s*VSC01_wB_s*VSC01_isd_pu_s;

% Algebraic equations:

VSC01_ALG01 = -VSC01_vld_pu_s+VSC01_vmd_pu_s-(1/sqrt(3))*VSC01_Rc_pu_s*VSC01_isd_pu_s-
VSC01_vgd_pu_s;

VSC01_ALG02 = -VSC01_vlq_pu_s+VSC01_vmq_pu_s-(1/sqrt(3))*VSC01_Rc_pu_s*VSC01_isq_pu_s-
VSC01_vgq_pu_s;

% Output equations:

VSC01_OUT01 = VSC01_isd_pu_s;
VSC01_OUT02 = VSC01_isq_pu_s;

% Putting all equations and variables in VSC01 matrices:

VSC01_difEquations = [VSC01_DIF01 VSC01_DIF02];
VSC01_algEquations = [VSC01_ALG01 VSC01_ALG02];
VSC01_outEquations = [VSC01_OUT01 VSC01_OUT02];

VSC01_difVariables = [VSC01_isd_pu_s VSC01_isq_pu_s];
VSC01_algVariables = [VSC01_vld_pu_s VSC01_vlq_pu_s];
VSC01_inputs = [VSC01_vmd_pu_s VSC01_vmq_pu_s VSC01_vgd_pu_s VSC01_vgq_pu_s];
```

PCS01 building block:

This building block controls includes the active power control (based on the droop control) and TVR. Note that the effect of fast dynamics is neglected. Therefore, the cascaded voltage and current control loops are not included in the model. A damping resistor is used to damp the oscillations around the grid nominal frequency. Following figure shows the PCS01 building block in detail.

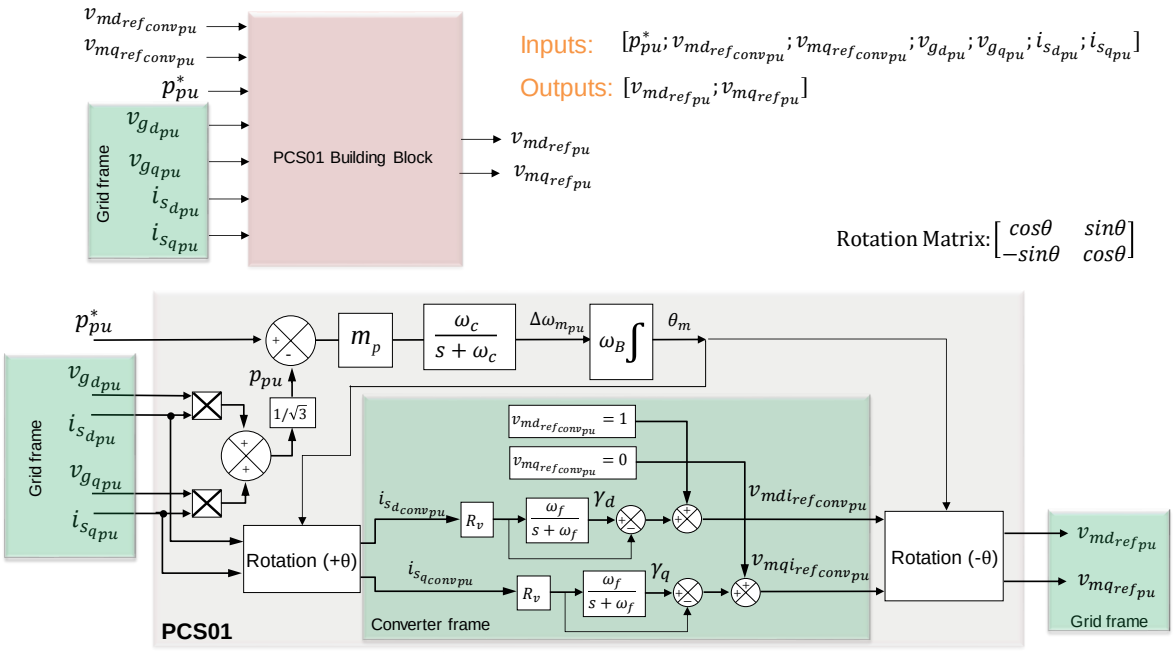

PCS01 building block presentation.

Following equations describe the PCS01 building block:

$$\frac{d\theta_m}{dt} = \omega_B . \Delta\omega_{m_{pu}}$$

$$\frac{d\Delta\omega_{m_{pu}}}{dt} = (p^*_{pu} - p_{pu}) m_p \omega_c - \Delta\omega_{m_{pu}} . \omega_c$$

$$\frac{d\gamma_d}{dt} = -\omega_f \gamma_d + R_v . \omega_f . i_{s_{d_{convpu}}}$$

$$\frac{d\gamma_q}{dt} = -\omega_f \gamma_q + R_v . \omega_f . i_{s_{q_{convpu}}}$$

$$0 = -p_{pu} + \frac{1}{\sqrt{3}} (v_{pcc_{d_{pu}}} . i_{s_{d_{pu}}} + v_{pcc_{q_{pu}}} . i_{s_{q_{pu}}})$$

$$0 = -i_{s_{d_{convpu}}} + i_{s_{d_{pu}}} . \cos(\theta_m) + i_{s_{q_{pu}}} . \sin(\theta_m)$$

$$0 = -i_{s_{q_{convpu}}} - i_{s_{d_{pu}}} . \sin(\theta_m) + i_{s_{q_{pu}}} . \cos(\theta_m)$$

$$0 = -v_{mdi_{ref_{convpu}}} - R_v . i_{s_{d_{convpu}}} + v_{md_{ref_{convpu}}} + \gamma_d$$

$$0 = -v_{mqi_{ref_{convpu}}} - R_v . i_{s_{q_{convpu}}} + v_{mq_{ref_{convpu}}} + \gamma_q$$

$$0 = -v_{md_{ref_{pu}}} + v_{mdi_{ref_{convpu}}} . \cos(-\theta_m) + v_{mqi_{ref_{convpu}}} . \sin(-\theta_m)$$

$$0 = -v_{mq_{ref_{pu}}} - v_{mdi_{ref_{convpu}}} . \sin(-\theta_m) + v_{mqi_{ref_{convpu}}} . \cos(-\theta_m)$$

The PCS01 building block is expressed in a Matlab script as follows:

```
%% PCS01: Power Control Strategy

% inputs : [PCS01_p_ref_pu PCS01_vmd_ref_conv_pu PCS01_vmq_ref_conv_pu PCS01_vgd_pu
PCS01_vgq_pu PCS01_isd_pu PCS01_isq_pu]
% outputs : [PCS01_vmd_ref_pu PCS01_vmq_ref_pu]

% states : [PCS01_thetam_rad PCS01_delta_wm_pu PCS01_gammad PCS01_gammaq]
% algebraic : [PCS01_p_pu PCS01_isd_conv_pu PCS01_isq_conv_pu PCS01_vmdi_ref_conv_pu
PCS01_vmqi_ref_conv_pu PCS01_vmd_ref_pu PCS01_vmq_ref_pu]

% Symbolic definition:
syms PCS01_mp_s PCS01_wB_s PCS01_wf_s PCS01_wc_s PCS01_Rv_pu_s PCS01_p_ref_pu_s
PCS01_p_pu_s PCS01_delta_wm_pu_s PCS01_thetam_rad_s
syms PCS01_vmd_ref_pu_s PCS01_vmq_ref_pu_s PCS01_vmd_ref_conv_pu_s PCS01_vmdi_ref_conv_pu_s
PCS01_vmqi_ref_conv_pu_s PCS01_vmq_ref_conv_pu_s
syms PCS01_vgd_pu_s PCS01_vgq_pu_s PCS01_isd_pu_s PCS01_isq_pu_s PCS01_isd_conv_pu_s
PCS01_isq_conv_pu_s
syms PCS01_gammad_s PCS01_gammaq_s

% Differential equations:

PCS01_DIF01 = GRD_wB_s * PCS01_delta_wm_pu_s;
PCS01_DIF02 = (PCS01_p_ref_pu_s-PCS01_p_pu_s)*PCS01_mp_s*PCS01_wc_s-
PCS01_delta_wm_pu_s*PCS01_wc_s;
PCS01_DIF03 = -PCS01_wf_s*PCS01_gammad_s+PCS01_Rv_pu_s*PCS01_wf_s*PCS01_isd_conv_pu_s;
PCS01_DIF04 = -PCS01_wf_s*PCS01_gammaq_s+PCS01_Rv_pu_s*PCS01_wf_s*PCS01_isq_conv_pu_s;

% Algebraic equations:

PCS01_ALG01 = -PCS01_p_pu_s+(1/sqrt(3))*(PCS01_vpccd_pu_s*PCS01_isd_pu_s+PCS01_vpccq_pu_s*
PCS01_isq_pu_s);
PCS01_ALG02 = -PCS01_isd_conv_pu_s
+PCS01_isd_pu_s*cos(PCS01_thetam_rad_s)+PCS01_isq_pu_s*sin (PCS01_thetam_rad_s);

PCS01_ALG03 = -PCS01_isq_conv_pu_s-
PCS01_isd_pu_s*sin(PCS01_thetam_rad_s)+PCS01_isq_pu_s*cos (PCS01_thetam_rad_s);
PCS01_ALG04 = -PCS01_vmdi_ref_conv_pu_s-PCS01_Rv_pu_s*PCS01_isd_conv_pu_s+
PCS01_vmd_ref_conv_pu_s+PCS01_gammad_s;
PCS01_ALG05 = -PCS01_vmqi_ref_conv_pu_s-PCS01_Rv_pu_s*PCS01_isq_conv_pu_s+
PCS01_vmq_ref_conv_pu_s+PCS01_gammaq_s;
PCS01_ALG06 = -PCS01_vmd_ref_pu_s+PCS01_vmdi_ref_conv_pu_s*cos(-PCS01_thetam_rad_s)+
PCS01_vmqi_ref_conv_pu_s* sin(-PCS01_thetam_rad_s);
PCS01_ALG07 = -PCS01_vmq_ref_pu_s-PCS01_vmdi_ref_conv_pu_s*sin(-PCS01_thetam_rad_s)+
PCS01_vmqi_ref_conv_pu_s*cos(-PCS01_thetam_rad_s);

% Output equations:

PCS01_OUT01 = PCS01_vmd_ref_pu_s;
PCS01_OUT02 = PCS01_vmq_ref_pu_s;

% Putting all equations and variables in PCS01 matrices:

PCS01_difEquations = [PCS01_DIF01 PCS01_DIF02 PCS01_DIF03 PCS01_DIF04];
PCS01_algEquations = [PCS01_ALG01 PCS01_ALG02 PCS01_ALG03 PCS01_ALG04 PCS01_ALG05
PCS01_ALG06 PCS01_ALG07];
PCS01_outEquations = [PCS01_OUT01 PCS01_OUT02];
PCS01_difVariables = [PCS01_thetam_rad_s PCS01_delta_wm_pu_s PCS01_gammad_s
PCS01_gammaq_s];
PCS01_algVariables = [PCS01_p_pu_s PCS01_isd_conv_pu_s PCS01_isq_conv_pu_s
PCS01_vmdi_ref_conv_pu_s PCS01_vmqi_ref_conv_pu_s PCS01_vmd_ref_pu_s PCS01_vmq_ref_pu_s];
PCS01_inputs = [PCS01_p_ref_pu_s PCS01_vmd_ref_conv_pu_s PCS01_vmq_ref_conv_pu_s
PCS01_vgd_pu_s PCS01_vgq_pu_s PCS01_isd_pu_s PCS01_isq_pu_s];
```

Building block assembly:

In this step, all there aforementioned building blocks are assembled is a single system by using coupling equations. The coupling equations are considered as the algebraic equations that relate the outputs of a building block to the inputs of the other building block. Note that a decoupling element (e.g., a high value of resistance) has to be defined in order to be able to connect the VSC01 building block to the GRD building block. The system assembly script is expressed as follows:

```
%% Building block assembly

CPLG_R=10000000;
syms CPLG_vd_pu_s CPLG_vq_pu_s CPLG_id_pu_s CPLG_iq_pu_s

% Step 01 : CPLG coupling equations and putting all equations and variables in system
matrices:

SYS_CPLG01 = - VSC01_vmd_pu_s + PCS01_vmd_ref_pu_s  ;
SYS_CPLG02 = - VSC01_vmq_pu_s + PCS01_vmq_ref_pu_s;

SYS_CPLG03 = - CPLG_id_pu_s + VSC01_isd_pu_s - GRD_igd_pu_s;
SYS_CPLG04 = - CPLG_iq_pu_s + VSC01_isq_pu_s - GRD_igq_pu_s;
SYS_CPLG05 = - CPLG_vd_pu_s + CPLG_R * CPLG_id_pu_s;
SYS_CPLG06 = - CPLG_vq_pu_s + CPLG_R * CPLG_iq_pu_s;

SYS_CPLG07 = - VSC01_vgd_pu_s + CPLG_vd_pu_s;
SYS_CPLG08 = - VSC01_vgq_pu_s + CPLG_vq_pu_s;
SYS_CPLG09 = - GRD_vgd_pu_s + CPLG_vd_pu_s;
SYS_CPLG10 = - GRD_vgq_pu_s + CPLG_vq_pu_s;

SYS_CPLG11 = - PCS01_vgd_pu_s + VSC01_vgd_pu_s;
SYS_CPLG12 = - PCS01_vgq_pu_s + VSC01_vgq_pu_s;
SYS_CPLG13 = - PCS01_isd_pu_s + VSC01_isd_pu_s;
SYS_CPLG14 = - PCS01_isq_pu_s + VSC01_isq_pu_s;


CPLG_algEquations = [SYS_CPLG01 SYS_CPLG02 SYS_CPLG03 SYS_CPLG04 SYS_CPLG05 SYS_CPLG06
SYS_CPLG07 SYS_CPLG08 SYS_CPLG09 SYS_CPLG10 SYS_CPLG11 SYS_CPLG12 SYS_CPLG13 SYS_CPLG14];

CPLG_algVariables = [VSC01_vmd_pu_s VSC01_vmq_pu_s CPLG_id_pu_s CPLG_iq_pu_s CPLG_vd_pu_s
CPLG_vq_pu_s VSC01_vg_pu_s VSC01_vgq_pu_s GRD_vgd_pu_s GRD_vgq_pu_s PCS01_vgd_pu_s
PCS01_vgq_pu_s PCS01_isd_pu_s PCS01_isq_pu_s];

SYS_OUT01 = PCS01_p_pu_s;   % Considering the VSC active power as the output

SYS_difEquations = [PCS01_difEquations VSC01_difEquations GRD_difEquations];

SYS_algEquations = [PCS01_algEquations VSC01_algEquations GRD_algEquations
CPLG_algEquations];

SYS_outEquations = [SYS_OUT01];

SYS_difVariables = [PCS01_difVariables VSC01_difVariables GRD_difVariables];

SYS_algVariables = [PCS01_algVariables VSC01_algVariables GRD_algVariables
CPLG_algVariables];

SYS_inputs = [PCS01_p_ref_pu_s PCS01_vmd_ref_conv_pu_s PCS01_vmq_ref_conv_pu_s
GRD_egd_pu_s GRD_egq_pu_s];
```

```
%% Giving the equation IDs

for i = 1 : length(SYS_difEquations)
    SYS_difEqIDs(i) = i;
    i = i+1;
end
k = 1;
for i = length(SYS_difEquations)+1 : length(SYS_algEquations)+length(SYS_difEquations)
    SYS_algEqIDs(k) = i;
    i = i+1;
    k = k+1;
end
k = 1;
for i = length(SYS_algEquations)+length(SYS_difEquations)+1 :
length(SYS_outEquations)+length(SYS_algEquations)+length(SYS_difEquations)
    SYS_outEqIDs(k) = i;
    i = i+1;
    k = k+1;
end

%Giving the variable IDs

SYS_difVarIDs = SYS_difEqIDs;
SYS_algVarIDs = SYS_algEqIDs;
k = 1;
for i = length(SYS_difVarIDs)+length(SYS_algVarIDs)+1 :
length(SYS_inpu_sts)+length(SYS_difVarIDs)+length(SYS_algVarIDs)
    SYS_inpu_stsVarIDs(k)=i;
    i = i+1;
    k = k+1;
end

SYS_JacobianFull_s = jacobian([SYS_difEquations SYS_algEquations
SYS_outEquations],[SYS_difVariables SYS_algVariables SYS_inputs]);

% Step 03 : Transforming symbolic to numerical

matlabFunction(SYS_JacobianFull_s,'FILE','SYS_Sym2NumJacobian');

SYS_JacobianFull =
SYS_Sym2NumJacobian(GRD_wB,GRD_Lg_pu,GRD_Rg_pu,GRD_wg_pu,PCS01_wB,PCS01_wc,PCS01_mp,PCS01_
wf,PCS01_Rv_pu,PCS01_isd0_pu,PCS01_isq0_pu,PCS01_vpccd0_pu,PCS01_vpccq0_pu,PCS01_thetam0_r
ad,PCS01_vmd0_ref_conv_pu,PCS01_vmq0_ref_conv_pu,VSC01_wB,VSC01_Lc_pu,VSC01_Rc_pu,VSC01_wg
_pu);
% Step 04 : Deducing A, B, C, D, E, F, G, H, K
SYS_dFdX = SYS_JacobianFull(SYS_difEqIDs,SYS_difVarIDs);
SYS_dFdY = SYS_JacobianFull(SYS_difEqIDs,SYS_algVarIDs);
SYS_dFdU = SYS_JacobianFull(SYS_difEqIDs,SYS_inpu_stsVarIDs);
SYS_dGdX = SYS_JacobianFull(SYS_algEqIDs,SYS_difVarIDs);
SYS_dGdY = SYS_JacobianFull(SYS_algEqIDs,SYS_algVarIDs);
SYS_dGdU = SYS_JacobianFull(SYS_algEqIDs,SYS_inpu_stsVarIDs);
SYS_dHdX = SYS_JacobianFull(SYS_outEqIDs,SYS_difVarIDs);
SYS_dHdY = SYS_JacobianFull(SYS_outEqIDs,SYS_algVarIDs);
SYS_dHdU = SYS_JacobianFull(SYS_outEqIDs,SYS_inpu_stsVarIDs);

% State space calculation: Deducing Ass, Bss, Css, Dss,
SYS_Ass = SYS_dFdX-SYS_dFdY*(inv(SYS_dGdY))*SYS_dGdX;
SYS_Bss = SYS_dFdU-SYS_dFdY*(inv(SYS_dGdY))*SYS_dGdU;
SYS_Css = SYS_dHdX-SYS_dHdY*(inv(SYS_dGdY))*SYS_dGdX;
SYS_Dss = SYS_dHdU-SYS_dHdY*(inv(SYS_dGdY))*SYS_dGdU;
```

It should be noted that the Jacobian function is available as a Matlab function. All the calculations are in symbolic, and the system Jacobian matrix is then converted to a numerical matrix. For this transformation, the initial operating point of the system to specify the initial voltages, currents and angles is needed.

Appendix C

Anti-windup:

During the operation of the converter in saturated mode, an anti-windup on the voltage PI controller is required. Following figure shows the implemented CSA and anti-windup strategy. In voltage control mode, $\Delta e_{g_d} = \Delta e_{g_q} = 0$ and the current magnitude is less than the threshold $I_{max_{SAT}}$. Therefore, the input "1" of the switches appears in the output ($i^*_{s_{dqS}} = i^*_{s_{dq}}$). When a fault activates the saturation mode, the input (2) passes through the switches. During the saturated operation mode, the integrator is frozen by multiplying its input to zero. Note that the voltage errors $\Delta e_{g_{dq}}$ are used to eliminate the switching effect around $I_{max_{SAT}}$. As soon as the voltage is recovered to 1 pu, $\Delta e_{g_{dq}} = 0$ and the converter switches back to the voltage control mode.

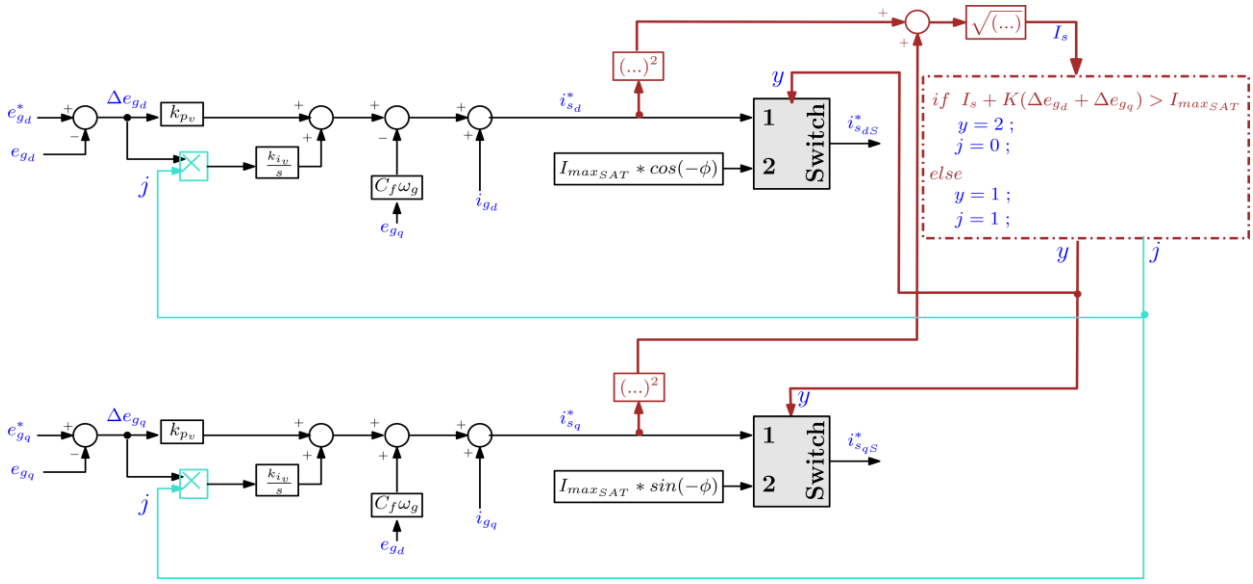

Structure of the implemented CSA and anti-windup ($K = 1$).

Appendix D

DC bus voltage controller:

Considering that total capacitance at the DC grid is $2C_{dc}$ as shown in following figure, the relation between the currents and voltages can be expressed as:

$$i_{dc} - i = 2C_{dc}\frac{du_{dc}}{dt}$$

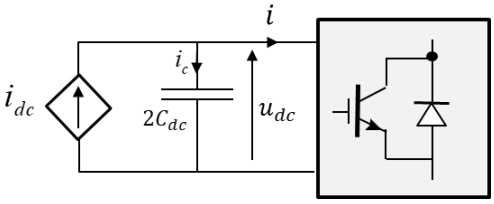

The DC side equation can be presented with respect to the active powers:

$$i_{dc}u_{dc} - iu_{dc} = 2C_{dc}\frac{du_{dc}}{dt}u_{dc} \;\Rightarrow\; p_{dc} - p = C_{dc}\frac{du_{dc}^2}{dt}$$

Following model is then derived to control the DC voltage:

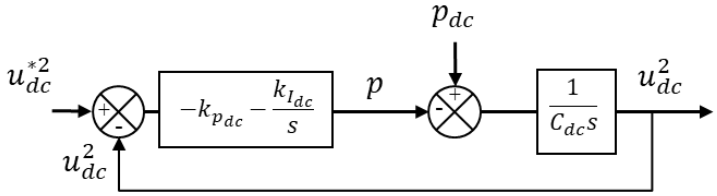

The closed-loop transfer function is obtained as follows:

$$\frac{u_{dc}^2}{u_{dc}^{*2}} = \frac{1 + \frac{k_{p_{dc}}}{k_{I_{dc}}}s}{1 + \frac{k_{p_{dc}}}{k_{I_{dc}}}s + \frac{C_{dc}}{k_{I_{dc}}}s^2}$$

The natural frequency ω_n and damping ratio ζ and as follow:

$$\omega_n = \sqrt{\frac{k_{I_{dc}}}{C_{dc}}} \quad , \quad \zeta = \frac{k_{p_{dc}}}{2\sqrt{k_{I_{dc}}C_{dc}}}$$

The response time of the DC controller is obtained by:

$$t_{r_{DC}} = \begin{cases} \frac{3}{\omega_n} & if\ \zeta = 0.7 \\ \frac{5}{\omega_n} & if\ \zeta = 1 \end{cases}$$

Grid-forming control strategies of power electronic converters in transmission grids: application to HVDC link

The rapid development of converter-based devices such as converter-interfaced renewable generations and high-voltage direct-current (HVDC) transmission links is causing a profound change into the very physics of the power system. In this scenario, the power generation is shifted from the pollutant synchronous generators based on nuclear or fossil fuels to converter-based renewable resources. The modeling, control, and stability of the power converters are now one of the focuses of attention for researchers. Today, power converters have the main function of injecting power into the utility grid, while relying on synchronous machines that ensure all system needs (e.g., ancillary services, provision of inertia and reliable power reserves). This operation mode of power converters is called "Grid-following". Grid-following converters have several limitations, such as: inability to operate in a standalone mode, stability issues under weak grids and faulty conditions and also, negative side effect on the system inertia. To tackle these challenges, the grid-forming control as an alternative has shown its appropriate performance that could make this kind of control a promising solution to respond to the system needs and to allow a stable and safe operation of power system with high penetration rate of power electronic converters.

In this thesis, a fundamental description of grid-forming control with a simplified quasi-static modeling approach aiming to regulate the converter active power by a voltage source behavior is presented. From the description, several variants of grid-forming strategies are identified that represent some differences in terms of active power dynamic behavior, inertia emulation capability and system frequency support. Hence, the presented grid-forming variants are then classified according to their capabilities/functionalities. From the small-signal stability and robustness point of view, the studied grid-forming controls, which are implemented to a 2-level VSC at first, show their ability to operate under very weak grid conditions. Moreover, the ancillary services such as inertial response and frequency support are appropriately provided to the AC grid.

The questions of the grid-forming converters protection against overcurrent and their post-fault synchronization while considering the current limitation are investigated and a new method is proposed to enhance the transient stability of the system. All the obtained results are then extended to a modular multi-level converter (MMC) topology successfully.

The use of a grid forming control in an HVDC converter is interesting for the grid to which it is connected due to the inertial effect that can be induced. Therefore, the final part of this thesis evaluates the dynamic performance of an HVDC link interconnecting two AC grids and highlights the proper strategy and requirements for inertia provision.

Keywords

Power converters, grid-forming control, HVDC interconnection, inertial effect, current limitation, transient stability

Contrôle en grid-forming pour convertisseurs d'électronique de puissance: application aux liaisons à courant continu de Haute Tension (HVDC)

Le développement rapide d'équipements raccordés sur les réseaux électriques avec des convertisseurs électroniques de puissance tels que les générateurs à base d'énergie renouvelable et les liaisons de transmission sous haute tension continue entraîne un changement profond dans la physique même du système électrique. Aujourd'hui, les convertisseurs de puissance ont pour fonction principale d'injecter de l'énergie dans le réseau électrique, ce dernier s'appuyant sur des machines synchrones pour assurer tous les besoins nécessaires au fonctionnement et à la conduite du système électrique (par exemple, les services auxiliaires, la fourniture de réserve inertielle énergétique et de réserves dynamiques et fiables de puissance). Ce mode de fonctionnement des convertisseurs de puissance est appelé "grid-following" car suivant la tension alternative imposée au point de raccordement. Il présente plusieurs limitations, telles que : l'incapacité de fonctionner en mode autonome, des problèmes de stabilité dans des réseaux faibles et des fonctionnements défectueux, ainsi que des effets secondaires négatifs sur l'inertie du système. Pour relever ces défis, une alternative est de contrôler le convertisseur électronique de puissance pour générer et contrôler lui-même cette tension alternative.

Dans cette thèse, une description fondamentale de cette commande en grid-forming est présentée avec une approche de modélisation quasi-statique simplifiée permettant de concevoir une régulation de la puissance active échangée avec le réseau AC. Plusieurs variantes de cette stratégie de contrôle sont mises en évidence et présentent des différences en termes de comportement dynamique sur la puissance active, de capacité d'émulation d'une réserve énergétique inertielle et de prise en charge de la fréquence du système. Les variantes sont ensuite classées en fonction de leurs capacités et fonctionnalités. Ces stratégies de commande ont été implémentées pour un convertisseur à 2 niveaux. Suivant une analyse de stabilité dite « petits signaux », la robustesse et leur capacité à fonctionner sur un réseau faible sont démontrées. De plus, les services auxiliaires tels que la réponse inertielle et le support au contrôle de la fréquence sont fournis de manière appropriée au réseau AC.

Les questions de la protection contre les surintensités et de la synchronisation après défaut (tout en tenant compte de la limitation de courant) sont étudiées et une nouvelle méthode est proposée pour améliorer la stabilité transitoire du système électrique. Les résultats obtenus sont ensuite généralisés à une topologie de convertisseur multi-niveaux modulaire (MMC) avec succès.

Avec cette commande, la fourniture d'une réserve inertielle est particulièrement intéressante pour gérer les transferts de puissance à l'interconnexion d'un réseau continu haute tension avec le réseau alternatif de transport d'électricité. La dernière partie de cette thèse évalue les performances dynamiques d'une liaison HVDC interconnectant deux réseaux AC et met en évidence la stratégie et les exigences appropriées pour la fourniture de réserve inertielle.

Mots clés

Convertisseur DC/AC-AC/DC, grid-forming contrôle, interconnexion de réseaux continus de haute tension (HVDC), effet d'inertie, limitation de courant, stabilité transitoire